

DISS. ETH NO. 26398

FUNCTIONAL COMPOSITES WITH CELLULOSE-BASED HIERARCHICAL STRUCTURE

A thesis submitted to attain the degree of

DOCTOR OF SCIENCES of ETH ZURICH

(Dr. sc. ETH Zurich)

Presented by

MICHAEL HAUSMANN

Ing. Sc. Mat. Dipl. EPF

École Polytechnique Fédérale de Lausanne

Born on 16.06.1990

Citizen of Switzerland, Medel (Lucmagn) GR

accepted on the recommendation of

Prof. André R. Studart

Prof. Ralph Spolenak

Prof. Marie-Pierre Laborie

Prof. Véronique Michaud

2019

To my Family

“The pessimist complains about the wind;

The optimist expects it to change;

The realist adjusts the sails.”

(William Arthur Ward)

I. Acknowledgements

I would like to thank Prof. André R. Studart, ETHZ, and Dr. Tanja Zimmermann, Empa, for having accepted me in their respective groups and for having supported and trusted me during my PhD thesis. I am grateful for their guidance and their challenging mindset which helped me to develop professionally and scientifically. I am also grateful for their perseverance to excellence which definitely is reflected in the scientific work of both respective groups I had the privilege of having been part of.

Above all, I would like to thank Gilberto Siqueira, Rafael Libanori and Patrick Rühls for their outstanding help, support, and motivation and for always being here when I needed them. Without them my PhD thesis would be far from what it is today. They were a true motivation and inspiration for my work and always supported even my craziest ideas. I also want to thank them for their time spent on correcting my papers and various texts without arguing or complaining. I will never forget the corrected red versions I received back and will forever be thankful for having been that patient.

I want to thank all the members of the “Cellulose & Wood Materials” group of Empa: Ahn Tran Ly, Alessia Pasqualini, Alexandre Poulin, Anja Huch, Arnold Martin, Daniel Heer, Etienne Cabane, Francis Schwarze, Gustav Nyström, Houssine Sehaqui, Hugh Morris, Huizhang Guo, Ingo Burget, Javier Ribera Regal, Liuyang Han, Marion Frey, Mark Schubert, Markus Heeb, Markus Rüggeberger, Marta Vidiella, Mirko Lukovic, Nico Kummer, Philippe Grönquist, Sandra Tadokoro, Sandro Stücki, Silvia Campioni, Selin Vitas, Tina Künniger, Thomas Geiger, Walter Risi, Yaru Wang. The awesome visiting members Alberto Giubilini, Débora Franca, Divya Khare, Electra D’Emilio, Kevin De France, Xavier Aeby, Yannick Nagel, Zihui Zeng as well as Dominic Welti, Gian-Luca Gehwolf and Tobias Tschichold. Special thank you goes to Esther Strub and Sefora Riillo who brought order and discipline to the labs and the group ;D.

Most of all I want to thank my former and present office mates who made my PhD life awesome and who were the principal reason to wake up and go to office everyday: Carlo Antonini, Franziska Grüneberger, Olivier Fourmann, Helen Kojelles, Luca Müller, Paola Orsolini, Rani Boons, Sarah Lämmlein, Tingting Wu and Tommaso Marchesi D’Alvise.

I want to thank all the members of “Complex Materials” ETHZ who always integrated me in the family although I was mostly present at Empa: Ahmad Rafsanjani, Ahmet Demirörs, Alessandro Ofner, David Moore, Davide Carnelli, Dimitri Kokkinis, Elena Tervoort-Gorokhova, Erik Poloni, Etienne Jeoffroy, Fabio Bargardi, Fergal Coulter, Florian Bouville, Hortense Le Ferrand, Iacopo Mattich, Jakob Faber, Jens Ammann, Julia Carpenter, Kunal Masania, Lauriane Alison, Lorenzo Barbera, Luca del Carro, Lucas Chiba De Castro, Madeleine Grossman, Manuel Schaffner, Marco Binelli, Marianne Sommer, Matthias Haug, Nicole Schai,

Patrick Rühs, Rafael Libanori, Rebecca Albers, Silvan Gantenbein, Stefano Menasce, Tommaso Magrini, Wilhelm Woigk, and Zuzana Tomasikova.

Especially I want to extend my thanks to Dimitri Kokkinis and Etienne Jeoffroy with whom I had the privilege to work and discuss during my PhD time. Their excellence and passion for science and detail greatly inspired me while their “PhD experience/wisdom” greatly helped me to take things easier and less serious. I also want to thank Sarah Lämmlein for having been my longest standing office partner and for her valuable help in debugging my Matlab codes in an efficient way!

During my thesis I received help from two brilliant students, Alina Hauser and Signe Line Vehusheia, who endured my crazy ideas, spent time accomplishing them with dedication and hard work and which eventually resulted in the successful accomplishment of the former. Related to their project I want to thank Alessandro Ofner, David Moor, Iacopo Mattich and Marco Binelli for their help and expertise in the field of microfluidics and polymer chemistry. Science would not be the same without collaborations; therefore I would also like to thank the persons with whom I had the chance to work with during my PhD thesis. Special thanks go to Dr. Jörg Läger and Prof. Peter Fisher without whom the work on rheology would not have been possible. I also want to Thank Antonia Neels from the X-ray center for having performed and spent significant time measuring all my samples. Dr. Viviane Lütz-Bueno and Dr. Guizar Sicaïros Manuel from Paul Scherrer Institut (PSI) for their help and time with the cSAXs tomography. I would like to thank Prof. Dr. Woo Soo Kim and Dr. Hugo Voisin for the two different and new work perspectives I had the chance to share during their exchange time here at Dübendorf.

Additionally, I want to thank Anne-Lise Eha, Débora Franca, Karlheinz Hausmann, Sandro Stücki, Silvia Campioni, Tingting Wu, Xavier Aeby, Yannick Nagel and Vincent Lavanchy for having added additional corrections to my thesis.

Also I would like to thank Andric Katerina and Lendvai Isabelle for their help in all the administrative matters both at Empa and ETHZ.

Aside from my PhD life I would actually like to extent my gratitude to Luis P. Canal and Petros Dafniotis who pushed me among others to decide for a PhD but who also always motivated and inspired me throughout my studies.

Finally and most importantly I am thankful to my friends and family for making my life awesome and not constrained to a lab. I specially want to thank my parents Caroline and Karlheinz who always inspired, supported and were there for me as well as Sébastien and Laura for having to deal with me in their private lives most of their time and without whom everything would be significantly different.

The research shown in this thesis has received funding from the Swiss National Science Foundation, Switzerland (Project 200021159906/1).

II. Summary

Controlling the material architecture at multiple length-scales is a key feature found in all living organisms. In Nature, this multi-scale structuring of materials allows biological systems to meet challenging requirements for specific functions such as mechanical performance, protection, camouflage and mating purposes. The increasing demand for functional materials and their impact on the environment drives the research toward renewable solutions and resources. Among the renewable solutions, nanofibrillated cellulose (NFCs) and cellulose nanocrystals (CNCs) gained particular interest for the fabrication of nano-reinforced composites. This interest has risen from their renewable character, biocompatibility, high potential for chemical functionalization and outstanding mechanical properties that are competitive with synthetic fibers such as carbon, glass or Kevlar. However, most of the above applications cannot fully benefit from the properties of cellulose due to the difficulty to control the orientation of such nano-scaled building blocks as well as its limited dispersability in certain polymer systems. Based on flow-induced strategies, we explore in this thesis two processing techniques to obtain functional hierarchical composites with controlled cellulose alignment: 3D printing and microfluidics. These processing techniques allow to combine multiple materials and take advantage of shear and extensional forces to structure the resulting composite at multiple length scales. The use of these techniques for the processing of cellulose-based materials requires control over the dispersion degree and the alignment dynamics of cellulose nanocrystals in highly concentrated suspensions upon application of shear and extensional forces. We systematically tackle these requirements in the three chapters presented in this thesis:

The first chapter presents an experimental study on the alignment dynamics of cellulose nanocrystals in concentrated suspensions subjected to controlled shear flow. Taking advantage of the birefringent optical properties of cellulose nanocrystals, *in-situ* polarized light rheology is utilized to quantify the alignment dynamics of CNC particles during shearing of the suspension. By measuring the opto-rheological response of a broad range of cellulose concentrations in suspension, the time required for particle alignment at a given shear rate is experimentally determined. Surprisingly, the time for alignment in such concentrated suspensions can be partly described using established physical models for the alignment of an isolated particle in a viscous medium. To bring this research closer to the flow conditions experienced by CNC particles during 3D printing, the alignment process was also studied using X-ray scattering techniques on a quartz capillary whose geometry resembles the steel needles commonly used for direct ink writing. This collaborative work with Empa's X-ray center and PSI allowed us to better understand the combined contribution of extensional and shear forces to the alignment of anisotropic particles during extrusion-based printing processes. Remarkably, the results revealed that extensional forces dominate the alignment process in the core of printed filaments, whereas shear forces enhance particle alignment at the filament shell.

In the second chapter, we present a novel strategy to 3D print complex-shaped composites comprising a high volume fraction of cellulose nanocrystals using the Direct Ink Writing method (DIW). This technique allows us to align cellulose nanocrystals and fibers by taking advantage of the shear and elongation forces resulting from the extrusion process. On the basis of the knowledge gained on the alignment dynamics study, processes parameters such as needle diameter and length are carefully adapted to enhance alignment depending on the ink properties. As the dispersion of non-modified nanocellulose in non-polar polymers or organic solvent systems is challenging, we propose an alternative aqueous-based printing route followed by a densification step in a poor organic solvent to generate 3D printed parts with unprecedented volume fraction levels of reinforcing elements. Adjusting the interaction between the cellulose nanocrystals and the organic solvent employed in the post-printing process allows us to obtain complex-shaped cellulose-based scaffolds with volume fractions of reinforcing elements that could not be achieved using conventional additive manufacturing techniques. Composites can be generated from these scaffolds by plunging the printed structure in a bath of different solvent composition. By adding a compatible monomer system in the solvent bath, the densified cellulose scaffolds are infused and photocured after solvent evaporation. Using this approach, we fabricate 3D-printed cellulose-based composites exhibiting up to 27 vol% of reinforcing elements with remarkable complex geometries and mechanical performance.

In the third chapter, we exploit extensional flows developed in microfluidic devices to control the alignment of cellulose nanocrystals within droplet templates and thus fabricate anisotropic microparticles with birefringent optical properties. Adding superparamagnetic nanoparticles to the droplet template makes these anisotropic microparticles also magnetically-responsive. The combined magnetic and birefringent properties can be exploited as rheological microprobe to quantify the viscosity of the medium around the suspended microparticle. This is possible through the magneto-optic coupling achieved when the microparticle is illuminated with polarized light while it rotates under a rotating magnetic field of known frequency. The viscosity of the medium can be estimated from the frequency at which the magneto-optic coupling effect is no longer observed.

Finally, the following chapters include the conclusions, outlook and the supplementary information relevant to the main chapters of this thesis. With this thesis, we have been able to better understand the alignment of cellulose nanocrystals and fibers under flow and leverage this knowledge to produce composites with both defined mechanical and optical properties. The 3D printing and microfluidic approaches proposed in this study are expected to offer a robust and versatile platform for the processing of sustainable cellulose-based composites for structural and optical applications.

III. Résumé

La cellulose est le biopolymère le plus abondant sur la terre. Extrait de plantes, d'arbres ou produit par certaines bactéries, elle peut être utilisée à différentes échelles, en tant que fibre macroscopique, microfibrille ou nanocristaux, selon le procédé d'extraction utilisé. En conséquence, la cellulose possède un large champ d'application allant de l'alimentaire, biomédical, traitement d'eau usagé aux applications structurelles.

Les applications structurelles et le renforcement de composites fondent le pilier central de cette thèse. Dans cette optique, les nanofibrilles de cellulose (NFCs) et les nanocristaux de cellulose (CNCs) ont reçu un intérêt croissant en tant que renforcement pour la production de composites dans de multiples secteurs comme le biomédical (production de guide et d'implants pour la croissance d'os et de cartilage ou d'autres tissus organiques), l'emballage (renforcement de film polymère) et l'optique (formation de structures photoniques) pour ne citer que quelques exemples. Cet engouement est dû à leur biocompatibilité, leur facilité à être modifié et fonctionnalisé chimiquement et à leurs propriétés mécaniques, rivalisant avec les fibres synthétiques comme le carbone, le verre et le Kevlar.

Toutefois, la plupart de ces applications ne peuvent pas profiter pleinement des propriétés de la cellulose dû à la difficulté de la dispersion dans certaines matrices polymères ainsi que la difficulté à contrôler l'orientation de ce nano-renforcement. Au fil des années, une nouvelle technique a émergé, offrant la possibilité de produire des pièces géométriquement complexes ainsi que de potentiellement contrôler sa microstructure : L'impression 3D. Un intérêt croissant autour de la cellulose a mené à de nombreux projets de recherches autour de l'impression 3D, qui, toutefois se retrouve confronté aux mêmes problèmes énumérés préalablement : la compatibilité et le choix des polymères ainsi qu'une compréhension claire de la microstructure du composite résultant du procédé.

Pour répondre à ces questions, le problème a été décomposé en trois parties centrales : La compréhension de la dynamique d'alignement de nano-cristaux de cellulose, le contrôle de l'alignement et de la densité de renforcement de pièces issues de l'impression 3D à base de cellulose et finalement, L'extension de ces concepts d'alignement et de renforcement à d'autres techniques.

La première partie consiste à comprendre la dynamique d'alignement de nano-cristaux de cellulose. En prenant avantage des propriétés biréfringentes des nano-cristaux de cellulose, des observations *in-situ* ont pu être effectuées en couplant un système d'imagerie à lumière polarisée avec un rhéomètre. Cette approche permet de corréler directement les données acquises par le rhéomètre avec les images obtenues de l'échantillon. En mesurant une vaste gamme de concentration d'encres à base de cellulose, les résultats obtenus ont permis l'élaboration d'un diagramme de phase combinant temps et contrainte de

cisaillement. En se référant à des modèles physiques existant, des conclusions générales applicables à l'alignement de particules colloïdales ont pu en être déduites.

Une approche plus quantitative a été conduite en se basant sur une analyse aux Rayons-X. Ce travail collaboratif entre le centre de compétence Rayon-X de l'Empa et du PSI consiste à analyser la dynamique d'alignement de cristaux de cellulose pendant leur extrusion dans une aiguille d'imprimante 3D. En utilisant une capillaire en quartz transparente aux rayons-x, l'effet des contraintes de cisaillement et les forces d'extensions ont pu être mise en évidence le long et au travers de la section de l'aiguille.

La seconde partie se focalise sur l'utilisation d'impression 3D comme outil pour produire des composites dont les propriétés sont contrôlées de manière précises grâce au renforcement de fibres et cristaux de cellulose. Étant donné que la cellulose se mélange difficilement avec certains polymères sans modification chimique préalable, une voie alternative est proposée permettant de contrôler autant la densité de renforcement que le choix de la matrice du composite. Cette approche se base sur l'utilisation de solvants à faible affinité pour la cellulose, forçant la structure imprimée à se contracter lorsqu'elle est mise en contact avec ce dernier. En contrôlant la composition du bain de coagulation et en choisissant le système de polymère adapté, la pièce peut être densifiée, infiltrée et photopolymérisée pour obtenir une structure complexe avec un large choix de propriété mécanique.

La troisième partie de la thèse consiste à appliquer les connaissances acquises autour de l'alignement et de l'extrusion de nanocristaux. Une technique alternative est explorée pour la production de composite avec architecture contrôlée, la microfluidique. En prenant avantage des forces élongationnels présentes dans ce système et en ajoutant des particules répondant à la présence de champs magnétiques, un nouveau procédé est proposé pour produire des microparticules anisotropes. Ces microparticules présentent une microstructure texturée et peuvent être orientées magnétiquement le long d'une direction spécifiée par un champ magnétique.

IV. Contents

Chapter 1. Introduction.....	1
1.1 Motivation and structure of thesis.....	1
1.2 Cellulosic materials: their origin	4
1.3 Mechanical and optical properties of nano-cellulose and its application in composites.....	5
1.4 Biological and bioinspired composites with tailored hierarchical structures	8
1.5 Cellulose-based structures with complex bulk geometries	11
1.6 Functional cellulose-based microparticles and microcapsules	13
1.7 References	15
 Chapter 2. Dynamics of cellulose nanocrystals alignment during 3D printing	25
2.1 Abstract.....	25
2.2 Introduction	26
2.3 Results and discussion	28
2.4 Conclusion	41
2.5 Experimental methods	41
2.5.1 Sample preparation.....	41
2.5.2 Transmission electron microscopy.....	41
2.5.3 Rheology.....	42
2.5.4 Image processing.....	42
2.5.5 3D printing.....	43
2.5.6 Optical microscopy.....	43
2.6 Acknowledgement.....	43
2.7 References	44
 Chapter 3. Alignment dynamics of cellulose nanocrystals under flow in a 3D printing nozzle.....	49
3.1 Abstract.....	49
3.2 Introduction	51
3.3 Results and discussion	53
3.4 Conclusion	61
3.5 Experimental methods	61
3.5.1 Materials.....	61
3.5.2 Sample preparation.....	61

3.5.3	Acknowledgement	63
3.5.4	References.....	63
Chapter 4.	Complex-shaped cellulose composites made by wet densification of 3D printed scaffolds	67
4.1	Abstract.....	67
4.2	Introduction	68
4.3	Results and discussion	69
4.4	Conclusions	78
4.5	Experimental methods	79
4.5.1	Preparation and characterization of composites.....	80
4.5.2	Mechanical and structural characterization of composites.....	82
4.6	Acknowledgements	84
4.7	References	84
Chapter 5.	Cellulose-based microparticles for magnetically-controlled optical modulation and sensing	89
5.1	Abstract.....	89
5.2	Introduction	90
5.3	Results and discussion	91
5.4	Conclusions	99
5.5	Experimental methods	99
5.5.1	Materials.....	99
5.5.2	Preparation of CNC suspensions	100
5.5.3	Microfluidic emulsification.....	100
5.5.4	Microscopy and image analysis.....	101
5.5.5	Rheology.....	101
5.5.6	Magnetic manipulation of microparticles.....	101
5.6	Acknowledgements	102
5.7	References	102
Chapter 6.	Conclusion	105
Chapter 7.	Outlook.....	109
Appendix A	117
Appendix B	135

Appendix C143
Appendix D169
Declaration177
Curriculum vitae and scientific contributions179

Chapter 1.

Introduction

1.1 Motivation and structure of thesis

The objective of this thesis is to explore the efficient use of nanocellulosic materials as functional building blocks for mechanical and magneto-optical applications in the form of complex-shaped bulk structures or responsive microscopic particles. In that direction, the thesis aims to explore the benefits of hierarchically organized microstructures on the global mechanical and optical properties of cellulose-based composites. The design of hierarchically structured composites requires a deep understanding and control over the alignment of cellulose nanocrystals (CNCs). To control nanocrystal alignment in bulk structures and in microparticles, 3D printing via Direct Ink Writing and microfluidic emulsification are used as enabling fabrication technologies. Understanding, controlling and exploiting the alignment of cellulose nanocrystals in specific geometries and applications form the main pillars of the thesis, as indicated in Figure 1.1.

The research begins with the rheological properties of suspensions of CNC particles and how these properties impact the alignment of individually dispersed cellulose nanocrystals (Figure 1.1a). After understanding the dynamics of cellulose nanocrystal alignment, 3D printing is utilized to create complex 3-dimensional structures featuring alignment control at the nano-, micro- and macro-scale (Figure 1.1b). Finally, a microfluidic emulsification platform is explored to produce cellulose-based anisotropic particles with nanoscale texture and unique magneto-optical properties (Figure 1.1c).

This thesis is divided in 7 chapters.

Chapter 1 is a general introduction into the topic of cellulose and hierarchically-structured composites. It explores the raw material, its origins, properties and fields of application, including different processing methods, their challenges and current limitations.

Chapter 2 sheds light on the dynamics of cellulose nanocrystals alignment in concentrated suspensions under shear stresses. The alignment dynamics of such anisotropic particles is studied using *in-situ* polarized light rheology at different shear stress conditions and volume fraction of cellulose nanocrystals. The time required for particle alignment under these conditions is directly correlated with the observed rupture of nematic domains and the alignment of cellulose crystals. This understanding is of relevance for Direct Ink Writing, which is an extrusion-based process that relies on material flow under shear through a nozzle prior to deposition on a building plate (Figure 1.1a-a1).

Following up on the research results discussed in chapter 2, Chapter 3 addresses the question of cellulose alignment under the actual extensional and shear flow conditions experienced by the material as it is pushed through a nozzle during direct ink writing. In this chapter, we employ X-ray techniques such as Small Angle X-ray Scattering (SAXS), 2D Wide Angle X-ray Scattering (2DWAXS) and computer tomography small angle X-ray scattering (cSAXs) to determine the microstructure and alignment degree of cellulose nanocrystals within extruded filaments. This collaborative work between Empa's X-ray research center and Paul Scherrer Institute (PSI) focuses on understanding the alignment dynamics of cellulose through the needle during the extrusion process. X-ray transparent quartz capillaries are employed as model needles to spatially resolve the level of cellulose alignment along the radius and the length of the extruded filament (Figure 1.1a-a2).

Chapter 4 will take a closer look at the manufacturing of strong and dense cellulose reinforced composites using the Direct Ink Writing approach. In this chapter, we propose a versatile method to control both the concentration of reinforcing particles and the type of polymer used as matrix between the reinforcement. By combining 3D printing with sequential solvent exchange and resin-infusion processes, complex-shaped bulk structures with unprecedentedly high concentration of cellulose particles are achieved. Through this approach we explore the fabrication of materials ranging from soft and elastic responsive hydrogels to stiff and strong microstructured composites (Figure 1.1b).

The utilization of cellulose building blocks beyond mechanical applications is demonstrated in chapter 5 by designing, synthesizing and characterizing cellulose-based microparticles with unique magneto-optical functionalities. Anisotropic, cellulose-filled microparticles exhibiting optical birefringence and magnetic response are produced from droplets created in a microfluidic emulsification platform. Using magnetic fields as an external trigger to control the orientation of the produced microparticles, we demonstrate the possibility to remotely manipulate light polarization and to assess the rheological properties of the fluid in which the particles are suspended. The microfluidic platform provides an effective processing route for the fabrication of magnetically-responsive cellulose-laden microrods with broad choice of aspect ratio and composition (Figure 1.1c).

Chapter 6 provides a general conclusion of the project while chapter 7 paves the way for future work and discusses open questions to be potentially explored in follow-up studies.

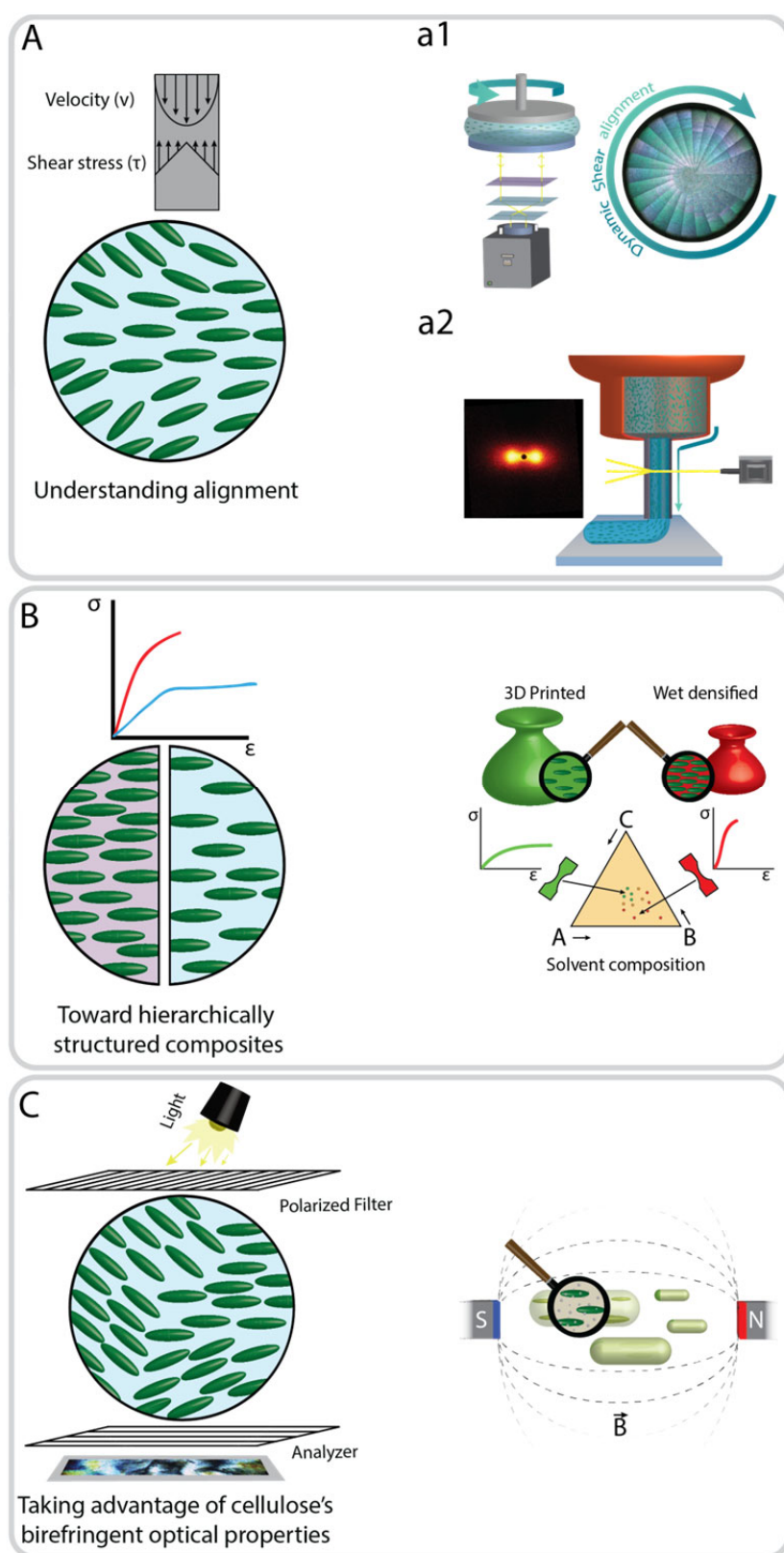


Figure 1.1 General organization of the thesis. Three main chapters are presented along with their subchapters. A) Understanding the alignment of cellulose through two different approaches: a1) utilizing *in-situ* polarized light rheology where we track the dynamic response of cellulose gels under shear and a2) applying X-rays to enable *in-situ* monitoring of the dynamic alignment of cellulose during extrusion. B) Production of complex-shaped composites with defined architecture and mechanical properties. This is achieved by 3D printing water-based cellulose gels, followed by solvent exchange and resin infusion steps to obtain composites with high cellulose content and enhanced mechanical properties. C) Exploiting the optical properties of cellulose nanocrystals. Development of magnetically- and optically-responsive microparticles. This is pursued by encapsulating and aligning cellulose nanocrystals, along with magnetic responsive nanoparticles, to create functional anisotropic microparticles

1.2 Cellulosic materials: their origin

With an annual biosphere production estimated around 7.5 million tons, cellulose is the most abundant renewable biopolymer on earth.¹ Cellulose is a high molecular weight homopolymer chain, composed of repeating glucose dimers (cellobiose, Figure 1.2). Tightly packed and held together *via* hydrogen bonds and van der Waals forces, cellulose chains form strong and stiff microfibrils. Also produced by bacteria, cellulose is the main constituent of all plants, where these microfibrils assemble into macrofibers, bearing the task of structural reinforcement. The macrofibers are strategically embedded in a matrix of hemicellulose, lignin or pectin, assembled to form ligno-cellulosic fibers, with specific orientations and packing densities depending on the local mechanical requirements.^{2, 3}

The properties of these fibers strongly depend on the source (plant, bacteria, vegetables, algae) which in turn determines the chemical composition of the fiber. In fact, the source producing cellulose will determine the internal strains of the resulting fibrils and consequently the quality of their packing, resulting in the alternation of well-organized, tightly packed bundles (crystalline) and less-organized (amorphous) domains with more and less chemical stability, respectively.

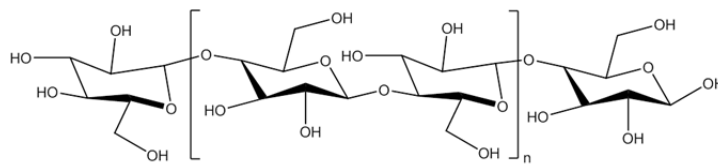


Figure 1.2 Cellulose chain with repeating cellobiose element.

The rich variety of cellulose structures present in nature has inspired the development of renewable materials with properties that arise from both their hierarchical organization and chemical composition. The hierarchical organization found in wood, for example, serves not only as a source of inspiration for material scientists but can also be decomposed, following a top-down method, in smaller building blocks at different length scales. The remarkable physical and chemical properties and biocompatibility of cellulose makes it an attractive renewable building block in the search for sustainable bio-composite applications.

This thesis focuses on two of these building blocks: cellulose nanocrystals (CNCs) and nanofibrillated cellulose (NFC), both extracted from wood-based cellulose fibers. As opposed to bacterial cellulose, readily produced as fiber from bacteria, cellulose fibers from wood are extracted from wood pulp, a product resulting from the mechanical milling or chemical cooking of wood chips and the chemical removal of undesired constituents such as lignin and hemicelluloses. These fibrillated cellulose fibers (NFC) are typically tens of nanometers in

diameter for a few micrometers in length and can be further reduced in size through controlled time/temperature acid-catalyzed degradation of the amorphous domains using sulfuric, phosphoric or hydrochloric acid. This results in needle-shaped crystallites with diameters and lengths ranging between 3 and 50 nm, and 25 and 1000 nm, respectively. The geometrical characteristics, such as dimensions and shape, of nanocellulose building blocks depend on the nature of the cellulose source as well as the purity of starting materials, the disintegration processes (grinding or homogenization) and the hydrolysis conditions (time, temperature, ultrasound treatment).^{4, 5}

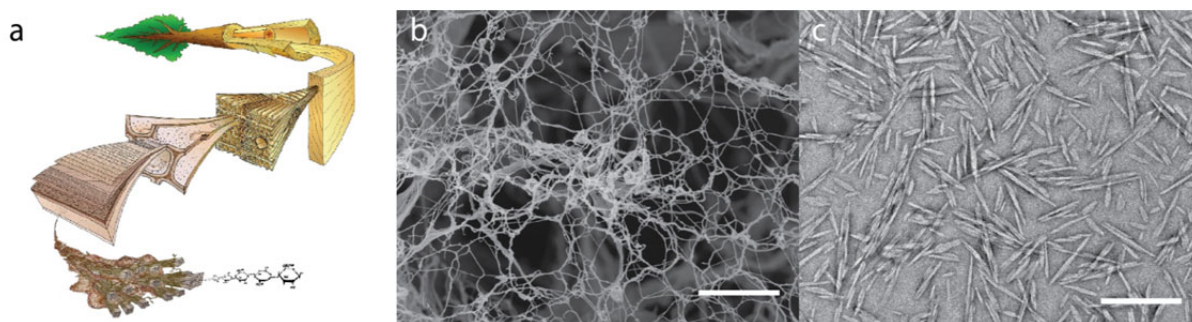


Figure 1.3 Hierarchical view of a tree and closer look into the micro and nano-scaled elements that form the structure of wood. a) Hierarchical cut of a tree from the macro- down to the nano-scale [Artwork M.Harrington. Copyright University of Canterbury, 1996⁶]. b) Scanning electron microscopy (SEM) image of microfibrillated cellulose (scale bar 6 μm). c) Transmission electron microscopy (TEM) image of wood-based cellulose nanocrystals (scale bar 200 nm) (images from Empa).

1.3 Mechanical and optical properties of nano-cellulose and its application in composites

In the composite field, extensive work has been carried out with fibrillated cellulose but less research was conducted on nanocrystalline cellulose.^{2, 7, 8} Most studies on nanocrystalline cellulose have focused on their optical properties, which will be discussed later in this section. In addition to their compelling optical properties, both fibrillated and nanocrystalline cellulose are also well-known as renewable natural resources with good mechanical strength and elastic modulus. As for all bio-materials, the mechanical properties depend on the origin or source they are extracted from. For wood-based cellulose nanofibrils, the Young's modulus was estimated to lie between 53 and 150 GPa (measured or calculated from AFM), whereas the tensile strength ranges from 400 to 700 MPa.^{7, 9, 10} Because of the alternating crystalline and amorphous segments along the fiber, the mechanical properties of fibrillated cellulose are inferior compared to those of other highly crystalline natural and synthetic fibers. Consequently, when extracting the defect-free crystalline domains through chemical hydrolysis, the properties of the resulting cellulose nanocrystals are greatly improved.

Cellulose nanocrystals (CNCs) present remarkable mechanical properties with Young's modulus ranging from 105 to 220 GPa and tensile strength as high as 10 GPa. Combined with a relatively low density ($\sim 1.58 \text{ g/cm}^3$) and a large aspect ratio, these mechanical properties make cellulose nanocrystals compete with other commonly-used synthetic reinforcing materials.^{2, 3, 9, 11-14} For comparison, the Young's modulus and tensile strength of carbon fibers lie in the ranges 100 – 1000 GPa and 2.5 – 3.5 GPa, respectively, whereas Kevlar fibers show Young's modulus and mechanical strength of 124-130 GPa and 3.5 GPa, respectively, for a density of 1.4 g/cm^3 . On the nanoscale, carbon nanotubes with diameters ranging from 1 to 100 nm and lengths of up to a few millimeters display mechanical strengths up to 63 GPa with densities as low as 1.3 g/cm^3 .¹⁵

To harness the remarkable mechanical properties of cellulose nanocrystals in composites at the macroscopic scale, it is crucial to understand and control the way these nanoscale building blocks are dispersed and aligned within a polymer matrix. The first cellulose reinforced composite was produced in 1995 by Favier et al., by reinforcing a styrene/acrylate-based polymer. The successful reinforcement resulted from the formation of a continuous cellulose percolating network held by hydrogen bonding, which efficiently transferred the applied stress between the matrix and the reinforcing elements.¹⁶

Multiple techniques were also explored to control the orientation of these anisotropic building blocks and consequently the resulting mechanical properties. Composite materials with textured architectures have been manufactured by self-organized templating approaches,¹⁷⁻¹⁹ solution casting,²⁰ shear casting,^{21, 22} film drawing,²³ electrospinning,²⁴⁻²⁹ melt extrusion^{30, 31} or using strong electric or magnetic fields.³²⁻³⁴ While templating approaches are entirely based on the self-assembling ability of CNCs, shear casting and film drawing exploit shear to align individual cellulose crystals. Because of the high shear applied during fabrication, these composites reach high degrees of alignment but are limited to thin films. Alternatively, electrospinning and extrusion-based processes can be used to produce membranes or fibers for several composite applications, despite the lower degrees of alignment as compared to film casting. Finally, electric and magnetic fields enable alignment of very diluted cellulose suspensions but require strong external fields. Therefore, the above-mentioned techniques still fail to provide a processing route to textured 3D cellulose-based composites as they are either limited to producing thin films or individual filaments.

In spite of the importance of mechanical properties in many applications, cellulose nanocrystals offer other attractive features and functionalities. These include their nanoscale dimensions, the anisotropic shape, the surface charges, the birefringent optical properties and their ability to self-assemble into liquid crystals. In particular, the birefringent behavior of CNCs finds promising functionalities in optical applications and allows for the direct observation of the effect of external factors such as electrical/magnetic fields or shear forces on the orientation of individual rods. Depending on the concentration, the self-organization of cellulose nanocrystals leads to a variety of mesoscale structures ranging from nematic to smectic to chiral nematic phases (Figure 1.4a-e). The organization of cellulose

crystals in suspension results in defined colored patterns under visible light or between polarized filters (Figure 1.4f, g). Therefore, the assembly of cellulose nanocrystals attracted significant attention in the field of optics, where anti-reflective³⁵ and UV-protected³⁶ thin film coatings have been prepared for security and display applications.^{37, 38}

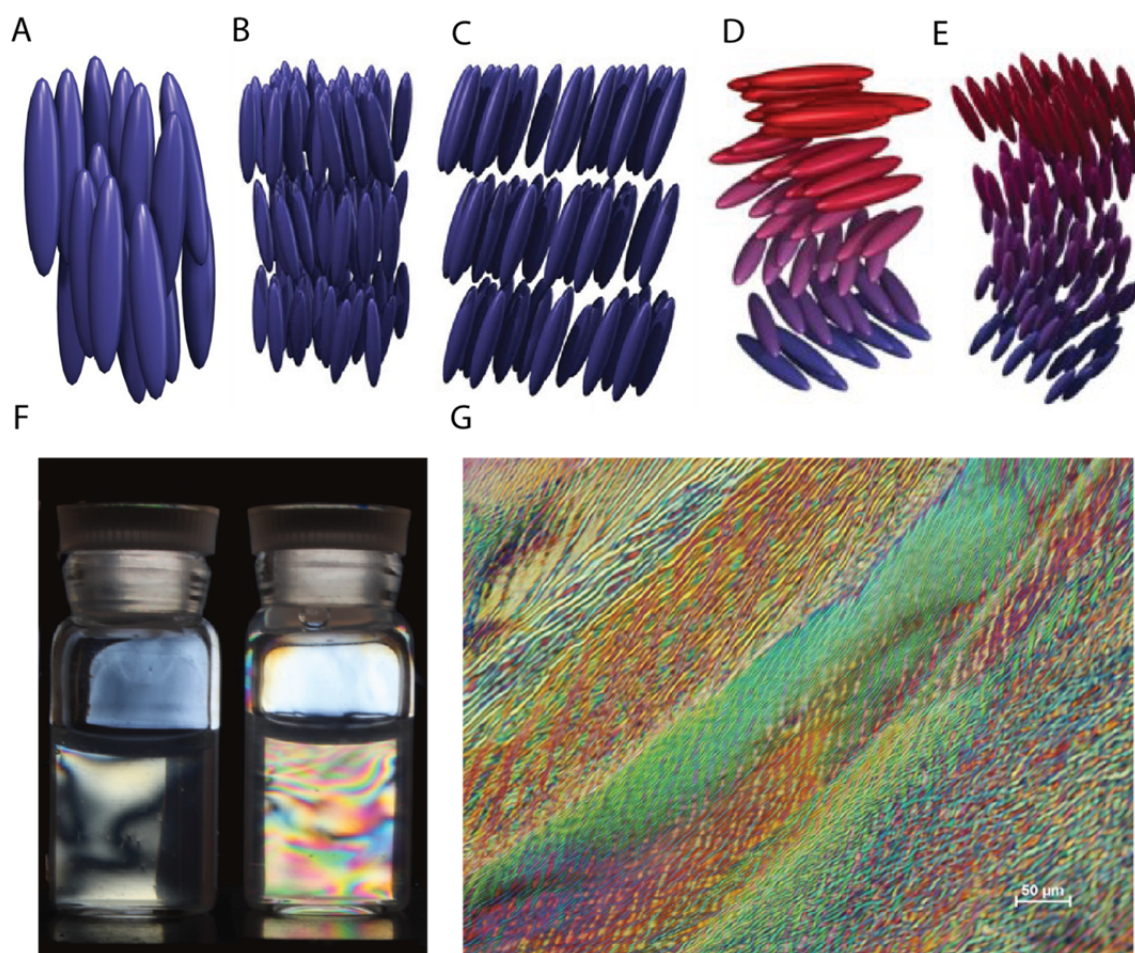


Figure 1.4 Liquid crystal ordering of liquid crystals. A) Nematic, no positional order but long-range directional order. B & C) Smectic, positional order along a direction. D) Chiral nematic and E) Chiral smectic, long-range ordered structure with finite angle twisting along the normal to the plane and positional ordering in a plane. F) Dispersion of cellulose nanocrystals in suspension exhibiting chiral nematic phases. G) Dried film with typical chiral nematic fingerprint.³⁹

Because of the versatile properties of wood and in particular cellulose, an ever-growing number of applications for these materials exist. At the macro-scale, bulk wood is utilized for building applications or is modified to achieve specific functionalities such as magnetic responses, fire-retardancy or waste-water cleaning.⁴⁰⁻⁴² At the micro- and nano-scales, cellulose fibers and nanocrystals have been used in the food industry, in water-cleaning applications and have a promising future in the field of biomedical engineering as wound-healing materials, tissue scaffolds, drug-delivery systems, biomedical implants or composite applications in general.⁴³⁻⁵³ Despite this wide range of functionalities and applications, organizing cellulose building blocks into hierarchical structures should open

new opportunities to tailor material properties across scales and thus fully benefit from the unique properties at the nanoscale in macroscopic objects and functional devices. The way nature builds hierarchical materials has long been a source of inspiration for researchers interested in tuning material properties through multiscale structural design. Therefore, many researchers have worked on translating natural design principles to bioinspired synthetic composites as a means to develop new materials with enhanced properties.

1.4 Biological and bioinspired composites with tailored hierarchical structures

Nature offers a wide range of examples of hierarchically-organized functional materials with sophisticated texture and properties. Spider silk, bone, wood and the chitin exoskeletons of crustaceans, insects or fish scales are prominent examples of biological hierarchical structures that reach remarkable properties using a relatively narrow range of building blocks (Figure 1.5). As described above, the complex hierarchical structure of wood is composed of only cellulose, lignin and hemicellulose as major building units. Despite the scarcity of building blocks, the structure of such biological materials is organized from the nano-scale up to the macro-scale to achieve mechanical and functional properties that remain unmatched by synthetic composites with comparable chemical composition. The design principle underlying these unique properties is the hierarchical organization of fiber-like building blocks across multiple length scales. This is a common hallmark of various biological materials. Starting with crystalline molecular building blocks dispersed in a matrix at the nanoscale, these biological structures exhibit fibrils and micro-scaled fibers at progressively larger length scales, which are eventually combined into complex geometries at the macroscopic level. This hierarchical organization can be easily observed in the multiscale architecture of bones, trees, crustaceans and spider silk (Figure 1.5). Despite these similarities, local variations in chemical composition and disposition of these building elements yields biological materials covering a broad spectrum of mechanical properties.

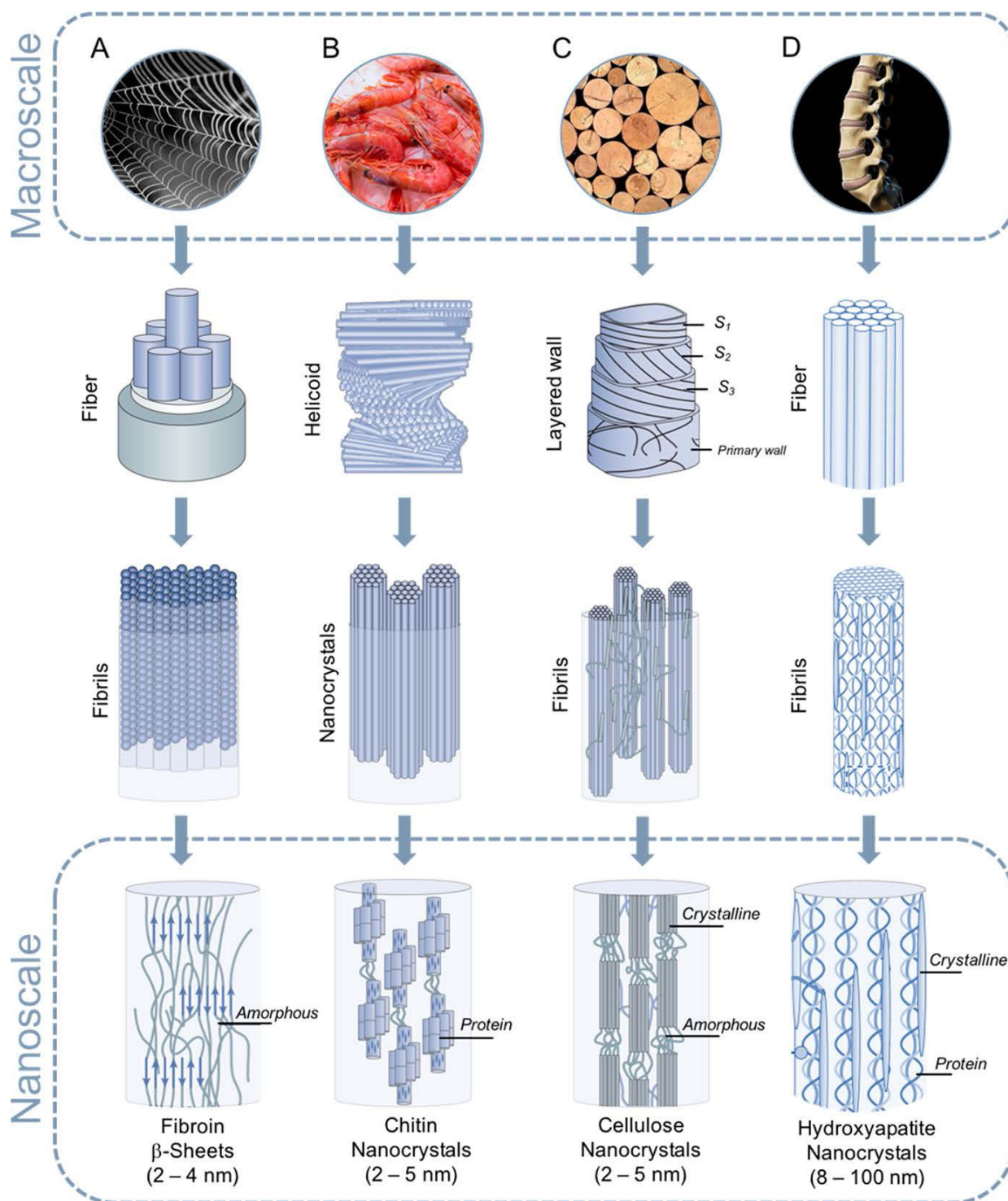


Figure 1.5 Hierarchical organization of different materials found in nature, from macroscale down to nanoscale. (A) spider silk with the hierarchical organization of silk fibroin into bundles, fibrils and macro-fibers. (B) Chitin structure, a complex multiscale arrangement of proteins found in crustacean exoskeletons. (C) Wood, a complex organization of cellulose polymer chains into bundles and fibers. (D) Bone, a complex composite consisting of hydroxyapatite crystals and collagen proteins. Image reproduced with permission from ACS.⁵⁴

The multi-scale organization and assembly of building blocks is utilized to tailor not only the mechanical properties of biological composites but also other functionalities, including their interaction with light and their ability to change shape in response to environmental stimuli.⁵⁵⁻⁵⁹ (refs)

As far as light interactions are concerned, living species utilize nano- and micro-structural architectures to produce so-called structural colors. Structure-derived colors play an important role in camouflaging effects and for the mating of living animals in nature.⁵⁹⁻⁶⁵ As opposed to artificial coloration, structural colors are obtained through the creation of microscopic patterns of nano-scaled reflective or birefringent materials. Since the size of the microscopic features is comparable to the wavelength of the incident light, the structure is able to interact with and diffract the incoming light in a highly selective manner. Through these selective interferences, only a certain range of the wavelengths is reflected or transmitted often resulting in a visible coloration of the material. Because the length of the light path through the structure changes with the refracting angles, the coloration we observe often depends on the angle at which the object is observed. The wing of the Morpho blue butterfly is a prominent example of a bright coloration created through light interference effects (Figure 1.6a-d). In addition to interference, light scattering is also used to generate bright color, as illustrated by the white scales of the *Cyphochilus* white beetle (Figure 1.6e-h). Finally, living organisms also exploit the birefringent properties of natural building blocks and structures to control light polarization and thus enable special optical sensing functionalities.^{64, 66}

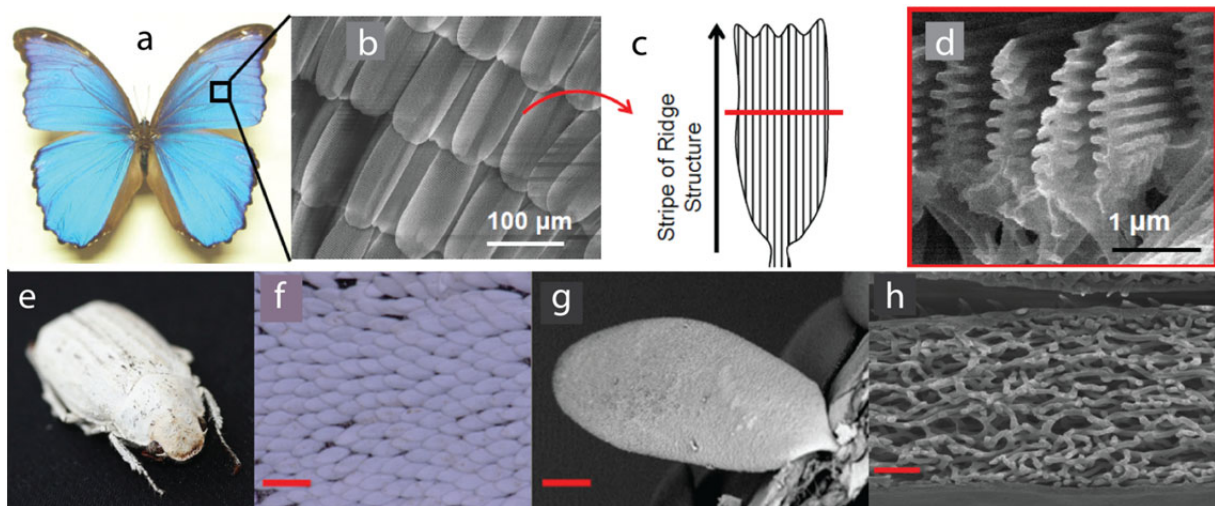


Figure 1.6 Examples of structural colors (Morpho butterfly) or color elimination (*Cyphochilus* white beetle) in nature. (a) Morpho butterfly. (b) SEM image of the scales of the butterfly wing. (c) Schematics of the ridge structure of one individual scale. (d) Cross-sectional cut of an individual scale along the red line shown in the schematic drawing (c). (e) *Cyphochilus* white beetle. (f) Microscopy image of the scales of the beetle (scale bar: 400 μm). (g) SEM image of an individual scale (scale bar: 25 μm). (h) Internal microstructure of an individual scale (2 μm). All images were adapted with permission from SPIE and Wiley (Adv. Opt. Mat.).^{62, 67}

The possibility to tailor mechanical properties through structural design rather than the choice of specific chemistries makes the design principles of biological materials attractive tools for the fabrication of sustainable materials and devices. Following this bio-inspired approach, one can envision the use of a few abundant building blocks to develop materials with a broad range of functional properties, depending on the design of the hierarchical structure.^{54, 68}

To pave the way towards such biologically-inspired composites, multiple techniques and materials have been explored, leading to hierarchical structures with promising mechanical or optical properties. Because of their unique mechanical properties, the nacre layer of mollusk shells or the hammer-like appendage of the mantis shrimp became famous models for materials with impressive fracture toughness and crack deflection ability. These structures have been replicated synthetically using building blocks such as clay or alumina platelets. To re-create the “brick-and-mortar” structure of nacre, molecular interactions or magnetic fields have been utilized.^{69, 70} In addition to fracture-resistant structures, bioinspired materials with shape-memory properties or programmable morphing capabilities have been recently obtained using 3D printing techniques.⁷¹⁻⁷³ The hierarchical structures of some of these materials have been created by combining 3D printing techniques with magnetic fields or ultrasound waves as external stimuli to guide the assembly of building blocks at multiple length-scales.^{74, 75} Similarly, complex emulsions have been used as feedstock ink in an extrusion-based 3D printer to fabricate light yet strong composite materials with hierarchical porous structure.^{76, 77} In another approach, living bacteria were combined with extrusion-based 3D printing to produce scaffolds and structures with metabolic functionalities provided by the entrapped living organisms.⁷⁸⁻⁸⁰ However, bio-inspired approaches have not yet been fully explored using sustainable resources.

Despite recent progresses in the development of bio-inspired hierarchical composites, the variety of bio-sourced and renewable building materials used in these materials is relatively limited and the potential of this approach in producing sustainable bulk structures remains largely unexploited. Among the possible bio-based building blocks, cellulose is an interesting candidate for composite applications due to its competitive mechanical properties and birefringent optical properties. To exploit its full potential, it is crucial to develop processing routes to control the alignment of individual cellulose crystals or fibers and create complex-shaped structures that meet the mechanical properties required in specific applications.

1.5 Cellulose-based structures with complex bulk geometries

Control over the orientation of reinforcing building blocks is indeed essential to enhance the mechanical properties of composites containing cellulose fibers and crystals. As mentioned in the previous chapter, various approaches were explored to control the orientation of cellulose-based materials but current methods are often limited to thin materials or lack freedom in geometry.

Among the possible processing techniques that provide geometrical freedom, 3D printing via Direct Ink Writing (DIW) is particularly interesting because it can also be used to exert shear forces to align cellulose building blocks during the fabrication process. Direct Ink Writing is an extrusion-based process in which a paste-like material (or gel) is extruded to generate complex-shaped 3D objects in a layer-by-layer approach. The key requirements to develop feedstock materials for DIW are twofold. First, the rheological behavior of the paste/ink needs to be controlled to ensure low viscosity and sufficiently high yield stress. Second, the ink must be solidified through, for example, drying or UV/thermal treatment to generate mechanically-stable objects.^{74, 81, 82} The viscosity and yield stress of the ink impact the printing behavior and shape fidelity of the printed part prior and after drying. These rheological properties can be easily adjusted by adding fillers to the ink.

Cellulose was processed with various other 3D printing techniques, such as Stereolithography (SLA), binder jetting and Inkjet Printing and Direct Ink Writing (DIW).⁸³⁻⁸⁷ Because of the gel-like behavior of aqueous suspensions containing a minimum percolating concentration of cellulose particles, direct ink writing revealed to be the most suitable technique for the 3D printing of cellulose-based materials. Indeed, the percolating network created by cellulose particles in water gives rise to the yield stress and shear-thinning behaviors necessary for direct ink writing. Initially, research was focused on gels containing 2-4 wt % nanofibrillated cellulose (NFC)^{53, 88-95}, whereas the 3D printing of cellulose nanocrystals (CNCs) has only recently been reported⁹⁶ and further explored.⁹⁷⁻¹⁰⁰

Three different routes have been used to print cellulose via DIW, depending on the protocol used to consolidate the printed object. The starting material is often a water-based gel containing either NFCs or CNCs at concentrations of 2-4 wt % or 20 wt %, respectively. After printing, the part is freeze-dried, super-critically dried or simply left as gel. These approaches result in three distinct types of materials: cryogels, aerogels or hydrogels, respectively.^{88-95, 98, 101} Cryogels and aerogels can be directly exploited as porous structures in different applications, whereas hydrogels need further consolidation to reach sufficient mechanical stability for handling. Cross-linking of printed cellulose hydrogels using ionic or covalent interactions is a common consolidation approach. Ionic bonds are obtained by adding alginate and sometimes gelatin to the cellulose aqueous paste followed by immersing of the part in calcium chloride (CaCl_2).^{89, 95, 102-104} Both alginate and gelatin are known for their bio-compatible properties but the low viscosity of aqueous solutions of these materials did not allow them to be processed into stable three-dimensional structures without the

addition of cellulose.¹⁰³ Covalent cross-linking was explored as a means to consolidate cellulose-based composites containing different polymers/monomers but very little work was translated to 3D printing.^{47, 105, 106} Cellulose-based materials in the form of porous structures (aerogel and cryogel) or hydrogels find promising applications in the biomedical field, as scaffolds for bone and cartilage regeneration as well as skin replacements.⁹⁷ In fact, CNCs and cellulose-based 3D structures have shown to promote and support the growth of various cell types.^{53, 107-109}

The promising prospects of cellulose-based materials can only be realized if the processing difficulties associated with cellulose, its inherent hydrophilicity and its relatively low thermal stability are properly addressed. Because of its hydrophilic nature and thermal degradation at mild temperatures, it is difficult to disperse cellulose in solvents different from water, in polar polymer systems and in polymers with high melting point. Furthermore, the small part sizes and commercial limitations faced by super-critical drying as well as the dramatic microstructural change induced by freeze-drying represent major drawbacks of the processes currently used to produce cryo- and aerogels. Consequently, the above approaches are not suitable to create cellulose-based composites that can be used in structural applications.

To tackle these challenges, preliminary research was conducted in our group to develop a strategy to disperse CNCs in a monomer/oligomer solution that displays the rheological properties needed for DIW while also being UV curable after the printing process. This is possible by dispersing CNCs in water/ethanol or water/isopropanol mixtures containing monomers and oligomers that are partially soluble in water. Through this approach we could show the potential of 3D printing cellulose-based composite materials using the DIW technique.⁹⁶ Nevertheless, this process required intensive mixing steps and the very high viscosity of the inks negatively impacted their printability. Furthermore, the difficulty to disperse the cellulose in the polymer aqueous solutions limited the maximal cellulose content to 10 wt %. Chemical modification of the cellulose crystals and fibers was required to reach a solid content of 20 wt %, which is still significantly lower than that achieved with other types of fillers. Additionally, the use of viscous polymers hinders the processability of the ink and prevents full alignment of the cellulose crystals in the resulting composite.

This thesis aims to tackle current limitations in 3D printing of dense cellulose-reinforced composite materials by proposing a simple and versatile approach that broadens the range of possible polymer matrices, enables control over the alignment of CNCs and further increases the maximum cellulose concentration in complex-shaped printed composites. The alignment of CNCs is a particularly interesting feature because it not only enhances the mechanical properties of printed composites along the aligned direction but it also introduces birefringent behavior in the resulting material. In this thesis, the shear-induced alignment of CNCs is exploited to reinforce bulk composites in specific orientations

or to create microparticles with special magneto-optical properties arising from the birefringent nature of their constituent cellulose nanocrystals.

1.6 Functional cellulose-based microparticles and microcapsules

Cellulose has attracted a lot of attention in the field of structural colors because of its liquid-crystal like behavior. Various factors such as cellulose aspect ratio, temperature, the addition of salt, polymers or the sonication time have been investigated to influence the pitch of the chiral nematic helicoidal organization and the resulting coloration of the dried cellulose film.^{39, 110-115} However, because of the birefringent nature of cellulose, these colorations are mostly observed between cross-polarized filters while they appear transparent or, depending on the viewing angle, iridescent in some cases.³⁷ By taking advantage of the self-assembling properties of cellulose, structural colors could also be obtained by producing sacrificial cellulose templates for various metallic nanoparticles.¹¹⁶ Nevertheless, self-assembling of cellulose lacks control over directionality and therefore limits this approach. To overcome this limitation, the use of magnetic or electric fields and shear were investigated.^{33, 115, 117, 118} Despite the high degree of alignment or the control of the resulting nematic pitch, these techniques also are limited to thin films when solution casted or very diluted systems to meet the required rheological properties of the particles to rotate. Therefore, interest lies in the possibilities to either confine the self-assembling of cellulose or to control their alignment in three dimensional structures.

In addition to complex-shaped bulk structures made by 3D printing, cellulose-based materials in the form of microparticles and microcapsules have also been explored as a means to generate attractive functional properties. In one example, hydrogel beads loaded with cellulose nanocrystals were produced from droplet templates made in microfluidic devices.¹¹⁹ Interestingly, cellulose nanocrystals were observed to reorganize into a spherical configuration when confined inside droplets.¹²⁰ An attractive feature of this production method is the strong elongation and shear forces involved in the emulsification process. These forces were shown to be sufficient to align fibers and particles along the flow direction.¹²¹ Additionally, microfluidic emulsification is a very versatile technique in terms of material composition, enabling the reproducible preparation of monodisperse individual micro-beads with tunable composition.

Microfluidic emulsification is typically achieved by extruding small quantities of fluids through narrow channels to create micrometer-scaled droplets.¹²² These channels are produced through photolithography or chemical etching using silicon, glass or poly(dimethylsiloxane) (PDMS) substrates. During the emulsification process, the different channels are filled with the liquid forming the droplet (inner-phase) and the immiscible surrounding medium (outer phase). As the inner phase is forced into the continuous medium, droplets are generated either by jetting or dripping mechanisms. Droplet pinch-off through either one of these mechanisms is possible using flow-focusing or step-

emulsification devices. Although the throughput of these systems is relatively low, great potential for upscaling has recently been demonstrated.¹²³

The microparticles and microcapsules made by emulsification techniques have promising applications in the bio-medical and pharmaceutical fields for targeted drug delivery.¹²⁴ Beyond biomedical applications, microparticles and microcapsules of tailored compositions also allow for the integration of novel functions and properties when added to a macroscale composite. This has led, for example, to self-healing composites¹²⁵ and anti-fouling coatings.¹²⁶ Depending on the application, these capsules can have a wide range of chemical compositions and structural complexity (single or double shells).¹²⁷ Because of the nature of the process, the geometry of particles and capsules generated from droplet templates is often limited to a spherical shape. Overcoming this limitation could lead to anisotropic microparticles that may find interesting applications as self-assembling large-area photonic crystals and optical devices.¹²⁷⁻¹²⁹

Various approaches have been explored to produce anisotropic microparticles, resulting in complex multiphase systems with a broad variety of shapes.^{130, 131} However, most of these approaches are based on chemical phase separation and reactions, limiting the processes to certain polymer combinations only.^{130, 132} Exploiting shear and extensional forces exerted in microfluidic channels is an interesting potential route to generate anisotropic microparticles that are less dependent on the chemistry of the constituent phases. If cellulose nano crystals are present in the droplet template, these forces are also expected to induce alignment of the particles inside the deformed droplet. The resulting anisotropic microparticles would therefore exhibit a textured architecture with cellulose nanocrystals aligned along the deformation direction. Because of the birefringent properties of the cellulose nanocrystals, these anisotropic microparticles could potentially be used in applications that require optical sensing or light modulation.

1.7 References

1. Habibi, Y., Key Advances in the Chemical Modification of Nanocelluloses. *Chem Soc Rev*, **2014**. 43: p. 1519-42.
2. Siqueira, G., J. Bras, and A. Dufresne, Cellulosic Bionanocomposites: A Review of Preparation, Properties and Applications. *Polymers-Basel*, **2010**. 2: p. 728-765.
3. Habibi, Y., L. Lucia, A., and O. Rojas, J., Cellulose Nanocrystals: Chemistry, Self-Assembly, and Applications. *Chem. Rev.*, **2010**. 110: p. 3479-3500.
4. Beck-Candanedo, S., M. Roman, and D.G. Gray, Effect of Reaction Conditions on the Properties and Behavior of Wood Cellulose Nanocrystal Suspensions. *Biomacromolecules*, **2005**. 6: p. 1048-54.
5. Dufresne, A., Nanocellulose from Nature to High Performance Tailored Materials. 2012, Berlin: Walter de Gruyter GmbH. 460.
6. Harrington, J.J., Hierarchical Modelling of Softwood Hygro-Elastic Properties. **2002**.
7. Zimmermann, T., E. Pöhler, and T. Geiger, Cellulose Fibrils for Polymer Reinforcement. *Adv. Eng. Mater.*, **2004**. 6: p. 754-761.

8. Tingaut, P., T. Zimmermann, and G. Sebe, Cellulose Nanocrystals and Microfibrillated Cellulose as Building Blocks for the Design of Hierarchical Functional Materials. *J. Mater. Chem.*, **2012**. 22: p. 20105-20111.
9. Iwamoto, S., W. Kai, A. Isogai, and T. Iwata, Elastic Modulus of Single Cellulose Microfibrils from Tunicate Measured by Atomic Force Microscopy. *Biomacromolecules*, **2009**. 10: p. 2571-2576.
10. Gao, X., E. Sozumert, Z. Shi, G. Yang, and V.V. Silberschmidt, Assessing Stiffness of Nanofibres in Bacterial Cellulose Hydrogels: Numerical-Experimental Framework. *Mater. Sci. Eng., Proc. Conf.*, **2017**. 77: p. 9-18.
11. Tashiro, K. and M. Kobayashi, Theoretical Evaluation of Three-Dimensional Elastic Constants of Native and Regenerated Celluloses: Role of Hydrogen Bonds. *Polymer*, **1991**. 32: p. 1516-1526.
12. Dufresne, A., Nanocellulose from Nature to High Performance Tailored Materials. 2012, Berlin Walter de Gruyter GmbH.
13. Moon, R.J., A. Martini, J. Nairn, J. Simonsen, and J. Youngblood, Cellulose Nanomaterials Review: Structure, Properties and Nanocomposites. *Chem. Soc. Rev.*, **2011**. 40: p. 3941-3994.
14. Helbert, W., J.Y. Cavallé, and A. Dufresne, Thermoplastic Nanocomposites Filled with Wheat Straw Cellulose Whiskers. Part I: Processing and Mechanical Behavior. *Polym. Compos.*, **1996**. 17: p. 604-611.
15. Coleman, J.N., U. Khan, W.J. Blau, and Y.K. Gun'ko, Small but Strong: A Review of the Mechanical Properties of Carbon Nanotube–Polymer Composites. *Carbon*, **2006**. 44: p. 1624-1652.
16. Favier, V., H. Chanzy, and J.Y. Cavaille, Polymer Nanocomposites Reinforced by Cellulose Whiskers. *Macromolecules*, **1995**. 28: p. 6365-6367.
17. Dagnon, K.L., A.E. Way, S.O. Carson, J. Silva, J. Maia, and S.J. Rowan, Controlling the Rate of Water-Induced Switching in Mechanically Dynamic Cellulose Nanocrystal Composites. *Macromolecules*, **2013**. 46: p. 8203-8212.
18. Dagnon, K.L., K. Shanmuganathan, C. Weder, and S.J. Rowan, Water-Triggered Modulus Changes of Cellulose Nanofiber Nanocomposites with Hydrophobic Polymer Matrices. *Macromolecules*, **2012**. 45: p. 4707-4715.
19. Siqueira, G., A.P. Mathew, and K. Oksman, Processing of Cellulose Nanowhiskers/Cellulose Acetate Butyrate Nanocomposites Using Sol–Gel Process to Facilitate Dispersion. *Compos. Sci. Technol.*, **2011**. 71: p. 1886-1892.
20. Benítez, A.J., F. Lossada, B. Zhu, T. Rudolph, and A. Walther, Understanding Toughness in Bioinspired Cellulose Nanofibril/Polymer Nanocomposites. *Biomacromolecules*, **2016**. 17: p. 2417-2426.
21. Reising, A.B., R.J. Moon, and J.P. Youngblood, Effect of Particle Alignment on Mechanical Properties of Neat Cellulose Nanocrystal Films. *J-FOR*, **2012**. 2: p. 32-41.
22. Diaz, J.A., X. Wu, A. Martini, J.P. Youngblood, and R.J. Moon, Thermal Expansion of Self-Organized and Shear-Oriented Cellulose Nanocrystal Films. *Biomacromolecules*, **2013**. 14: p. 2900-2908.
23. Wang, B., J.G. Torres-Rendon, J. Yu, Y. Zhang, and A. Walther, Aligned Bioinspired Cellulose Nanocrystal-Based Nanocomposites with Synergetic Mechanical Properties and Improved Hygromechanical Performance. *ACS Appl. Mater. Interfaces*, **2015**. 7: p. 4595-4607.
24. Endo, R., T. Saito, and A. Isogai, Tempo-Oxidized Cellulose Nanofibril/Poly(Vinyl Alcohol) Composite Drawn Fibers. *Polymer*, **2013**. 54: p. 935-941.

25. Jalal Uddin, A., J. Araki, and Y. Gotoh, Toward “Strong” Green Nanocomposites: Polyvinyl Alcohol Reinforced with Extremely Oriented Cellulose Whiskers. *Biomacromolecules*, **2011**. 12: p. 617-624.
26. Iwamoto, S., A. Isogai, and T. Iwata, Structure and Mechanical Properties of Wet-Spun Fibers Made from Natural Cellulose Nanofibers. *Biomacromolecules*, **2011**. 12: p. 831-836.
27. Ureña-Benavides, E.E., P.J. Brown, and C.L. Kitchens, Effect of Jet Stretch and Particle Load on Cellulose Nanocrystal–Alginate Nanocomposite Fibers. *Langmuir*, **2010**. 26: p. 14263-14270.
28. Håkansson, K.M.O., A.B. Fall, F. Lundell, S. Yu, C. Krywka, S.V. Roth, G. Santoro, M. Kvik, L. Prahl Wittberg, L. Wågberg, and L.D. Söderberg, Hydrodynamic Alignment and Assembly of Nanofibrils Resulting in Strong Cellulose Filaments. *Nat Commun*, **2014**. 5.
29. Dong, H., K.E. Strawhecker, J.F. Snyder, J.A. Orlicki, R.S. Reiner, and A.W. Rudie, Cellulose Nanocrystals as a Reinforcing Material for Electrospun Poly(Methyl Methacrylate) Fibers: Formation, Properties and Nanomechanical Characterization. *Carbohydr. Polym.*, **2012**. 87: p. 2488-2495.
30. Ben Azouz, K., E.C. Ramires, W. Van den Fonteyne, N. El Kissi, and A. Dufresne, Simple Method for the Melt Extrusion of a Cellulose Nanocrystal Reinforced Hydrophobic Polymer. *ACS Macro Lett.*, **2012**. 1: p. 236-240.
31. Nicharat, A., J. Sapkota, C. Weder, and E.J. Foster, Melt Processing of Polyamide 12 and Cellulose Nanocrystals Nanocomposites. *J. Appl. Polym. Sci.*, **2015**. 132: p. n/a-n/a.
32. Pullawan, T., A.N. Wilkinson, and S.J. Eichhorn, Influence of Magnetic Field Alignment of Cellulose Whiskers on the Mechanics of All-Cellulose Nanocomposites. *Biomacromolecules*, **2012**. 13: p. 2528-2536.
33. Bordel, D., J.-L. Putaux, and L. Heux, Orientation of Native Cellulose in an Electric Field. *Langmuir*, **2006**. 22: p. 4899-4901.
34. Sugiyama, J., H. Chanzy, and G. Maret, Orientation of Cellulose Microcrystals by Strong Magnetic Fields. *Macromolecules*, **1992**. 25: p. 4232-4234.
35. Podsiadlo, P., L. Sui, Y. Elkasabi, P. Burgardt, J. Lee, A. Miryala, W. Kusumaatmaja, M.R. Carman, M. Shtein, J. Kieffer, J. Lahann, and N.A. Kotov, Layer-by-Layer Assembled Films of Cellulose Nanowires with Antireflective Properties. *Langmuir*, **2007**. 23: p. 7901-7906.
36. Mhd Haniffa, M.A.C., Y.C. Ching, L.C. Abdullah, S.C. Poh, and C.H. Chuah, Review of Bionanocomposite Coating Films and Their Applications. *Polymers-Basel*, **2016**. 8: p. 246.
37. Zhang, Y.P., V.P. Chodavarapu, A.G. Kirk, and M.P. Andrews, Nanocrystalline Cellulose for Covert Optical Encryption. *Journal of Nanophotonics*, **2012**. 6: p. 1-10, 10.
38. Fukuzumi, H., T. Saito, T. Iwata, Y. Kumamoto, and A. Isogai, Transparent and High Gas Barrier Films of Cellulose Nanofibers Prepared by Tempo-Mediated Oxidation. *Biomacromolecules*, **2009**. 10: p. 162-165.
39. Gray, D. and X. Mu, Chiral Nematic Structure of Cellulose Nanocrystal Suspensions and Films; Polarized Light and Atomic Force Microscopy. *Mater.*, **2015**. 8: p. 5427.
40. Vidiella del Blanco, M., E.J. Fischer, and E. Cabane, Underwater Superoleophobic Wood Cross Sections for Efficient Oil/Water Separation. *Advanced Materials Interfaces*, **2017**. 4: p. 1700584.

41. Merk, V., M. Chanana, T. Keplinger, S. Gaan, and I. Burgert, Hybrid Wood Materials with Improved Fire Retardance by Bio-Inspired Mineralisation on the Nano- and Submicron Level. *Green Chemistry*, **2015**. 17: p. 1423-1428.
42. Wang, Y., W. Yan, M. Frey, M. Vidiella del Blanco, M. Schubert, M. Adobes-Vidal, and E. Cabane, Liquid-Like SiO₂-G-Pdms Coatings on Wood Surfaces with Underwater Durability, Antifouling, Antismudge, and Self-Healing Properties. *Advanced Sustainable Systems*, **2019**. 3: p. 1800070.
43. Bledzki, A.K. and J. Gassan, Composites Reinforced with Cellulose Based Fibres. *Prog. Polym. Sci.*, **1999**. 24: p. 221-274.
44. Foster, E.J., *et al.*, Current Characterization Methods for Cellulose Nanomaterials. *Chem. Soc. Rev.*, **2018**. 47: p. 2609-2679.
45. Xue, Y., Z. Mou, and H. Xiao, Nanocellulose as a Sustainable Biomass Material: Structure, Properties, Present Status and Future Prospects in Biomedical Applications. *Nanoscale*, **2017**. 9: p. 14758-14781.
46. Jorfi, M. and E.J. Foster, Recent Advances in Nanocellulose for Biomedical Applications. *J. Appl. Polym. Sci.*, **2015**. 132.
47. De France, K.J., T. Hoare, and E.D. Cranston, Review of Hydrogels and Aerogels Containing Nanocellulose. *Chem. of Mater.*, **2017**. 29: p. 4609-4631.
48. Voisin, H., L. Bergström, P. Liu, and A. Mathew, Nanocellulose-Based Materials for Water Purification. *Nanomater.*, **2017**. 7: p. 57.
49. Nogi, M., S. Iwamoto, A.N. Nakagaito, and H. Yano, Optically Transparent Nanofiber Paper. *Adv. Mater.*, **2009**. 21: p. 1595-1598.
50. Zoppe, J.O., R.A. Venditti, and O.J. Rojas, Pickering Emulsions Stabilized by Cellulose Nanocrystals Grafted with Thermo-Responsive Polymer Brushes. *J. Colloid. Interface Sci.*, **2012**. 369: p. 202-209.
51. Lee, H., J. Sundaram, and S. Mani, Production of Cellulose Nanofibrils and Their Application to Food: A Review, in *Nanotechnology: Food and Environmental Paradigm*, R. Prasad, V. Kumar, and M. Kumar, Editors. 2017, Springer Singapore: Singapore. p. 1-33.
52. Kim, T., C. Bao, M. Hausmann, G. Siqueira, T. Zimmermann, and W.S. Kim, Electrochemical Sensors: 3d Printed Disposable Wireless Ion Sensors with Biocompatible Cellulose Composites (Adv. Electron. Mater. 2/2019). *Advanced Electronic Materials*, **2019**. 5: p. 1970007.
53. Voisin, H.P., K. Gordeyeva, G. Siqueira, M.K. Hausmann, A.R. Studart, and L. Bergström, 3d Printing of Strong Lightweight Cellular Structures Using Polysaccharide-Based Composite Foams. *ACS Sustainable Chem. Eng.*, **2018**. 6: p. 17160-17167.
54. Martin-Martinez, F.J., K. Jin, D. López Barreiro, and M.J. Buehler, The Rise of Hierarchical Nanostructured Materials from Renewable Sources: Learning from Nature. *ACS Nano*, **2018**. 12: p. 7425-7433.
55. Studart, A.R. and R.M. Erb, Bioinspired Materials That Self-Shape through Programmed Microstructures. *Soft Matter*, **2014**. 10: p. 1284-1294.
56. Bar-On, B., F.G. Barth, P. Fratzl, and Y. Politi, Multiscale Structural Gradients Enhance the Biomechanical Functionality of the Spider Fang. *Nat Commun*, **2014**. 5: p. 3894.
57. Fratzl, P., Biomimetic Materials Research: What Can We Really Learn from Nature's Structural Materials? *J. R. Soc., Interface*, **2007**. 4: p. 637-642.
58. Fratzl, P. and R. Weinkamer, Nature's Hierarchical Materials. *Prog. Mater. Sci.*, **2007**. 52: p. 1263-1334.

59. Duarte Rafael, C., A.V. Flores Augusto, and M. Stevens, Camouflage through Colour Change: Mechanisms, Adaptive Value and Ecological Significance. *Philosophical Transactions of the Royal Society B: Biological Sciences*, **2017**. 372: p. 20160342.
60. Deravi, L.F., A.P. Magyar, S.P. Sheehy, G.R.R. Bell, L.M. Mäthger, S.L. Senft, T.J. Wardill, W.S. Lane, A.M. Kuzirian, R.T. Hanlon, E.L. Hu, and K.K. Parker, The Structure-Function Relationships of a Natural Nanoscale Photonic Device in Cuttlefish Chromatophores. *J R Soc Interface*. 11: p. 20130942-20130942.
61. Wardill, T.J., P.T. Gonzalez-Bellido, R.J. Crook, and R.T. Hanlon, Neural Control of Tuneable Skin Iridescence in Squid. *Proceedings of the Royal Society B: Biological Sciences*, **2012**. 279: p. 4243-4252.
62. Cortese, L., L. Pattelli, F. Utel, S. Vignolini, M. Burrelli, and D.S. Wiersma, Anisotropic Light Transport in White Beetle Scales. *Adv. Opt. Mater.*, **2015**. 3: p. 1337-1341.
63. Teyssier, J., S.V. Saenko, D. van der Marel, and M.C. Milinkovitch, Photonic Crystals Cause Active Colour Change in Chameleons. *Nat. Commun.*, **2015**. 6: p. 6368.
64. Mäthger Lydia, M., J. Denton Eric, N.J. Marshall, and T. Hanlon Roger, Mechanisms and Behavioural Functions of Structural Coloration in Cephalopods. *J. R. Soc., Interface*, **2009**. 6: p. S149-S163.
65. Dumanli, A.G. and T. Savin, Recent Advances in the Biomimicry of Structural Colours. *Chem. Soc. Rev.*, **2016**. 45: p. 6698-6724.
66. Kraft, P., C. Evangelista, M. Dacke, T. Labhart, and M.V. Srinivasan, Honeybee Navigation: Following Routes Using Polarized-Light Cues. *Philos Trans R Soc Lond B Biol Sci*, **2011**. 366: p. 703-708.
67. Saito, A., M. Nakajima, Y. Miyamura, K. Sogo, Y. Ishikawa, and Y. Hirai, Morpho Blue Reproduced by Nanocasting Lithography. *Spie Optics + Photonics*. Vol. 6327. 2006: SPIE.
68. Studart, A.R., Towards High-Performance Bioinspired Composites. *Adv. Mater.*, **2012**. 24: p. 5024-5044.
69. Zhu, B., N. Jasinski, A. Benitez, M. Noack, D. Park, A.S. Goldmann, C. Barner-Kowollik, and A. Walther, Hierarchical Nacre Mimetics with Synergistic Mechanical Properties by Control of Molecular Interactions in Self-Healing Polymers. *Angew. Chem., Int. Ed.*, **2015**. 54: p. 8653-8657.
70. Grossman, M., F. Bouville, F. Erni, K. Masania, R. Libanori, and A.R. Studart, Mineral Nano-Interconnectivity Stiffens and Toughens Nacre-Like Composite Materials. *Adv. Mater.*, **2017**. 29: p. 1605039.
71. Sydney Gladman, A., E.A. Matsumoto, R.G. Nuzzo, L. Mahadevan, and J.A. Lewis, Biomimetic 4d Printing. *Nat. Mater.*, **2016**. 53: p. 413-418.
72. Gantenbein, S., K. Masania, W. Woigk, J.P.W. Sesseg, T.A. Tervoort, and A.R. Studart, Three-Dimensional Printing of Hierarchical Liquid-Crystal-Polymer Structures. *Nature*, **2018**. 561: p. 226-230.
73. Schaffner, M., J.A. Faber, L. Pianegonda, P.A. Rühs, F. Coulter, and A.R. Studart, 3d Printing of Robotic Soft Actuators with Programmable Bioinspired Architectures. *Nat. Commun.*, **2018**. 9: p. 878.
74. Kokkinis, D., M. Schaffner, and A.R. Studart, Multimaterial Magnetically Assisted 3d Printing of Composite Materials. *Nat Commun*, **2015**. 6: p. 8643.
75. Collino, R.R., T.R. Ray, L.M. Friedrich, J.D. Cornell, C.D. Meinhart, and M.R. Begley, Scaling Relationships for Acoustic Control of Two-Phase Microstructures During Direct-Write Printing. *Mater. Res. Lett.*, **2018**. 6: p. 191-198.

76. Sommer, M.R., L. Alison, C. Minas, E. Tervoort, P.A. Ruhs, and A.R. Studart, 3d Printing of Concentrated Emulsions into Multiphase Biocompatible Soft Materials. *Soft Matter*, **2017**. 13: p. 1794-1803.
77. Minas, C., D. Carnelli, E. Tervoort, and A.R. Studart, 3d Printing of Emulsions and Foams into Hierarchical Porous Ceramics. *Adv. Mater.*, **2016**. 28: p. 9993-9999.
78. Schaffner, M., P.A. Rühs, F. Coulter, S. Kilcher, and A.R. Studart, 3d Printing of Bacteria into Functional Complex Materials. *Sci. Adv.*, **2017**. 3: p. eaao6804.
79. Lehner, B.A.E., D.T. Schmieden, and A.S. Meyer, A Straightforward Approach for 3d Bacterial Printing. *ACS Synthetic Biology*, **2017**. 6: p. 1124-1130.
80. Barry III, R.A., R.F. Shepherd, J.N. Hanson, R.G. Nuzzo, P. Wiltzius, and J.A. Lewis, Direct-Write Assembly of 3d Hydrogel Scaffolds for Guided Cell Growth. *Adv. Mater.*, **2009**. 21: p. 2407-2410.
81. Compton, B.G. and J.A. Lewis, 3d-Printing of Lightweight Cellular Composites. *Adv Mater*, **2014**. 26: p. 5930-5.
82. Lewis, J.A., Direct Ink Writing of 3d Functional Materials. *Adv. Funct. Mater.*, **2006**. 16: p. 2193-2204.
83. Kumar, S., M. Hofmann, B. Steinmann, E.J. Foster, and C. Weder, Reinforcement of Stereolithographic Resins for Rapid Prototyping with Cellulose Nanocrystals. *ACS Appl. Mater. Interfaces*, **2012**. 4: p. 5399-5407.
84. Maren, R. and N. Fernando, Deposition of Cellulose Nanocrystals by Inkjet Printing, in *Model Cellulosic Surfaces*. 2009, American Chemical Society. p. 157-171.
85. Palaganas, N.B., J.D. Mangadlao, A.C.C. de Leon, J.O. Palaganas, K.D. Pangilinan, Y.J. Lee, and R.C. Advincula, 3d Printing of Photocurable Cellulose Nanocrystal Composite for Fabrication of Complex Architectures Via Stereolithography. *ACS Appl. Mater. Interfaces*, **2017**. 9: p. 34314-34324.
86. Suwanprateeb, J., Improvement in Mechanical Properties of Three-Dimensional Printing Parts Made from Natural Polymers Reinforced by Acrylate Resin for Biomedical Applications: A Double Infiltration Approach. *Polymer International*, **2006**. 55: p. 57-62.
87. Studart, A.R., Additive Manufacturing of Biologically-Inspired Materials. *Chem Soc Rev*, **2016**. 45: p. 359-76.
88. Martínez Ávila, H., S. Schwarz, N. Rotter, and P. Gatenholm, 3d Bioprinting of Human Chondrocyte-Laden Nanocellulose Hydrogels for Patient-Specific Auricular Cartilage Regeneration. *Bioprinting*, **2016**. 1–2: p. 22-35.
89. Rees, A., L.C. Powell, G. Chinga-Carrasco, D.T. Gethin, K. Syverud, K.E. Hill, and D.W. Thomas, 3d Bioprinting of Carboxymethylated-Periodate Oxidized Nanocellulose Constructs for Wound Dressing Applications. *Biomed Res Int*, **2015**. 2015: p. 925757.
90. Wang, B., A.J. Benitez, F. Lossada, R. Merindol, and A. Walther, Bioinspired Mechanical Gradients in Cellulose Nanofibril/Polymer Nanopapers. *Angew. Chem., Int. Ed.*, **2016**. 55: p. 5966-5970.
91. Leppiniemi, J., P. Lahtinen, A. Paajanen, R. Mahlberg, S. Metsä-Kortelainen, T. Pinomaa, H. Pajari, I. Vikholm-Lundin, P. Pursula, and V.P. Hytonen, 3d-Printable Bioactivated Nanocellulose-Alginate Hydrogels. *ACS Appl Mater Interfaces*, **2017**. 9: p. 21959-21970.
92. Li, V.C.F., A. Mulyadi, C.K. Dunn, Y. Deng, and H.J. Qi, Direct Ink Write 3d Printed Cellulose Nanofiber Aerogel Structures with Highly Deformable, Shape Recoverable, and Functionalizable Properties. *ACS Sustainable Chem. Eng.*, **2018**. 6: p. 2011-2022.

93. Håkansson, K.M.O., I.C. Henriksson, C. de la Peña Vázquez, V. Kuzmenko, K. Markstedt, P. Enoksson, and P. Gatenholm, Solidification of 3d Printed Nanofibril Hydrogels into Functional 3d Cellulose Structures. *Adv. Mater. Technol.*, **2016**: p. 1600096-n/a.
94. Markstedt, K., A. Escalante, G. Toriz, and P. Gatenholm, Biomimetic Inks Based on Cellulose Nanofibrils and Cross-Linkable Xylans for 3d Printing. *ACS Appl. Mater. Interfaces*, **2017**. 9: p. 40878-40886.
95. Markstedt, K., A. Mantas, I. Tournier, H. Martínez Ávila, D. Hägg, and P. Gatenholm, 3d Bioprinting Human Chondrocytes with Nanocellulose–Alginate Bioink for Cartilage Tissue Engineering Applications. *Biomacromolecules*, **2015**. 16: p. 1489-1496.
96. Siqueira, G., D. Kokkinis, R. Libanori, M.K. Hausmann, A.S. Gladman, A. Neels, P. Tingaut, T. Zimmermann, J.A. Lewis, and A.R. Studart, Cellulose Nanocrystal Inks for 3d Printing of Textured Cellular Architectures. *Adv. Funct. Mater.*, **2017**.
97. Sultan, S., G. Siqueira, T. Zimmermann, and A.P. Mathew, 3d Printing of Nano-Cellulosic Biomaterials for Medical Applications. *Current Opinion in Biomedical Engineering*, **2017**. 2: p. 29-34.
98. Sultan, S. and A.P. Mathew, 3d Printed Scaffolds with Gradient Porosity Based on a Cellulose Nanocrystal Hydrogel. *Nanoscale*, **2018**. 10: p. 4421-4431.
99. Li, V.C.-F., C.K. Dunn, Z. Zhang, Y. Deng, and H.J. Qi, Direct Ink Write (Diw) 3d Printed Cellulose Nanocrystal Aerogel Structures. *Sci. Rep.*, **2017**. 7: p. 8018.
100. Dai, L., T. Cheng, C. Duan, W. Zhao, W. Zhang, X. Zou, J. Aspler, and Y. Ni, 3d Printing Using Plant-Derived Cellulose and Its Derivatives: A Review. *Carbohydr. Polym.*, **2019**. 203: p. 71-86.
101. Buchtová, N. and T. Budtova, Cellulose Aero-, Cryo- and Xerogels: Towards Understanding of Morphology Control. *Cellulose*, **2016**. 23: p. 2585-2595.
102. Müller, M., E. Öztürk, Ø. Arlov, P. Gatenholm, and M. Zenobi-Wong, Alginate Sulfate–Nanocellulose Bioinks for Cartilage Bioprinting Applications. *Ann. Biomed. Eng.*, **2017**. 45: p. 210-223.
103. Basu, A., J. Lindh, E. Ålander, M. Strømme, and N. Ferraz, On the Use of Ion-Crosslinked Nanocellulose Hydrogels for Wound Healing Solutions: Physicochemical Properties and Application-Oriented Biocompatibility Studies. *Carbohydr. Polym.*, **2017**. 174: p. 299-308.
104. Shin, S., S. Park, M. Park, E. Jeong, K. Na, H.J. Youn, and J. Hyun, Cellulose Nanofibers for the Enhancement of Printability of Low Viscosity Gelatin Derivatives. *BioResources*, **2017**. 12: p. 2941-2954.
105. Grützmacher, H., J. Wang, A. Chiappone, I. Roppolo, F. Shao, E. Fantino, M. Lorusso, D. Rentsch, K. Dietliker, and C.F. Pirri, All-in-One Cellulose Nanocrystals for 3d Printing of Nanocomposite Hydrogels. *Angew. Chem., Int. Ed.*, **2017**: p. n/a-n/a.
106. Chinga-Carrasco, G., Cellulose Fibres, Nanofibrils and Microfibrils: The Morphological Sequence of Mfc Components from a Plant Physiology and Fibre Technology Point of View. *Nanoscale Res. Lett.*, **2011**. 6: p. 417-417.
107. Torres-Rendon, J.G., M. Köpf, D. Gehlen, A. Blaeser, H. Fischer, L.D. Laporte, and A. Walther, Cellulose Nanofibril Hydrogel Tubes as Sacrificial Templates for Freestanding Tubular Cell Constructs. *Biomacromolecules*, **2016**. 17: p. 905-913.
108. Malinen, M.M., L.K. Kanninen, A. Corlu, H.M. Isoniemi, Y.-R. Lou, M.L. Yliperttula, and A.O. Urtti, Differentiation of Liver Progenitor Cell Line to Functional Organotypic Cultures in 3d Nanofibrillar Cellulose and Hyaluronan-Gelatin Hydrogels. *Biomaterials*, **2014**. 35: p. 5110-5121.

109. Yan-Ru, L., K. Liisa, K. Tytti, N. Johanna, N.L. A., B. Deborah, U. Arto, and Y. Marjo, The Use of Nanofibrillar Cellulose Hydrogel as a Flexible Three-Dimensional Model to Culture Human Pluripotent Stem Cells. *Stem Cells and Development*, **2014**. 23: p. 380-392.
110. Qiao, C., G. Chen, J. Zhang, and J. Yao, Structure and Rheological Properties of Cellulose Nanocrystals Suspension. *Food Hydrocolloids*, **2016**. 55: p. 19-25.
111. Araki, J., M. Wada, and S. Kuga, Steric Stabilization of a Cellulose Microcrystal Suspension by Poly(Ethylene Glycol) Grafting. *Langmuir*, **2001**. 17: p. 21-27.
112. Hirai, A., O. Inui, F. Horii, and M. Tsuji, Phase Separation Behavior in Aqueous Suspensions of Bacterial Cellulose Nanocrystals Prepared by Sulfuric Acid Treatment. *Langmuir*, **2009**. 25: p. 497-502.
113. Orts, W.J., L. Godbout, R.H. Marchessault, and J.F. Revol, Enhanced Ordering of Liquid Crystalline Suspensions of Cellulose Microfibrils: A Small Angle Neutron Scattering Study. *Macromolecules*, **1998**. 31: p. 5717-5725.
114. Gray, D.G., Chiral Nematic Ordering of Polysaccharides. *Carbohydr. Polym.*, **1994**. 25: p. 277-284.
115. Pan, J., W. Hamad, and S.K. Straus, Parameters Affecting the Chiral Nematic Phase of Nanocrystalline Cellulose Films. *Macromolecules*, **2010**. 43: p. 3851-3858.
116. Kelly, J.A., K.E. Shopsowitz, J.M. Ahn, W.Y. Hamad, and M.J. MacLachlan, Chiral Nematic Stained Glass: Controlling the Optical Properties of Nanocrystalline Cellulose-Templated Materials. *Langmuir*, **2012**. 28: p. 17256-17262.
117. Frka-Petesic, B. and S. Vignolini, So Much More Than Paper. *Nature Photonics*, **2019**. 13: p. 365-367.
118. Bruno, F.P., R. Harisoa, J. Bruno, and H. Laurent, Dynamically Controlled Iridescence of Cholesteric Cellulose Nanocrystal Suspensions Using Electric Fields. *Adv. Mater.*, **2017**. 29: p. 1606208.
119. Ye, C., L. Kennedy, K. Shirk, U.M. Córdova-Figueroa, J. Youngblood, and C.J. Martinez, Cnc-Loaded Hydrogel Particles Generated from Single- and Double-Emulsion Drops. *Green Materials*, **2015**. 3: p. 25-34.
120. Parker, R.M., B. Frka-Petesic, G. Guidetti, G. Kamita, G. Consani, C. Abell, and S. Vignolini, Hierarchical Self-Assembly of Cellulose Nanocrystals in a Confined Geometry. *ACS Nano*, **2016**. 10: p. 8443-8449.
121. Håkansson, K., Orientation of Elongated Particles in Shear and Extensional Flow, in *Trita-MEK*. 2012, KTH Royal Institute of Technology: Stockholm. p. viii, 25.
122. Neethirajan, S., I. Kobayashi, M. Nakajima, D. Wu, S. Nandagopal, and F. Lin, Microfluidics for Food, Agriculture and Biosystems Industries. *Lab on a Chip*, **2011**. 11: p. 1574-1586.
123. Ofner, A., D.G. Moore, P.A. Rühs, P. Schwendimann, M. Eggersdorfer, E. Amstad, D.A. Weitz, and A.R. Studart, High-Throughput Step Emulsification for the Production of Functional Materials Using a Glass Microfluidic Device. *Macromol. Chem. Physic.*, **2017**. 218: p. 1600472.
124. Singh, M.N., K.S.Y. Hemant, M. Ram, and H.G. Shivakumar, Microencapsulation: A Promising Technique for Controlled Drug Delivery. *Research in pharmaceutical sciences*, **2010**. 5: p. 65-77.
125. Neuser, S., P.W. Chen, A.R. Studart, and V. Michaud, Fracture Toughness Healing in Epoxy Containing Both Epoxy and Amine Loaded Capsules. *Adv. Eng. Mater.*, **2014**. 16: p. 581-587.

126. Andersson Trojer, M., L. Nordstierna, J. Bergek, H. Blanck, K. Holmberg, and M. Nydén, Use of Microcapsules as Controlled Release Devices for Coatings. *Advances in Colloid and Interface Science*, **2015**. 222: p. 18-43.
127. Dendukuri, D. and P.S. Doyle, The Synthesis and Assembly of Polymeric Microparticles Using Microfluidics. *Adv. Mater.*, **2009**. 21: p. 4071-4086.
128. Velikov, K.P., T.v. Dillen, A. Polman, and A.v. Blaaderen, Photonic Crystals of Shape-Anisotropic Colloidal Particles. *Applied Physics Letters*, **2002**. 81: p. 838-840.
129. Cederquist, K.B., S.L. Dean, and C.D. Keating, Encoded Anisotropic Particles for Multiplexed Bioanalysis. *Wiley Interdisciplinary Reviews: Nanomedicine and Nanobiotechnology*, **2010**. 2: p. 578-600.
130. Lee, K.J., J. Yoon, and J. Lahann, Recent Advances with Anisotropic Particles. *Current Opinion in Colloid & Interface Science*, **2011**. 16: p. 195-202.
131. Shum, H.C., A.R. Abate, D. Lee, A.R. Studart, B. Wang, C.-H. Chen, J. Thiele, R.K. Shah, A. Krummel, and D.A. Weitz, Droplet Microfluidics for Fabrication of Non-Spherical Particles. *Macromol. Rapid Commun.*, **2010**. 31: p. 108-118.
132. Kim, B., S. Lee, and S.H. Kim, Double-Emulsion-Templated Anisotropic Microcapsules for Ph-Triggered Release. *Advanced Materials Interfaces*, **2018**. 5.

Chapter 2.

Dynamics of cellulose nanocrystals alignment during 3D printing

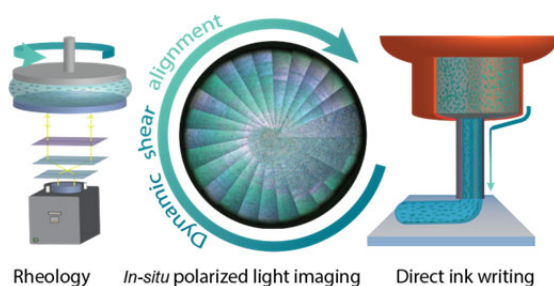
Michael K. Hausmann^{1,2}, Patrick A. Rühs^{1*}, Gilberto Siqueira^{1,2*}, Jörg Läger³, Rafael Libanori¹, Tanja Zimmermann² and André R. Studart^{1*}

¹Complex Materials, Department of Materials, ETH Zürich, 8093 Zürich, Switzerland

²Empa, Swiss Federal Laboratories for Materials Science and Technology, Applied Wood Materials Laboratory, 8600 Dübendorf, Switzerland

³Anton Paar Germany GmbH, Helmuth-Hirth-Strasse 6, D-73760 Ostfildern, Germany

This chapter is published in *ACS Nano*, 2018, 12 (7), pp 6926-6937



2.1 Abstract

The alignment of anisotropic particles during ink deposition directly affects the microstructure and properties of materials manufactured by extrusion-based 3D printing. Although particle alignment in diluted suspensions is well described by analytical and numerical models, the dynamics of particle orientation in the highly concentrated inks typically used for printing *via* direct ink writing (DIW) remains poorly understood. Using cellulose nanocrystals (CNCs) as model building blocks of increasing technological relevance, we study the dynamics of particle alignment under the shear stresses applied to concentrated inks during DIW. With the help of *in-situ* polarization rheology, we find that the time period needed for particle alignment scales inversely with the applied shear rate and directly with the particle concentration. Such dependences can be quantitatively described by a simple scaling relation and qualitatively interpreted in terms of steric and hydrodynamic interactions between particles at high shear rates and particle concentrations. Our understanding of the alignment dynamics is then utilized to estimate the effect of shear stresses on the orientation of particles during the printing process. Finally, proof-of-concept experiments show that the combination of shear and extensional flow in 3D printing nozzles of different geometries provides an effective means to tune the orientation of CNCs from fully aligned to core-shell architectures. These findings offer powerful quantitative guidelines for the digital manufacturing of composite materials with programmed particle orientations and properties.

2.2 Introduction

Three-dimensional (3D) printing is an enticing manufacturing technology because it enables the fabrication of materials with intricate macroscopic shapes and controlled microstructures and properties.¹⁻⁶ An effective way to locally control the structure and functionalities of composite materials is to align anisotropic particles in deliberate orientations to reach site-specific properties. Controlled particle orientation during 3D printing has been achieved using for example magnetic fields,⁷⁻¹⁰ shear stresses,^{9, 11-13} or acoustic waves¹⁴ in extrusion-based and stereolithographic processes. Among the anisotropic particles used thus far in 3D-printed composites, cellulose is of particular relevance, as it is a sustainable resource that combines biocompatibility with interesting mechanical and optical properties.^{13, 15-24} Cellulose can be found as anisotropic reinforcing material in the form of small, stiff nanocrystals (CNCs) or long and flexible fibrils (CNFs).

The alignment of CNCs and other anisotropic particles during 3D printing holds enormous potential since it allows one to mimic the design principles underlying the exquisite multiscale architectures of biological materials such as wood, plant stems, bone, and mollusk shells.² Alignment of such particles by shear stresses is a particularly interesting approach because shear-inducing flow is intrinsically present in extrusion-based 3D printing processes.^{1, 2, 11-13, 25} While it is well known that anisotropic particles align during extrusion, only a few studies have attempted to quantify the degree and dynamics of alignment in particle-filled inks.^{9, 11, 13} Prior to alignment, anisotropic particles tend to form percolating networks that give rise to a finite yield stress, below which the ink does not flow. Particle alignment above the yield stress results in a strong shear-thinning response of the ink and thus a pronounced parabolic velocity flow profile within the nozzle.²⁶⁻²⁸ Understanding the dynamics of particle alignment and the flow behavior of the resulting non-Newtonian fluids is therefore required to design inks, nozzles, and extrusion conditions to 3D print composites with programmed local structures and properties.

The alignment dynamics determine whether anisotropic particles will be oriented by the flow within the residence time in the nozzle. Particle alignment can be induced by both shear and extensional flow.²⁹ For the well-studied case of pure shear flow, particles move following orbital trajectories, known as Jeffery orbitals.^{30, 31} The time period (t) that an anisotropic particle needs to undergo a full rotation within a Jeffery orbital scales with the inverse of the applied shear rate ($\dot{\gamma}$): $t \sim 1/\dot{\gamma}$.³²⁻³⁴ When suspended in non-Newtonian fluids, particles show Jeffery orbitals that drift over time until an equilibrium orientation is reached.^{30, 31} Because they do not take into account steric, hydrodynamic, and contact interactions between particles, such theoretical analyses are usually not sufficient to describe the alignment of anisotropic particles at high volume fractions. Recent work has shown that contact interactions play a key role in the microstructures and properties of highly concentrated suspensions of short fiber bundles used for composite fabrication.^{35, 36} Experimental validation of these models requires the use of analytical tools that can follow

particle orientation during flow. Several experimental methods have been employed for that purpose, including rheology, neutron and X-ray scattering techniques, and optical microscopy.³⁷⁻⁴⁵

Another attractive tool for the experimental study of the flow-induced alignment of optically anisotropic materials is the polarized light imaging technique. In this approach, particle orientation is tracked during flow by color changes resulting from the varying angle between the particle axis and the orientation of the polarizer/analyzer. Polarized light imaging has been extensively used to investigate the effect of flow on the structure of liquid crystal polymers under shear flow.^{33, 46-50} The different nematic, smectic, and cholesteric phases that result from the self-assembly of liquid crystals were found to be directly affected by flow. When subjected to shear flow, for example, such phases transform into stripes with herringbone patterns, whose thickness decreases with the applied shear.⁵¹ Such flow-induced textures further expand the rich phase behavior of such self-assembling systems.

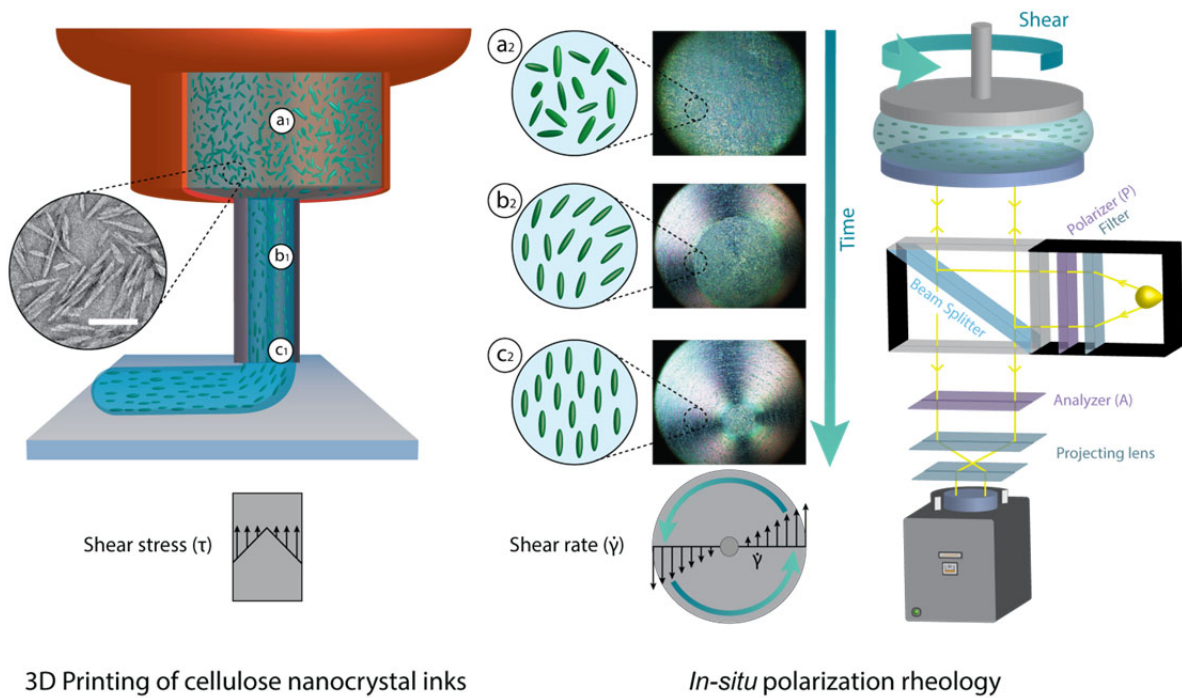
While theoretical models have been put forward to describe the flow-induced orientation in particle suspensions and studies on liquid crystal polymers have provided important insights into the phase behavior of self-assembling systems under flow, experimental investigations on the dynamics of alignment of self-assembling anisotropic particles in highly concentrated suspensions of relevance for 3D printing remain scarce.^{9, 44} The self-assembly of Brownian anisotropic particles in concentrated printable inks promotes the formation of liquid crystalline phases prior to the extrusion process. Liquid crystalline nematic domains, for example, form at concentrations as low as 0.5 wt % if the aspect ratio of the anisotropic particles is higher than 100. For CNCs with an aspect ratio of 20, this critical concentration increases to 3 wt %.⁵²⁻⁶¹ In the absence of flow, particles are locally aligned within the liquid crystal domains but the different orientation of individual domains leads to a global random distribution of particle orientations. Understanding how these domains reorganize under flow and determine the microstructure during extrusion is crucial for the design of inks and for establishing manufacturing conditions suitable for the 3D printing of composites loaded with anisotropic particles.

Here, we use shear-induced polarized light imaging to study the alignment dynamics of cellulose nanocrystals under shear flow in suspensions with high volume fractions of particles. Because of the high volume fractions in the range from 10 to 40 wt %, the investigated CNC inks show a well-defined yield stress and a strong shear thinning behavior. First, we evaluate the effect of the yield stress on the alignment of CNCs under increasing shear deformation. This is followed by steady-state rheological experiments, in which we quantify the degree of alignment over time for suspensions of different CNC volume fractions subjected to varying shear rates. This dependence on shear rates is then utilized to estimate the level of alignment during extrusion if only shear forces are considered. Comparison of these estimates with experiments in model capillaries allows us to propose guidelines for the design of inks and extrusion geometries according to the level of

alignment targeted in the final 3D-printed composites. This fundamental understanding sheds light into the possible range of microstructures achievable by direct ink writing of inks containing high concentrations of anisotropic CNC particles, which we introduced in a previous publication.¹¹

2.3 Results and discussion

The dynamics of the orientation of anisotropic particles under shear flow depends to the shear rate imposed to the suspending fluid. In 3D printing by direct ink writing (DIW), the fluid is deposited on a substrate in a spatially controlled manner through the application of an external pressure along the nozzle. Because of wall friction, the shear stresses $[\tau]$ arising from the applied pressure are maximal at the nozzle wall and decrease linearly toward the center of the nozzle (Scheme 2.1). The rheological properties of the ink determine the characteristic velocity and shear rate profiles that will result from these imposed stresses. Therefore, understanding particle alignment dynamics during the 3D printing process requires a quantitative analysis of the rheological behavior of the ink and of the response of the anisotropic particles to the applied shear rate. For stress-sensitive anisotropic inks, such as cellulose nanocrystal gels, the alignment of particles itself changes the rheological properties of the fluid. This leads to a complex interplay between the ink rheological behavior, the orientation dynamics of particles, and the local shear rates applied through the nozzle. To understand this interdependency, we simplify the problem by studying first the effect of a fixed shear rate profile on the alignment dynamics of cellulose nanocrystals.



Scheme 2.1. Alignment of cellulose nanocrystal particles during shearing in a direct ink writing process (left) and in an in-situ polarization rheological setup (right). Left: Schematic of a 3D printing process with (a1) randomly organized cellulose nanocrystals in the cartridge, (b1) shear-induced alignment during extrusion through the nozzle and (c1) the final oriented extruded segment. During extrusion, the CNC is aligned due to a velocity profile that arises from the shear stress

imposed on the suspension (TEM image with scale bar 100 nm). Right: Alignment of CNCs under shearing conditions visualized through *in-situ* polarization rheology using a parallel plate geometry. The polarized light imaging system is integrated in the rheometer setup to enable investigation of the effect of shear rate and time on the CNC orientation process (a2, b2, and c2).⁴⁷

Particle alignment dynamics at controlled shear rates is investigated using *in-situ* polarization rheology. In this technique, the time-dependent alignment of cellulose nanocrystals can be quantified by optical imaging the suspension while it is subjected to a well-controlled shear rate in a rheometer (Scheme 2.1). Because cellulose nanocrystals are optically anisotropic, they display different colors depending on their orientation, when observed between two cross-polarized filters. The observed color depends on the orientation and spacing between the individual crystals. As an example, particles exhibiting circumferential orientation around a central axis lead to a characteristic Maltese cross under cross-polarizers (Scheme 2.1, c₂). The dark and colored areas in this characteristic image emerge from either complete or partial light extinction as it passes through the two polarizers, respectively (Appendix Section A4).^{41, 62}

The alignment of the nanosized cellulose crystals under pure shear flow was measured *in-situ* using suspensions with varying particle concentrations in a parallel plate geometry. As opposed to the linear increase in shear stress along the radius of the printer's nozzle, rotation of the upper plate leads to a linear increase in shear rate from the center to the rim of the discs. Our experiments show that the lyotropic, needle-shaped cellulose crystals transiently orient from the rim toward the center of the disc in response to the linear gradient in shear rate. This is reflected by the gradual transition in colors (Scheme 2.1, a₂ to c₂) between the center and the rim of the disc as well as the broadening of the extinction or transmission areas. Note that the camera used to record this transient alignment was placed slightly off-centered to obtain a full view of the side and the middle of the shearing plane. Using this technique, it is possible to track the evolution of alignment quality in CNC suspensions as a function of time for well-defined shear deformations or shear rates.

Our analysis of the alignment of CNC particles using *in-situ* polarization rheology was first carried out by applying a constantly increasing shear deformation or shear stress to suspensions containing volume fractions between 10 and 40 wt% of particles. These concentrations lie above the threshold volume fraction beyond which the particles form a space-filling percolating network (Appendix A5). As a result, all the suspensions investigated in this study form a gel with a well-defined yield stress.⁶³ Because of the high volume fraction used, the CNC particles are also expected to self-assemble into chiral nematic domains throughout the suspension.^{37, 61, 64-66} The formation of nematic domains was experimentally confirmed for suspensions containing more than 10 wt% CNCs (Figure A. 2 and Figure A. 6)

Flow-induced alignment of the particles is therefore only possible if the applied stress surpasses the yield stress of the suspension. Indeed, our measurements show that the shear

stresses at which the initial color pattern starts to change in the cross-polarized images are in good agreement with the yield stress of the gel detected through the inflection point in the rheological flow curve. Because the shear stress scales with the shear deformation at low rotational displacements, the shear stress applied in these measurements increases linearly from the center to the rim of the disc. The nominal shear stresses reported here correspond to the stress applied at the plate's rim. Taking a suspension with 20 wt% CNC as an example, no preferential orientation of particles is observed under cross-polarized light when the shear stress applied at the rim is lower than the yield stress of the gel (Figure 2.1a, I). But if the nominal yield stress value of 200 Pa is reached at the rim, the gel starts to flow and CNC orientation is observed at this outer region of the plate (II). The fraction of aligned CNCs increases as the local shear stress progressively increases (III-IV). Eventually, higher stress levels result in CNC alignment along the rotation direction throughout the whole probed volume (V).

The yield stress of the CNC suspensions was found to increase significantly from 30 to 4220 Pa as the concentration of particles increased from 10 to 40 wt % (Figure 2.1b). This dependence can be described by the simple power law: $\tau_y = k\phi^p$, where τ_y is the yield stress of the gel, ϕ is the volume fraction of particles, k is a constant that depends on the interparticle interactions and particle size, and p is an exponent that depends on the microstructure of the particle network. The exponent $p = 3$ obtained by fitting the measured data with the power law function lies within the range 1.4 – 5.0 typically found in the literature (Figure 2.1c; see also Appendix A5).^{67, 68}

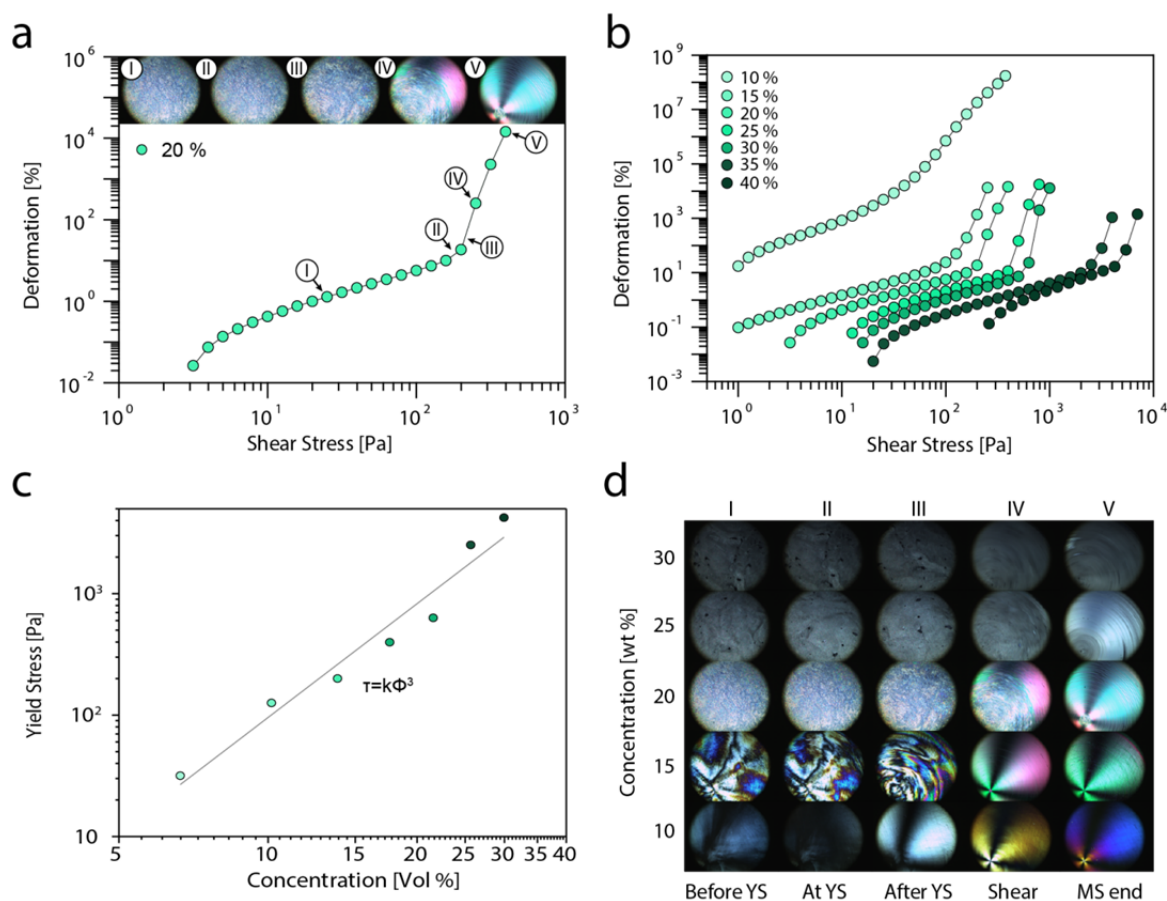


Figure 2.1. Flow and alignment of CNCs as a function of applied shear stress and cellulose concentration. (a) Yield stress (YS) measurement for a 20 wt % CNC ink and the corresponding polarized images recorded before the yield stress (I), at the yield stress (II), after the yield stress (III)-(IV), and at the end of the measurement (V). (b) Yield stress measurements of CNC suspensions at 10, 15, 20, 25, 30, 35, and 40 wt %. (c) Yield stress values extracted from (b) for inks with different concentrations of CNCs. The yield stress dependence on the CNC volume fraction is shown to be well described by an experimentally fitted power law. (d) In-situ rheology imaging as a function of CNC concentration at varying applied shear stresses (I-V).

The observed power law dependence of the yield stress on the volume fraction of particles is often interpreted in terms of the underlying microstructure of the load-bearing particle network.⁶⁹ In the case of spherical particles, the network is usually formed by fractal-like agglomerates that connect to each other to fill up the entire volume of the suspension. Such agglomerates are larger and less dense if the volume fraction of particles is lower. By contrast, higher particle volume fractions lead to smaller and denser agglomerates. In analogy to fractal-like agglomerates, our yield stress data suggest that the formation of load-bearing structural units of different sizes and densities depend on the CNC concentration. Indeed, the size of nematic domains was observed to decrease with increasing concentrations of CNCs in the suspension (Figure 2.1d). At the lowest concentration of 10 wt %, large domains are clearly visible. Increasing the CNC weight fraction to 15 and 20 wt % leads to smaller domains with distinct alignment directions. Above 20 wt %, these domains become even smaller and are no longer easily visible by optical microscopy (Figure 2.1d). This interpretation is supported by earlier studies that showed a decrease of the

interparticle spacing within liquid crystalline phases with increasing particle volume fraction.^{24, 70, 71}

Once the yield stress of the CNC suspension is reached, particles are expected to align parallel to the imposed shear forces. Since the alignment process of particles in highly concentrated suspensions is poorly understood, we investigate the effect of the imposed shear rates on the alignment dynamics of particles in suspensions with varying CNC concentrations. This was experimentally accomplished by exploiting the linear radial distribution of the shear rate applied in the parallel plate geometry used for the rheological measurements. Because of this linear distribution, the alignment time at different shear rates can be directly assessed in one single measurement at a constant global rotational speed of the plate.

The time-dependent alignment process for a 20 wt % CNC suspension at a fixed global rotational speed of the plate is shown in Figure 2.2a. The global rotation speed is indicated in terms of the maximum shear rate at the rim of the plate, which in this example was kept constant at 150 s^{-1} . The cross-polarized snapshots reveal that alignment starts at the rim of the plate and progresses toward the center of the plate, in response to the imposed linear gradient in shear rate. The alignment time at one given shear rate can thus be directly assessed from the optical images. To demonstrate the alignment dynamics visually, polarizing light images were taken at precise time intervals and stacked into a 3D image (Figure 2.2b and Appendix A6). Extracting a vertical slice of such 3D image allows us to directly determine the alignment time as a function of local shear rate (Figure 2.2c). By repeating this procedure for different suspensions and distinct maximal applied shear rates, it was possible to determine the alignment time for a wide range of shear rates and CNC concentrations (Figure 2.2d, e). Because of the linear shear rate distribution, the alignment time data overlap into a single curve regardless of the maximal shear rate applied. This confirms that the alignment time is solely governed by the local shear rate rather than the maximum applied shear rate (Figure 2.2d). Plotting the alignment time data obtained at different particle concentrations, we obtain a design diagram that indicates the minimum time and shear rate necessary to induce alignment of the CNCs under shear flow (Figure 2.2e).

Our experimental results reveal that the alignment time at a given shear rate is strongly influenced by the concentration of CNC particles. For example, the alignment time at 20 s^{-1} increases approximately 2-fold if the CNC concentration increases from 20 to 25 wt %. The alignment of CNCs under shear flow is accompanied by significant changes in the microstructure and rheological properties of the suspension (Appendix A6 and S7). The longer alignment times measured for concentrated suspensions is probably related to the stronger steric and hydrodynamic interactions between particles at high CNC volume fractions (Figure 2.2e and Appendix A6 and A7). Following the interpretation provided to explain the yield stress data, the alignment dynamics should be affected by the size and

density of the nematic domains formed within the suspension. At the low concentrations ranging from 10 to 15 wt %, the larger nematic domains formed by the CNC crystals are less dense and easier to break and align under external shear. This phenomenon is also typically observed in liquid crystals.^{50, 72} The much smaller and denser domains formed at concentrations above 20 wt % are more difficult to rupture and thus require shearing for longer times to achieve particle alignment (Figure A. 5-7).

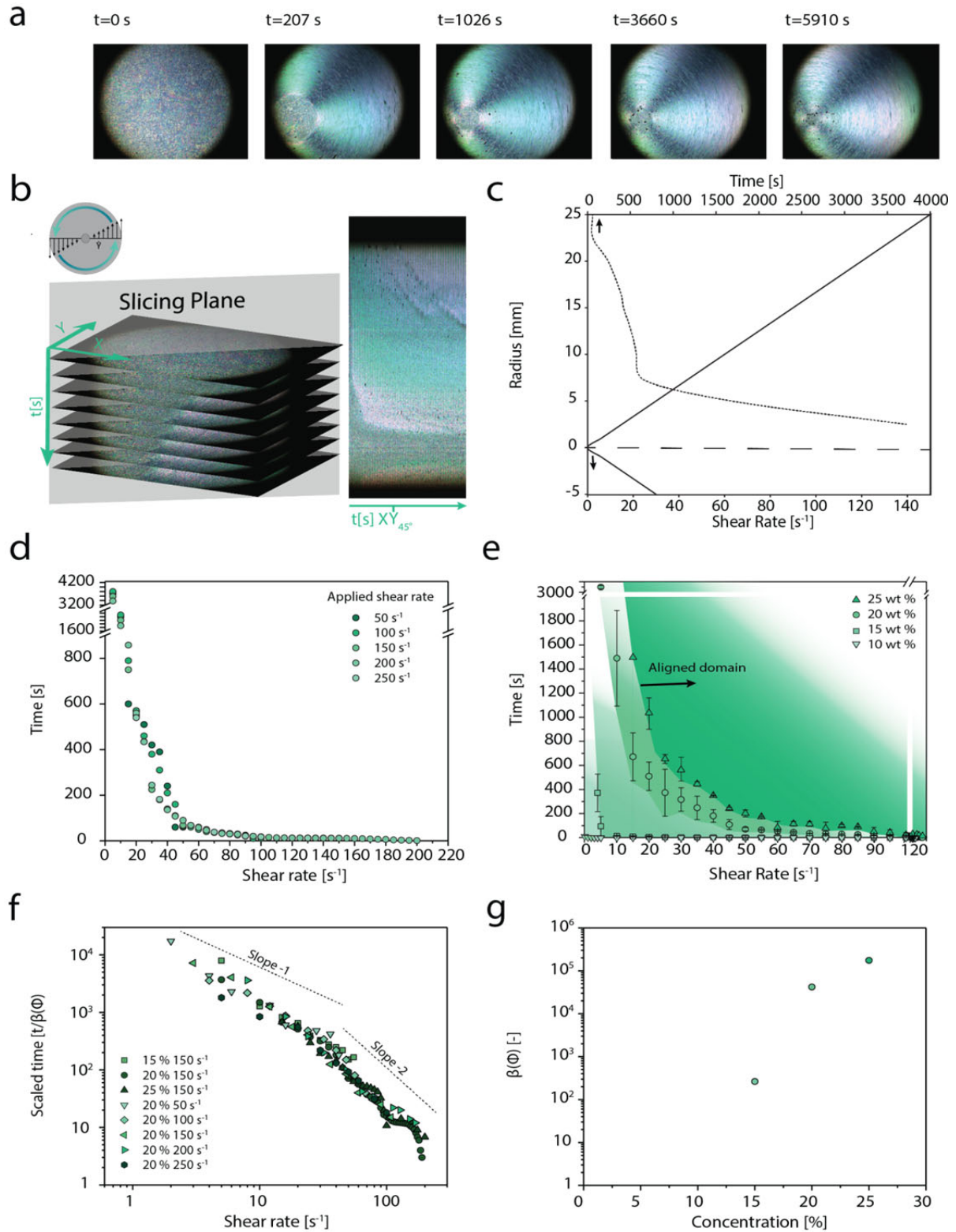


Figure 2.2. Alignment of CNCs as a function of time for fixed applied shear rates and CNC concentrations. (a) Snapshots taken at different time intervals highlighting the dynamic alignment of a 20 wt % ink at a constant shear rate of 150 s^{-1} . (b) Stack of polarized light images obtained for an ink containing 20 wt% CNC subjected to a constant shear rate of 50 s^{-1} . Vertical slicing of the image stack at an arbitrary angle of $\pm 45^\circ$ enables direct visualization of the alignment process as a function of time. (c) Shear rate distribution in a parallel plate system and the evolution of the alignment time as a function of the plate radius extracted from the sliced stack of pictures. (d) Dependence of the alignment time on the local shear rate for a 20 wt% CNC ink subjected to different maximal applied shear rates (shear rate at the rim). (e) Alignment dynamics diagram displaying the average alignment times as functions of shear rates for different CNC concentrations of

10, 15, 20 and 25 wt %. (f) Log-log master plot of the alignment time as a function of shear rate with corresponding slopes of -1 and -2. (g) Variation of the scaling factor, $\beta(\Phi)$, with the CNC concentration.

Besides the effect of CNC concentration on alignment times, our experimental results also provide insights into the dependence of the alignment dynamics on the applied shear rate. According to predictions for an isolated anisotropic particle suspended in a Newtonian fluid, the time it takes for the particles to align (t) is inversely proportional to the applied shear rate ($\dot{\gamma}$).³² However, it is questionable whether this simple scaling relation also holds true for a particle assembled within a nematic domain of the complex multidomain microstructure obtained at high CNC volume fractions. To address this question, we combined all the experimental data obtained from our transient shearing tests in a single log-log plot displaying the alignment time as a function of the applied shear rate (Figure 2.2f). To account for the slower alignment process in suspensions with higher CNC volume fractions, the alignment time was scaled with a constant term β that should capture the effect of steric and hydrodynamic interactions on particle reorientation under shear. In this analysis, β depends only on the volume fraction of particles (Figure 2.2g), leading to the following relation:

$$t = \frac{\beta(\phi)}{\dot{\gamma}} \quad Eq. 1$$

This simple scaling describes quite well the dynamics of the alignment process, since all the experimental data were found to fall in a single master curve in the log-log plot (Figure 2.2f). Analysis of the slope of the resulting master curve allows us to compare the effect of shear rate on alignment dynamics in concentrated suspensions with the dependence expected for a model single particle. Surprisingly, we observe that the slope of -1 expected for a single particle provides a good approximation of the shear rate dependence of the alignment times at low shear rates. This suggests that, if the applied shear rates are low, the simple relation $t \sim 1/\dot{\gamma}$ is still a reasonable approximation even if particles are part of crystalline domains at high volume fractions. By contrast, the alignment time shows a stronger shear rate dependence when higher shear rates are applied. In this case, we find that the alignment time scales with $1/\dot{\gamma}^2$. This indicates that in concentrated inks subjected to high shear rates particles align faster than expected for a diluted suspension. Although further work is needed to explain the underlying physics giving rise to this unusual scaling relation, such a stronger effect of the shear rate suggests that hydrodynamic and steric interactions between the particles at high volume fractions and high shear rates might facilitate their alignment by shear. Such interparticle interactions increase significantly with the CNC volume fractions, which is reflected in higher values for the scaling factor $\beta(\phi)$ (Figure 2.2g). It is important to note that the above physical description of the alignment dynamics should be universal and applicable to other concentrated colloidal systems, as long as the anisotropic particles interact repulsively like the model CNC particles used in our experiments. Our analysis might also be applicable to more complex fluids containing distinct types of particles, if such particles are sufficiently different in size to enable a coarse-

grained description in which the larger particles are assumed to be suspended in a homogeneous fluid containing the smaller particles. Beyond these simplifying assumptions, this study provides a basis for future investigations of the alignment dynamics in more complex colloidal suspensions containing for example several types of particles that interact through attractive and repulsive forces.

Our understanding of the effect of particle concentration on the yield stress and alignment dynamics allows us to estimate the contribution of shear flow alone on the alignment of anisotropic particles during 3D printing. Using a glass capillary as model nozzle and pressures within the range applied for direct ink writing, we evaluate the level of particle alignment expected throughout the nozzle radius (Appendix A8). The quartz capillaries used have a diameter ($2R$) and length (L) of 0.3 mm and 80 mm, respectively. Since the CNC inks exhibit a finite yield stress (Figure 2.1a-c), a fraction of the material will not experience any shear flow during extrusion. This fraction is located in the inner core of the extrudate, where the shear stress applied is lower than the yield stress of the ink. By comparing the yield stress of the ink with the linear change in shear stress along the nozzle radius, one can obtain the critical radius below which the material will not experience shear flow. We call this critical radius the plug-flow radius (r_{pf}). The plug-flow radius depends on the yield stress of the ink, on the geometry of the nozzle, and pressure applied during printing. For a given nozzle length and applied pressure, r_{pf} increases linearly with the yield stress of the ink (Figure 2.3a).

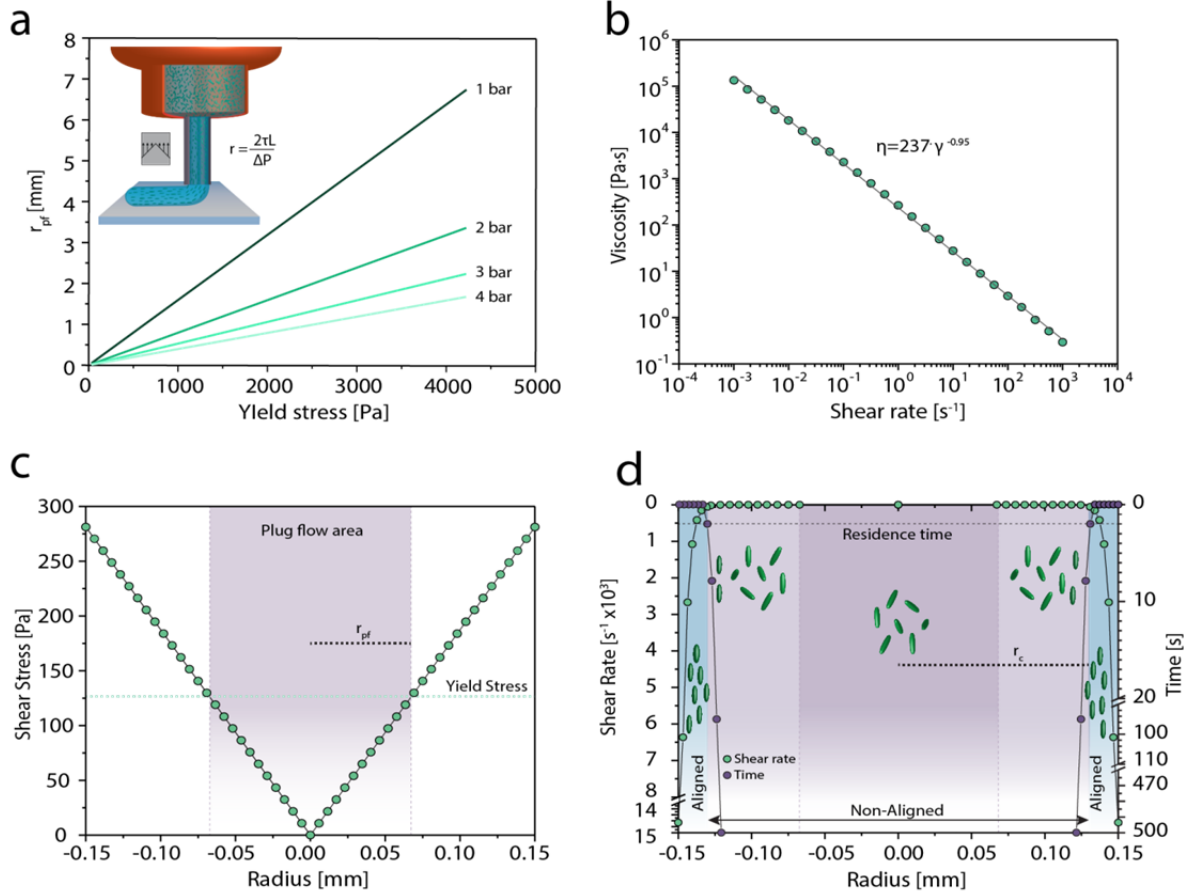


Figure 2.3. Estimation of shear-induced particle alignment expected during 3D printing of an exemplary ink containing 15 wt% CNC. (a) General dependence of the plug-flow radius (r_{pf}) on the yield stress of the ink for different applied pressures, assuming a printing needle with a diameter of 0.3 mm and length of 80 mm. (b) Flow curve for the 15 wt % ink and its description using a power law fit. (c) Shear stress distribution across the radius of a nozzle with 80 mm length and 0.3 mm diameter. The yield stress of the 15 wt % CNC ink is also indicated to show the plug-flow area of the nozzle. (d) Shear rate profile and corresponding alignment times along the nozzle radius. The residence time of the 15 wt % CNC ink is also shown to establish the differential flow domain and the region of the nozzle where shear-induced alignment of the particles is expected.

Between the plug-flow radius (r_{pf}) and the nozzle radius (R), the ink experiences shear flow. This leads to the so-called differential flow region, where shear-induced alignment of the anisotropic particles may occur. The level of particle alignment within the differential flow region of the nozzle can be estimated from the alignment time data obtained from the opto-rheological measurements. To this end, we must first determine the local shear rate imposed on the ink as a function of the nozzle radius. This is possible by translating the linear shear stress profile across the nozzle radius into a shear rate profile using the rheological behavior of the ink. As an illustrative example, we estimate the shear rate profile for an exemplary ink containing 15 wt % of CNC particles (Figure 2.3c) and subjected to a pressure of 3 bar through a model nozzle. The shear rate is given by the derivative of the velocity profile, which is strongly influenced by the rheological properties of the ink. We find that the following simple power law describes well the shear-thinning behavior of the ink (Figure 2.3b): $\eta = k\dot{\gamma}^{n-1}$, where η is the viscosity, k is the flow consistency index, and n is the flow behavior index. The obtained flow index n of this 15 wt % ink is on the same order of magnitude as the values observed for CNFs and diluted CNC suspensions.^{64, 73} Such a low n value reflects the strong shear thinning nature of the ink. Using such a rheological description, the geometry of the nozzle, and the pressure applied, we calculated the shear profile expected during extrusion of the ink with 15 wt % CNC (Figure 2.3d and Appendix A8 and A9).

Once the shear rate profile is known, one can use equation (1) to estimate the alignment time expected for different radii across the nozzle. Comparison of this alignment time with the residence time in the nozzle finally leads to the critical radius, r_c , above which particle alignment is expected within the differential flow region (Figure 2.3d). By combining equation (1) with the estimated residence time and shear rate profile we find the following prediction for the critical radius (Appendix A9):

$$\frac{r_c}{R} = \left[\frac{R\beta(\Phi)n}{L(3n+1)} \right]^n \quad Eq. 2$$

Such relation neglects any time dependence of the rheological properties of the ink. This is a reasonable assumption for the inks investigated in this work, in view of the relatively weak change of their viscosity as a function of time (Figure A. 4).

The identified plug-flow (r_{pf}) and critical (r_c) radii eventually define three distinct flow regions within the nozzle. This is illustrated in Figure 2.3d for the exemplary ink with 15 wt % CNCs. The dark purple area displays the plug flow region where no shear occurs ($r_{pf} = 0.0672$ mm). The light purple and blue areas highlight the differential flow region. Alignment due to shear forces alone is expected within the blue area. Because of the relatively short residence time (2 s for this capillary) and strong non-Newtonian nature of the ink, high shear rates are only exerted very close to the nozzle's wall. For this 15 wt % ink, we estimate the relative critical radius (r_c/R) to be around 0.83. This means that shear-induced alignment of the CNC particles of this ink is expected to occur within a distance of 25 μm from the nozzle wall. Such an aligned region corresponds to 27 % of the total volume of the filament. Following this rationale, equation (2) can be used to estimate the region of shear-induced alignment for other nozzle geometries, ink compositions, and printing conditions. The same reasoning can be repeated with 3D printing needles of different geometries (Appendix A9).

To qualitatively validate the above prediction, we performed additional experiments in which a 15 wt % CNC suspension is forced through a long glass needle at a fixed pressure, thus simulating the extrusion process. The experimental setup was designed to ensure that only shear deformation is imposed on the suspension during extrusion. This was achieved by constructing a capillary device that features a widening diameter at the entrance (Figure 2.4a). Such widening leads to an abrupt decrease in flow velocity, thus generating extensional forces that erase any alignment previously imposed to the particles.^{74, 75} Using such a device, we assessed the level of alignment of the CNC particles by taking cross-polarized optical images at different positions along the length of the glass capillary. The experiment confirms that the CNC particles are aligned only within an outer skin of the ink close to the wall of the capillary. This is clearly indicated by the darker region next to the glass wall when the capillary is observed under cross polarizers (Figure 2.4a – V).

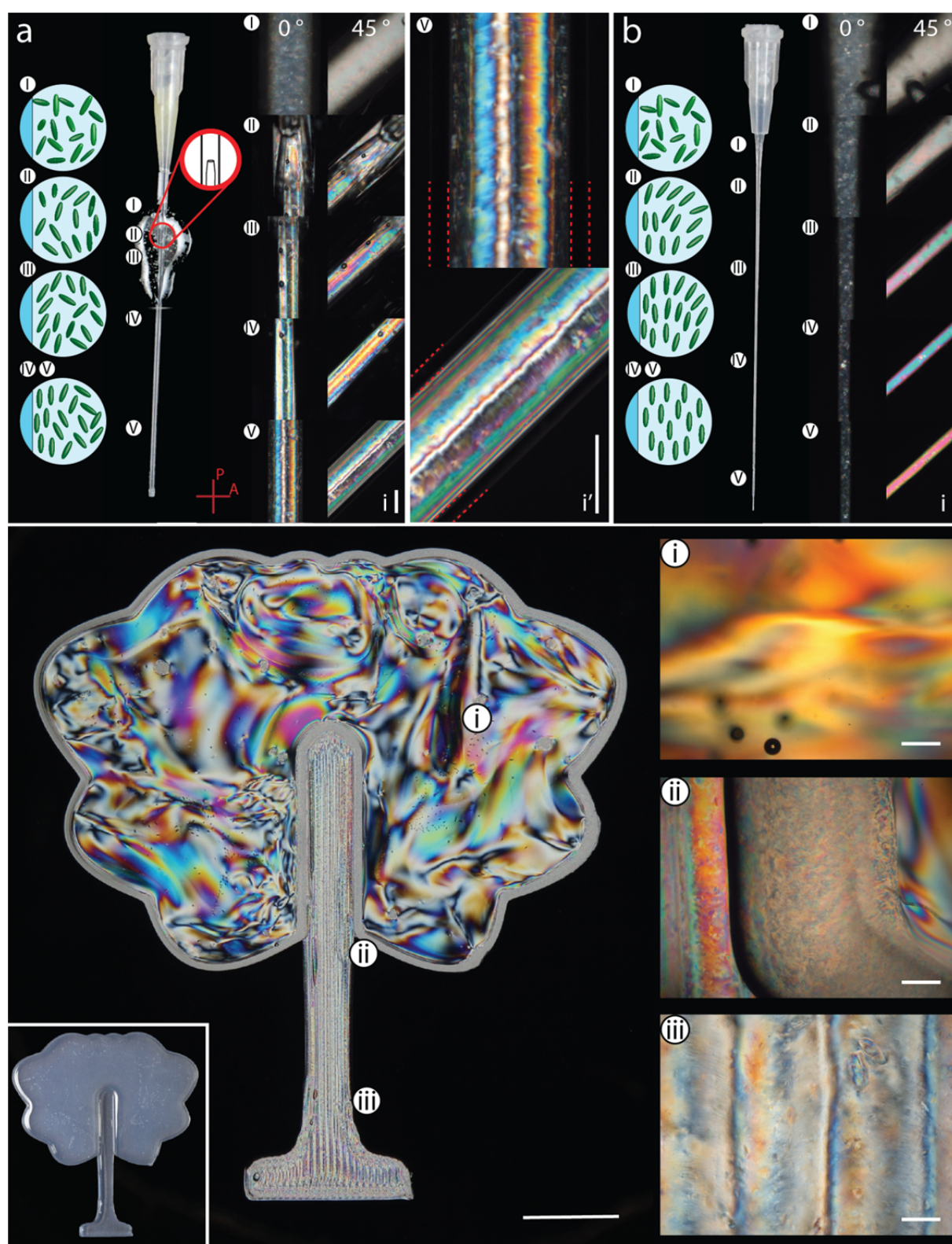


Figure 2.4. Visual assessment of CNC alignment during extrusion of a 15 wt % ink through model capillaries and an artistic illustration of our ability to locally control the orientation of printed CNC particles. (a) Polarized light imaging along a quartz capillary designed to ensure pure shear flow during extrusion. The diverging tapered geometry of the inner capillary erases possible previous alignment of particles caused by extensional flow. Extrusion was carried out at 3 bar. Polarized images captured at 0° and 45° orientation with respect to analyzer filter indicate the level of alignment of the CNC particles along the capillary length. Scale bar i: 500 μm. The zoom-in of section V highlights the alignment of CNC particles close to the capillary wall. Scale bar i': 500 μm. The walls of the capillary are indicated by dashed red lines. (b) Polarized light imaging at angles 0° and 45° along a quartz capillary with a converging tapered section (extrusion at 3

bar). Scale bar is: 500 μm . (c) Printed tree created using different inks and imaged by cross-polarized light. Scale bar: 1 cm. The inset on the left shows the tree pattern under normal illumination. OM images of selected areas containing inks with different compositions deposited with distinct approaches: (i) 10 wt % casted, (ii) interfaces between 15 wt % and 20 wt % printed inks (left), and 20 wt % printed and 10 wt % casted (right), and (iii) 15 wt % printed. Scale bar of zoomed-in sections: 200 μm .

The observation that shear-induced alignment is restricted to the skin of the printed filament contrasts with previous studies in which stronger particle alignment has been achieved by direct ink writing.^{9, 11, 13} To reconcile these observations, we conducted additional alignment experiments in capillaries with a tapered geometry. Such geometry imposes extensional flow along the entire capillary length and is representative of the shape of some of the nozzles used for direct ink writing. Extensional flow is known to be an effective means to impose orientation in anisotropic fluids.^{25, 29, 76} Indeed, our results reveal that strong alignment is achieved along the entire cross-section of the capillary if extensional flow is imposed on the CNC suspension (Figure 2.4b).

The ability to spatially tune the level of alignment of anisotropic particles through changes in the nozzle geometry, the rheological properties of the ink, and the printing operating conditions provides a wide design space for the fabrication of printed objects with controlled site-specific particle orientation. This increases the palette of possible microstructural libraries that are accessible *via* 3D printing of anisotropic particles. Different types of microstructures are needed depending on the properties required in the end function or application. Exploiting a broad range of microstructural designs to manipulate local properties is the strategy used by many living organisms to cope with the functional demands of their living environment using a limiting number of building blocks.^{77, 78} Following this rationale, one would expect that filaments with alignment restricted to the skin might combine interesting antagonistic properties, such as high wear resistance and high stretchability. Like the Byssus threads produced by mussels, these properties would arise from the combination of a softer inner core and a stiffer outer layer. By contrast, filaments containing anisotropic particles fully aligned within the entire cross-section would enable maximum reinforcement in specific directions subjected to the highest mechanical loads. This is a common design strategy in nature to create strong and stiff materials, such as those in the nacreous layer of mollusk shells.

We visually demonstrate this concept of tunable local structuring by 3D printing and casting a colorful tree pattern consisting only of CNC particles as building blocks (Figure 4c). In this artistic representation, the center of the tree consists of a 10 wt % ink with large and colorful nematic domains, whereas the trunk consists of a 15 wt % CNC ink extruded along a specific direction to locally align the CNC particles. Besides these two local microstructures, the outline of the tree crown consists of a 20 wt % ink where the CNC particles are expected to align only very close to the filament surface.

2.4 Conclusion

The level of particle alignment achieved through extrusion-based 3D printing of cellulose-containing inks can be varied widely depending on the rheological properties of the ink and the type of flow imposed during the printing process. Filament architectures comprising an aligned shell around a randomly oriented core are typically produced under pure shear conditions, whereas stronger alignment is observed if the printing nozzle geometry is designed to also induce extensional flow. The first condition required for particle alignment under pure shear flow is that the applied shear stresses overcome the yield stress of the ink. Once this condition is satisfied, the time required for the alignment of anisotropic particles under shear can be quantified using a simple scaling relation that takes into account the shear rate applied and interactions between the particles at different volume fractions. At low applied shear rates, a linear dependence between the alignment time and the inverse of the shear rate was found to be a good approximation for the alignment dynamics. Deviation from this linear dependence is found at higher shear rates, where steric and hydrodynamic interactions between particles are expected to play a stronger role. Although further work is required to fully elucidate the effect of particle concentration on the alignment dynamics, our study offers quantitative parameters for the design of nozzle dimensions, printing conditions, and rheological properties required to tune the shear-induced orientation of anisotropic particles during 3D printing of composite inks.

2.5 Experimental methods

2.5.1 Sample preparation

Cellulose nanocrystals were prepared *via* sulfuric acid hydrolysis of eucalyptus pulp at the USDA Forest Service, Forest Products Laboratory (Madison, WI, USA), according to a published procedure.⁵⁶ Freeze-dried CNCs (0.98 wt % sulfur content) with a measured length of 100 ± 40 nm and a diameter of 6.5 ± 2 nm (TEM image in Appendix Figure A. 1) were dispersed in water at different concentrations, ranging from 10 wt % up to 40 wt % and mixed for 5 min at 2500 and 3500 rpm, respectively, with a speed mixer (model DAC 150.1 FVZ). Previous work on these CNC particles has shown that they exhibit zeta potentials in the range of -40 to -45 mV when suspended in water containing 10 mM NaCl.⁷⁹ This high electrical potential results in repulsive forces between the particles in the aqueous medium. The resulting CNC gel was left overnight for swelling, mixed at 3500 rpm for 5 min, and stored in a refrigerator prior to testing. Before the measurements the samples were premixed at 3500 rpm for 5 min.

2.5.2 Transmission electron microscopy

Cellulose nanocrystals were characterized by transmission electron microscopy (TEM, Jeol JEM-2200FS, USA Inc.) using an acceleration voltage of 200 kV. Plasma-activated carbon-coated grids were used as support onto which a 0.02 wt % diluted suspension of the

cellulose nanocrystals was deposited and stained with a 2 wt % solution of uranyl acetate for 30 s. The average lengths and diameters of CNCs were measured with the software ImageJ.

2.5.3 Rheology

The rheometer setup (Anton Paar MCR502) was modified with a reflection polariscope known as shear-Induced Polarized Light Imaging (SIPLI) to enable *in-situ* polarization microscopy. In this setup, the shearing plate acts simultaneously as optical mirror (roughness about 1 μm) and rheological shearing tool. A Peltier temperature control unit with a transparent bottom plate (P-PTD 200/GI) and a corresponding Peltier-controlled hood (H-PTD 200) provides a uniform temperature distribution and optical access to the sample.

Working with a high-intensity white light source, the LED light is projected onto the beam splitter of the polariscope after passing a first homogenizing filter, a collimating lens, and the first linear polarizer (0°), as shown in Scheme 2.1b. The beam splitter reflects the incident beam of the light source toward the sample and transmits its reflection toward a second series of lenses and an orthogonally oriented linear polarizer (90°) onto the HR camera. A detailed description of this setup and approach was previously reported by Mykhaylyk *et al.* and Völker-Pop.^{41, 47}

Measurements were carried out using a parallel plate (50 mm diameter) gap of 0.2 mm (unless specified otherwise) and at a constant temperature of 20 $^\circ\text{C}$. The gap was chosen to enable visualization of CNC alignment. Higher gap sizes and acquisition times were shown to give equivalent results in preliminary rheological tests (Appendix Figure A. 3). Differences between the rheological properties obtained using cone-plate and parallel plate geometries were also found to be minimal in shear sweep measurements (Appendix Figure A. 4).

Yield stress measurements were performed in rotation under increasing shear stresses from 0.01 to 1000 Pa for concentrations below 30 wt %. Shear stresses up to 2000 Pa were applied for concentrations above 30 wt%. Using time intervals of 25 s for each data point, a total of 34 points were acquired during these stress sweep tests.

Flow curves under shear rates ranging from 10 s^{-1} to 350 s^{-1} were obtained through time-controlled measurements. Time sweeps at constant shear rates were performed using time intervals of 4.5 s per measuring point.

2.5.4 Image Processing

Images were processed using the software FIJI (ImageJ) V.1.51h.

2.5.5 3D printing

Printing experiments were performed using the Bioplotter Manufacturing series from EnvisionTEC. The material was extruded under controlled pressure ranging from 0.5 to 1.2 bar depending on the needle and material concentration.

Nozzles with different dimensions and geometries were prepared to study particle alignment under an optical microscope by using 80 mm long and 0.3 mm diameter quartz capillaries from Hilgenberg. The capillaries were mounted on the printer by connecting them to standard DIW needles using an adapter obtained from Nordson. The tapered capillary utilized to demonstrate the effect of extensional forces on particle alignment was prepared by connecting two circular glass capillaries with different inner diameters of 2 and 0.5 mm, respectively (World Precision Instruments). The tapered section was produced by hot pulling (Sutter Instrument Co – Model p97). The capillaries were held together with double-component epoxy glue.

The tree pattern was printed using inks containing 10, 15, and 20 wt % of CNC particles. Inks loaded with 15 and 20 wt % CNC were used to build the contour and the trunk, whereas the 10 wt % ink was casted within the boundaries of the printed contour.

2.5.6 Optical microscopy

All optical microscopy analyses were performed on an Axioplan microscope from Zeiss equipped with cross-polarized filters. The capillaries were placed between the polarized filters for imaging.

2.6 Acknowledgement

We thank P.Fischer for the scientific contribution and advices, J.Kohlbrecher for providing the additional rheometer, L. Völkerpop for the logistics between Anton Paar and ETH, as well as E. Jeoffroy and A.Demirörs for the scientific discussions and A.Huch for the TEM imaging. P.A.R. and A.R.S. greatly acknowledge the financial support from the Swiss National Science Foundation (Consolidator Grant number BSCGIO_157696). R.L. is thankful for the financial support from the Swiss Competence Center for Energy Research SCCER Mobility and the Swiss Innovation Agency Innosuisse. M.K.H and G.D.S greatly acknowledge the financial support from the Swiss National Science Foundation (200021_159906/1). This work also benefitted from support from the Swiss National Science Foundation through the National Center of Competence in Research Bio-Inspired Materials.

2.7 References

1. Compton, B.G. and J.A. Lewis, 3d-Printing of Lightweight Cellular Composites. *Adv Mater*, **2014**. 26: p. 5930-5.
2. Studart, A.R., Additive Manufacturing of Biologically-Inspired Materials. *Chem Soc Rev*, **2016**. 45: p. 359-76.
3. Gross, B.C., J.L. Erkal, S.Y. Lockwood, C. Chen, and D.M. Spence, Evaluation of 3d Printing and Its Potential Impact on Biotechnology and the Chemical Sciences. *Anal Chem*, **2014**. 86: p. 3240-53.
4. Khoo, Z.X., J.E.M. Teoh, Y. Liu, C.K. Chua, S.F. Yang, J. An, K.F. Leong, and W.Y. Yeong, 3d Printing of Smart Materials: A Review on Recent Progresses in 4d Printing. *Virtual Phys Prototy*, **2015**. 10: p. 103-122.
5. Schaffner, M., P.A. Rühls, F. Coulter, S. Kilcher, and A.R. Studart, 3d Printing of Bacteria into Functional Complex Materials. *Sci. Adv.*, **2017**. 3.
6. Farahani, R.D., K. Chizari, and D. Therriault, Three-Dimensional Printing of Freeform Helical Microstructures: A Review. *Nanoscale*, **2014**. 6: p. 10470-10485.
7. Kokkinis, D., M. Schaffner, and A.R. Studart, Multimaterial Magnetically Assisted 3d Printing of Composite Materials. *Nat Commun*, **2015**. 6: p. 8643.
8. Martin, J.J., M.S. Riederer, M.D. Krebs, and R.M. Erb, Understanding and Overcoming Shear Alignment of Fibers During Extrusion. *Soft Matter*, **2015**. 11: p. 400-405.
9. Feilden, E., C. Ferraro, Q. Zhang, E. Garcia-Tunon, E. D'Elia, F. Giuliani, L. Vandeperre, and E. Saiz, 3d Printing Bioinspired Ceramic Composites. *Sci Rep*, **2017**. 7: p. 13759.
10. Martin, J.J., B.E. Fiore, and R.M. Erb, Designing Bioinspired Composite Reinforcement Architectures Via 3d Magnetic Printing. *Nat Commun*, **2015**. 6: p. 8641.
11. Siqueira, G., D. Kokkinis, R. Libanori, M.K. Hausmann, A.S. Gladman, A. Neels, P. Tingaut, T. Zimmermann, J.A. Lewis, and A.R. Studart, Cellulose Nanocrystal Inks for 3d Printing of Textured Cellular Architectures. *Adv. Funct. Mater.*, **2017**.
12. Lewis, J.A., Direct Ink Writing of 3d Functional Materials. *Adv. Funct. Mater.*, **2006**. 16: p. 2193-2204.
13. Sydney Gladman, A., E.A. Matsumoto, R.G. Nuzzo, L. Mahadevan, and J.A. Lewis, Biomimetic 4d Printing. *Nat Mater*, **2016**. advance online publication.
14. Collino, R.R., T.R. Ray, L.M. Friedrich, J.D. Cornell, C.D. Meinhart, and M.R. Begley, Scaling Relationships for Acoustic Control of Two-Phase Microstructures During Direct-Write Printing. *Mater. Res. Lett.*, **2018**. 6: p. 191-198.
15. Siqueira, G., J. Bras, and A. Dufresne, Cellulosic Bionanocomposites: A Review of Preparation, Properties and Applications. *Polymers-Basel*, **2010**. 2: p. 728-765.
16. Ansari, F., A. Sjöstedt, P.T. Larsson, L.A. Berglund, and L. Wågberg, Hierarchical Wood Cellulose Fiber/Epoxy Biocomposites – Materials Design of Fiber Porosity and Nanostructure. *Composites, Part A*, **2015**. 74: p. 60-68.
17. Favier, V., H. Chanzy, and J.Y. Cavaille, Polymer Nanocomposites Reinforced by Cellulose Whiskers. *Macromolecules*, **1995**. 28: p. 6365-6367.
18. Siro, I. and D. Plackett, Microfibrillated Cellulose and New Nanocomposite Materials: A Review. *Cellulose*, **2010**. 17: p. 459-494.
19. Habibi, Y., Key Advances in the Chemical Modification of Nanocelluloses. *Chem Soc Rev*, **2014**. 43: p. 1519-42.
20. Habibi, Y., L. Lucia, A., and O. Rojas, J., Cellulose Nanocrystals: Chemistry, Self-Assembly, and Applications. *Chem. Rev.*, **2010**. 110: p. 3479-3500.

21. Moon, R.J., A. Martini, J. Nairn, J. Simonsen, and J. Youngblood, Cellulose Nanomaterials Review: Structure, Properties and Nanocomposites. *Chem. Soc. Rev.*, **2011**. 40: p. 3941-3994.
22. Zimmermann, T., E. Pöhler, and T. Geiger, Cellulose Fibrils for Polymer Reinforcement. *Adv. Eng. Mater.*, **2004**. 6: p. 754-761.
23. Endes, C., S. Camarero-Espinosa, S. Mueller, E.J. Foster, A. Petri-Fink, B. Rothen-Rutishauser, C. Weder, and M.J.D. Clift, A Critical Review of the Current Knowledge Regarding the Biological Impact of Nanocellulose. *J. Nanobiotechnol.*, **2016**. 14: p. 78.
24. Schütz, C., M. Agthe, A.B. Fall, K. Gordeyeva, V. Guccini, M. Salajková, T.S. Plivelic, J.P.F. Lagerwall, G. Salazar-Alvarez, and L. Bergström, Rod Packing in Chiral Nematic Cellulose Nanocrystal Dispersions Studied by Small-Angle X-Ray Scattering and Laser Diffraction. *Langmuir*, **2015**. 31: p. 6507-6513.
25. Håkansson, K.M.O., A.B. Fall, F. Lundell, S. Yu, C. Krywka, S.V. Roth, G. Santoro, M. Kvick, L. Prahl Wittberg, L. Wågberg, and L.D. Söderberg, Hydrodynamic Alignment and Assembly of Nanofibrils Resulting in Strong Cellulose Filaments. *Nat Commun*, **2014**. 5.
26. Scales, P.J., S.B. Johnson, T.W. Healy, and P.C. Kapur, Shear Yield Stress of Partially Flocculated Colloidal Suspensions. *AIChE J.*, **1998**. 44: p. 538-544.
27. Yanez, J.A., T. Shikata, F.E. Lange, and D.S. Pearson, Shear Modulus and Yield Stress Measurements of Attractive Alumina Particle Networks in Aqueous Slurries. *J. Am. Ceram. Soc.*, **1996**. 79: p. 2917-2924.
28. Santos de Oliveira, I.S., A. van den Noort, J.T. Padding, W.K. den Otter, and W.J. Briels, Alignment of Particles in Sheared Viscoelastic Fluids. *J Chem Phys*, **2011**. 135: p. 104902.
29. Håkansson, K., Orientation of Elongated Particles in Shear and Extensional Flow, in *Trita-MEK*. 2012, KTH Royal Institute of Technology: Stockholm. p. viii, 25.
30. Jeffrey, D.J. and A. Acrivos, The Rheological Properties of Suspensions of Rigid Particles. *AIChE J.*, **1976**. 22: p. 417-432.
31. Jeffery, G.B., The Motion of Ellipsoidal Particles Immersed in a Viscous Fluid. *Proceedings of the Royal Society A: Mathematical, Physical and Engineering Sciences*, **1922**. 102: p. 161-179.
32. Mewis, J. and N.J. Wagner, Colloidal Suspension Rheology. Cambridge Series in Chemical Engineering. 2011, Cambridge: Cambridge University Press.
33. Marrucci, G. and F. Greco, Flow Behavior of Liquid Crystalline Polymers, in *Advances in Chemical Physics*. 2007, John Wiley & Sons, Inc. p. 331-404.
34. Mueller, S., E.W. Llewellyn, and H.M. Mader, The Rheology of Suspensions of Solid Particles. *Proceedings of the Royal Society a-Mathematical Physical and Engineering Sciences*, **2010**. 466: p. 1201-1228.
35. Orgéas, L., P. Dumont, and S.L. Corre, 5 - Rheology of Highly Concentrated Fiber Suspensions A2 - Chinesta, Francisco, in *Rheology of Non-Spherical Particle Suspensions*, G. Ausias, Editor. 2015, Elsevier. p. 119-166.
36. Correa-Duarte, M.A., M. Grzelczak, V. Salgueirino-Maceira, M. Giersig, L.M. Liz-Marzan, M. Farle, K. Sieradzki, and R. Diaz, Alignment of Carbon Nanotubes under Low Magnetic Fields through Attachment of Magnetic Nanoparticles. *J. Phys. Chem. B*, **2005**. 109: p. 19060-19063.

37. Orts, W.J., L. Godbout, R.H. Marchessault, and J.F. Revol, Enhanced Ordering of Liquid Crystalline Suspensions of Cellulose Microfibrils: A Small Angle Neutron Scattering Study. *Macromolecules*, **1998**. 31: p. 5717-5725.
38. Gorsche, C., T. Koch, N. Moszner, and R. Liska, Exploring the Benefits of B-Allyl Sulfones for More Homogeneous Dimethacrylate Photopolymer Networks. *Polym. Chem.*, **2015**. 6: p. 2038-2047.
39. Lauger, J., R. Linemann, and W. Richtering, Shear Orientation of a Lamellar Lyotropic Liquid-Crystal. *Rheol. Acta.*, **1995**. 34: p. 132-136.
40. Camerel, F., J.C.P. Gabriel, P. Batail, P. Panine, and P. Davidson, Combined SxS–Rheological Studies of Liquid-Crystalline Colloidal Dispersions of Mineral Particles. *Langmuir*, **2003**. 19: p. 10028-10035.
41. Volker-Pop, L.M., Optical Methods in Rheology: Polarized Light Imaging. *Chem Listy*, **2014**. 108: p. 707-710.
42. Saarikoski, E., T. Saarinen, J. Salmela, and J. Seppala, Flocculated Flow of Microfibrillated Cellulose Water Suspensions: An Imaging Approach for Characterisation of Rheological Behaviour. *Cellulose*, **2012**. 19: p. 647-659.
43. Bercea, M. and P. Navard, Shear Dynamics of Aqueous Suspensions of Cellulose Whiskers. *Macromolecules*, **2000**. 33: p. 6011-6016.
44. Shafiei-Sabet, S., W.Y. Hamad, and S.G. Hatzikiriakos, Rheology of Nanocrystalline Cellulose Aqueous Suspensions. *Langmuir*, **2012**. 28: p. 17124-33.
45. Saarinen, T., S. Haavisto, A. Sorvari, J. Salmela, and J. Seppala, The Effect of Wall Depletion on the Rheology of Microfibrillated Cellulose Water Suspensions by Optical Coherence Tomography. *Cellulose*, **2014**. 21: p. 1261-1275.
46. Gleeson, J.T., R.G. Larson, D.W. Mead, G. Kiss, and P.E. Cladis, Image-Analysis of Shear-Induced Textures in Liquid-Crystalline Polymers. *Liq. Cryst.*, **1992**. 11: p. 341-364.
47. Mykhaylyk, O.O., N.J. Warren, A.J. Parnell, G. Pfeifer, and J. Laeuger, Applications of Shear-Induced Polarized Light Imaging (Sipli) Technique for Mechano-Optical Rheology of Polymers and Soft Matter Materials. *J. Polym. Sci. Pol. Phys.*, **2016**. 54: p. 2151-2170.
48. Hongladarom, K., V. Secakusuma, and W.R. Burghardt, Relation between Molecular-Orientation and Rheology in Lyotropic Hydroxypropylcellulose Solutions. *J. Rheol.*, **1994**. 38: p. 1505-1523.
49. Burghardt, W.R., Molecular Orientation and Rheology in Sheared Lyotropic Liquid Crystalline Polymers. *Macromol. Chem. Physic.*, **1998**. 199: p. 471-488.
50. Lettinga, M.P., Z. Dogic, H. Wang, and J. Vermant, Flow Behavior of Colloidal Rodlike Viruses in the Nematic Phase. *Langmuir*, **2005**. 21: p. 8048-57.
51. Larson, R.G. and D.W. Mead, Development of Orientation and Texture During Shearing of Liquid-Crystalline Polymers. *Liq. Cryst.*, **1992**. 12: p. 751-768.
52. Ben Azouz, K., E.C. Ramires, W. Van den Fonteyne, N. El Kissi, and A. Dufresne, Simple Method for the Melt Extrusion of a Cellulose Nanocrystal Reinforced Hydrophobic Polymer. *ACS Macro Lett.*, **2012**. 1: p. 236-240.
53. Ranby, B.G., Aqueous Colloidal Solutions of Cellulose Micelles. *Acta Chem. Scand.*, **1949**. 3: p. 649-650.
54. Gray, D.G. and M. Roman, Self-Assembly of Cellulose Nanocrystals: Parabolic Focal Conic Films, in *Cellulose Nanocomposites*. 2006, American Chemical Society. p. 26-32.

55. Urena-Benavides, E.E., G.Y. Ao, V.A. Davis, and C.L. Kitchens, Rheology and Phase Behavior of Lyotropic Cellulose Nanocrystal Suspensions. *Macromolecules*, **2011**. 44: p. 8990-8998.
56. Beck-Candanedo, S., M. Roman, and D.G. Gray, Effect of Reaction Conditions on the Properties and Behavior of Wood Cellulose Nanocrystal Suspensions. *Biomacromolecules*, **2005**. 6: p. 1048-54.
57. Liu, D.G., S. Wang, Z.S. Ma, D.L. Tian, M.Y. Gu, and F.Y. Lin, Structure-Color Mechanism of Iridescent Cellulose Nanocrystal Films. *RSC Adv.*, **2014**. 4: p. 39322-39331.
58. Liu, D.G., X.Y. Chen, Y.Y. Yue, M.D. Chen, and Q.L. Wu, Structure and Rheology of Nanocrystalline Cellulose. *Carbohydr. Polym.*, **2011**. 84: p. 316-322.
59. Azzam, F., L. Heux, and B. Jean, Adjustment of the Chiral Nematic Phase Properties of Cellulose Nanocrystals by Polymer Grafting. *Langmuir*, **2016**. 32: p. 4305-12.
60. Liu, Q. and Smalyukh, I., Liquid Crystalline Cellulose-Based Nematogels. *Sci Adv*, **2017**. 3: p. e1700981.
61. Gray, D.G., Chiral Nematic Ordering of Polysaccharides. *Carbohydr. Polym.*, **1994**. 25: p. 277-284.
62. Parker, R.M., B. Frka-Petescic, G. Guidetti, G. Kamita, G. Consani, C. Abell, and S. Vignolini, Hierarchical Self-Assembly of Cellulose Nanocrystals in a Confined Geometry. *ACS Nano*, **2016**. 10: p. 8443-8449.
63. Barnes, H.A., The Yield Stress—a Review or ‘Πάντα Ρεῖ’—Everything Flows? *J. Non-Newtonian Fluid Mech.*, **1999**. 81: p. 133-178.
64. Qiao, C., G. Chen, J. Zhang, and J. Yao, Structure and Rheological Properties of Cellulose Nanocrystals Suspension. *Food Hydrocolloids*, **2016**. 55: p. 19-25.
65. Araki, J., M. Wada, and S. Kuga, Steric Stabilization of a Cellulose Microcrystal Suspension by Poly(Ethylene Glycol) Grafting. *Langmuir*, **2001**. 17: p. 21-27.
66. Hirai, A., O. Inui, F. Horii, and M. Tsuji, Phase Separation Behavior in Aqueous Suspensions of Bacterial Cellulose Nanocrystals Prepared by Sulfuric Acid Treatment. *Langmuir*, **2009**. 25: p. 497-502.
67. Zhou, Z.W., M.J. Solomon, P.J. Scales, and D.V. Boger, The Yield Stress of Concentrated Flocculated Suspensions of Size Distributed Particles. *J. Rheol.*, **1999**. 43: p. 651-671.
68. Thomas, D.G., Transport Characteristics of Suspensions: Iii. Laminar-Flow Properties of Flocculated Suspensions. *A.I.Ch.E. Journal*, **1961**: p. 431-437.
69. Studart, A.R., E. Amstad, and L.J. Gauckler, Yielding of Weakly Attractive Nanoparticle Networks. *Soft Matter*, **2011**. 7: p. 6408-6412.
70. Debord, S.B. and L.A. Lyon, Influence of Particle Volume Fraction on Packing in Responsive Hydrogel Colloidal Crystals. *J Phys Chem B*, **2003**. 107: p. 2927-2932.
71. Hao, T. and R.E. Riman, Calculation of Interparticle Spacing in Colloidal Systems. *J Colloid Interface Sci*, **2006**. 297: p. 374-7.
72. Ureña-Benavides, E.E. and C.L. Kitchens, Wide-Angle X-Ray Diffraction of Cellulose Nanocrystal–Alginate Nanocomposite Fibers. *Macromolecules*, **2011**. 44: p. 3478-3484.
73. Leppiniemi, J., P. Lahtinen, A. Pääjärvi, R. Mählberg, S. Metsä-Kortelainen, T. Pinomaa, H. Pajari, I. Vikholm-Lundin, P. Pursula, and V.P. Hytönen, 3d-Printable Bioactivated Nanocellulose-Alginate Hydrogels. *ACS Appl Mater Interfaces*, **2017**. 9: p. 21959-21970.

74. Mercader, C., A. Lucas, A. Derré, C. Zakri, S. Moisan, M. Maugey, and P. Poulin, Kinetics of Fiber Solidification. *Proceedings of the National Academy of Sciences*, **2010**. 107: p. 18331-18335.
75. Trebbin, M., D. Steinhauser, J. Perlich, A. Buffet, S.V. Roth, W. Zimmermann, J. Thiele, and S. Förster, Anisotropic Particles Align Perpendicular to the Flow Direction in Narrow Microchannels. *Proc. Natl. Acad. Sci. U. S. A.*, **2013**. 110: p. 6706-6711.
76. Nesaie, S., M. Rock, Y. Wang, M.R. Kessler, and A. Gozen, Additive Manufacturing with Conductive, Viscoelastic Polymer Composites: Direct-Ink-Writing of Electrolytic and Anodic Poly(Ethylene Oxide) Composites. *Journal of Manufacturing Science and Engineering*, **2017**. 139: p. 111004-111004-12.
77. Dunlop, J.W.C. and P. Fratzl, Biological Composites. *Annu Rev Mater Res*, **2010**. 40: p. 1-24.
78. Fratzl, P. and R. Weinkamer, Nature's Hierarchical Materials. *Prog. Mater. Sci.*, **2007**. 52: p. 1263-1334.
79. Reid, M.S., M. Villalobos, and E.D. Cranston, Benchmarking Cellulose Nanocrystals: From the Laboratory to Industrial Production. *Langmuir*, **2017**. 33: p. 1583-1598.

Chapter 3.

Alignment dynamics of cellulose nanocrystals under flow in a 3D printing nozzle

Michael K. Hausmann^{1,2}, Rafael Libanori², Gilberto Siqueira¹, Antonia Neels³, Felix Reifler³, Viviane Bueno Lutz⁴, Manuel Guizar-Sicairos⁴, Tanja Zimmermann¹, André R. Studart²

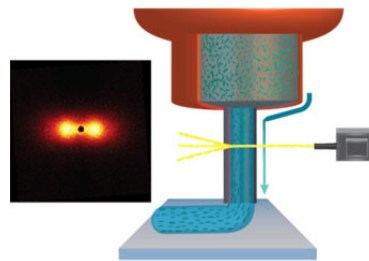
¹*Empa, Swiss Federal Laboratories for Materials Science and Technology, Applied Wood Materials Laboratory, 8600 Dübendorf, Switzerland*

²*Complex Materials, Department of Materials, ETH Zürich, 8093 Zürich, Switzerland*

³*Empa, Swiss Federal Laboratories for Materials Science and Technology, Center for X-ray Analytics, 8600 Dübendorf, Switzerland*

⁴*Swiss Light Source, Paul Scherrer Institute, 5232 Villigen PSI, Switzerland*

This chapter has not been published



3.1 Abstract

The alignment of anisotropic particles in composites directly influences their microstructure and mechanical properties. Control over particle alignment during composite fabrication is possible using extrusion-based 3D printing processes such as Direct Ink Writing (DIW). In such process, alignment is induced by flow and is strongly affected by both the rheological properties of the material and the geometry of the extrusion nozzle. To the best of our knowledge, most studies on flow-induced alignment of anisotropic particles have been conducted in diluted conditions. These conditions are not representative of the highly concentrated suspensions that are typically used for DIW processes. Additionally, only a few detailed *in-situ* studies have been reported in the literature on the flow and alignment dynamics of anisotropic particles during the extrusion process. Using cellulose nanocrystals as anisotropic model particles, we investigate the contributions of both extensional and shear forces on the dynamics of the particle alignment process. In order to reproduce the extrusion process occurring in DIW, we designed a pressure-controlled extrusion stage that allows us to perform *in-situ* X-ray scattering measurements during flow of a concentrated suspension through a quartz capillary. By moving the beam along the radius and length of the quartz capillary, we are able to monitor changes in particle alignment during flow and

after relaxation using both small- and wide-angle X-ray scattering techniques. This approach allows to locally resolve the relative degree of alignment and the preferential orientation of cellulose nanocrystals within the capillary. For the geometry studied here, we observe that extensional forces dominate the alignment of particles at the entry of the capillary system, whereas shear forces increase the degree of alignment in a thin layer of suspension close to the walls along the length of the capillary. These findings support earlier predictions and provide a better understanding of the mechanisms underlying the alignment of cellulose nanocrystals during the DIW process.

3.2 Introduction

Three-dimensional (3D) printing is a fast growing technology as it enables the fabrication of objects and composite materials with defined architecture at several length scales. Some of the design possibilities to tune the architecture and the resulting properties of composite materials through 3D printing involves the control of the alignment of micro or nano-scaled anisotropic particles. Alignment control is of interest to mimic and capture the exquisite multi-scaled architecture of biological materials such as bones, mollusk shells, plants or trees.¹⁻⁴ Therefore, efforts have been invested in controlling the alignment of these anisotropic particles by combining various techniques such as magnetic fields⁵⁻⁸, acoustic waves^{9, 10} or shear stresses^{7, 11-15}. The control over the alignment of anisotropic particles has allowed for improvements in the mechanical properties of the resulting composites and for the development of materials with shape memory or self-actuating properties.^{13, 16-18} Because of their biocompatibility as well as their mechanical and optical properties, bio-sourced materials such as cellulose has gained increasing attention as anisotropic reinforcing material.^{13, 19-28} Extracted from plants or produced by bacteria, cellulose can be processed as long and flexible fibers (MFCs or NFCs) or short and stiff cellulose nanocrystals (CNCs).^{23, 25, 29}

The anisotropic shape of cellulose nanocrystals leads to alignment along the flow direction under the action of shear and extensional forces.^{30, 31} This is of particular interest when working with 3D printing techniques such as Direct Ink Writing (DIW), a process in which extensional and shear stresses can be easily applied on gel-like materials with defined rheological properties by extruding it through a nozzle. Cellulose-based gels with ideal rheological properties are easily obtained due to the formation of a percolation network held via strong interparticle interactions.^{11, 32-35} Among the rheological properties of cellulose inks, the yield stress and the shear thinning behavior have shown to strongly affect the alignment quality of cellulose nanocrystals under shear.^{7, 30, 36, 37} These parameters can be easily adjusted by varying material compositions or physical properties, such as the cellulose content, the nozzle geometry or the extrusion pressure.^{14, 38-40} Therefore, understanding the dynamics of particle alignment under flow of non-Newtonian fluids is of utmost importance for 3D printing of complex 3D structures.

Because of their liquid crystal behavior and their birefringent nature, the alignment of cellulose crystals has been extensively studied using cross-polarized microscopy. The self-assembly of cellulose crystals results in the formation of chiral nematic phases that can be readily observed under cross-polarizers. When shear is applied to such self-assembled structures, individual crystals orient along specific directions resulting in well-defined colors.⁴¹⁻⁴³ The effect of the addition of salts or polymers, changes in temperature, pH or sonication time on the assembly of CNCs was investigated and assessed optically in several previous studies.⁴⁴⁻⁴⁹ To quantify the degree of alignment of CNCs, Chowdhury and coworkers proposed a method that combines polarized light imaging with UV-visible spectrometry. The results were validated with state-of-the-art X-ray diffraction

measurements.⁵⁰ In fact, cellulose systems have been extensively investigated using X-ray analytical techniques.

Small angle X-ray scattering, for example, has been combined with rheology to study diluted cellulose systems under shear.^{51, 52} The colloidal behavior and alignment of the cellulose particles were found to strongly depend on the applied shear rates. Two possible phenomenon were proposed to explain the alignment of the cellulose crystals under shear. At rest, the cellulose nanocrystals are known to form micro-domains with locally aligned particles but no global preferred orientation. When exposed to high shear rates, these domains rupture, allowing individual crystals to align along the shear direction. At low shear rates, forces are not sufficiently high to disrupt the domains and the alignment is strongly dependent on the domain size. The formation and disruption of domains under shear was also observed under *in-situ* polarized light rheology.³⁰ Another relevant phenomenon is the possible tumbling of cellulose nanocrystals along specific directions at low shear rates. In this case, higher shear rates restrict their freedom of rotation, thus favoring a preferential orientation along the flow direction.^{51, 53} Despite the important research on the self-assembly of cellulose suspensions,²⁸ their dynamic response in concentrated suspensions under shear and extensional flow is not yet fully understood. Indeed, the majority of the studies were conducted at relatively low concentrations of nanocellulose (~6 wt %) or only considered self-assembling processes in the absence of flow. Moreover, most studies were conducted on flexible nanofibrillated cellulose (NFCs) of larger aspect ratio, while research on CNCs is still limited.^{36, 54}

For 3D printing, cellulose nanocrystal concentrations typically higher than 15 wt % are required to meet the rheological properties needed to avoid macroscopic creeping and shape distortions.¹¹ At these conditions, the volume fraction of particles is significantly above the percolation threshold. This makes tumbling processes more complicated and favors the formation of micro-domains that are not always visible under the optical microscope. While rheology has been extensively utilized to characterize the material prior to the extrusion process, X-ray scattering is mostly applied to analyze the structure of the final printed material. Because of the high flow-induced forces expected in the nozzle, alignment is often taken as granted in inks used for direct ink writing processes. Although shear and extensional forces are known to strongly affect the degree of alignment of particles during extrusion-based 3D printing, the contribution of these two parameters are highly dependent on the nozzle geometry and thus remain poorly understood.^{7, 14, 55, 56}

Here, we investigate the effect of shear and extensional stresses on the alignment of cellulose nanocrystals during extrusion of CNC inks through a quartz capillary with the geometry of a 3D printing nozzle. To image the flow behavior of cellulose nanocrystals suspensions through the capillary, we utilize Wide Angle (WAXS) and Small Angle (SAXS) X-ray scattering techniques. *In-situ* visualization of the flow process is achieved by designing an extrusion system with controlled pressure. This customized extrusion stage offers the

possibility to measure the alignment dynamics of cellulose dispersions of various concentrations under flow with SAXS and to prepare samples for WAXS measurements under controlled conditions. Additional SAXS experiments using a high-intensity beam line at the synchrotron light source were also utilized to prepare 3D tomography reconstructions of the suspension inside the representative capillary. With this fundamental study, we determine the contributions of shear and extensional forces to the alignment of CNCs during the direct ink writing process.³⁰

3.3 Results and discussion

During 3D printing processes such as direct ink writing (DIW), a fluid ink (dispersion) is deposited on a substrate by extrusion from a cartridge system through a thin nozzle of defined dimensions. This extrusion process subjects the ink to both extensional and shear forces that arise from the changes in geometrical sections and from the friction with the walls of the nozzles. The magnitude of these forces is defined by external parameters, such as the applied pressure and the geometry of the system, as well as by the rheological properties of the ink. Understanding the interplay between the rheological properties of the ink and the resulting forces is of importance, particularly when the ink composition involves anisotropic nanoparticles. For inks containing cellulose nanocrystals, the rheological response of the material is strongly dependent on the applied shear and extensional forces due to changes in the microstructure of the ink and degree of particle alignment during extrusion. This microstructural change of the material is a consequence of the reorganization and orientation of individual cellulose nanocrystals or microscopic nematic domains. In our previous work, we applied rheology and polarized microscopy to assess the contribution of shear forces to the degree of alignment of CNCs.³⁰ Our experiments revealed that shear forces contribute to the alignment of CNCs next to the wall of the nozzle. Although the effect of extensional forces was also qualitatively assessed, a quantitative analysis of the particle alignment dynamics under flow in a 3D printing nozzle was not possible.

To this end, we replaced the original steel nozzle by a X-ray transparent quartz capillary that enables the *in-situ* observation of flow-driven CNC alignment using X-ray scattering techniques. Particle alignment was investigated under controlled 3 bar pressure on a typical extrusion cartridge connected to the capillary (Figure 3.1). This setup permits to measure *in situ* the dynamic response of CNCs under controlled pressure during and after the extrusion process. By moving the X-ray beam along the capillary's length and radius, we used this setup to quantify the alignment dynamics of CNCs through 2D projections of the scattered beam.

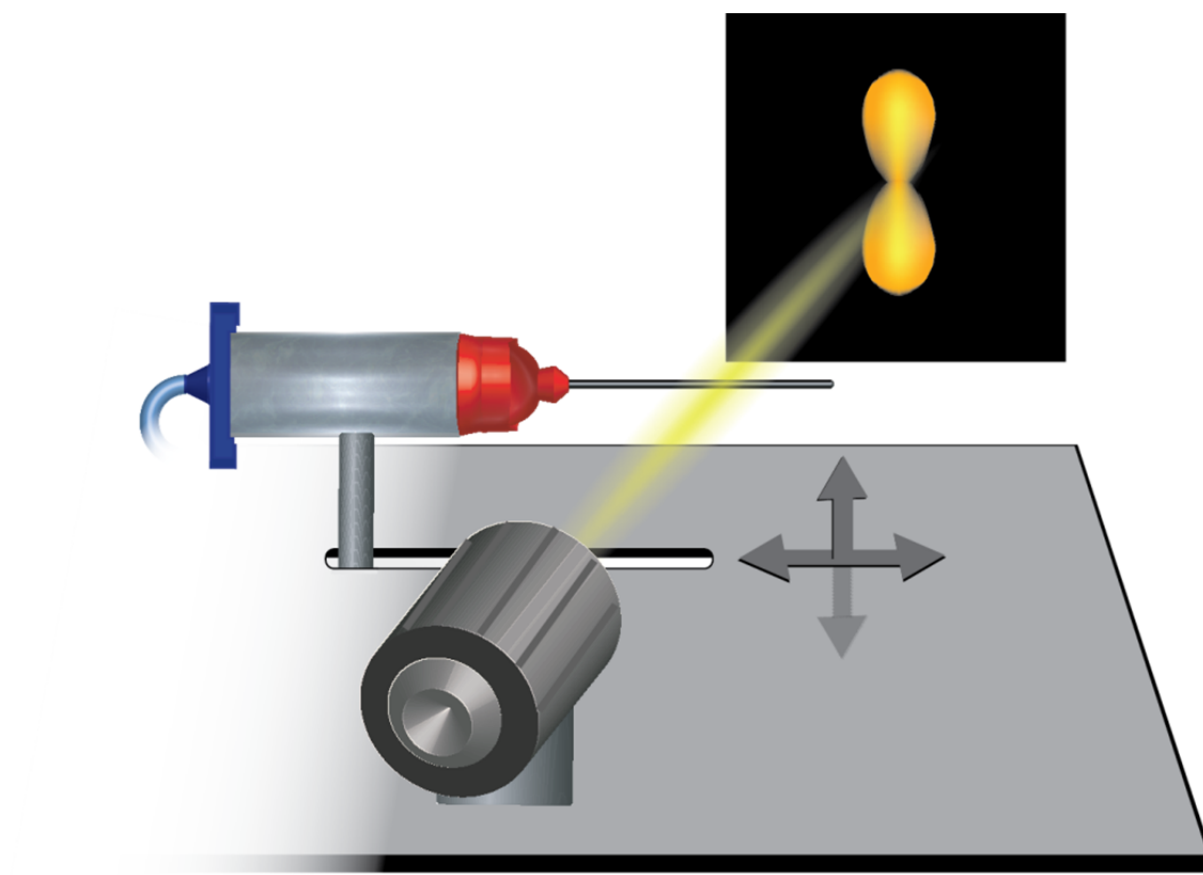


Figure 3.1 X-ray measurement setup. The quartz capillary is mounted on a typical plastic cartridge used for 3D printing and connected to pressurized air. The exact position of the capillary can be controlled in X,Y and Z while the flow is regulated by the pressure.

We employ 2D Wide Angle X-Ray scattering (2DWAXS) to first estimate the degree of alignment of CNCs along the length of the quartz capillary. The degree of alignment of CNCs is represented by the full width at half maximum (FWHM) of the scattered intensity from the 200 plane as a function of the incident angle at different positions along the capillary length. Low FWHM values indicate strong alignment of the particles.

Scattering measurements performed on suspensions containing 15, 20 and 25wt% CNCs reveals an increase in the degree of alignment along the length of the nozzle (Figure 3.2). The degree of alignment is significantly enhanced when the concentration of CNCs increases from 15 to 20 wt %. This is likely related to the higher viscosity and the formation of liquid crystal domains in the more concentrated dispersions. The presence of liquid crystal domains ensures pre-alignment of the particles at the microscale. Orientation of such pre-aligned domains along the flow direction is then favoured by the high shear forces imposed

by fluids with higher viscosities. Indeed, increasing the concentration from 15 to 25 wt % results in a decreasing FWHM from 72 to 37.4 at position 5 along the capillary (Figure 3.2a). Interestingly, the increase in concentration from 15 to 20 wt % induces a more pronounced change in the degree of alignment as compared to the increase in concentration from 20 to 25 wt %. This difference in behaviour is in good agreement with the rheological response exhibited by these inks with three different concentrations. Inks with 20 and 25 wt % CNC present a strong shear thinning behaviour and a well-defined yield stress well above 100 Pa, while inks with 15 wt % CNC barely fulfils the conditions to print structures with high shape fidelity.^{11, 30} The shear thinning behaviour and yield stress shown by the concentrated CNC inks may arise from the break-up of the initial particle network under the imposed flow and eventually the alignment of the CNC particles by extensional and shear forces. As it was demonstrated in previous research, these concentrations lie above the percolation threshold and have the tendency to form micro-domains, the size of which decreases with increasing concentration. Therefore, the shear thinning behaviour is not only influenced by the alignment of individual CNCs but also by the alignment of these micro-domains.³⁰

Comparison of these scattering data with previously studied systems provides further insights into the alignment of CNCs during the extrusion process.^{37, 51} The degree of alignment measured for the 20 wt % dispersion is in the same range as the one measured in printed structures investigated in previous publication.¹¹ In accordance with other studies, the lower degree of alignment observed for dispersions with 15 wt % CNC can be a consequence of higher probability of particle tumbling induced by the high shear and extensional deformations developed during flow and next to the capillary's wall. The nematic domains and the percolating network of particles formed in pastes containing 20 and 25 wt % CNC is expected to hinder tumbling of individual crystals. The poor particle orientation of non-percolating systems is also observed for lower CNC concentrations, such as 10 wt % (Figure B. 1) or for diluted 1-2 wt % cellulose nanofibrils (CNF) suspensions extruded through capillary systems.⁵⁴ Interestingly, particle tumbling has been observed in both extensional and shear flows. The probability of particle tumbling decreases with increasing extensional forces, which makes this phenomenon more pronounced in pure shear systems. This observation can be explained by the fact that anisotropic particles aligned with the flow are more stable in an extensional flow as compared to a pure shear flow.^{54, 57} Our *in-situ* investigation suggests that tumbling does not govern particle orientation in the highly concentrated nanocellulose suspensions used in 3D printing processes. This is probably caused by the assembly of individual particles in domains and the high extensional flow at the entrance of the nozzle.

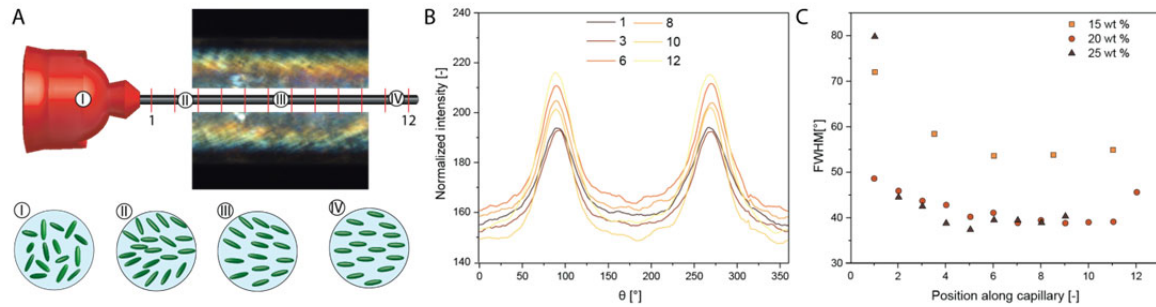


Figure 3.2 2DWAXS measurement along the length of the quartz capillary. **A)** Schematic illustration of the alignment dynamics along the capillary at various positions (I to IV) and polarized light microscopy image of a 15 wt % CNC dispersion. The red lines indicate the measurement positions employed in the 2DWAXs experiment. The polarized light image provides experimental evidence of particle alignment along the flow direction. **B)** Radial integration resulting from scattering patterns measured along the length of the capillary at 12 different positions for a 20 wt % CNC dispersion. **C)** Full width at half maximum (FWHM) values as a function of the position along the capillary for dispersions containing 15, 20 and 25 wt % cellulose nanocrystals.

In addition to the changes in particle average orientation along the length of the capillary, the degree of particle alignment is also expected to vary across the radius of the nozzle due to the shear stress gradient formed within the nozzle during extrusion. Indeed, the shear stress profile along the capillary's diameter is not spatially uniform, which leads to a distribution of alignment angles across the cross section of the capillary. An accurate assessment of the alignment angle across the diameter of the capillary is not possible using the 2DWAXS technique because the maximum resolution available in this experimental setup is comparable in size with the capillary's diameter. Thus, coherent Small Angle X-Ray Scattering using synchrotron radiation was employed to resolve the dependence of the alignment angle as a function of the position across the cross section of the capillary.

As the time required for sample preparation and for the measurements stretches typically over several hours, preliminary SAXS experiments were performed to evaluate possible microstructural changes that may occur in the inks after sample preparation. The temporal stability of a 20 wt % CNC dispersion is assessed by running consecutive measurements at the same position of the capillary. Measurements were obtained during material flow shortly after injection in the capillary, right after the flow was ceased and a after a relaxation period of 17 h. No visible changes are noticeable between these 3 different snapshots (Figure 3.3a), indicating that the material preserves its microstructure even after pressure removal and flow cessation. Moreover, our experimental results show that the CNC microstructure developed during the extrusion process of such concentrated dispersion is not affected by thermal motion of the constituent colloidal particles. The scattering profile of suspensions containing different particle concentrations reveal a strong peak for vector length (q) values in the range $0.01 - 0.05 \text{ \AA}^{-1}$ for inks loaded with 15 and 20wt% CNCs (Figure 3.3b).

Our SAXS measurements also reveal that the characteristic length scale of the scattering elements in our concentrated suspensions changes from 38.0 to 27.2 to 20.0 nm, as the CNC contents increase from 10 to 15 to 20 wt% (Figure 3.3b). This finding corroborate the observation that particle tumbling is less favoured in highly concentrated dispersions as the particle mobility is reduced due to the smaller interparticle distances and stronger shear and extensional forces. Once the stability of the ink microstructure over several hours was confirmed, we performed high resolution SAXS measurements in a synchrotron facility to study the alignment of CNC particles along the radius and cross-section of the capillary.^{58, 59}

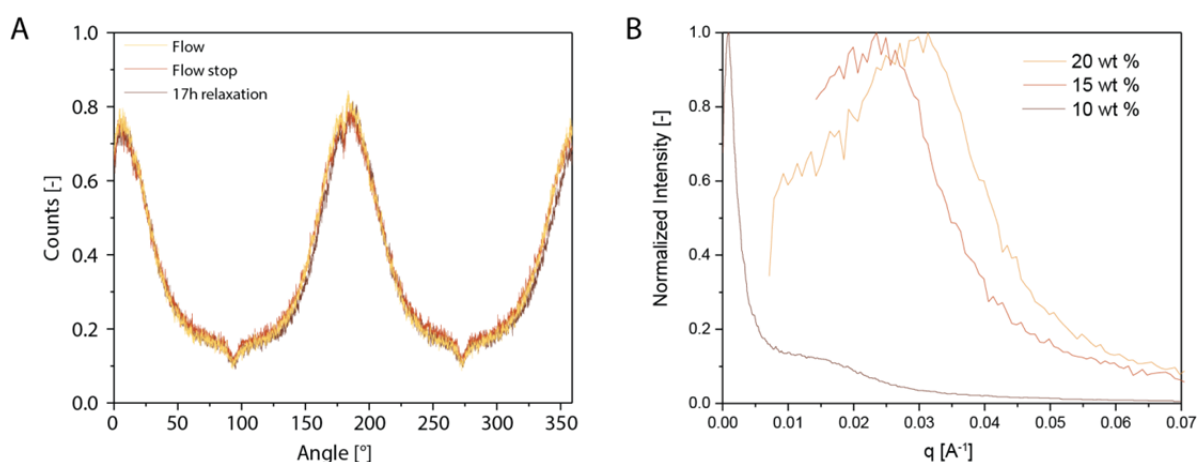


Figure 3.3 Conventional SAXS measurements of suspensions containing various CNC concentrations. **A)** Temporal relaxation of CNCs in a quartz capillary observed by SAXS. Measurement performed at the centre of the capillary during flow, after flow cessation and after a relaxation time of 17 h. **B)** Determination of d-spacing between repeating units.

In the synchrotron experiments, the CNC alignment angle and the relative degree of alignment across the cross section of the capillary was resolved using a squared $10 \times 10 \mu\text{m}^2$ beam that scanned through pre-defined areas comprising the initial and final sections of the quartz capillary sample. The two-dimensional scattering patterns obtained from these measurements show that the CNC particles are strongly oriented along the longitudinal axis of the capillary (Figure 3.4a). The preferential alignment angle of the cellulose nanocrystals relative to the longitudinal axis is about 0° at the centre of the capillary and increases to up to 20° at the capillary walls, forming a symmetrical 2D pattern. The tilting of the anisotropic cellulose nanoparticles close to the capillary walls is observed at both the beginning and the end sections of the capillary (Figure 3.4b). While further experiments are needed to clarify the underlying mechanism leading to such tilting effect, the preferred orientation of the CNC particles close to the wall is likely influenced by the tapered geometry of the capillary used in our experiments (Appendix B2).

The difference between the microstructure at the beginning and at the end of the capillary sections can be quantified by calculating the relative degree of CNC orientation. The

relative degree of CNC orientation was defined by normalizing the measured degree of alignment obtained from the SAXS data. This degree of alignment is derived from a cosine fitting to the scattered intensity (I) as a function of the incidence angle, X :⁶⁰

$$I(X) = a_0 + a_1 \cos(2X + \beta) \quad Eq. 1$$

where a_0 is the average baseline intensity, a_1 is the amplitude and β is a shifting factor. The degree of alignment can be quantified using the anisotropy factor (Af) of this function:

$$Af = \frac{a_1}{a_0} \quad Eq. 2$$

The X-ray scattering data indicate that the relative degree of alignment of CNC particles along the capillary radius evolves from the beginning to the end of the capillary (Figure 3.4c). The relative degree of alignment is the local A_f value obtained in the slice of a cSAXs 2D projection normalized by the maximum value. The degree of alignment along the radius is based on data obtained from a single slice of the tomographic image because an analysis carried out on the entire 2D projection tends to overestimate the alignment of particles in the center of the capillary (Figure B. 5, Appendix B4). At the beginning, the relative degree of alignment is relatively uniform along the entire radius of the capillary. By contrast, stronger CNC alignment is observed close to the walls compared to the centre at the end of the capillary. This difference in CNC alignment behaviour can be understood by considering the interplay between shear and extensional forces along the capillary length. At the entry of the capillary, a strong reduction in cross-sectional area occurs as the materials flows from the very large barrel (cartridge) into the quartz capillary. This change in cross-sectional area induces strong extensional forces on the material, as it moves from a slow velocity towards a fast velocity region. After this first transition, the material flows along the slightly tapered capillary (Appendix B2). The gradual change in cross-sectional area along the capillary length leads to much lower extensional forces between the beginning and the end of the capillary as compared to the transition from the cartridge to the capillary. Therefore, the relative degree of alignment in this region is predominantly affected by the shear forces developed close to the capillary wall. As the extruded dispersion exhibit a relatively high viscosity with a shear-thinning behaviour and a finite yield stress, the core of ink within the capillary is expected to undergo plug flow. In plug flow conditions, only a small volume of the material close to the walls is subjected to shear forces that are high enough to disrupt the percolated network and enhance the degree of alignment of particles.³⁰ Our measurements confirm that the presence of shear forces results in a significant increase of the degree of

alignment close to the walls as compared to the centre of the capillary, explaining the orientation distribution profile measured at the end of the capillary. Such orientation distributions obtained from synchrotron measurements across the cross section of the capillary show similar patterns to those obtained in a conventional SAXS equipment, providing further experimental support to the interpretation above (Appendix B3, B5).

The combination of multiple two-dimensional projections obtained from various rotational and tilting angle scans from the same sample allows us to extract three-dimensional tomographic snapshots of the suspension. The 3D tomographic reconstruction is based on a simulated reproduction of the real scattering pattern obtained following the procedure described earlier in the literature (Appendix B4).⁵⁸ The 3D tomography data confirms the stronger degree of alignment of the CNC particles at the walls compared to the centre of the capillary (Appendix B4 with Figure B. 6 to 7). It is important to note that the numerical values of the degree of alignment obtained from the tomographies (Figure 3.4d,e) cannot be directly compared to those extracted from the 2D patterns (Figure 3.4b), because the former have been calculated based on spherical harmonics instead of a cosine fitting approach.⁵⁸ To enable an one-to-one comparison between these data, we extracted slices from the centreline of the tomographies and used them to back-calculate the degree of alignment using the cosine fitting analysis. The obtained degree of alignment calculated using this method is comparable to that from the 2D patterns, thus validating the tomographic reconstruction (Figure B. 8).

Overall, our results highlight the contribution of both extensional and shear forces to the alignment of particles during extrusion of concentrated CNC suspensions. Sectional changes provide the highest contribution to the alignment of anisotropic particles while the contribution of shear forces occurs predominantly at the capillary walls and is limited by the rheological properties of the material. While this study sheds light on the interplay between shear and extensional forces during the extrusion process, additional investigations are required to fully quantify the relative contributions of these different forces. By using the inverted extensional flow system we prepared in our previous work³⁰, one can erase the previously induced alignment obtained by extensional flow and study a pure shear case. Combined with numerical models, this fundamental understanding is of interest to design 3D printing nozzles that can result in different degrees of alignment within a printed structure.

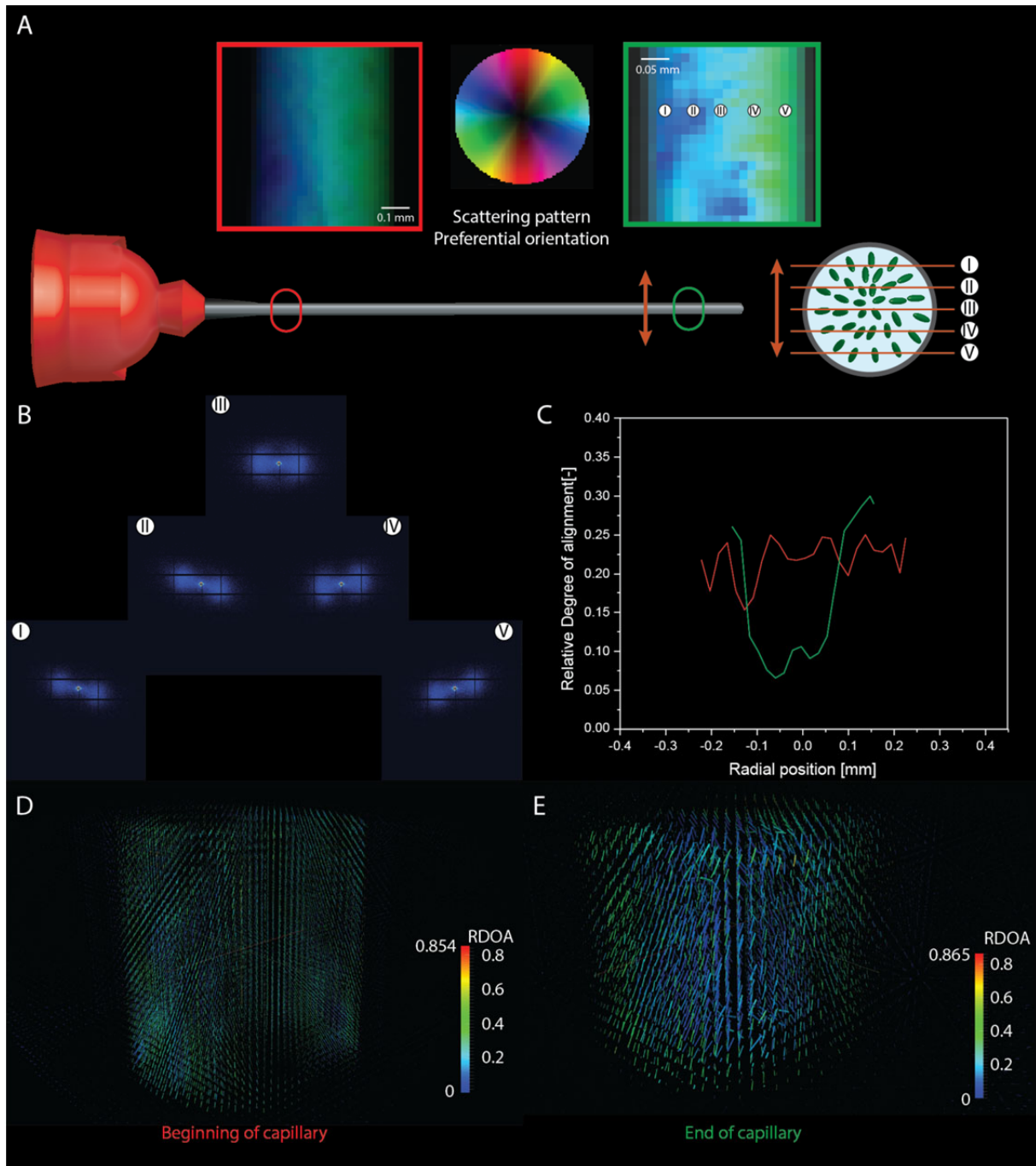


Figure 3.4 Coherent SAXS measurements performed with a high-luminance source beam in a synchrotron facility to study the alignment of CNC particles along the radius and length of the capillary. **A)** Particle alignment maps obtained from 2D projections of two capillary sections: beginning (red) and end (green), showing the preferential orientation of cellulose nanocrystals along the longitudinal direction. **B)** Scattering patterns measured along the radius of the capillary. **C)** Integrated relative degree of alignment calculated for the beginning and the end of the capillary using a single 2D project slice from the 3D tomographic reconstruction. **D,E)** 3D tomographic reconstruction of the degree of alignment of the CNC particles at **(D)** the beginning and **(E)** the end of the capillary.

3.4 Conclusion

The alignment dynamics of anisotropic particles during extrusion-based 3D printing processes is strongly influenced by the extensional and shear forces developed within the printing nozzle. CNC particles were found to align preferentially along the longitudinal direction of the extruded filament due to the action of extensional forces at the entry of the nozzle-like capillary. As the suspension moves along the length of the capillary, the strong initial alignment across the entire cross-section of the nozzle is maintained and the alignment at the edge of the capillary is further enhanced. This is caused by the high shear forces developed close to the capillary wall. The contribution of shear forces is mostly limited to the walls of the capillary because of the high yield stress exhibited by concentrated CNC dispersions. Previous analysis of the flow profile within the nozzle suggests that inks with high yield stress undergo plug-type flow. Since plug flow is more pronounced in suspensions with high particle concentrations, shear forces play a limited role on the overall degree of alignment in systems containing high CNC contents. These results underline the important correlation between rheological properties of the ink and nozzle geometry on the degree of particle alignment achieved during 3D printing. Although additional work is required to understand the contribution of the nozzle geometry to the level of particle alignment, the effect of the CNC concentration is clearly related to changes in the rheological properties and the formation of liquid crystal domains in the suspension. While rheological properties of the printing formulations are controlled by the concentration of CNCs in the ink, geometrical factors define the contribution of extensional and shear forces to the alignment of these nanoparticles. Combining nozzle geometry and material composition can therefore enable the production of 3D printed parts with programmed CNC architectures and tailored mechanical properties.

3.5 Experimental methods

3.5.1 Materials

Cellulose nanocrystals (CNCs) were purchased from the USDA Forest Service – Forest Products Laboratory (Madison, WI). Such crystals were prepared via sulfuric acid hydrolysis of eucalyptus pulp according to a published procedure.⁶¹ Freeze-dried CNCs (0.98 wt % sulfur content) were dispersed in water for 5 min at 2500 and 3500 rpm, respectively, in a speed mixer (model DAC 150.1 FVZ). Gels containing 15, 20 and 25 wt % of CNCs were prepared through this mixing procedure. The cellulose-based gels were left for swelling for one night, before conducting an additional speed mixing step at 3500 rpm for 5 min and storing in the fridge until testing. The quartz capillaries had an inner diameter of 0.3 mm and a length of 80 mm (Hilgenberg.)

3.5.2 Sample preparation

Small Angle X-Ray Scattering (SAXS)

Small Angle X-Ray Scattering was performed on a Bruker Nanostar U diffractometer (Bruker AXS, Karlsruhe, Germany) using a Copper K- α radiation source ($\lambda = 1.54187 \text{ \AA}$) and a Vantec-2000 MikroGap detection system. The distance between the sample and the detector, the beam diameter and the irradiation time per frame were set to 99.7 cm, 0.3 mm and 300 s, respectively. Pinholes of 550 and 300 μm were utilized with a beam stop of 3.15 mm.

The cartridge and the capillary were mounted in the measurement chamber on a movable plate (see Appendix B5). The movable plate allowed us to position the capillary in front of the X-ray beam. With this setup, the whole length and cross-section of the capillary can be scanned with the X-ray beam. A pressure inlet was inserted through a hole at the back of the measurement chamber to enable a precise control of the extrusion pressure and the material flow. This configuration enables scattering measurements under continuous material flow or during relaxation.

2D-Wide Angle X-Ray Scattering (2DWAXS)

Two-dimensional wide-angle X-ray diffraction (2D-WAXD; STOE IPDS-II, 0.71073 Mo K α radiation source) was used to investigate the degree of alignment of CNC dispersions extruded through quartz capillaries. The equipment was operated at 40 mA and 50 kV for 30 min using a beam diameter of 0.5 mm in transmission mode. The samples were prepared by first filling the paste into an adapted quartz capillary and then extruding the material at a controlled pressure of 3 bar. This was achieved by connecting the cartridge to a Direct Ink Writing (DIW) 3D Printer (EnvisionTEC, Bioplotter Manufacturing series). Once the capillary was filled, the pressure was removed and the capillary was sealed with a fast-curing glue. The capillary was then fixed perpendicularly to the beam on the goniometer head. The 2D-WAXD patterns were recorded on an Image Plate Detector System with a 340 mm diameter placed at a distance of 200 mm from the sample. The sample was shifted after each measurement to cover the length of the capillary. A full image covering a 2θ range from 3 to 40° was recorded for each position. Azimuthal scans were integrated for the cellulose (200) reflection.

Coherent Small Angle X-Ray Scattering (cSAXS)

cSAXS measurements were performed at the Swiss Light Source beamline at the Paul Scherrer Institute (PSI). The beam was focused at an area of $10 \times 10 \mu\text{m}^2$ with a sample-to-detector distance of 7.185 m and a beam photon energy of 12.4 KeV. Two-dimensional scattering patterns were collected using a 2M Pilatus detector (1475 x 1679 pixels, pixel size $172 \times 172 \mu\text{m}^2$). Samples were prepared similarly to those utilized for 2DWAXS

measurements. The 3D tomography and data analysis were performed using a Matlab code developed and provided by PSI and described elsewhere.⁵⁸

3.5.3 Acknowledgement

We greatly thank P. R  hs for the extensive scientific discussions. A.R.S. acknowledges the financial support from the Swiss National Science Foundation (Consolidator Grant number BSCGIO_157696). M.K.H and G.D.S are thankful to the financial support from the Swiss National Science Foundation (200021_159906/1). R.L. is grateful for the financial support from the Swiss Competence Center for Energy Research SCCER Mobility and the Swiss Innovation Agency Innosuisse. This work also benefitted from support from the Swiss National Science Foundation through the National Center of Competence in Research Bio-Inspired Materials.

3.5.4 References

1. Dunlop, J.W.C. and P. Fratzl, Biological Composites. *Annu Rev Mater Res*, **2010**. 40: p. 1-24.
2. Fratzl, P., Biomimetic Materials Research: What Can We Really Learn from Nature's Structural Materials? *J. R. Soc., Interface*, **2007**. 4: p. 637-642.
3. Fratzl, P., R. Elbaum, and I. Burgert, Cellulose Fibrils Direct Plant Organ Movements. *Faraday Discuss.*, **2008**. 139: p. 275-282.
4. Fratzl, P. and R. Weinkamer, Nature's Hierarchical Materials. *Prog. Mater. Sci.*, **2007**. 52: p. 1263-1334.
5. Kokkinis, D., M. Schaffner, and A.R. Studart, Multimaterial Magnetically Assisted 3d Printing of Composite Materials. *Nat Commun*, **2015**. 6: p. 8643.
6. Martin, J.J., M.S. Riederer, M.D. Krebs, and R.M. Erb, Understanding and Overcoming Shear Alignment of Fibers During Extrusion. *Soft Matter*, **2015**. 11: p. 400-405.
7. Feilden, E., C. Ferraro, Q. Zhang, E. Garcia-Tunon, E. D'Elia, F. Giuliani, L. Vandeperre, and E. Saiz, 3d Printing Bioinspired Ceramic Composites. *Sci Rep*, **2017**. 7: p. 13759.
8. Martin, J.J., B.E. Fiore, and R.M. Erb, Designing Bioinspired Composite Reinforcement Architectures Via 3d Magnetic Printing. *Nat Commun*, **2015**. 6: p. 8641.
9. Collino, R.R., T.R. Ray, L.M. Friedrich, J.D. Cornell, C.D. Meinhart, and M.R. Begley, Scaling Relationships for Acoustic Control of Two-Phase Microstructures During Direct-Write Printing. *Mater. Res. Lett.*, **2018**. 6: p. 191-198.
10. Llewellyn-Jones, T.M., B.W. Drinkwater, and R.S. Trask, 3d Printed Components with Ultrasonically Arranged Microscale Structure. *Smart Materials and Structures*, **2016**. 25: p. 02LT01.
11. Siqueira, G., D. Kokkinis, R. Libanori, M.K. Hausmann, A.S. Gladman, A. Neels, P. Tingaut, T. Zimmermann, J.A. Lewis, and A.R. Studart, Cellulose Nanocrystal Inks for 3d Printing of Textured Cellular Architectures. *Adv. Funct. Mater.*, **2017**. 27: p. 1604619.

12. Lewis, J.A., Direct Ink Writing of 3d Functional Materials. *Adv. Funct. Mater.*, **2006**. 16: p. 2193-2204.
13. Sydney Gladman, A., E.A. Matsumoto, R.G. Nuzzo, L. Mahadevan, and J.A. Lewis, Biomimetic 4d Printing. *Nat. Mater.*, **2016**. 53: p. 413–418.
14. Lewicki, J.P., J.N. Rodriguez, C. Zhu, M.A. Worsley, A.S. Wu, Y. Kanarska, J.D. Horn, E.B. Duoss, J.M. Ortega, W. Elmer, R. Hensleigh, R.A. Fellini, and M.J. King, 3d-Printing of Meso-Structurally Ordered Carbon Fiber/Polymer Composites with Unprecedented Orthotropic Physical Properties. *Sci. Rep.*, **2017**. 7: p. 43401.
15. Gantenbein, S., K. Masania, W. Woigk, J.P.W. Sesseg, T.A. Tervoort, and A.R. Studart, Three-Dimensional Printing of Hierarchical Liquid-Crystal-Polymer Structures. *Nature*, **2018**. 561: p. 226-230.
16. Lee, A.Y., J. An, and C.K. Chua, Two-Way 4d Printing: A Review on the Reversibility of 3d-Printed Shape Memory Materials. *Engineering*, **2017**. 3: p. 663-674.
17. Khoo, Z.X., J.E.M. Teoh, Y. Liu, C.K. Chua, S.F. Yang, J. An, K.F. Leong, and W.Y. Yeong, 3d Printing of Smart Materials: A Review on Recent Progresses in 4d Printing. *Virtual Phys Prototy*, **2015**. 10: p. 103-122.
18. Le Duigou, A., M. Castro, R. Bevan, and N. Martin, 3d Printing of Wood Fibre Biocomposites: From Mechanical to Actuation Functionality. *Mater. Des.*, **2016**. 96: p. 106-114.
19. Siqueira, G., J. Bras, and A. Dufresne, Cellulosic Bionanocomposites: A Review of Preparation, Properties and Applications. *Polymers-Basel*, **2010**. 2: p. 728-765.
20. Ansari, F., A. Sjöstedt, P.T. Larsson, L.A. Berglund, and L. Wågberg, Hierarchical Wood Cellulose Fiber/Epoxy Biocomposites – Materials Design of Fiber Porosity and Nanostructure. *Composites, Part A*, **2015**. 74: p. 60-68.
21. Favier, V., H. Chanzy, and J.Y. Cavaille, Polymer Nanocomposites Reinforced by Cellulose Whiskers. *Macromolecules*, **1995**. 28: p. 6365-6367.
22. Siro, I. and D. Plackett, Microfibrillated Cellulose and New Nanocomposite Materials: A Review. *Cellulose*, **2010**. 17: p. 459-494.
23. Habibi, Y., Key Advances in the Chemical Modification of Nanocelluloses. *Chem Soc Rev*, **2014**. 43: p. 1519-42.
24. Habibi, Y., L. Lucia, A., and O. Rojas, J., Cellulose Nanocrystals: Chemistry, Self-Assembly, and Applications. *Chem. Rev.*, **2010**. 110: p. 3479-3500.
25. Moon, R.J., A. Martini, J. Nairn, J. Simonsen, and J. Youngblood, Cellulose Nanomaterials Review: Structure, Properties and Nanocomposites. *Chem. Soc. Rev.*, **2011**. 40: p. 3941-3994.
26. Zimmermann, T., E. Pöhler, and T. Geiger, Cellulose Fibrils for Polymer Reinforcement. *Adv. Eng. Mater.*, **2004**. 6: p. 754-761.
27. Endes, C., S. Camarero-Espinosa, S. Mueller, E.J. Foster, A. Petri-Fink, B. Rothen-Rutishauser, C. Weder, and M.J.D. Clift, A Critical Review of the Current Knowledge Regarding the Biological Impact of Nanocellulose. *J. Nanobiotechnol.*, **2016**. 14: p. 78.
28. Schütz, C., M. Agthe, A.B. Fall, K. Gordeyeva, V. Guccini, M. Salajková, T.S. Plivelic, J.P.F. Lagerwall, G. Salazar-Alvarez, and L. Bergström, Rod Packing in Chiral Nematic Cellulose Nanocrystal Dispersions Studied by Small-Angle X-Ray Scattering and Laser Diffraction. *Langmuir*, **2015**. 31: p. 6507-6513.
29. Eichhorn, S.J., *et al.*, Review: Current International Research into Cellulose Nanofibres and Nanocomposites. *J. Mater. Sci.*, **2009**. 45: p. 1.

30. Hausmann, M.K., P.A. Rühs, G. Siqueira, J. Läger, R. Libanori, T. Zimmermann, and A.R. Studart, Dynamics of Cellulose Nanocrystal Alignment During 3d Printing. *ACS Nano*, **2018**. 12: p. 6926-6937.
31. Bercea, M. and P. Navard, Shear Dynamics of Aqueous Suspensions of Cellulose Whiskers. *Macromolecules*, **2000**. 33: p. 6011-6016.
32. Dai, L., T. Cheng, C. Duan, W. Zhao, W. Zhang, X. Zou, J. Aspler, and Y. Ni, 3d Printing Using Plant-Derived Cellulose and Its Derivatives: A Review. *Carbohydr. Polym.*, **2019**. 203: p. 71-86.
33. Voisin, H.P., K. Gordeyeva, G. Siqueira, M.K. Hausmann, A.R. Studart, and L. Bergström, 3d Printing of Strong Lightweight Cellular Structures Using Polysaccharide-Based Composite Foams. *ACS Sustainable Chem. Eng.*, **2018**. 6: p. 17160-17167.
34. Wang, Q., J. Sun, Q. Yao, C. Ji, J. Liu, and Q. Zhu, 3d Printing with Cellulose Materials. *Cellulose*, **2018**. 25: p. 4275-4301.
35. Kim, T., C. Bao, M. Hausmann, G. Siqueira, T. Zimmermann, and W.S. Kim, Electrochemical Sensors: 3d Printed Disposable Wireless Ion Sensors with Biocompatible Cellulose Composites (Adv. Electron. Mater. 2/2019). *Advanced Electronic Materials*, **2019**. 5: p. 1970007.
36. Håkansson, K.M.O., A.B. Fall, F. Lundell, S. Yu, C. Krywka, S.V. Roth, G. Santoro, M. Kvik, L. Prahl Wittberg, L. Wågberg, and L.D. Söderberg, Hydrodynamic Alignment and Assembly of Nanofibrils Resulting in Strong Cellulose Filaments. *Nat Commun*, **2014**. 5.
37. Håkansson, K., Orientation of Elongated Particles in Shear and Extensional Flow, in *Trita-MEK*. 2012, KTH Royal Institute of Technology: Stockholm. p. viii, 25.
38. Scales, P.J., S.B. Johnson, T.W. Healy, and P.C. Kapur, Shear Yield Stress of Partially Flocculated Colloidal Suspensions. *AIChE J.*, **1998**. 44: p. 538-544.
39. Yanez, J.A., T. Shikata, F.E. Lange, and D.S. Pearson, Shear Modulus and Yield Stress Measurements of Attractive Alumina Particle Networks in Aqueous Slurries. *J. Am. Ceram. Soc.*, **1996**. 79: p. 2917-2924.
40. Santos de Oliveira, I.S., A. van den Noort, J.T. Padding, W.K. den Otter, and W.J. Briels, Alignment of Particles in Sheared Viscoelastic Fluids. *J Chem Phys*, **2011**. 135: p. 104902.
41. Benítez, A.J., F. Lossada, B. Zhu, T. Rudolph, and A. Walther, Understanding Toughness in Bioinspired Cellulose Nanofibril/Polymer Nanocomposites. *Biomacromolecules*, **2016**. 17: p. 2417-2426.
42. Reising, A.B., R.J. Moon, and J.P. Youngblood, Effect of Particle Alignment on Mechanical Properties of Neat Cellulose Nanocrystal Films. *J-FOR*, **2012**. 2: p. 32-41.
43. Diaz, J.A., X. Wu, A. Martini, J.P. Youngblood, and R.J. Moon, Thermal Expansion of Self-Organized and Shear-Oriented Cellulose Nanocrystal Films. *Biomacromolecules*, **2013**. 14: p. 2900-2908.
44. Qiao, C., G. Chen, J. Zhang, and J. Yao, Structure and Rheological Properties of Cellulose Nanocrystals Suspension. *Food Hydrocolloids*, **2016**. 55: p. 19-25.
45. Araki, J., M. Wada, and S. Kuga, Steric Stabilization of a Cellulose Microcrystal Suspension by Poly(Ethylene Glycol) Grafting. *Langmuir*, **2001**. 17: p. 21-27.
46. Hirai, A., O. Inui, F. Horii, and M. Tsuji, Phase Separation Behavior in Aqueous Suspensions of Bacterial Cellulose Nanocrystals Prepared by Sulfuric Acid Treatment. *Langmuir*, **2009**. 25: p. 497-502.

47. Gray, D.G., Chiral Nematic Ordering of Polysaccharides. *Carbohydr. Polym.*, **1994**. 25: p. 277-284.
48. Pan, J., W. Hamad, and S.K. Straus, Parameters Affecting the Chiral Nematic Phase of Nanocrystalline Cellulose Films. *Macromolecules*, **2010**. 43: p. 3851-3858.
49. Gray, D. and X. Mu, Chiral Nematic Structure of Cellulose Nanocrystal Suspensions and Films; Polarized Light and Atomic Force Microscopy. *Mater.*, **2015**. 8: p. 5427.
50. Chowdhury, R.A., S.X. Peng, and J. Youngblood, Improved Order Parameter (Alignment) Determination in Cellulose Nanocrystal (Cnc) Films by a Simple Optical Birefringence Method. *Cellulose*, **2017**. 24: p. 1957-1970.
51. Ebeling, T., M. Paillet, R. Borsali, O. Diat, A. Dufresne, J.Y. Cavallé, and H. Chanzy, Shear-Induced Orientation Phenomena in Suspensions of Cellulose Microcrystals, Revealed by Small Angle X-Ray Scattering. *Langmuir*, **1999**. 15: p. 6123-6126.
52. Orts, W.J., L. Godbout, R.H. Marchessault, and J.F. Revol, Enhanced Ordering of Liquid Crystalline Suspensions of Cellulose Microfibrils: A Small Angle Neutron Scattering Study. *Macromolecules*, **1998**. 31: p. 5717-5725.
53. Marchessault, R.H., F.F. Morehead, and M.J. Koch, Some Hydrodynamic Properties of Neutral Suspensions of Cellulose Crystallites as Related to Size and Shape. *J. Colloid Sci.*, **1961**. 16: p. 327-344.
54. Håkansson, K.M.O., F. Lundell, L. Prahl-Wittberg, and L.D. Söderberg, Nanofibril Alignment in Flow Focusing: Measurements and Calculations. *The Journal of Physical Chemistry B*, **2016**. 120: p. 6674-6686.
55. Mercader, C., A. Lucas, A. Derré, C. Zakri, S. Moisan, M. Maugey, and P. Poulin, Kinetics of Fiber Solidification. *Proceedings of the National Academy of Sciences*, **2010**. 107: p. 18331-18335.
56. Trebbin, M., D. Steinhauser, J. Perlich, A. Buffet, S.V. Roth, W. Zimmermann, J. Thiele, and S. Förster, Anisotropic Particles Align Perpendicular to the Flow Direction in Narrow Microchannels. *Proc. Natl. Acad. Sci. U. S. A.*, **2013**. 110: p. 6706-6711.
57. Plan, E.L.C.V.M., Tumbling, Bending, Stretching : Particles in Laminar and Chaotic Flows. 2017, Université Côte d'Azur.
58. Liebi, M., M. Georgiadis, A. Menzel, P. Schneider, J. Kohlbrecher, O. Bunk, and M. Guizar-Sicairos, Nanostructure Surveys of Macroscopic Specimens by Small-Angle Scattering Tensor Tomography. *Nature*, **2015**. 527: p. 349.
59. Lutz-Bueno, V., J. Zhao, R. Mezzenga, T. Pfohl, P. Fischer, and M. Liebi, Scanning-Saxs of Microfluidic Flows: Nanostructural Mapping of Soft Matter. *Lab on a Chip*, **2016**. 16: p. 4028-4035.
60. Bunk, O., M. Bech, T.H. Jensen, R. Feidenhans'l, T. Binderup, A. Menzel, and F. Pfeiffer, Multimodal X-Ray Scatter Imaging. *New Journal of Physics*, **2009**. 11: p. 123016.
61. Beck-Candanedo, S., M. Roman, and D.G. Gray, Effect of Reaction Conditions on the Properties and Behavior of Wood Cellulose Nanocrystal Suspensions. *Biomacromolecules*, **2005**. 6: p. 1048-54.

Chapter 4.

Complex-shaped cellulose composites made by wet densification of 3D printed scaffolds

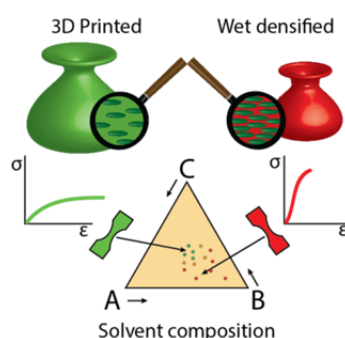
Michael K. Hausmann^{1,2}, Gilberto Siqueira^{1*}, Rafael Libanori^{2*}, Dimitri Kokkinis², Antonia Neels³, Tanja Zimmermann¹, André R. Studart^{2*}

¹*Empa, Swiss Federal Laboratories for Materials Science and Technology, Cellulose and Wood Materials Laboratory, 8600 Dübendorf, Switzerland*

²*Complex Materials, Department of Materials, ETH Zürich, 8093 Zürich, Switzerland*

³*Empa, Center for X-ray Analytics, 8600 Dübendorf, Switzerland*

This chapter has been submitted to *Advanced Functional Materials*, 2019



4.1 Abstract

Cellulose is an attractive material resource for the fabrication of sustainable functional products, but its processing into structures with complex architecture and high cellulose content remains challenging. Such limitation has prevented cellulose-based synthetic materials from reaching the level of structural control and mechanical properties observed in their biological counterparts, such as wood and plant tissues. To address this issue, we report a simple approach to manufacture complex-shaped cellulose-based composites, in which the shaping capabilities of 3D printing technologies are combined with a wet densification process that increases the concentration of cellulose in the final printed material. Densification is achieved by exchanging the liquid medium of the wet printed material with a poor solvent mixture that induces attractive interactions between the cellulose particles. The effect of the solvent mixture on the final cellulose concentration is rationalized using solubility parameters that quantify the attractive interparticle interactions. Using X-ray diffraction analysis and mechanical tests, we show that 3D printed composites obtained through this process exhibit highly aligned microstructures and mechanical properties significantly higher than those obtained by earlier additively-manufactured cellulose-based materials. These features enable the fabrication of cellulose-rich synthetic structures that more closely resemble the exquisite designs found in biological materials grown by plants in nature.

4.2 Introduction

Cellulose offers a sustainable natural resource for the manufacturing of a broad variety of materials in the form of thin films,¹ emulsion stabilizers,² membranes or foams for waste water management,^{3, 4} food packaging and food additives,⁵ and reinforcements for composites.^{6, 7} Whereas the extensive research on cellulose has made available a wide range of cellulose-based building blocks for many applications, current manufacturing technologies do not allow yet for full exploitation of their potential. This is evident by comparing the relatively simple structure of synthetic cellulose-based materials with the hierarchical architecture of biological materials made predominantly from cellulose, such as wood. Further advancements in manufacturing technologies are crucial to enable harnessing the potential of cellulose as a sustainable material resource for the future.

The wide availability of 3D printing technologies has recently given new impulse on the search for manufacturing approaches that offer greater control over the shape and structure of synthetic materials.⁸⁻¹¹ Using stereolithographic, ink jetting, laser- or extrusion-based processes, 3D printing provides shaping capabilities thus far inaccessible by other manufacturing processes.¹²⁻¹⁵ The control over the macroscopic shape inherent of these additive technologies has been combined with different approaches to structure the printed material at smaller length scales below the resolution of the printer. This is possible by designing inks or resins with building blocks that can assemble into controlled structures during or after printing. The assembly process can be directed by external forces, using for example light, magnetic fields, acoustic waves, or shear forces imposed by an extrusion nozzle.¹⁶⁻¹⁹ In recent examples, 3D printing of inks programmed to undergo directed assembly has allowed for the creation of self-shaping composites inspired by the morphology of seedpods and flowers.^{20, 21} Alternatively, polymer objects with reinforcement architectures that resemble the hierarchical structure of wood have been 3D printed using self-assembling liquid crystalline building blocks.²²

Although the shear-induced assembly of cellulose fibrils and nanocrystals in extrusion-based 3D printing has already been demonstrated,²³⁻²⁵ the concentration of cellulose that can be added to the inks remains very limited, typically below 6.6 vol % for unmodified cellulose nanocrystals (CNCs) dispersed in a polymer matrix and 1.3 – 2.6 vol % for cellulose nanofibers (CNFs) dispersed in water.²⁶⁻³¹ Such diluted conditions are appropriate for the ink-jet printing of cellulose micropatterns on flat substrates¹³ or the stereolithographic printing of liquid resins into CNC-laden complex geometries,^{14, 32} but is not sufficient to create 3D objects with high cellulose content. 3D printed objects with high mechanical properties and volume fraction of cellulose acetate (35 wt%) have been recently reported, but the absence of filler particles in this system prevents the design of more elaborate bioinspired cellulose architectures.³³ Other recent works have shown that inks with up to 30-40 wt% CNC can be printed into complex-shaped scaffolds and composites.^{24, 34} However, these very high CNC concentrations lead to drying issues at the printing nozzle

and to very high viscosity and yield stress levels that prevent the flow-induced alignment of cellulose nanocrystals at reasonable applied pressures.^{8, 35} By contrast, the volume fraction of cellulose in biological materials like wood can reach levels as high as 40-50 wt %.⁷ Due to the low volume fraction achieved with current manufacturing processes, 3D printed objects cannot fully benefit from the attractive mechanical and functional properties of cellulose-based building blocks. Moreover, the use of cellulose as a sustainable material resource can only be fully justified if its concentration reaches a significant level in final cellulose-based products. This challenge becomes even more critical in view of the anisotropic nature of cellulose fibrils and nanocrystals, which reduces the maximum volume fraction of particles that can be used before the ink becomes too viscous.

Here, we report a simple approach to manufacture complex-shaped 3D printed polymer composites with volume fraction of nanocelluloses (CNC and CNF) that can be varied from about 13 vol % up to a thus far inaccessible level of 27.35 vol %. In this approach, the interactions between nanocellulose particles suspended in water are first tuned to achieve the rheological properties required for extrusion-based printing of distortion-free structures. After the printing process, the structure is densified by inducing attractive interactions between the cellulose nanoparticles upon exchange of water by a poor solvent. To illustrate this simple processing route and identify the parameters controlling this wet densification process, we study the effect of different solvent mixtures on the volume fraction of nanocelluloses in 3D printed objects. Next, X-ray diffraction experiments are performed to quantify the level of alignment of the cellulose nanoparticles after the printing and solvent exchange processes. The impact of the wet densification process on the mechanical properties of composites produced using this route is then investigated and compared to those of other cellulose-based 3D printed materials. Finally, the shaping freedom enabled by additive manufacturing is combined with the wet densification process to manufacture 3D printed demonstrators with unique geometrical complexity and load-bearing capacity.

4.3 Results and discussion

The manufacturing of complex-shaped composites with high nanocellulose concentrations is demonstrated using two main steps: (a) 3D printing of a cellulose scaffold with highly aligned microstructure and (b) wet densification of the printed scaffold through a solvent exchange process (Figure 4.1). The printing step requires the formulation of nanocellulose-based inks displaying rheological properties suitable for the direct ink writing (DIW) process. Previous works have shown that shear-thinning behavior, minimum yield stress, minimum elastic modulus and fast elastic recovery are key rheological properties for the 3D printing of distortion-free structures by DIW.^{23, 24} These properties can be potentially achieved if the ink contains particles that form a percolating attractive network under rest. Because the main goal was to maximize the cellulose concentration in the final printed scaffold, our ink was designed to contain the highest possible CNC content while still

ensuring a shear-thinning behavior and sufficiently low viscosity for extrusion under moderate applied pressures. Shear-thinning is favored in such inks due to the alignment of the CNC particles during the extrusion process (Figure 4.1a). In addition to this high CNC content, a small fraction of cellulose nanofibers (CNFs) was added to the formulation to increase the yield stress, storage modulus and elastic recovery of the ink (Appendix C1 and Figure C. 1). Due to its very high aspect ratio in the order of 200, CNFs favor the formation of the desired percolating network of particles.⁷ Based on these considerations, a final ink containing 20 wt % CNC and 1 wt % CNF suspended in water was used for 3D printing of cellulose scaffolds. At this solid fraction of CNCs, the fast drying issues typically observed in highly concentrated inks are circumvented^{24, 34} and the viscosity and yield stress of the ink are sufficiently low to enable the partial alignment of cellulose nanocrystals during extrusion.

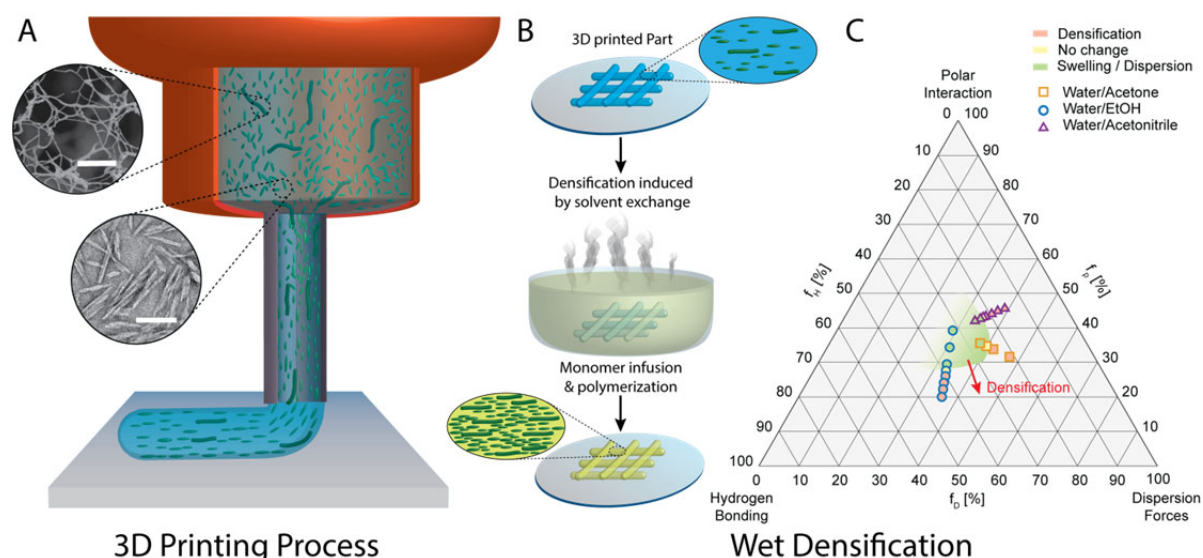


Figure 4.1 Illustration of the 3D printing and wet densification processes used to produce complex-shaped objects with high cellulose concentration. **A)** The alignment of cellulose nanofibers (CNF) and nanocrystals (CNC) during the flow of the ink within the extrusion nozzle. The insets show electron microscopy images of CNFs (top) and CNCs (bottom) obtained from diluted suspensions. Scale bar: 2 μm and 100 nm, respectively. **B)** Wet densification process induced by solvent exchange, followed by polymerization of infiltrated monomers initially present in the solvent bath. **C)** Ternary diagram indicating the relative weight of the solubility parameters of the solvent mixtures used for wet densification. The solubility parameters are presented in terms of relative fractions of hydrogen bonding interactions (f_H), dispersion forces (f_D) and polar interactions (f_P). The colors indicate the solvent mixtures that lead to swelling/dispersion, no dimensional changes and wet densification of the printed objects.

Cellulose scaffolds were densified in a subsequent step by immersing the printed object into a solvent bath of selected composition (Figure 4.1B). Densification is achieved when the liquid in the bath is a poor solvent for the cellulose particles, leading to the development of attractive interparticle interactions (Appendix C2 and Figure C. 2). Under such conditions, the average distance between the particles within the printed object reduces, leading to macroscopic shrinkage and densification. To assess the quality of the

solvent with respect to the nanocellulose particles, we use Hansen solubility parameters previously reported in the literature (Figure 4.1C and Table C. 2). According to Hansen, the total solubility parameter of a liquid (δ_T) is determined by three contributions: (i) the hydrogen bonding component (δ_H), the polar component (δ_P), and the dispersive component (δ_D).^{36, 37} Overall, a poor solvent is expected to exhibit Hansen solubility parameters that differ significantly from those of the suspended particles. Earlier work³⁸⁻⁴² has shown that the range of solubility parameters for acid-hydrolyzed nanocellulose particles matches well the δ_H , δ_D and δ_P values of water, which explains the good dispersibility of the as-hydrolyzed CNC/CNF particles in aqueous medium. To achieve the desired poor solvent condition required for scaffold densification, water-miscible solvents such as ethanol, acetone and acetonitrile can be added to the initial aqueous phase (Figure 4.1C and Appendix C3 and Figure C. 3-6).

We investigate the effect of the solvent composition on the densification process by systematically changing the solubility parameters of the liquid mixture relative to that of cellulose. Our experiments indicate that the scaffold densifies continuously when immersed in an aqueous solution containing increasing concentrations of ethanol, acetone or acetonitrile in water (Figure 4.2A). Taking mixtures of water and ethanol as an example, we observe a change in solid volume fraction from 3.67 vol % to 24.5 vol %, as the fraction of ethanol is increased from 65.5 vol % to 100 vol %. This trend is in agreement with the qualitative description of the effect of solvents with distinct solubility parameters on the densification of cellulose-based membranes produced through spinning processes.⁴³ Based on these data, it is possible to define an area in a solubility diagram that leads to dispersion or densification of the cellulose scaffold (green area in Figure 4.1C).

To gain a better quantitative understanding of the physical processes that control the wet densification process, our results were interpreted in terms of the cohesive energy density (CED) of cellulose compared to that of the different solvent mixtures. The CED corresponds to the increase in internal energy per unit volume of a substance if all intermolecular forces are removed.⁴⁴⁻⁴⁷ This parameter is therefore an indicator of the energy gained through attractive intermolecular interactions within a substance and can be determined from the total Hansen solubility parameters as follows:

$$CED = \delta_T^2 = \delta_P^2 + \delta_D^2 + \delta_H^2 \quad Eq. 1$$

where δ_H , δ_P and δ_D represent, respectively, the hydrogen bonding, the polar and the dispersive contributions to the total solubility parameter.

For our CNC suspensions, liquid mixtures with CED values comparable to those of the suspended particles tend to be good solvents since the replacement of particle-particle

interactions by particle-liquid interactions does not lead to a major net change in internal energy. By contrast, a mismatch between the CED values of the particles and of the liquid mixture will result in separation into particle-rich and liquid-rich phases. Because the estimated CED of hydrolyzed cellulose is comparable to that of water but higher than that of pure ethanol, acetone and acetonitrile (Figure 4.2B), the addition of these non-aqueous solvents into the liquid mixture will favor attractive interactions between the cellulose nanoparticles. Following this rationale, we take the mismatch in CED between particles and liquid mixture as an estimate of the reduction in internal energy of the wet scaffold achieved upon solvent exchange. This net change in CED can be physically interpreted as an internal stress that pulls particles together as a result of the increased attractive interactions between cellulose molecules. Taking such internal stress as the driving force of the wet densification process, one should expect the final relative density of the cellulose scaffolds to be proportional to the net change in CED after solvent exchange.

Indeed, our experimental data show that the solid content in the printed nanocellulose objects increase logarithmically with the net change in CED (Figure 4.2B). The obtained trend resembles the compaction behavior of powders in pressing operations, where a logarithmic dependence is also found between the relative density of the powder and the pressure applied onto the compact.^{48, 49} Such analogy supports our physical interpretation that internal stresses induced by molecular interactions are at the origin of the wet densification process.

While the logarithmic dependence on the net CED change is observed for all the tested solvents, a stronger densification effect is achieved with ethanol and acetonitrile. To shed light on the possible causes of this difference, our physical picture of the densification process is complemented by a chemical description of the underlying molecular interactions (Figure 2B). From a chemical viewpoint, the development of internal stresses results from the replacement of the highly polar and hydrogen-bonding -OH groups from the water molecules by solvent molecular moieties that display weaker interactions with the -OH groups present on the surface of the cellulose particles. Because of their enhanced polar nature and hydrogen-bonding capability, the -OH groups of water molecules interact more strongly with the cellulose surface, preventing the hydroxyl groups of CNCs/CNFs from establishing attractive molecular interactions between neighbor particles. This screening effect of the water molecules is attenuated by replacing them with (excess) solvent molecules containing less polar and hydrogen-bonding functional groups. The less interacting solvent molecules are eventually displaced by direct attractive interactions between the -OH groups on the cellulose surface, leading to the observed densification phenomenon. According to this interpretation, the excess of solvent molecules needed to remove water molecules from the cellulose surface will depend on their polar character and hydrogen-bonding ability. Based on the Hansen solubility parameters, we note that ethanol and acetonitrile show either polar or hydrogen-bonding values that come close to those of water (Appendix C3). As a result, these two solvents can easily replace H₂O molecules from

the cellulose surface and thus induce densification. By contrast, the polar and hydrogen-bonding Hansen parameters of acetone are both significantly lower compared to water. Consequently, a far greater excess of acetone is needed to remove water molecules from the cellulose surface and promote attractive interparticle interactions. Since the CED net change resulting from the solvent exchange with acetone still predicts densification to be more thermodynamically stable, we expect the shielding effect imposed by the water molecules to be only a kinetic constraint that can be overcome if enough time is provided for the densification process.

Besides the solvent quality, a cross-linker ion such as Ca^{2+} can also be used to increase the solid content of the printed cellulose object when the concentration of poor solvent (e.g. ethanol) in the mixture is kept low. Due to their opposite charges, the Ca^{2+} ions and the hydrolyzed cellulose nanoparticles establish attractive electrostatic interactions that decrease the distance between nanocellulose particles, thus increasing the solid fraction of the object. To illustrate this effect, we evaluated the density of cellulose objects after introducing them in an immersion bath comprising a water-ethanol mixture with different concentrations of Ca^{2+} -containing aqueous phase. Cross-linking with Ca^{2+} leads to the formation of a percolating network of CNC/CNF particles that remains cohesive and gelled even in the absence of the poor solvent (ethanol). A CNC/CNF object immersed in an ethanol-free aqueous solution with 4 wt % CaCl_2 shows a solid content of 15.7 vol %, which is slightly higher than the initial CNC/CNF concentration of 14.6 vol % present in the initial ink. By contrast, immersion in a Ca-free aqueous solution without ethanol leads to complete disintegration of the object (Figure C. 5). The cross-linking effect of Ca^{2+} can be combined with the solvent-induced densification effect through the addition of ethanol to the Ca^{2+} -containing aqueous solution used as immersion bath (Figure 4.2C). For ethanol concentrations higher than 70.4 vol % in the Ca^{2+} -containing bath, the solid fraction reaches values comparable to those obtained using Ca-free water-ethanol mixtures. At this point, the relative density of the object becomes dominated by the quality of the solvent (Figure 4.2C and D).

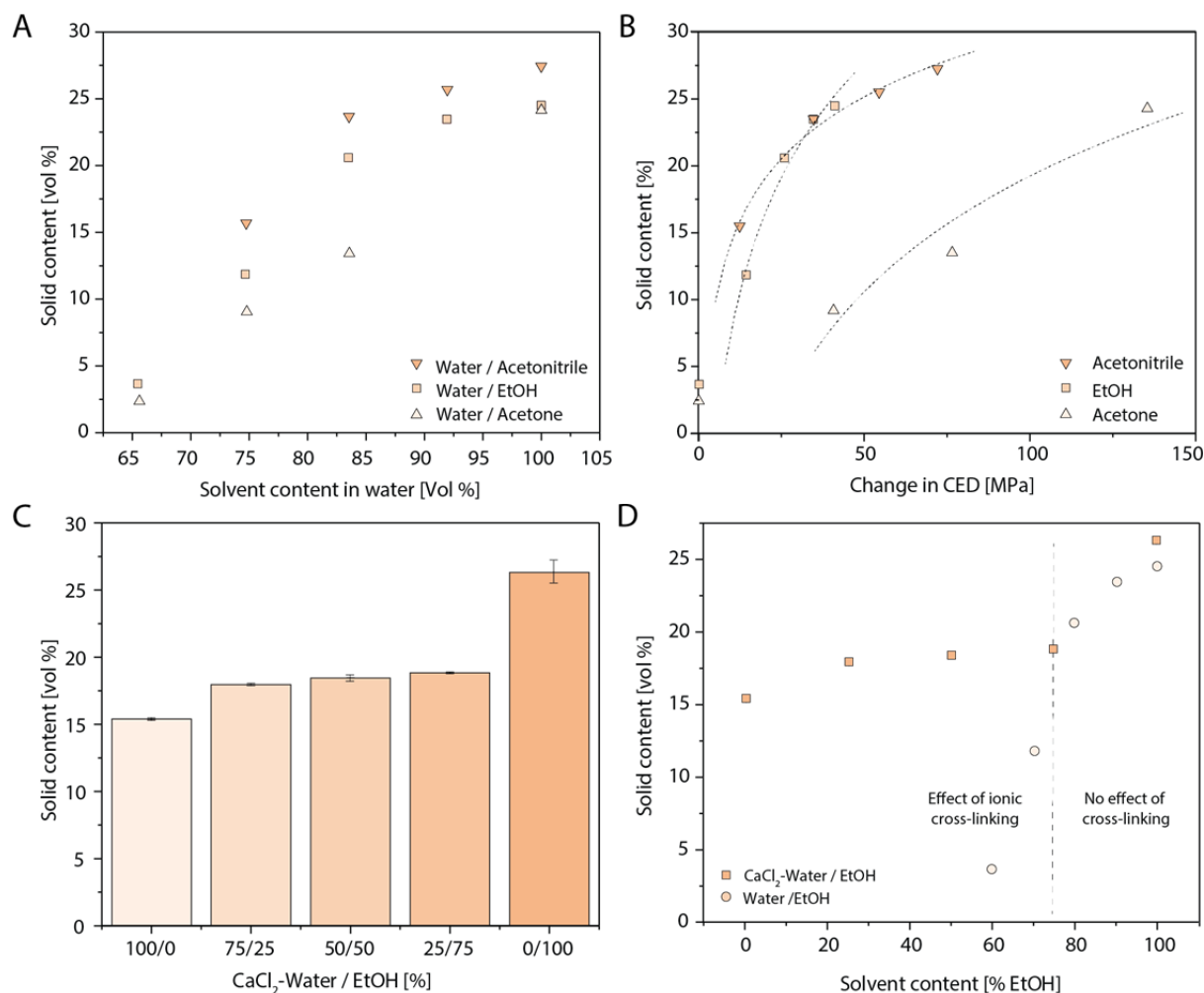


Figure 4.2 Solids content of cellulose scaffolds obtained via wet densification using solvent mixtures of different compositions. **A)** Solid content of the scaffold as a function of the concentration of acetonitrile, ethanol (EtOH) and acetone used in the aqueous solvent mixtures. **B)** Dependence of the solid content on the net change in CED induced by the solvent exchange process. The lines were obtained by fitting the data with a logarithmic function. **C)** Effect of the relative fraction between Ca-containing water (4wt % CaCl_2) and ethanol on the solid content of scaffolds immersed in water/ethanol (EtOH) solutions. **D)** Comparison of the solids content achieved using water/EtOH solutions in the presence or absence of 4wt % CaCl_2 .

3D printed nanocellulose objects subjected to wet densification can be further processed into composites containing very high concentrations of cellulose. Composites are generated here by introducing a polymer phase between the CNC/CNF particles using two different routes: supercritical drying of the wet printed material followed by infiltration of monomers or infiltration of the printed materials with a monomer in the wet state (Appendix C4 and Figure C. 7-9,14). The wet infiltration route is illustrated here as a mean to obtain large nanocellulose-based composites without the need of costly equipment, which drastically simplifies the process as compared to the impregnation of supercritically-dried scaffolds (Appendix C2 and C4). Advantages and limitations of these and other manufacturing routes used throughout this study are listed in Table C. 1. In this process, a mixture of monomer, cross-linker and photoinitiator is dissolved into the solvent bath used for the wet densification procedure. The presence of these components does not affect the

wet densification step. As observed with the monomer-free mixtures, solvent exchange leads to a linear shrinkage of 40 % relative to the initial printed dimensions. Because of its lower vapor pressure compared to ethanol, the monomer infiltrates the nanocellulose object during evaporation of the solvent. Following this approach, composites with nanocellulose concentrations of 27.35 vol % were generated by polymerizing the infiltrated monomer using UV light. The infiltration of the CNC/CNF scaffolds with the monomer enhances significantly the cohesion between filaments by forming a single continuous phase throughout the printed object (Figure C. 4-8). Additionally, our experiments showed that the solvent exchange process can be carried without undesired shape distortion effects if the wall thickness of the 3D printed objects is smaller than approximately 5mm. 3D scaffolds with thicker walls would require the use of solvents with a smaller CED mismatch to prevent differential shrinkage and distortion of the wall. For wall thicknesses equal or below 5mm, we experimentally observed that the solvent exchange process takes less than 30 minutes. It is important to note that the shrinkage associated with the wet densification process should also be taken into account when designing the dimensions of the 3D printed object. Very recent work on cellulose-based structures subjected to solvent-induced shrinkage has shown that a compensation factor can be introduced in the design model to reach 3D objects with predictable final dimensions.⁵⁰

In addition to the high concentration of cellulose, 3D printing followed by wet densification also allows one to preserve the alignment of cellulose nanocrystals and nanofibers resulting from the DIW process and thus obtain 3D objects with deliberate CNC orientations. This feature enables the manufacturing of objects with aligned architectures inspired by wood and other biological materials (see Appendix C5 – C7). A high nanocellulose particle orientation was confirmed by diffraction measurements and scanning electron microscopy (SEM, Figure C. 10-13 and Table C. 3). Our SEM images show that the aligned CNC/CNF particles form a very dense microstructure that resembles the fibrillated architecture of the thickest and supporting cell wall layer S2 present in the secondary walls of plant cells.⁵¹

Control over the alignment of CNCs/CNFs and the formation of strong interfaces between filaments and the polymer matrix enables the fabrication of semi-transparent cellulose-based 3D-printed composites with tunable anisotropic mechanical properties (Figures S10 and S16). To quantify the reinforcing effect of the CNC/CNF particles and the anisotropic properties of the resulting composites, we performed tensile and three-point bending tests in specimens exhibiting different particle orientations (Figure 4.3, Figure C. 17-19.). Composite samples were compared to the non-reinforced polymer matrix alone (cellulose-free) and to specimens obtained by simply drying the CNC/CNF scaffolds in air. The mechanical results indicate that the polymer matrix is very soft and weak, with elastic modulus and tensile strength values of 1.6 and 7 MPa, respectively. Remarkably, the incorporation of 27.35 vol % of nanocellulose particles in this polymer matrix enhances the modulus and strength of the material by several orders of magnitude (Figure 4.3a, b). As

expected, this is accompanied by a significant reduction of the ductility of the material. The major reinforcing effect imparted by the nanocellulose results from their high concentration in the composite and their intrinsically high mechanical properties. Surprisingly, the CNC-based printed scaffolds alone show quite high mechanical properties, comparable to wood, even before infiltration and polymerization of the monomer (Figure 4.3a-c), which suggests that the wet densification process drastically increases the density of hydrogen bonds between cellulose particles in the printed object. Comparison of the mechanical properties of the composite with those of the pure nanocellulose specimen reveals that the concentration of CNC/CNF used in the composite is sufficient to harness the high modulus and strength of the cellulose particles alone while keeping some of the ductility associated with the polymer matrix (Figure 4.3a-c and Appendix C9). When tested in the transverse direction using a 3-point bending setup, the composites show high flexural modulus and strength (Figure C. 18). This reflects the high adhesion between printed filaments and indicate that the nanocellulose particles are able to reinforce the polymer matrix even when aligned perpendicular to the main stress direction. Overall, the high concentration of CNC/CNF particles achieved through the wet densification process leads to a reinforcement effect significantly stronger than that observed in CNC-based 3D printed composites and scaffolds previously reported in the literature.^{24, 34} The mechanical properties of the composites are expected to be further improved if the CNC particles are combined with stronger polymer matrices. Taking for example cellulose acetate as polymer matrix, it should be possible to generate strong and stiff 3D printed objects featuring complex shapes and an all-cellulose hierarchical architecture.^{33, 52}

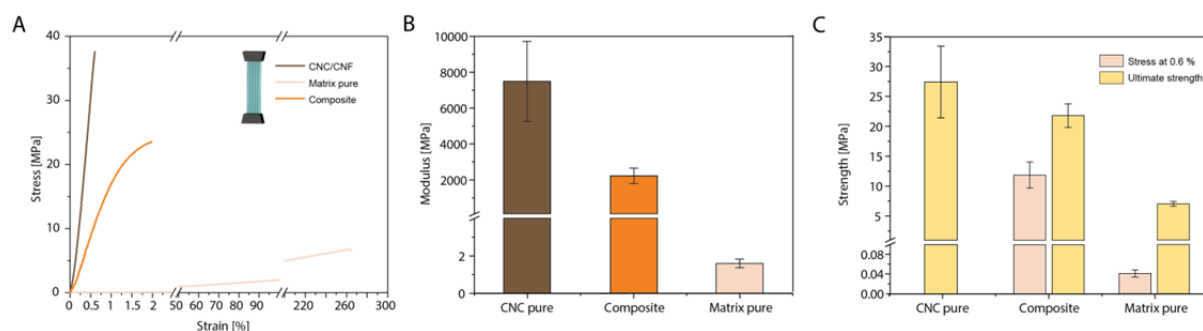


Figure 4.3 Mechanical performance in tensile mode of 3D-printed composites obtained through the wet densification approach. (A) Representative stress-strain curves obtained under tension for the matrix, 3D printed dry scaffold and composite. (B) Elastic modulus, (C) strength at 0.6 % deformation and maximum strength of the matrix, 3D printed dry scaffold, and composite.

The high cellulose concentration and mechanical properties demonstrated using simple filaments and films were eventually translated to more complex 3D geometries by taking advantage of the intrinsic shaping freedom of extrusion-based 3D printing technologies. We demonstrate the geometrical design freedom accessible with our nanocellulose-based inks by first printing a complex-shaped jar exhibiting overhangs and asymmetric features (Figure 4.4a-d). After printing, the jar was subjected to wet densification, followed by wet monomer infiltration and light-induced polymerization. Notably, the fine geometrical features remain undistorted during the wet densification step,

in spite of the large linear shrinkage of approximately 40 % that occurs in this process. This high shrinkage led to a remarkable cellulose concentration of 27.35 vol % in the final composite. A hollow truncated cone and a honeycomb design were also 3D printed, as examples of lightweight structures that can be manufactured with our process. To illustrate the high stiffness and strength of the final printed objects, we fabricated a hook that can bear a load that is 737 times higher than its own weight without significant extension or rupture (Figure 4.4a). The mechanical properties can be further controlled by infiltrating the printed scaffolds with different polymer matrices (Appendix C10 and Figure C. 20).

While a high concentration of nanocellulose particles is required to print stiff and load-bearing structures, the use of inks with lower cellulose contents that can be cross-linked with Ca^{2+} ions and swollen in water offer the possibility to produce soft hydrogels exhibiting tailored macroscopic geometries and mechanical response. This was demonstrated by immersing an as-printed grid-like structure into a Ca-containing aqueous solution loaded with monomers, followed by light-induced polymerization of the monomer to create a soft composite with squared cellular architecture. The lateral compliance of the final structure depends on the angle at which it is mechanically loaded. Loading along the struts leads to a stiff response, whereas a more compliant behavior is observed when the mechanical load is applied at an angle of 45° with respect to the strut axis (Figure 4.4e-j). The possibility to tailor the mechanical response of such structures by tuning the nanocellulose concentration in the precursor hydrogel and the cellular architecture of the printed object opens a large parameter space for the design of biocompatible cellulose-based gels and composites for biomedical and functional applications

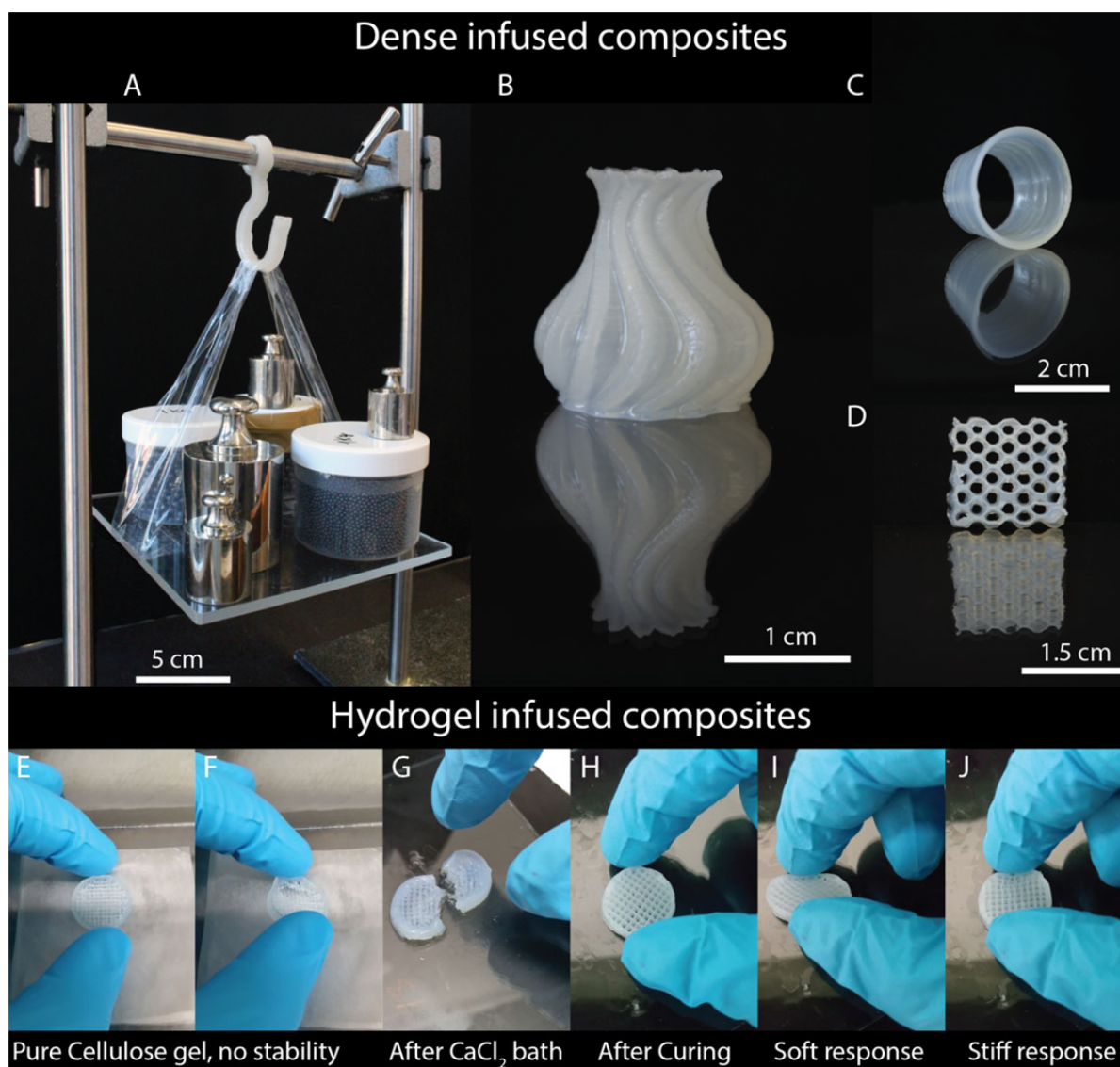


Figure 4.4 3D printed functional parts with high volume fraction of cellulose (27.35 vol %). (A) Printed hook (6.1 g) carrying a load of 4.5 kg. (B) Printed jar with complex geometry. (C,D) Printed trunked cone and honeycomb structures. (E-J) Cellulose-based 3D printed composites prepared from hydrogels with lower cellulose concentration: (E-F) hydrogel with no mechanical stability obtained right after printing and (G) hydrogel after one day in bath of CaCl_2 solution, showing improved stiffness but low strength, and (H-J) composite obtained after infiltration of hydrogel with monomer and UV curing. The infiltrated composite shows a stiff response when compressed along the strut direction and an elastic deformation when tested at an angle of 45° relative to the strut axis. (See Supporting videos 1,2 and 3).

4.4 Conclusions

Complex-shaped composites with cellulose concentration up to 27.35 vol % can be created through the wet densification of 3D printed scaffolds. The densification process involves the exchange of the aqueous phase of the printed wet scaffold by a liquid mixture that works as a poor solvent for the cellulose particles. The poor solvent characteristics of the liquid mixture can be quantified using Hansen solubility parameters, which provide a measure of the cohesive energy density (CED) of the solvent mixture. Liquids with CED comparable to that of cellulose will work as good solvents, enabling the dispersion of a high

concentration of cellulose particles in the ink used for 3D printing. By contrast, solvents with significantly different CED values will exhibit poor dispersion capabilities and induce attractive interactions between the cellulose particles within the 3D printed scaffolds. The increase in scaffold density during wet densification was found to be directly proportional to the change in CED resulting from the solvent exchange process. This quantitative relationship offers a sound physical interpretation of the wet densification phenomenon and provides guidelines for the selection of solvent mixtures that can effectively increase the cellulose content of 3D printed scaffolds. Because of their high cellulose concentration, composites obtained via infiltration of wet densified scaffolds with an organic phase show significantly higher fracture strength and stiffness compared to state-of-the-art 3D printed cellulose-based materials. This strengthening effect arises from the very high concentration of cellulose achieved in the final composite and is also partly affected by the strong alignment of the cellulose particles along the extrusion direction during the printing process. Such alignment can be combined with the shaping freedom enabled by 3D printing and the flexibility in materials choice offered by the densification and infiltration procedures to manufacture complex-shaped objects with unprecedentedly high mechanical properties and volume fraction of cellulose. The high level of structural complexity and control achieved with this combined process opens the way to the fabrication of cellulose-based materials that capture some of the design principles of biological structures like wood and morphing plant structures. Since mechanical stability and high cellulose content are key to achieve long-term durability and to fully benefit from the sustainable nature of this material resource, the proposed manufacturing workflow is also expected to have a major impact in future cellulose-based structural, biomedical and energy-related products.

4.5 Experimental methods

Materials

2-Hydroxyethyl methacrylate (HEMA) (98%), N-isopropylacrylamide (NIPAM) and N,N'-methylenebis(acrylamide) (MBA) were purchased from Sigma-Aldrich. The functional PUA oligomers (BR3741AJ and BR571) and the photoinitiator bis(2,4,6-trimethylbenzoyl)-phenylphosphineoxide (Irgacure 819) were generously provided by Dymax and BASF, respectively. Calcium chloride powder (CaCl_2) was purchased from Merck. Cellulose nanocrystals (CNCs) were prepared via sulfuric acid hydrolysis of eucalyptus pulp according to a published procedure⁵³ and were purchased from the USDA Forest Service – Forest Products Laboratory (Madison, WI). Never-dried elemental chlorine free (ECF) cellulose fibers from bleached softwood pulp (*Picea abies* and *Pinus spp.*) were obtained from Stendal GmbH (Berlin, Germany) and used for the production of cellulose nanofibers (CNFs). Transmission Electron Microscopy (TEM) images of CNCs and CNFs used in the study are shown in Appendix Figure C. 21 and S22. 2,2,6,6-Tetramethyl-1-piperidinyloxy (TEMPO) and sodium hypochlorite (NaClO) solutions (12-14 % chlorine) were purchased from VWR

International. Sodium bromide ($\text{NaBr} \geq 99\%$) and sodium hydroxide ($\text{NaOH} \geq 99\%$) were obtained from Sigma-Aldrich (Buchs, Switzerland).

Preparation and characterization of inks

Cellulose-based inks

TEMPO-CNFs were produced according to a well-established protocol from Saito et al.⁵⁴, which is extensively described elsewhere.⁵⁵ Freeze-dried CNCs (0.98 wt % sulfur content Figure C. 21) and never-dried TEMPO-CNFs in water (CNF concentration of 1.33 wt % relative to water Figure C. 22) were mixed for 5 min at 2500 and 3500 rpm, respectively, in a speed mixer (model DAC 150.1 FVZ). The resulting gel contained 20 wt % CNC and 1 wt % CNF. This cellulose-based gel was left for swelling for one night, mixed at 3500 rpm for 5 min and stored in the fridge prior to testing. Before further processing and printing, the gel was filled in plastic cartridges and centrifuged for 10 min at 3500 rpm to remove bubbles.

Rheology of inks

The rheological characterization of the inks was performed using a MCR 302 rheometer from Anton Paar. Measurements were carried out using a plate-plate geometry with 50 mm diameter and a gap of 0.5 mm at a constant temperature of 20 °C. Shear rate sweeps were performed at shear rates ranging from 0.001 s^{-1} to 1000 s^{-1} at logarithmically-spaced intervals with 4 points per decade. Amplitude sweeps were performed from 0.1 to 1000 % using similar logarithmic intervals at a frequency of 1 Hz. The yield stress of the inks was determined by applying an increasing shear stress from 1 to 1000 Pa and measuring the deformation response. The stress corresponding to the change in slope in the shear stress versus deformation curves was taken as the yield stress of the ink.

4.5.1 Preparation and characterization of composites

3D printing

Cellulose scaffolds were printed using a direct ink writer (DIW) from EnvisionTEC (Bioplotter Manufacturing series). The gels were filled in plastic cartridges and extruded through uniform steel needles with compressed air at pressures in the range 2.1 - 2.4 bar and at a fixed temperature of 20 °C. The extrusion needles were 27 mm long and exhibited a non-tapered geometry with diameter of 0.41 mm.

Freeze-drying

Freeze-dried scaffolds were prepared by plunging printed gel structures into liquid nitrogen and placing the sample in the freeze-dryer (SRK System Technik GmbH - LYOVAC) for removal of the aqueous phase. Freeze-drying was accomplished by changing the temperature and pressure in the chamber so as to directly sublime the ice.

Super-critical drying

Some of the scaffolds were dried under super-critical conditions. Prior to super-critical drying, the water-based gel was plunged into an ethanol bath. The ethanol was changed several times to make sure most of the water is eliminated. Super-critical drying was conducted in a dedicated equipment (Quorum Technologies - Polaron), where the ethanol is first replaced by liquid CO₂ before removal of the liquid phase under super-critical conditions (37 °C, 100 bar).

Resin formulation

The resin used as polymer matrix of the composite is a mixture of HEMA / BR-3741 AJ / Irgacure 819 at weight fractions of 50, 49.5 and 0.5 wt % respectively. The resin was diluted with the solvent for the infiltration step. When pure ethanol was used as solvent, a solvent:resin weight ratio of 2:1 was utilized. The resin:water ratio for the hydrogels was adjusted to achieve the targeted final water content desired for the gel.

Infiltration of super-critically dried scaffolds

Super-critically dried samples were plunged into a liquid bath of HEMA and isostatically pressed at 5000 bar for 5 minutes prior to a one week vacuum infiltration process. After infiltration, the samples were UV cured for 10 minutes on both sides under continuous nitrogen (N₂) flow to avoid oxygen inhibition of the polymer reaction.

Infiltration of wet scaffolds

Some of the scaffolds were directly infiltrated with monomer while still in the wet state. In this case, the aqueous phase of the printed scaffolds was first solvent exchanged with ethanol to enable wet densification. After water removal, the ethanol bath was either replaced by an ethanol solution of HEMA (2:1 weight ratio of ethanol: HEMA/BR). The samples were kept in the bath under vacuum for 1 week to allow for infiltration of the resin and complete elimination of the ethanol. Infiltrated scaffolds were UV-cured for 10 minutes on both sides under continuous nitrogen (N₂) flow. We also explored the possibility to directly infiltrate the wet scaffolds in a or a pure HEMA/BR resin bath which is also feasible. The concentration of cellulose nanocrystals in the final composites was estimated using Archimedes and geometrical methods (Appendix S12).

4.5.2 Mechanical and structural characterization of composites

3-Point-Bending measurements

3D printed samples for three-point-bending measurements were produced according to the standard ISO D790-03⁵⁶. Tests were conducted in an universal mechanical testing machine (Shimadzu AGS-X, Japan) equipped with a 1 kN load cell. Samples were tested using a span width of 40 mm and a displacement rate of 1 mm/min.

Tensile tests

3D printed single- and double-layered films were printed and tested in tensile mode using an uniaxial Mechanical tester (Zwick Roell) with a load cell of 500 N. Measurements were performed in 12 mm x 2 mm dog bone samples that were punched out from printed sheets (single and double layers). Stress data were recorded while applying a displacement rate of 5 mm/min. Strain was measured based on cross-head motion. Pure CNC/CNF dog-bone-shaped samples were obtained by stamping out films that were wet-densified films via solvent exchange and dried in air. Dog-bone-shaped specimens of CNC/CNF composites were prepared from UV-cured composite films generated through the wet densification and infiltration processes.

Dynamic mechanical analysis (DMA)

Single and double layered films were printed and cut for DMA analysis (TA RSAIII). Cut samples were 5 mm wide, 40 mm long and 0.35 mm thick. Tests were conducted using a span of 35 mm. Samples were measured with a frequency of 1 Hz while heated from -100 °C to 100 °C at a rate of 2 °C/min and a pre-strain of 0.04 %.

Differential scanning calorimetry (DSC)

DSC measurements were performed at heating and cooling rates of 20 °C/min (DSC7 and DSC8000, Perkin Elmer). The experimental run consisted of a heating cycle from -90 °C to 60 °C, followed by a ramp-down to -90 °C, a holding time of 5 min at -90 °C before a final heating to 60 °C.

UV/Vis Spectroscopy

Light transmittance of 3D-printed films was measured on a Shimadzu UV-3600 at wavelengths ranging from 300 to 1500 nm. The single- and double-layered samples used in these measurements had a thickness of around 0.32 and 0.6 mm, respectively.

Transmission electron microscopy (TEM)

Cellulose nanocrystals were characterized by transmission electron microscopy (TEM, Jeol JEM-2200FS, USA Inc.) using an acceleration voltage of 200 kV. Plasma activated (30 s) carbon-coated grids were used as a support onto which a 0.02 wt % suspension of the

cellulose nanocrystals was deposited and stained with a 2 wt % solution of uranyl acetate for 30 s. The average lengths and diameters of the CNCs were measured with the software Image J.

Scanning electron microscopy (SEM)

Scanning electron microscopy (SEM) was performed on a LEO 1530 using an accelerating voltage of 2kV and a working distance of 5mm. Sample cross-sections prior and after resin infiltration or mechanical testing were imaged. Before imaging, the samples were either glued with carbon adhesive tape onto aluminum sample holders or held with screw fastening systems. Samples were coated for 30 sec at a current of 40 mA, a pressure of 0.8 Pa and a working distance of 5 cm with tungsten to avoid surface charging.

Optical microscopy (OM)

All optical microscopy analyses were performed on an Axioplan microscope from Zeiss equipped with cross-polarized filters.

Wide angle X-ray diffraction (WAXD)

Two-dimensional wide-angle X-ray diffraction (2D-WAXD; STOE IPDS-II, 0.71073 Mo K α radiation source) was used to study the degree of CNC alignment within the printed filaments and films. The equipment was operated at 40 mA and 50 kV for 30 min using a beam diameter of 0.5mm in transmission mode. The samples were fixed on the goniometer head and then placed perpendicular to the beam to allow the X-rays to pass only through the specimen. The 2D-WAXD patterns were recorded on an Image Plate Detector System with a 340mm diameter placed at a distance of 200mm from the sample. For each sample position a full image was recorded covering a 2Theta range from 3 to 40°. Azimuthal scans were integrated for the cellulose (200) reflection. Curves shown in Figure C. 10 have been obtained after subtraction of the background noise to the original curve.

4.6 Acknowledgements

We thank B. Fisher for the DSC analysis, A. Huch for the TEM imaging, C. Affolter and B. Weisse for allowing us to use the mechanical testing equipment as well as R. Carron for the help with UV Spectroscopy and Dr. E. Jeoffroy for the scientific discussions. A.R.S. greatly acknowledge the financial support from the Swiss National Science Foundation (Consolidator Grant number BSCGI0_157696). R.L. is thankful for the financial support from the Swiss Competence Center for Energy Research SCCER Mobility and the Swiss Innovation Agency Innosuisse. M.K.H and G.D.S greatly acknowledge the financial support from the Swiss National Science Foundation (200021_159906/1). This work also benefitted from support from the Swiss National Science Foundation through the National Center of Competence in Research Bio-Inspired Materials.

4.7 References

1. Nogi, M., S. Iwamoto, A.N. Nakagaito, and H. Yano, Optically Transparent Nanofiber Paper. *Adv. Mater.*, **2009**. 21: p. 1595-1598.
2. Zoppe, J.O., R.A. Venditti, and O.J. Rojas, Pickering Emulsions Stabilized by Cellulose Nanocrystals Grafted with Thermo-Responsive Polymer Brushes. *J. Colloid. Interface Sci.*, **2012**. 369: p. 202-209.
3. Kollarigowda, R.H., S. Abraham, and C.D. Montemagno, Antifouling Cellulose Hybrid Biomembrane for Effective Oil/Water Separation. *ACS Appl. Mater. Interfaces*, **2017**. 9: p. 29812-29819.
4. Zhang, Z., G. Sèbe, D. Rentsch, T. Zimmermann, and P. Tingaut, Ultralightweight and Flexible Silylated Nanocellulose Sponges for the Selective Removal of Oil from Water. *Chem. of Mater.*, **2014**. 26: p. 2659-2668.
5. Lee, H., J. Sundaram, and S. Mani, Production of Cellulose Nanofibrils and Their Application to Food: A Review, in *Nanotechnology: Food and Environmental Paradigm*, R. Prasad, V. Kumar, and M. Kumar, Editors. 2017, Springer Singapore: Singapore. p. 1-33.
6. Moon, R.J., A. Martini, J. Nairn, J. Simonsen, and J. Youngblood, Cellulose Nanomaterials Review: Structure, Properties and Nanocomposites. *Chem. Soc. Rev.*, **2011**. 40: p. 3941-3994.
7. Dufresne, A., Nanocellulose from Nature to High Performance Tailored Materials. 2012, Berlin Walter de Gruyter GmbH.
8. Lewis, J.A., Direct Ink Writing of 3d Functional Materials. *Adv. Funct. Mater.*, **2006**. 16: p. 2193-2204.
9. Studart, A.R., Additive Manufacturing of Biologically-Inspired Materials. *Chem Soc Rev*, **2016**. 45: p. 359-76.
10. Dai, L., T. Cheng, C. Duan, W. Zhao, W. Zhang, X. Zou, J. Aspler, and Y. Ni, 3d Printing Using Plant-Derived Cellulose and Its Derivatives: A Review. *Carbohydr. Polym.*, **2019**. 203: p. 71-86.
11. Chimene, D., K.K. Lennox, R.R. Kaunas, and A.K. Gaharwar, Advanced Bioinks for 3d Printing: A Materials Science Perspective. *Ann. Biomed. Eng.*, **2016**. 44: p. 2090-2102.
12. Kumar, S., M. Hofmann, B. Steinmann, E.J. Foster, and C. Weder, Reinforcement of Stereolithographic Resins for Rapid Prototyping with Cellulose Nanocrystals. *ACS Appl. Mater. Interfaces*, **2012**. 4: p. 5399-5407.
13. Maren, R. and N. Fernando, Deposition of Cellulose Nanocrystals by Inkjet Printing, in *Model Cellulosic Surfaces*. 2009, American Chemical Society. p. 157-171.
14. Palaganas, N.B., J.D. Mangadlao, A.C.C. de Leon, J.O. Palaganas, K.D. Pangilinan, Y.J. Lee, and R.C. Advincula, 3d Printing of Photocurable Cellulose Nanocrystal Composite for Fabrication of Complex Architectures Via Stereolithography. *ACS Appl. Mater. Interfaces*, **2017**. 9: p. 34314-34324.
15. Suwanprateeb, J., Improvement in Mechanical Properties of Three-Dimensional Printing Parts Made from Natural Polymers Reinforced by Acrylate Resin for Biomedical Applications: A Double Infiltration Approach. *Polymer International*, **2006**. 55: p. 57-62.
16. Kokkinis, D., M. Schaffner, and A.R. Studart, Multimaterial Magnetically Assisted 3d Printing of Composite Materials. *Nat Commun*, **2015**. 6: p. 8643.

17. Minas, C., D. Carnelli, E. Tervoort, and A.R. Studart, 3d Printing of Emulsions and Foams into Hierarchical Porous Ceramics. *Adv. Mater.*, **2016**. 28: p. 9993-9999.
18. Collino, R.R., T.R. Ray, L.M. Friedrich, J.D. Cornell, C.D. Meinhart, and M.R. Begley, Scaling Relationships for Acoustic Control of Two-Phase Microstructures During Direct-Write Printing. *Mater. Res. Lett.*, **2018**. 6: p. 191-198.
19. Kim, T., R. Trangkanukulkij, and W.S. Kim, Nozzle Shape Guided Filler Orientation in 3d Printed Photo-Curable Nanocomposites. *Sci. Rep.*, **2018**. 8: p. 3805.
20. Sydney Gladman, A., E.A. Matsumoto, R.G. Nuzzo, L. Mahadevan, and J.A. Lewis, Biomimetic 4d Printing. *Nat. Mater.*, **2016**. 53: p. 413-418.
21. Miao, S., N. Castro, M. Nowicki, L. Xia, H. Cui, X. Zhou, W. Zhu, S.-j. Lee, K. Sarkar, G. Vozzi, Y. Tabata, J. Fisher, and L.G. Zhang, 4d Printing of Polymeric Materials for Tissue and Organ Regeneration. *Mater. Today*, **2017**. 20: p. 577-591.
22. Gantenbein, S., K. Masania, W. Woigk, J.P.W. Sesse, T.A. Tervoort, and A.R. Studart, Three-Dimensional Printing of Hierarchical Liquid-Crystal-Polymer Structures. *Nature*, **2018**. 561: p. 226-230.
23. Hausmann, M.K., P.A. R  hs, G. Siqueira, J. L  uger, R. Libanori, T. Zimmermann, and A.R. Studart, Dynamics of Cellulose Nanocrystal Alignment During 3d Printing. *ACS Nano*, **2018**. 12: p. 6926-6937.
24. Siqueira, G., D. Kokkinis, R. Libanori, M.K. Hausmann, A.S. Gladman, A. Neels, P. Tingaut, T. Zimmermann, J.A. Lewis, and A.R. Studart, Cellulose Nanocrystal Inks for 3d Printing of Textured Cellular Architectures. *Adv. Funct. Mater.*, **2017**. 27: p. 1604619.
25. H  kansson, K.M.O., A.B. Fall, F. Lundell, S. Yu, C. Krywka, S.V. Roth, G. Santoro, M. Kvik, L. Prahl Wittberg, L. W  gberg, and L.D. S  derberg, Hydrodynamic Alignment and Assembly of Nanofibrils Resulting in Strong Cellulose Filaments. *Nat Commun*, **2014**. 5.
26. Mart  nez   vila, H., S. Schwarz, N. Rotter, and P. Gatenholm, 3d Bioprinting of Human Chondrocyte-Laden Nanocellulose Hydrogels for Patient-Specific Auricular Cartilage Regeneration. *Bioprinting*, **2016**. 1-2: p. 22-35.
27. Rees, A., L.C. Powell, G. Chinga-Carrasco, D.T. Gethin, K. Syverud, K.E. Hill, and D.W. Thomas, 3d Bioprinting of Carboxymethylated-Periodate Oxidized Nanocellulose Constructs for Wound Dressing Applications. *Biomed Res Int*, **2015**. 2015: p. 925757.
28. Leppiniemi, J., P. Lahtinen, A. Paajanen, R. Mahlberg, S. Mets  -Kortelainen, T. Pinomaa, H. Pajari, I. Vikholm-Lundin, P. Pursula, and V.P. Hytonen, 3d-Printable Bioactivated Nanocellulose-Alginate Hydrogels. *ACS Appl Mater Interfaces*, **2017**. 9: p. 21959-21970.
29. Li, V.C.F., A. Mulyadi, C.K. Dunn, Y. Deng, and H.J. Qi, Direct Ink Write 3d Printed Cellulose Nanofiber Aerogel Structures with Highly Deformable, Shape Recoverable, and Functionalizable Properties. *ACS Sustainable Chem. Eng.*, **2018**. 6: p. 2011-2022.
30. H  kansson, K.M.O., I.C. Henriksson, C. de la Pe  a V  zquez, V. Kuzmenko, K. Markstedt, P. Enoksson, and P. Gatenholm, Solidification of 3d Printed Nanofibril Hydrogels into Functional 3d Cellulose Structures. *Adv. Mater. Technol.*, **2016**. p. 1600096-n/a.
31. Markstedt, K., A. Mantas, I. Tournier, H. Mart  nez   vila, D. H  gg, and P. Gatenholm, 3d Bioprinting Human Chondrocytes with Nanocellulose-Alginate Bioink for Cartilage Tissue Engineering Applications. *Biomacromolecules*, **2015**. 16: p. 1489-1496.

32. Li, V.C.-F., X. Kuang, A. Mulyadi, C.M. Hamel, Y. Deng, and H.J. Qi, 3d Printed Cellulose Nanocrystal Composites through Digital Light Processing. *Cellulose*, **2019**. 26: p. 3973-3985.
33. Pattinson, S.W. and A.J. Hart, Additive Manufacturing of Cellulosic Materials with Robust Mechanics and Antimicrobial Functionality. *Adv. Mater. Technol.*, **2017**. 2: p. 1600084.
34. Li, V.C.-F., C.K. Dunn, Z. Zhang, Y. Deng, and H.J. Qi, Direct Ink Write (Diw) 3d Printed Cellulose Nanocrystal Aerogel Structures. *Sci. Rep.*, **2017**. 7: p. 8018.
35. Compton, B.G. and J.A. Lewis, 3d-Printing of Lightweight Cellular Composites. *Adv Mater*, **2014**. 26: p. 5930-5.
36. Hansen, C.M., Hansen Solubility Parameters: A User's Handbook. Second edition 2007, Boca Raton FL: CRC Press, Inc., .
37. Hansen, C.M., The Three Dimensional Solubility Parameter and Solvent Diffusion Coefficient: Their Importance in Surface Coating Formulation. 1967: Danish Technical Press.
38. Reid, M.S., M. Villalobos, and E.D. Cranston, Cellulose Nanocrystal Interactions Probed by Thin Film Swelling to Predict Dispersibility. *Nanoscale*, **2016**. 8: p. 12247-12257.
39. Peng, S.X., H. Chang, S. Kumar, R.J. Moon, and J.P. Youngblood, A Comparative Guide to Controlled Hydrophobization of Cellulose Nanocrystals Via Surface Esterification. *Cellulose*, **2016**. 23: p. 1825-1846.
40. Gårdebjer, S., M. Andersson, J. Engström, P. Restorp, M. Persson, and A. Larsson, Using Hansen Solubility Parameters to Predict the Dispersion of Nano-Particles in Polymeric Films. *Polym. Chem.*, **2016**. 7: p. 1756-1764.
41. Charles Bruel, Q.B., Jason R. Tavares, Pierre J. Carreau, Marie-Claude Heuzey, The Apparent Structural Hydrophobicity of Cellulose Nanocrystals. *J-FOR*, **2018**. 7.
42. Yoo, Y. and J.P. Youngblood, Green One-Pot Synthesis of Surface Hydrophobized Cellulose Nanocrystals in Aqueous Medium. *ACS Sustainable Chem. Eng.*, **2016**. 4: p. 3927-3938.
43. Jie, X., Y. Cao, J.-J. Qin, J. Liu, and Q. Yuan, Influence of Drying Method on Morphology and Properties of Asymmetric Cellulose Hollow Fiber Membrane. *Journal of Membrane Science*, **2005**. 246: p. 157-165.
44. Kolker, A.M., V.P. Korolev, and D.V. Batov, Relationship between the Internal Pressure and Cohesive Energy Density of Liquids. *Journal of Structural Chemistry*, **2005**. 46: p. 927-930.
45. Bruel, C., J.R. Tavares, P.J. Carreau, and M.-C. Heuzey, The Structural Amphiphilicity of Cellulose Nanocrystals Characterized from Their Cohesion Parameters. *Carbohydr. Polym.*, **2019**. 205: p. 184-191.
46. Marcus, Y., Relationships between the Internal Pressure, the Cohesive Energy, and the Surface Tension of Liquids. *Physics and Chemistry of Liquids*, **2017**. 55: p. 522-531.
47. Dack, M., Solvent Structure. The Use of Internal Pressure and Cohesive Energy Density to Examine Contributions to Solvent-Solvent Interactions. *Australian Journal of Chemistry*, **1975**. 28: p. 1643-1648.
48. Heckel, R., Density-Pressure Relationships in Powder Compaction. *Trans Metall Soc AIME*, **1961**. 221: p. 671-675.
49. Panelli, R. and F. Ambrozio Filho, Compaction Equation and Its Use to Describe Powder Consolidation Behavior. *Powder Metallurgy*, **1998**. 41: p. 131-133.

50. Thibaut, C., A. Denneulin, S. Rolland du Roscoat, D. Beneventi, L. Orgéas, and D. Chaussy, A Fibrous Cellulose Paste Formulation to Manufacture Structural Parts Using 3d Printing by Extrusion. *Carbohydr. Polym.*, **2019**. 212: p. 119-128.
51. Zeng, Y., M.E. Himmel, and S.-Y. Ding, Visualizing Chemical Functionality in Plant Cell Walls. *Biotechnol. Biofuels*, **2017**. 10: p. 263.
52. Chen, S., G. Schueneman, R.B. Pipes, J. Youngblood, and R.J. Moon, Effects of Crystal Orientation on Cellulose Nanocrystals–Cellulose Acetate Nanocomposite Fibers Prepared by Dry Spinning. *Biomacromolecules*, **2014**. 15: p. 3827-3835.
53. Beck-Candanedo, S., M. Roman, and D.G. Gray, Effect of Reaction Conditions on the Properties and Behavior of Wood Cellulose Nanocrystal Suspensions. *Biomacromolecules*, **2005**. 6: p. 1048-54.
54. Saito, T. and A. Isogai, Tempo-Mediated Oxidation of Native Cellulose. The Effect of Oxidation Conditions on Chemical and Crystal Structures of the Water-Insoluble Fractions. *Biomacromolecules*, **2004**. 5: p. 1983-1989.
55. Weishaupt, R., G. Siqueira, M. Schubert, P. Tingaut, K. Maniura-Weber, T. Zimmermann, L. Thöny-Meyer, G. Faccio, and J. Ihssen, Tempo-Oxidized Nanofibrillated Cellulose as a High Density Carrier for Bioactive Molecules. *Biomacromolecules*, **2015**. 16: p. 3640-3650.
56. Standard Test Methods for Flexural Properties of Unreinforced and Reinforced Plastics and Electrical Insulating Materials.

Chapter 5.

Cellulose-based microparticles for magnetically-controlled optical modulation and sensing

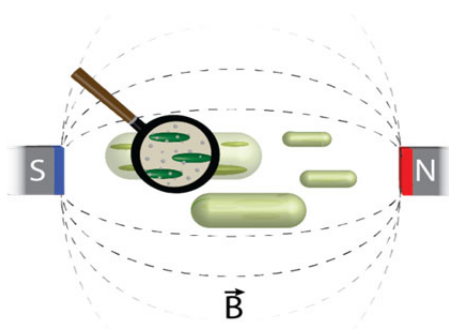
Michael K. Hausmann^{1,3}, Alina Hauser^{1,3}, Gilberto Siqueira^{1*}, Rafael Libanori^{3*}, Signe Lin Vehusheia³, Simone Schürle², Tanja Zimmermann¹, André R. Studart^{3*}

¹ Empa, Swiss Federal Laboratories for Materials Science and Technology, Cellulose & Wood Materials Laboratory, 8600 Dübendorf, Switzerland

² Institute for Translational Medicine, Department of Health Science and Technology, ETH Zurich, 8092 Zurich, Switzerland

³ Complex Materials, Department of Materials, ETH Zurich, 8093 Zurich, Switzerland

This chapter has been submitted to *Small*, 2019



5.1 Abstract

Responsive materials with birefringent optical properties have been exploited for the manipulation of light in several modern electronic devices. While electrical fields are often utilized to achieve optical modulation, magnetic stimuli may offer an enticing complementary approach to control and manipulate light remotely. Here, we report on the synthesis and characterization of magnetically-responsive birefringent microparticles with unusual magneto-optical properties. These functional microparticles are prepared via a microfluidic emulsification process, in which water-based droplets are generated in a flow-focusing device and stretched into anisotropic shapes before conversion into particles via photopolymerization. Birefringence properties are achieved by aligning cellulose nanocrystals (CNCs) within the microparticles during droplet stretching, whereas magnetic responsiveness results from the addition of superparamagnetic nanoparticles (SPIONs) to the initial droplet template. When suspended in a fluid, the microparticles can be controllably manipulated via an external magnetic field to result in unique magneto-optical coupling effects. Using a remotely actuated magnetic field coupled to a polarized optical microscope, we show how these microparticles can be employed to convert magnetic into optical signals or to estimate the viscosity of the suspending fluid through magnetically-driven microrheology.

5.2 Introduction

Controlling the optical properties of materials with an external source of energy forms the basis of a wide range of display, laser and data transmission technologies present in modern life.^{1, 2} In most of these applications, an external electrical field is used either to change the electrical permittivity of the material along specific directions or to manipulate pigment particles in a suspending fluid to create color. Electrical fields in the form of an action potential are also used by living organisms for camouflaging optical effects induced by the deliberate contraction of pigment-laden cells.³⁻⁵ As an alternative to electrical stimuli, magnetic fields have also been explored to change the optical properties of materials both at the molecular level^{6, 7} as well as at the colloidal scale.⁸⁻¹² Although less explored than their electrical counterparts, magnetic systems offer as main advantages the possibility of contactless remote manipulation, the potentially stronger forces generated in field gradients, and the higher penetration depth in a variety of liquids and solids.

The ability to combine magnetic and optically-active building blocks in the same system makes composite particles suspended in a fluid an attractive platform for the development of magnetically-tunable optical devices. To change the optical properties of the suspensions on demand, two specific requirements have to be fulfilled. First, the dispersed particles need to be made magnetically-responsive to thus translate or rotate when exposed to the external magnetic field. Second, the translation or rotation of the particles must affect the optical properties of the suspension such as to achieve a color change. The first requirement can be easily fulfilled by adding magnetic nanoparticles to the system.¹³⁻¹⁶ However, the usual dark color of magnetic materials reduces the transparency of the suspension. This can be tackled by decreasing the concentration of magnetic material to levels that ensure enough optical transmittance. Since magnetic forces scale linearly with the volume of the particle, a low concentration of magnetic material can be compensated by forming larger microparticles that in turn become increasingly responsive to external fields. The second requirement concerning the color change can be met by orienting anisotropic particles in a specific direction to vary the total cross-sectional area of particles that is exposed to the incoming light. Following this approach, mirror-like aluminum flakes dispersed in a diluted ferrofluid were magnetically manipulated to change from light to dark the color of a display-like prototype.¹⁷ In another system, magnetically-responsive composite platelets suspended in a fluid were used to change the color of the resulting suspension depending on the direction of the externally applied magnetic field.^{14, 18} Color changes in these examples are achieved via orientation-dependent light absorption, fluorescence¹⁸ or reflection¹⁷ phenomena.

In spite of the various types of light-matter interactions that have been exploited so far, current particle-based systems do not allow for control of the polarization of light using magnetic fields. Polarized light is widely used in liquid crystal displays (LCDs), photography filters, and glasses to dynamically change color, remove undesired glare or achieve

stereoscopic effects for 3D visualization.^{19, 20} In LCDs, rod-shaped molecules are electrically-oriented in specific directions to block or partially transmit light travelling between cross-polarizers, thus allowing for dynamic color and brightness control. This widespread concept relies on the birefringent nature of the electrically-responsive liquid crystalline molecules placed at the core of the display. Besides these everyday technologies, polarized light is also used by flying and marine animals, such as bees, octopus and shrimps, for communication, vision and navigation in the natural world.^{3, 21-25} Given the widespread use of polarized light in synthetic and biological systems, new mechanisms of control of light polarization may have important implications in a broad range of research fields and technologies.

In this paper, we report on the design, synthesis and characterization of composite microparticles that enable control of light polarization using an external magnetic field. Similar to the rod-shaped molecules used in liquid crystal displays, cellulose nanocrystals (CNCs) are used as birefringent building blocks inside the microparticles to manipulate light polarization (Figure 5.1a). To render the microparticles responsive to magnetic fields, the CNC building blocks are combined with small concentrations of superparamagnetic iron oxide nanoparticles (SPIONs). Such composite microparticles are produced using liquid droplet templates that are elongated in microfluidic tubes to generate the birefringent properties required for polarization control (Figure 5.1b, c). The detailed synthesis of these functional microparticles is presented below, followed by an evaluation of their geometrical and optical properties. Finally, the response of CNC-laden particles to magnetic fields is studied to illustrate the potential of the proposed system as a means to achieve optical modulation or perform microrheological measurements using contactless, remote magnetic stimuli.

5.3 Results and discussion

Composite microparticles with birefringent properties are created from water-based droplet templates generated in a microfluidic platform (Figure 5.1b, c and Figure D. 1). The microfluidic platform is built from glass capillaries, which are arranged to form water-in-oil droplets using the flow-focusing approach.²⁶⁻²⁸ In this setup, the inner aqueous phase is pumped through a cylindrical capillary, which is encased in a concentric square capillary that hosts the flowing outer oil phase. Flow-focusing is induced at the tip of the inner capillary, resulting in the breakup of the aqueous phase into monodisperse droplets of water suspended in the continuous oil phase. Water-soluble monomers are added to the droplets to enable their conversion into microparticles upon UV irradiation. A hexadecane solution containing the surfactant polyglycerol polyricinoleate (PGPR) is used as the outer oil phase. To ensure the formation of monodisperse droplets, the flow rates of the inner and outer phases were adjusted until the conditions for dripping-controlled emulsification were achieved.

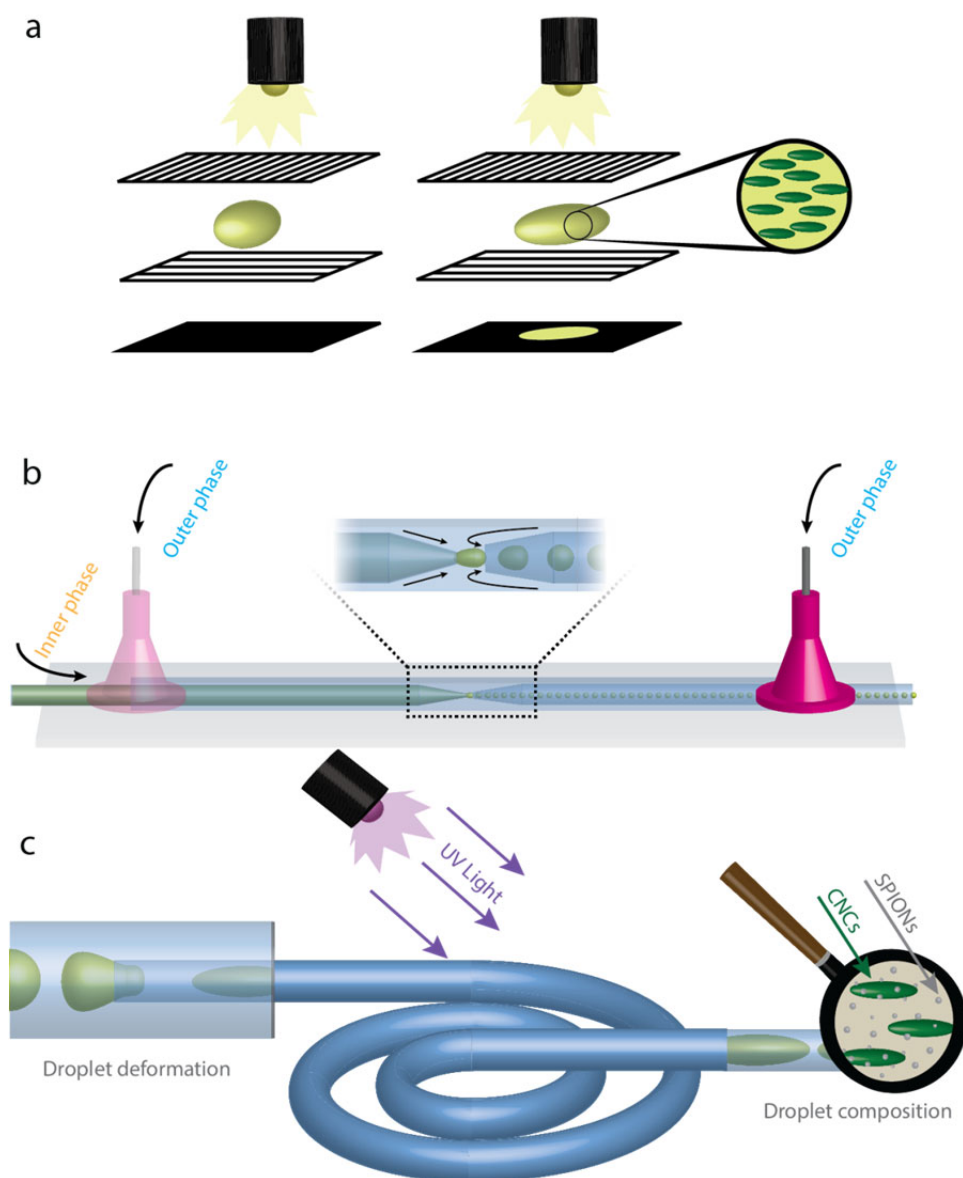


Figure 5.1 Birefringent properties and microfluidic assembly of microparticles containing cellulose nanocrystals (CNCs). (a) Schematic illustration of a display-like functional device in which the orientation of a birefringent CNC-laden microparticle is used to control the intensity of light transmitted through cross-polarizers. (b) Capillary-based microfluidic device used for the creation of CNC-laden magnetic microparticles from water-in-oil emulsions. (c) Spiraling cylindrical tube utilized to elongate the emulsion droplets before consolidation into anisotropic microparticles by UV-induced polymerization.

Microparticles that are simultaneously birefringent and magnetically responsive are obtained by loading such monomer-containing droplets with both CNC nanoparticles and SPIONs. Because the CNC nanoparticles do not show a preferential orientation in the aqueous phase, the freshly-formed droplets are pushed into a long polyethylene tube of smaller diameter to align the birefringent nanocrystals before UV polymerization. Alignment results from the extensional forces developed inside the droplet as it is stretched inside the tube. This leads to microparticles with birefringent behaviour after polymerization. To keep the aqueous phase sufficiently fluid for microfluidic emulsification while ensuring a strong

birefringent response, CNC concentrations in the range of 4-10 wt % were used (Figure D. 2). Another important role of the small-diameter tube is to deform the originally spherical droplets into an elongated rod-like geometry that is preserved in the microparticles upon UV irradiation. This anisotropic shape allows for rotation of the SPION-laden microparticle using an external magnetic field, giving rise to the coupled magneto-optical response.

The birefringent properties of the microparticles rely on the quick polymerization of the monomer-containing aqueous droplet while it is stretched inside the small-diameter tube. Fast curing of the monomer preserves the anisotropic shape of the microparticles and prevents the misalignment of the CNC nanoparticles by Brownian motion when the droplet exits the tube. To ensure that the curing timescale is shorter than the residence time of the droplet in the tube, we indirectly quantified the polymerization kinetics of the monomer-containing aqueous phase through bulk rheological measurements of CNC suspensions with the same composition as that of the droplet (Figure 5.2a). Measurements were performed by tracking the storage and loss moduli of the suspension under a fixed amplitude strain of 1%. The curing timescale was determined as the time elapsed between the moment when the UV illumination was turned on and the time point at which the storage modulus surpasses the loss modulus of the suspension. The results show that aqueous monomer suspensions containing 8wt% CNC cure within approximately 12.5 seconds. The addition of ~2 wt % SPIONs to this CNC suspension was found to increase this timescale to 35 seconds, which is explained by the high light absorption characteristics of the iron oxide particles (Figure 5.2a, b). Because of the longer timescale required to polymerize the SPION-containing droplets, their residence time in the tube was increased by at least a factor of 3 compared to those typically employed for the preparation of SPION-free particles. This was accomplished by using a collecting tube with up to 30 cm in length.

The *in-situ* stretching of droplets inside the smaller-diameter tube enables the preparation of microparticles with controlled aspect ratio after the polymerization step. By varying the flow rate of the continuous phase and using tubes with diameters of 0.20 and 0.28 mm, we obtained anisotropic microparticles with aspect ratio covering a broad range between 1.6 and 12.9 (Figure 5.2c, Figure D. 3, Figure D. 4 and Table D. 1). The alignment of CNCs inside such droplets leads to microparticles with strong birefringence response (Figure 5.2d). This is readily observed when microparticles are placed in a light microscope under cross polarizers. Depending on the orientation of the microparticle relative to the direction of the polarizer/analyzer, distinct intensities of light are transmitted through the CNC-laden material. As expected, maximum intensity is observed when the microparticle is oriented at an angle of 45°, whereas full extinction of light is found when the microparticle's long axis coincides with the direction of the polarizer.²⁹ If the droplets are intentionally made long enough to generate curved microparticles after polymerization, both dark and bright regions can be observed in the same microparticle under cross polarizers. (Figure 5.2d). For comparison, the polymerization of droplets that were not stretched in the microfluidic tube

led to spherical microparticles with ill-defined optical transmittance under cross-polarizers (Figure D. 5).

Besides the unique birefringent optical properties, the presence of SPIONs in the CNC-laden microparticles makes them responsive to an external magnetic field (Figure 5.2e). When immersed in a fluid, the microparticles can be deliberately oriented along the direction of the imposed uniform magnetic field. Changes in the field direction lead to re-alignment of the microparticles within a timescale that depends on the viscosity of the surrounding fluid as well as the dimensions and the magnetization of the particle (Figure 5.2f). Alignment experiments using aqueous solutions with different concentrations of glycerol show that the timescale needed for particle re-orientation is linearly proportional to the viscosity (η) of the fluid for η values in the range of 0.01 – 0.05 Pa.s. This scaling suggests that the rotational motion of the investigated microparticle is controlled by the viscous forces exerted by the fluid, as expected in a dampened mechanical system.

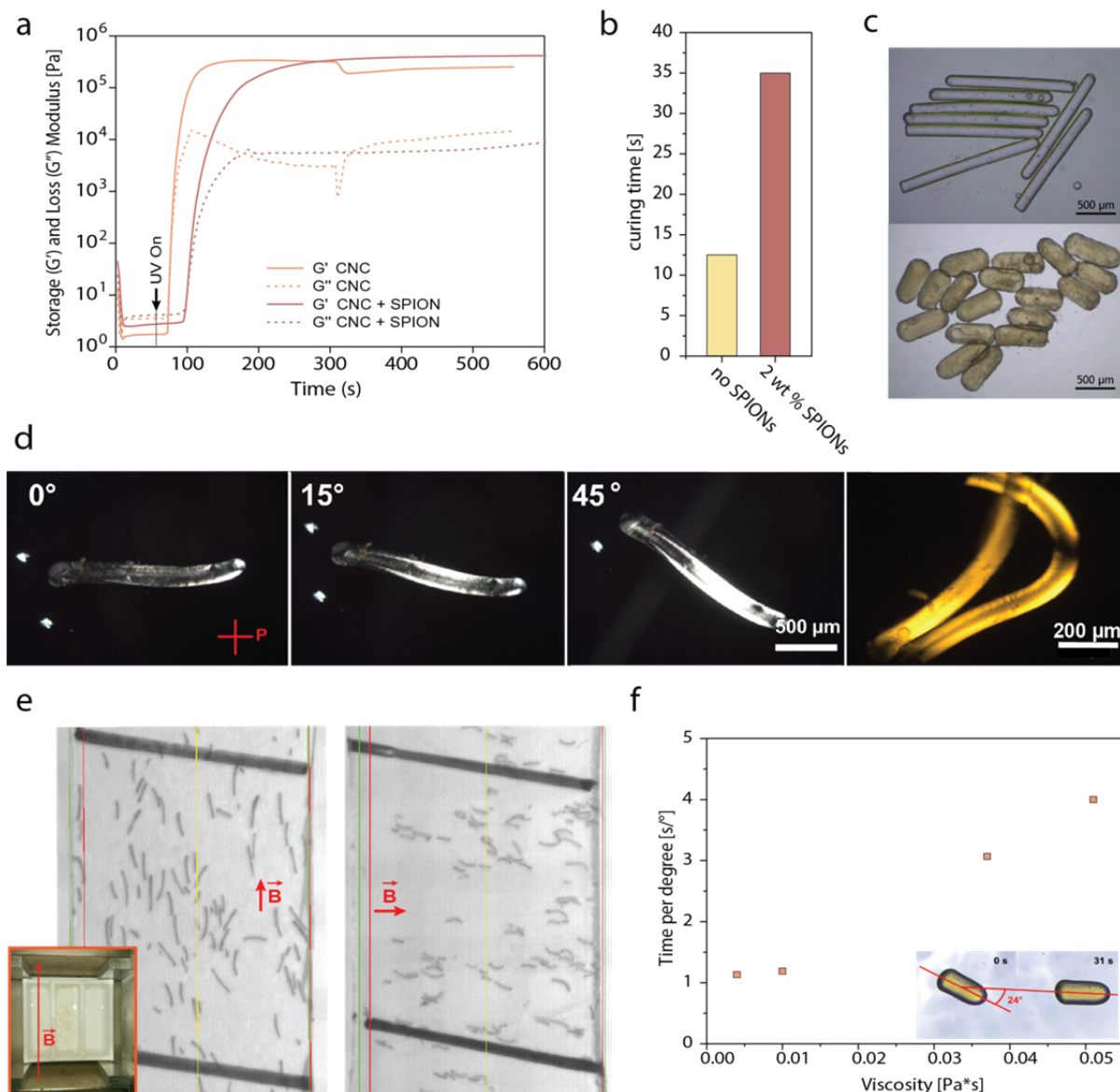


Figure 5.2 Polymerization kinetics of CNC-laden suspensions and magnetically-responsive birefringent microparticles. (a) Oscillatory rheological measurements used to quantify the polymerization kinetics of aqueous suspensions containing CNC nanoparticles, monomers and initiator in the presence or not of superparamagnetic iron oxide nanoparticles (SPIONs). (b) Effect of 2 wt % SPIONs on the timescale required for curing of the suspensions under UV light. (c) Examples of anisotropic microparticles with different aspect ratios produced through elongation of the liquid droplets. (d) Cross-polarized optical microscopy of CNC-laden microparticles, indicating the birefringent properties arising from the presence of aligned cellulose nanocrystals. (e) Magnetic orientation control of microparticles loaded with CNCs and SPIONs. The vector \vec{B} indicates the direction of the external magnetic field. The inset image shows the macroscopic setup used for magnetic manipulation, in which a permanent magnet is positioned on the side of a tray containing suspended microparticles. (f) Averaged timescale needed to magnetically change the orientation of the microparticle suspended in fluids of distinct viscosities. The inset image shows an example of the raw data obtained in such an experiment for particles under a magnetic field of 5170 A/m.

We exploit these combined magnetic and birefringent responses to create functional microparticles that can translate magnetic into optical signals. To demonstrate this functionality, we designed an experiment in which we record the light transmitted through a single microparticle when it is exposed to a rotating input magnetic field between cross-

polarizers (Figure 5.3). In this setup, the microparticle is suspended in an aqueous-based Newtonian fluid with tunable viscosity. The rotating magnetic field was applied using a set of solenoids assembled around the sample holder under an optical microscope (Figure 5.3a).^{30, 31} Input currents with sinusoidal wavefunction of frequency ω_{mag} and pre-defined offsets were applied to the solenoids to create the rotating external field. The input rotating field was represented by the variation of its x- and y-components over time, whereas the output signal was obtained by tracking the light transmitted through the magneto-responsive microparticle. Snapshots of the microparticle taken during a quarter of a full period ($0.25/\omega_{mag}$) show that full brightness occurs when the long axis of the particle lies at an angle of $\pi/4$ relative to the axes of the polarizers (Figure 5.3b). Plotting the intensity of the transmitted light over two full rotations nicely demonstrates the ability of the functional microparticle to translate a magnetic input signal into a well-defined optical output (Figure 5.3c, d). Because a bright light signal is observed in every quarter of a full period, the output optical signal oscillates at a frequency ω_{opt} that is 4 times higher than that of the rotating magnetic input (ω_{mag}).

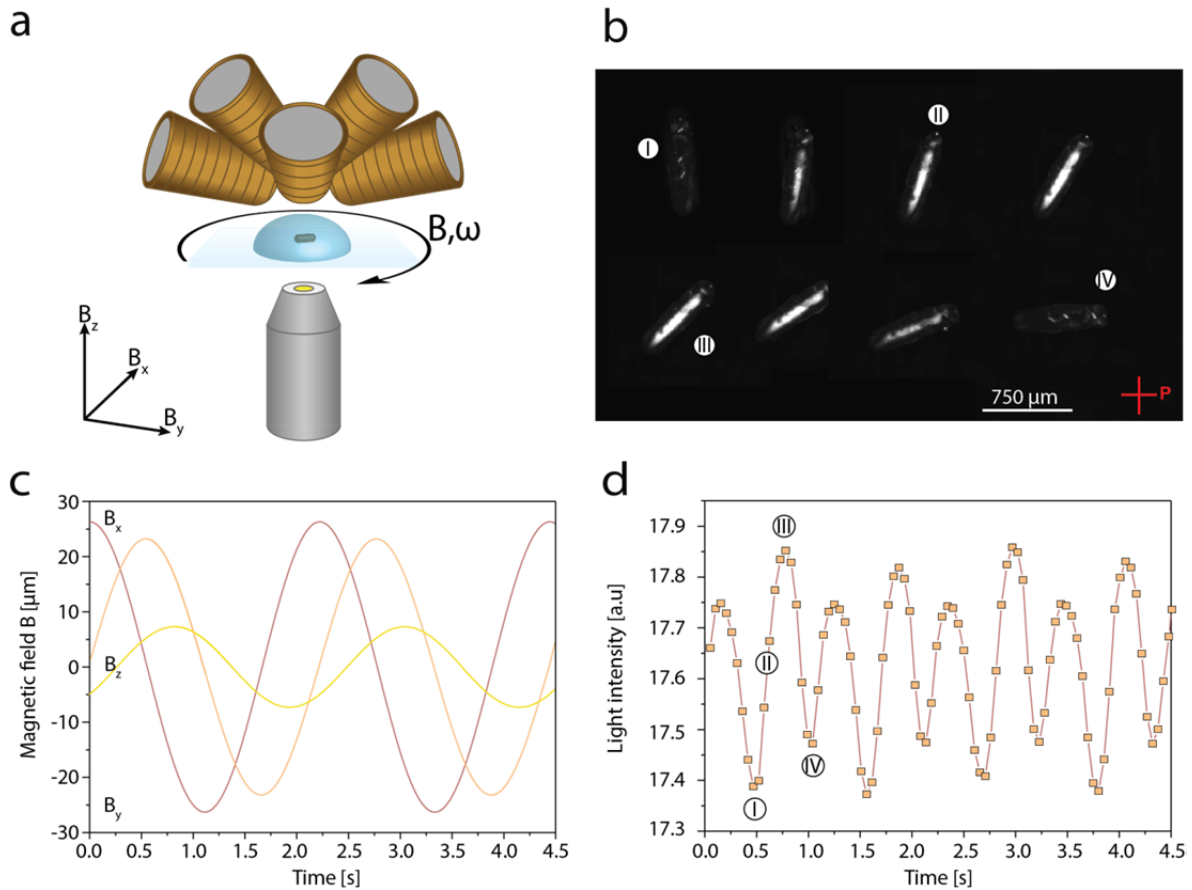


Figure 5.3 Magneto-optical coupling enabled by the CNC-laden birefringent microparticles. (a) Experimental setup used for optical imaging of an individual microparticle when subjected to a rotating in-plane magnetic field.³¹ (b) Cross-polarized optical images obtained from an individual microparticle at distinct magnetically-controlled orientations. (c) Temporal evolution of the magnetic field used as input signal to move the suspended CNC-laden microparticle. In this example, an oscillating frequency (ω_{mag}) of 0.45 Hz was used. A low magnitude magnetic field in the out-of-plane

direction (B_z) helped counteract the gravitational force and thus keep the microparticle suspended in the fluid. (d) Optical response of the microparticle subjected to the oscillating magnetic field shown in (c). This output optical signal corresponds to the total intensity of light transmitted through the cross-polarizers. Roman algorithms are used to correlate the optical data with the snapshots displayed in (b).

Coupling between the magnetic and optical signals is observed as long as the rotating magnetic field of fixed amplitude is sufficiently slow to allow for the microparticle to follow its motion (Figure 5.4a). That is because the suspending fluid exerts a drag force that opposes the motion of the microparticle along the rotating magnetic field vector. Due to this drag force, the oscillating optical output lags behind the imposed magnetic input signal. The resulting phase lag increases with the increase in the frequency of the applied magnetic field until a critical frequency $\omega_{mag,c}$, also called “step-out” frequency, is achieved. At the step-out frequency, the microparticles can no longer follow the imposed magnetic field, leading to decoupling between the magnetic and optical signals. For CNC-laden magnetic microparticles suspended in water, such decoupling was experimentally observed to occur when the frequency of the applied magnetic field reaches approximately 0.55 Hz (Figure 5.4a).

The critical frequency $\omega_{mag,c}$ depends on the physical forces acting on the microparticle under the imposed magnetic field. Assuming the motion of the microparticle in the coupled regime to be dominated by magnetic and viscous drag forces, one can estimate the critical frequency $\omega_{mag,c}$ from a simple torque balance, as follows:^{32, 33}

$$\omega_{mag,c} = \frac{\mu_0 \chi^2 H_0^2}{18(f/f_0)\eta(\chi + 2)} \quad Eq. 1$$

where H_0 is the amplitude of the applied magnetic field, χ is the magnetic susceptibility of the microparticle, η is the viscosity of the suspending fluid, μ_0 is the magnetic permeability of free space ($\mu_0 = 4\pi * 10^{-7}$ H/m) and f/f_0 is the Perrin friction factor. The magnetic susceptibility, χ , is given by $\chi_f \phi_f$, where χ_f and ϕ_f are the magnetic susceptibility and the volume fraction of SPIONs, respectively.

To test the validity of this simple torque balance in describing the dynamics of the CNC-laden microparticles under a rotating magnetic field, we use the above relation to predict the magnetic susceptibility of the SPIONs (χ_{ff}) based on experimental measurements of the other relevant parameters (Appendix D4). Our calculation lead to a χ_{ff} value of 21.2, which agrees very well with the SPION magnetic susceptibility of 21 previously reported in the literature.³² This indicates that the motion of the microparticle seems to be indeed controlled by a balance between magnetic and viscous forces.

The torque balance above also predicts an inverse dependence between the critical frequency, $\omega_{mag,c}$ and the viscosity of the suspending fluid, η . This offers the possibility to predict the viscosity of a fluid using the CNC-based microparticles as microrheological probes. To demonstrate this functionality, we measured the critical frequency for an individual microparticle suspended in a series of fluids of distinct viscosities (Figure 5.4b-d). The experimental results show a two-fold decrease in the critical frequency when the fluid viscosity is increased from 0.9 to 2.1 mPa.s. Plotting the measured data in a double logarithmic graph, we find that the critical frequency scales with $\eta^{-0.85}$. Such scaling is reasonably close to the relation $\omega_{mag,c} \sim \eta^{-1}$ expected from the torque balance, suggesting that this simple analytical model provides a good first approximation of the viscosity of the suspending fluid. Although our experimental demonstration is focused on the steady-state analysis of simple Newtonian fluids, more sophisticated models and experimental protocols can be envisioned to assess the microrheology of complex fluids using our magneto-optical probes. By measuring for example the phase-lag of the microprobe when subjected to small oscillatory strains, the proposed magneto-optic microparticles can potentially be used to remotely assess the viscoelastic properties of fluids.

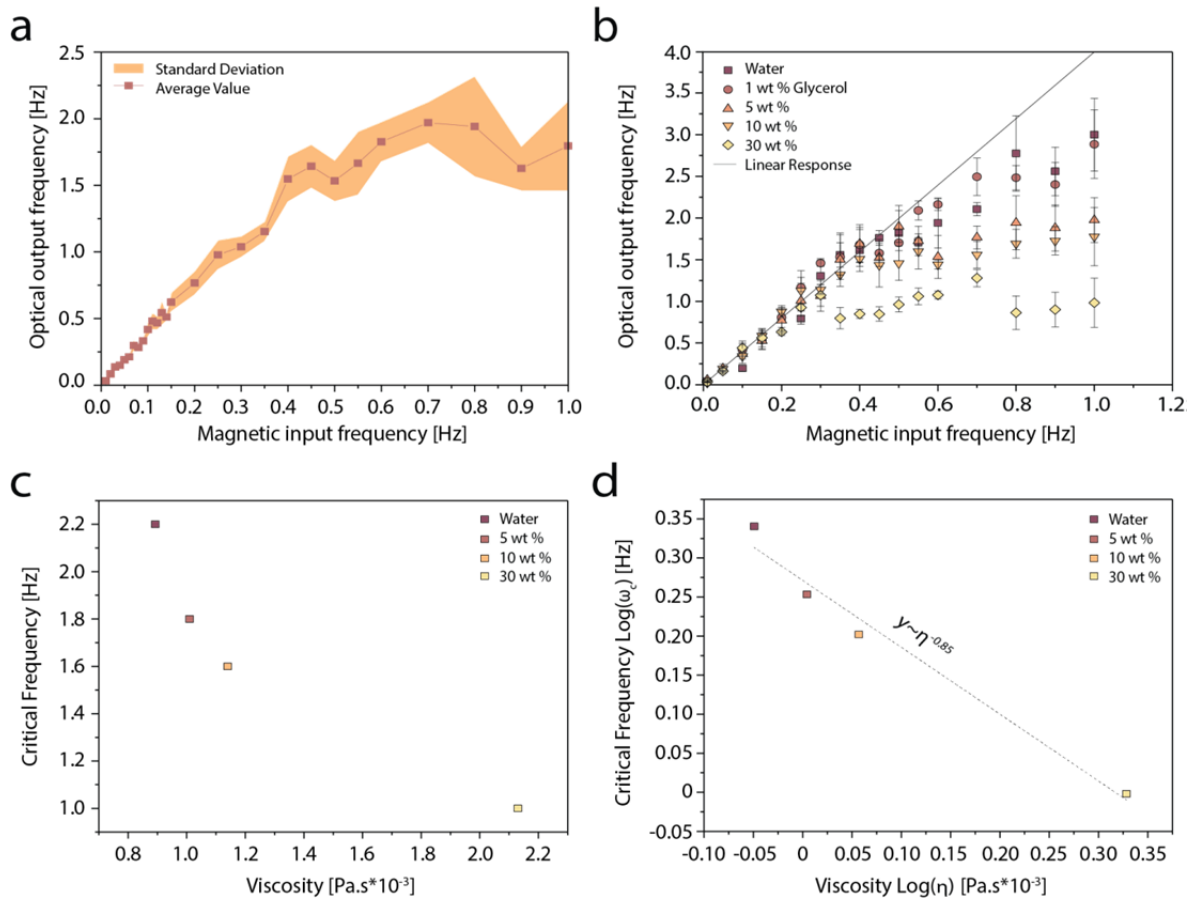


Figure 5.4 Correlation between optical and magnetic signals when CNC-laden microparticles are used as rheological microprobes. (a) Linear relation between the frequency of the input magnetic signal and the frequency of the optical output data up until the critical frequency $\omega_{mag,c}$ is reached. In this example, microparticles containing 8 wt% CNCs and 2 wt% SPIONs are suspended in water and are optically imaged while exposed to an oscillating magnetic field of increasing

frequency. (b) Magneto-optical frequency correlation for an individual microparticle suspended in aqueous solutions with different glycerol concentrations. (c) Dependence of the critical frequency $\omega_{mag,c}$ on the viscosity of the glycerol-containing aqueous solutions. (d) Double logarithmic plot showing the scaling relation between the critical frequency and the viscosity of the suspending fluid.

5.4 Conclusions

Magnetically-responsive birefringent microparticles with unique magneto-optical coupling properties can be created from liquid droplet templates in a microfluidic platform. Such functional microparticles are made through the elongation followed by polymerization of water droplets loaded with cellulose nanocrystals (CNCs), superparamagnetic iron oxide nanoparticles (SPIONs) and a reactive monomer system. The birefringent properties of the microparticles result from the flow-induced alignment of the CNCs during elongation of the droplets in a microfluidic tube. In addition to birefringence, anisotropic microparticles with tunable aspect ratio can be produced by controlling the degree of droplet elongation after emulsification. The microparticle's magnetic response arises from the presence of iron oxide nanoparticles in the initial droplet template. The use of a small SPION concentration of up to 2 wt % leads to strong magnetic response while keeping light absorption by the iron oxide sufficiently low to not affect the photopolymerization process. When suspended in a fluid, the resulting microparticle can be magnetically manipulated using relatively low external fields, providing a unique mechanism to remotely control light. Because of their combined magnetic and birefringent properties, the microparticles are able to directly translate an oscillating input magnetic stimulus into an output optical signal with well-defined frequency. This coupled response is valid up to a critical frequency, above which high viscous forces prevent the microparticles from rotating with the external magnetic field. The magneto-optical coupling effect at sufficiently low frequencies allows one to exploit the microparticles either to modulate optical data or to sense the local rheological properties of a fluid using a remote external magnetic field. This functionality may find interesting applications in display technologies, micro-rheological analysis and camouflaging systems.

5.5 Experimental methods

5.5.1 Materials

The monomers acrylamide ($M_w = 71.08$ g/mol) and N,N'-methylenebisacrylamide ($M_w = 154.17$ g/mol) were purchased from Fluka BioChemika. Hydroxy-4'-(2-hydroxyethoxy)-2-methylpropiophenone (HHMPP – Irgacure 2959), hexadecane (99 %), trimethoxy(octadecyl)silane (ODTMS – 90 %) and butylamine (99 %) were acquired from Sigma Aldrich. Polyglycerol-polyricinoleate (PGPR – Nutrition Biosciences) was obtained from DuPont, whereas the superparamagnetic iron oxide nanoparticles (SPIONs, type EMG 605) were purchased from FerroTech. Cellulose nanocrystals (CNCs 0.98 wt% sulfur content) were prepared via sulfuric acid hydrolysis of eucalyptus pulp at the USDA Forest Service – Forest products Laboratory (Madison, WI), according to a previously published procedure.³⁴

5.5.2 Preparation of CNC suspensions

The aqueous suspensions used to generate the magnetic and birefringent microparticles contained water, CNCs, monomers, photoinitiator and SPIONs. The concentration of CNCs in these suspensions was varied between 6 and 10 wt%, whereas the total amount of monomers was held constant at 25 wt % of the total suspension mass. Suspensions were prepared by first adjusting the pH of deionized water to 9 by adding 0.1 M solution of NaOH. This was required to ensure the colloidal stability of the SPIONs in the aqueous suspension. SPIONs were then incorporated by adding 2 wt % of EMG 605 suspension to the aqueous solution, followed by homogenization for 5 min in an ultrasound bath. The CNCs were added to the suspension using a speed mixer running at 2500 and 3500 rpm for 5 min at each speed (model DAC 150.1 FVZ). A monomer mixture comprising 21 wt % acrylamide and 4 wt % bis-acrylamide was afterwards added to the suspension, followed by another mixing step. Before filling the syringe used for microfluidic emulsification, 0.05 wt% of initiator (Irgacure 2959) was added to the suspension using a conditioning mixer (Thinky ARE-250) for 5 min at 2000 rpm followed by a 5 min degassing mixing at 2200 rpm.

5.5.3 Microfluidic emulsification

Glass capillary microfluidic devices were prepared according to established procedures previously reported in the literature.²⁶ Microfluidic emulsification was performed using an aqueous suspension of CNCs, SPIONs, monomers and initiator as inner phase. Droplets of such aqueous suspension were created by operating the device under flow-focusing dripping conditions using hexadecane as outer oil phase. The surfactant PGPR was added to the oil phase to stabilize the water-in-oil emulsions. The dimensions of the cylindrical glass capillaries were adjusted depending on the composition of the aqueous phase used as inner phase. For suspensions containing 6 wt% of CNCs, emitting and collecting capillaries with diameters of 226 μm and 435 μm , respectively, were used. These inner capillaries were assembled inside a squared outer capillary, keeping a distance of 69 μm between each other. Suspensions prepared with 8 and 10 wt% of CNCs were emulsified in devices featuring emitting and collecting capillaries with diameters of 223 μm and 320 μm , respectively. In this case, an inter-capillary spacing of 50 μm was utilized. The capillaries were hydrophobized using a solution of toluene containing 2 wt % ODTMS and 0.2 wt % butylamine. The ends of the emitting and collecting capillaries were connected to poly(tetrafluoroethylene) (PTFE) tubes with inner and outer diameters of 0.8 mm and 1.6 mm, respectively (Bola S1810-10). The inner and outer fluids were injected into the capillaries with the help of syringe pumps (Harvard apparatus). The flow rates of the inner and outer fluids were adjusted to ensure emulsification under dripping mode. The cylindrical PTFE tube used for droplet elongation displayed an inner diameter of 0.20 mm (Bola S1810-02) or 0.28 mm (Scientific commodities Inc., BB31695-PE). Such tube was wound into a spiral geometry and made long enough to ensure polymerization of the aqueous phase before exit of the droplet into a collecting bath. The spiraled tube was kept in a closed chamber

equipped with a UV light source for photopolymerization (365 nm wavelength, Omnicure Series 100, APM Technology, Switzerland). Care was taken to reduce the curvature of the spiral for the preparation of high aspect-ratio particles, which otherwise would keep the curved geometry of the tube. The spiral was partially submerged in cold water to avoid melting of the tube under UV light. The microfluidic setup was covered with aluminum to protect it from light and thus premature curing of the droplets. The particles were collected in an hexadecane bath, washed with deionized water and filtered with a metallic mesh of 50 μm pore size. The cured particles were rinsed several times prior to storing in deionized water.

5.5.4 Microscopy and image analysis

Polarized light images of the as-prepared microparticles were obtained with an optical microscope (Leica and Zeiss Axioplan) and were analyzed with ImageJ (Fiji software, Win64-bit). The alignment of CNCs inside the microparticles was assessed by rotating the sample holder from 0 ° to 45 °.

5.5.5 Rheology

Curing kinetics

Rheological measurements were performed to assess the curing kinetics of the aqueous suspensions containing 6 and 8 wt % CNCs with and without SPIONs. By using a rheological stage that allows for the transmission of UV light, measurements were conducted while the suspension was photopolymerized. The storage and loss moduli of the suspension were determined from oscillatory shear measurements with a fixed amplitude strain of 1% and frequency of 1 rad/s at 20 °C. Data were collected every 2.5 seconds for up to 10 minutes using a plate-plate geometry with 50 mm diameter and 0.5 mm gap distance between the plates. The UV light was turned on 60 seconds after the start of the measurement and the samples were kept under illumination until the end of the experiment.

Viscosity of the suspending fluids

The viscosity of the glycerol aqueous solutions used to suspend the functional microparticles was measured by steady-state shear rheology in a double gap cylindrical setup. Measurements were conducted by applying a shear rate sweep between 0.01 and 10 1/s with log-spaced intervals and 5 data points per decade. An equilibration time of 10 minutes was used before the start of each experimental run. Experiments were carried out at 20 °C until a total of 16 data points was collected. Aqueous solutions containing glycerol concentrations ranging from 10 to 90 wt% were characterized.

5.5.6 Magnetic manipulation of microparticles

The timescale required for alignment of the functional microparticles under an external magnetic field was assessed by suspending them in aqueous solutions with varying glycerol concentrations ranging from 10 to 50 wt%. After positioning the external magnet, the motion of the microparticle was tracked in an optical microscope (Leica, DMIL LED).

The dynamics of the microparticle when exposed to a rotating magnetic field was characterized using a set of solenoids (Magnebotix MFG100-1) mounted on an optical microscope (Nikon Eclipse Ti2). The amplitude of the applied magnetic field was fixed at 25 mT, whereas the rotation frequency was varied between 0.01 Hz to 1 Hz.

5.6 Acknowledgements

We thank D. Von Arx and N. Mirkhani for the scientific discussions and the support with the magnetic manipulation experiments using solenoids. We are also thankful to A. Ofner, D. Moore, M. Binelli, I. Mattich, E. Jeoffroy and P. Rühs for the helpful scientific discussions and for the support while using specific equipment. M.K.H and G.D.S greatly acknowledge the financial support from the Swiss National Science Foundation (grant 200021_159906/1). This work also benefitted from support from the Swiss National Science Foundation through the National Center of Competence in Research Bio-Inspired Materials.

5.7 References

1. Gibbons, W.M., P.J. Shannon, S.-T. Sun, and B.J. Swetlin, Surface-Mediated Alignment of Nematic Liquid Crystals with Polarized Laser Light. *Nature*, **1991**. 351: p. 49-50.
2. Drzaic, P.S., Polymer Dispersed Nematic Liquid Crystal for Large Area Displays and Light Valves. *Journal of Applied Physics*, **1986**. 60: p. 2142-2148.
3. Duarte Rafael, C., A.V. Flores Augusto, and M. Stevens, Camouflage through Colour Change: Mechanisms, Adaptive Value and Ecological Significance. *Philosophical Transactions of the Royal Society B: Biological Sciences*, **2017**. 372: p. 20160342.
4. Deravi, L.F., A.P. Magyar, S.P. Sheehy, G.R.R. Bell, L.M. Mäthger, S.L. Senft, T.J. Wardill, W.S. Lane, A.M. Kuzirian, R.T. Hanlon, E.L. Hu, and K.K. Parker, The Structure-Function Relationships of a Natural Nanoscale Photonic Device in Cuttlefish Chromatophores. *J R Soc Interface*. 11: p. 20130942-20130942.
5. Wardill, T.J., P.T. Gonzalez-Bellido, R.J. Crook, and R.T. Hanlon, Neural Control of Tuneable Skin Iridescence in Squid. *Proceedings of the Royal Society B: Biological Sciences*, **2012**. 279: p. 4243-4252.
6. Christianen, P.C.M., I.O. Shklyarevskiy, M.I. Boamfa, and J.C. Maan, Alignment of Molecular Materials in High Magnetic Fields. *Physica B: Condensed Matter*, **2004**. 346-347: p. 255-261.
7. Böker, A., H. Elbs, H. Hänsel, A. Knoll, S. Ludwigs, H. Zettl, V. Urban, V. Abetz, A.H.E. Müller, and G. Krausch, Microscopic Mechanisms of Electric-Field-Induced Alignment of Block Copolymer Microdomains. *Phys. Rev.Lett.*, **2002**. 89: p. 135502.
8. Lee, S., J.Y. Kim, S. Cheon, S. Kim, D. Kim, and H. Ryu, Stimuli-Responsive Magneto-/Electro-Chromatic Color-Tunable Hydrophobic Surface Modified Fe₃O₄@SiO₂ Core–

- Shell Nanoparticles for Reflective Display Approaches. *RSC Adv.*, **2017**. 7: p. 6988-6993.
9. He, L., M. Wang, J. Ge, and Y. Yin, Magnetic Assembly Route to Colloidal Responsive Photonic Nanostructures. *Accounts of Chemical Research*, **2012**. 45: p. 1431-1440.
 10. Ge, J., H. Lee, L. He, J. Kim, Z. Lu, H. Kim, J. Goebel, S. Kwon, and Y. Yin, Magnetochromatic Microspheres: Rotating Photonic Crystals. *J. Am. Chem. Soc.*, **2009**. 131: p. 15687-15694.
 11. Zhao, Z., R. Fang, Q. Rong, and M. Liu, Bioinspired Nanocomposite Hydrogels with Highly Ordered Structures. *Adv. Mater.*, **2017**. 29: p. 1703045.
 12. Pullawan, T., A.N. Wilkinson, and S.J. Eichhorn, Influence of Magnetic Field Alignment of Cellulose Whiskers on the Mechanics of All-Cellulose Nanocomposites. *Biomacromolecules*, **2012**. 13: p. 2528-2536.
 13. Libanori, R., F.H.L. Münch, D.M. Montenegro, and A.R. Studart, Hierarchical Reinforcement of Polyurethane-Based Composites with Inorganic Micro- and Nanoplatelets. *Compos. Sci. Technol.*, **2012**. 72: p. 435-445.
 14. Le Ferrand, H., F. Bouville, and A.R. Studart, Design of Textured Multi-Layered Structures Via Magnetically Assisted Slip Casting. *Soft Matter*, **2019**. 15: p. 3886-3896.
 15. Le Ferrand, H., S. Bolisetty, A.F. Demirörs, R. Libanori, A.R. Studart, and R. Mezzenga, Magnetic Assembly of Transparent and Conducting Graphene-Based Functional Composites. *Nat. Commun.*, **2016**. 7: p. 12078.
 16. Zeltner, M., R.N. Grass, A. Schaez, S.B. Bubenhofer, N.A. Luechinger, and W.J. Stark, Stable Dispersions of Ferromagnetic Carbon-Coated Metal Nanoparticles: Preparation Via Surface Initiated Atom Transfer Radical Polymerization. *J. Mater. Chem.*, **2012**. 22: p. 12064-12071.
 17. Bubenhofer, S.B., E.K. Athanassiou, R.N. Grass, F.M. Koehler, M. Rossier, and W.J. Stark, Magnetic Switching of Optical Reflectivity in Nanomagnet/Micromirror Suspensions: Colloid Displays as a Potential Alternative to Liquid Crystal Displays. *Nanotechnology*, **2009**. 20: p. 485302.
 18. Libanori, R., F.B. Reusch, R.M. Erb, and A.R. Studart, Ultrahigh Magnetically Responsive Microplatelets with Tunable Fluorescence Emission. *Langmuir*, **2013**. 29: p. 14674-14680.
 19. Kim, K.-H. and J.-K. Song, Technical Evolution of Liquid Crystal Displays. *Npg Asia Materials*, **2009**. 1: p. 29.
 20. Ercole, F., T.P. Davis, and R.A. Evans, Photo-Responsive Systems and Biomaterials: Photochromic Polymers, Light-Triggered Self-Assembly, Surface Modification, Fluorescence Modulation and Beyond. *Polym. Chem.*, **2010**. 1: p. 37-54.
 21. Cortese, L., L. Pattelli, F. Utel, S. Vignolini, M. Burrese, and D.S. Wiersma, Anisotropic Light Transport in White Beetle Scales. *Adv. Opt. Mater.*, **2015**. 3: p. 1337-1341.
 22. Teyssier, J., S.V. Saenko, D. van der Marel, and M.C. Milinkovitch, Photonic Crystals Cause Active Colour Change in Chameleons. *Nat. Commun.*, **2015**. 6: p. 6368.
 23. Mäthger Lydia, M., J. Denton Eric, N.J. Marshall, and T. Hanlon Roger, Mechanisms and Behavioural Functions of Structural Coloration in Cephalopods. *J. R. Soc., Interface*, **2009**. 6: p. S149-S163.
 24. Dumanli, A.G. and T. Savin, Recent Advances in the Biomimicry of Structural Colours. *Chem. Soc. Rev.*, **2016**. 45: p. 6698-6724.

25. Kraft, P., C. Evangelista, M. Dacke, T. Labhart, and M.V. Srinivasan, Honeybee Navigation: Following Routes Using Polarized-Light Cues. *Philos Trans R Soc Lond B Biol Sci*, **2011**. 366: p. 703-708.
26. Utada, A.S., E. Lorenceau, D.R. Link, P.D. Kaplan, H.A. Stone, and D.A. Weitz, Monodisperse Double Emulsions Generated from a Microcapillary Device. *Science*, **2005**. 308: p. 537-541.
27. Ye, C., L. Kennedy, K. Shirk, U.M. Córdova-Figueroa, J. Youngblood, and C.J. Martinez, CNC-Loaded Hydrogel Particles Generated from Single- and Double-Emulsion Drops. *Green Materials*, **2015**. 3: p. 25-34.
28. Parker, R.M., B. Frka-Petesic, G. Guidetti, G. Kamita, G. Consani, C. Abell, and S. Vignolini, Hierarchical Self-Assembly of Cellulose Nanocrystals in a Confined Geometry. *ACS Nano*, **2016**. 10: p. 8443-8449.
29. Hausmann, M.K., P.A. Rühs, G. Siqueira, J. Läger, R. Libanori, T. Zimmermann, and A.R. Studart, Dynamics of Cellulose Nanocrystal Alignment During 3D Printing. *ACS Nano*, **2018**. 12: p. 6926-6937.
30. Schuerle, S., S. Erni, M. Flink, B.E. Kratochvil, and B.J. Nelson, Three-Dimensional Magnetic Manipulation of Micro- and Nanostructures for Applications in Life Sciences. *IEEE Transactions on Magnetics*, **2013**. 49: p. 321-330.
31. Schuerle, S., I.A. Vizcarra, J. Moeller, M.S. Sakar, B. Özkale, A.M. Lindo, F. Mushtaq, I. Schoen, S. Pané, V. Vogel, and B.J. Nelson, Robotically Controlled Microprey to Resolve Initial Attack Modes Preceding Phagocytosis. *Science Robotics*, **2017**. 2: p. eaah6094.
32. Erb, R.M., J. Segmehl, M. Charilaou, J.F. Löffler, and A.R. Studart, Non-Linear Alignment Dynamics in Suspensions of Platelets under Rotating Magnetic Fields. *Soft Matter*, **2012**. 8: p. 7604-7609.
33. Erb, R.M., L. Rafael, N. Rothfuchs, and A.R. Studart, Composites Reinforced in Three Dimensions by Using Low Magnetic Fields. *Schience*, **2012**. 335: p. 199-204.
34. Beck-Candanedo, S., M. Roman, and D.G. Gray, Effect of Reaction Conditions on the Properties and Behavior of Wood Cellulose Nanocrystal Suspensions. *Biomacromolecules*, **2005**. 6: p. 1048-1054.

Chapter 6.

Conclusion

The alignment of cellulose-based building blocks revealed to be crucial to control both optical and mechanical properties of the resulting composite. Understanding how shear and extensional forces impact the alignment of anisotropic nanoparticles allowed us to fabricate structured composites in the form of complex-shaped bulk objects or functional magneto-optic microparticles. In the case of bulk objects, the alignment of cellulose nanocrystals and wet densification of 3D printed parts greatly increases the solid content of reinforcement without the use of surfactants and chemical modification, thus enhancing the mechanical performance of the host matrix by 3 orders of magnitude. For the microparticles, the alignment of cellulose nanocrystals inside droplets made it possible to benefit from the cellulose's optical birefringence at a larger scale by creating rheological microprobes and optical modulators that remotely couple light transmission with external magnetic fields.

The alignment dynamics of cellulose nanocrystals suspended in a liquid was investigated under the effect of shear and extensional forces using polarized optical imaging and X-ray scattering techniques. By coupling a polarized light microscope to a rheometer, we were able, for the first time, to describe quantitatively the temporal alignment behavior of optically-active cellulose nanocrystals in concentrated suspensions upon application of steady or oscillatory shear stresses. In such concentrated suspensions, the cellulose nanocrystals form liquid crystal domains that can be directly visualized under the polarized light microscope. As expected, the sizes of liquid crystalline domains and their responses to shear stresses are strongly dependent on the concentration of cellulose nanocrystals. Using this method, we show that the time required for alignment scales inversely with the shear rate and directly with the particle concentration. Additionally, the scaling of the alignment time with the applied shear was found to be different at low and high shear rates. The appearance of two different scaling domains can be a consequence of the increased particle interactions when the concentrated CNC suspensions are subjected to high shear rates. This study provides important insights about the dynamic alignment behavior of anisotropic particles in concentrated suspensions under shear stresses. Because of the shear stresses developed inside extruding nozzles, it provides new design criteria to maximize the alignment degree of particles during the extrusion-based 3D printing process.

In addition to the shear forces generated next to the capillary walls, extensional forces also play a significant role in the alignment of anisotropic particles during 3D printing processes. To quantify the contribution of such forces during printing, we studied the alignment dynamics of these nanoparticles using a combination of multiple X-ray scattering techniques. The development of an X-Ray transparent extrusion stage enabled us to

measure in-situ the alignment dynamics of CNC-based inks at different concentrations. The experimental results revealed that extensional forces generated at cross-sectional constrictions of the cartridge system contribute to high extent to the alignment of CNCs in the center of the capillary, whereas shear forces enhance alignment close to the capillary walls. Because extensional forces develop primarily at the entrance of the capillary and shear forces develop along the capillary length, the region of the ink exhibiting strongest particle alignment shifts from the center to the walls as the suspension travels through the nozzle. Although high CNC contents are required in these inks to adjust the rheological properties and enable effective 3D printing, they lead to a significant reduction of the contribution of shear forces on the alignment dynamics, as most of the volume of the material undergoes plug flow during extrusion. In agreement with the predictions shown in Chapter 3, we show through high-resolution 2D SAXS that indeed only a small volume fraction of the extruded ink has its alignment degree affected by shear forces during the extrusion process. Understanding the importance of extensional forces resulting from changes in needle cross-section not only can lead to the design of novel needle geometries but also to the development of microfluidic systems that exploit these extensional forces to align CNCs in programmable composite architectures.

3D printing of highly-loaded cellulose composites remains a challenge in the scientific community, which has limited its broader application in industry. This challenge is mainly due to the difficulty to disperse cellulose particles within the polymer matrix and the prohibitively high viscosity that results from this poor dispersion. Extensive mixing, the use of surfactants or chemical modification are often required to improve the dispersability of cellulose particles in the polymer matrix. However, cellulose-based inks with concentrations higher than 20 wt% were found to require prohibitively high pressures to be printed via direct ink writing process when combined to polymerizable monomer systems. The 3D printing process followed by a wet densification step developed here allowed us to print cellulose-based scaffolds in water at a CNC content of 20 wt %, which are subsequently further densified to reach a final cellulose concentration of 37 wt %. This densification is achieved by plunging the sample in a poor solvent mixture that increases the interactions between the CNCs particles, thus inducing isotropic shrinkage of the printed structure. We introduced an additional infusion step after the densification process that allowed us to produce cellulose-based composites with unprecedentedly complex geometries and tunable mechanical properties. The final properties of the composite can be determined by the choice of polymer/monomer system utilized during the infusion. This allows us to prepare either strong composites or very soft hydrogels. Consequently, the wet densification of cellulose scaffolds developed in this study offers a versatile solution to the production of complex-shaped cellulose composites with tailored mechanical properties and compositions.

The alignment of CNCs under shear stress and extensional flow was also extended beyond the scope of 3D printing applications to create functional anisotropic microparticles from droplet templates. In this study, birefringent magnetically-responsive microparticles

were prepared by incorporating an extensional flow element in a microfluidic emulsification platform. Aqueous micro-droplets loaded with CNCs, superparamagnetic iron oxide nanoparticles (SPIONs) and a reactive monomer system were fabricated using a double emulsification setup. The initially spherical droplets were subsequently deformed by reducing the cross-sectional area of the collecting tube and polymerized under UV-light to fix the flow-aligned CNCs and the resulting anisotropic shape of the microparticles. The addition of cellulose and superparamagnetic nanoparticles to the system leads to microparticles with two main functionalities. First, the alignment of individual CNCs by extensional forces at the micro-scale makes the microparticles optically birefringent. Second, the presence of SPIONs provides magnetic response to the resulting microparticles, allowing us to remotely control their position and orientation at the macro-scale. Taking advantage of the anisotropic optical properties of cellulose nanocrystals and the anisotropic shape of the SPION-laden microparticles, a direct correlation can be established between the optical and magnetic responses of the microparticles. Under a rotating magnetic field, the multifunctional microparticles can be used to probe the rheological properties of the suspending medium or to modulate the intensity of polarized light. Aside from this specific example, our microfluidic platform offers a versatile approach to the production of textured anisotropic micro-particles, which can be applied to a wide choice of polymer and particle systems.

Chapter 7.

Outlook

Over the last years, the interest on cellulose-based materials has been growing, mostly driven by environmental concerns related to our current lifestyle and the sustainable nature of cellulose. In addition, their great mechanical properties as well as their biocompatibility are making cellulose an ideal candidate for various fields such as bio-medical applications, packaging, and electronics, among others. To meet the requirements of different applications, it is essential to understand and control the processing parameters that determine the structure and properties of cellulose-based materials. Throughout this thesis, the alignment of cellulose nanoparticles under shear and extensional flow was experimentally studied and novel techniques to develop cellulose-based materials with textured architectures were proposed. Despite the significant contribution of this study, the renewable nature of cellulose resources and the versatility of the printing and emulsification processes explored open several other possibilities for the controlled fabrication of sustainable cellulose-based materials. Below, we propose specific research topics that could be pursued in further studies to better understand or exploit some of the phenomena and processes discussed in this thesis.

Understanding and controlling the alignment of cellulose nanocrystals is a topic that deserves further attention in future work. The alignment of cellulose nanocrystals was investigated in this thesis using rheology coupled with optical imaging and X-ray scattering techniques to evaluate the role of shear and extensional flows on particle orientation in two specific plate-plate and capillary geometries. Combining rheology, imaging and scattering techniques in one *in-situ* measurement set-up could be an interesting approach to observe and better quantify the rheology and alignment behavior of nanocellulose network. Such a setup would enable one to combine the large-volume sampling advantage of scattering techniques with the particle-level structural information offered by imaging analysis. Furthermore, other flow geometries should be considered. For example, the capillary system used for the X-ray study induced strong extensional forces to the material prior the entry of the capillary. These extensional forces markedly influenced the alignment of CNC particles, as shown in the experiments performed in transparent glass capillaries (chapter 2 and 3). In order to better understand the alignment of cellulose particles under the flow profile imposed solely by the capillary, the alignment history of the sample should be completely erased. This could be obtained by increasing the cross section of the capillary prior to the measurement area, taking advantage of the resulting diverging flow to erase any prior alignment (chapter 2). We already explored the feasibility of this erasing strategy in the study that combined rheology and polarized optical microscopy. Additionally, the study could be extended to other cellulose/polymer systems to evaluate the effect of viscosity and

interparticle interactions in other polymer systems on the alignment dynamics of CNC particles. Since the geometry of the extrusion system and the rheological properties of the material strongly influence the degree of alignment, future work should also explore the possibility of controlling particle alignment “on-the-fly” using a printing nozzle with reconfigurable geometry. The resulting shear and extensional forces induced by the needle geometry could be exploited to control and vary the alignment of cellulose nanoparticles within the printed filaments. To this end, one could design needles with integrated flexible membranes that would allow for local changes of the nozzle cross-section. This flexible membrane could be actuated using hydraulic systems, for example. Such an approach would vary the extensional forces at that specific section and influence the resulting alignment of the extruded material. Additionally, by limiting the alignment to the walls through plug-type flow in an un-tapered nozzle, it should be possible to produce core-shell structures with an even stronger alignment contrast compared to that shown in the thesis. These core-shell structures would present an aligned shell with a randomly organized core. This multi-structural printed filament could have optimized strength and crack deflection properties, as demonstrated in previous research.¹

3D printing is a game-changing technique for certain niche applications in biomedical technologies, aeronautics, electronics and rapid prototyping, where small quantities or highly customized products are required. Furthermore, the additive nature of 3D printing processes provides the potential to create composites with defined multiscale architecture for structural, functional or optical applications. Since cellulose-based building blocks can be used as feedstock in 3D printing systems, these opportunities has recently awakened the interest of the cellulose community. In fact, the main challenge for many applications involving cellulose nanocrystals as reinforcing building block lies on the combination of both control over the orientation of these nanoscale particles and the fabrication of complex three-dimensional structures. Combined to the biocompatible and renewable properties of cellulose, niche domains such as the medical field might very well profit from research on this topic. For example, the production of patient-specific implants for regenerative medicine are currently limited by the choice of materials. Therefore, an interesting application is the production of cellulose-based implants for cartilage regeneration. Current tissue engineering solutions are not resorbable and usually remain in the body unless they are removed by another surgery. Furthermore, they do not, or in a very limited way, promote cell regeneration. It has long been shown that cells survive and proliferate well in hydrogel-like materials containing the right culture medium.^{2, 3} However, hydrogels have usually relatively weak mechanical properties on the order of a few kPa, whereas cartilage is stronger and presents anisotropic microstructure and mechanical properties gradients to better respond to the dynamic loading conditions in the human body. The combination of cellulose with a 3D printable bio-degradable hydrogel system might allow for the reconstruction of missing cartilage parts with defined mechanical properties via precise spatial distribution of cellulose particles. The biodegradable constituents of such hydrogel

could later be resorbed by the surrounding tissue while cells regenerate the original cartilage and cellulose is excreted by the body.

Beyond complex-shaped cellulose parts, the wet densification process of 3D printed scaffolds proposed in this thesis can potentially be explored with other nanoparticle compositions to generate composites for a multitude of other applications. As the system suggests, the approach is not limited to cellulose but can be further extended to any nano-scaled material. The main requirement of this densification approach is to find combinations of poor and good solvents to obtain a considerable densification of the printed scaffold without causing redispersion of the constituent building blocks. The major advantage noticed during the process is the ability of cellulose to form strong interparticle hydrogen bonds, which contribute significantly to the cohesion of the structure when immersed in a non-solvent. This cohesiveness might also be achieved with other nano-particle systems. Depending on the nanoparticles used, the wet densification conditions of the printed samples may depend on their surface chemistry and the nature of the interactions among the nanoparticles as well as other processing parameters relevant during drying, sintering or wet-infusion. In preliminary experiments, the possibility to densify ceramic materials such as silicium, zirconium or aluminum oxides was investigated following the same approach shown in chapter 4. The wet densification of scaffolds of silica particles showed promising results. The major limitation faced with these oxide nanoparticles, as compared to cellulose, is the development of strong repulsive inter-particle interactions, which presumably result in sample cracking upon sintering. Therefore, the application of the wet densification route to oxide nanoparticles still requires extensive research and optimization. In contrast to fully sintered oxide scaffolds, the preparation of polymer-based composites is an attractive alternative to circumvent these cracking issues. For example, any prior problems related to the formation of aggregates and the homogeneous dispersion of the cellulose in the polymer matrix can be avoided if the cellulose scaffold is first 3D printed from aqueous-based inks and later infused with a suitable monomer system after being printed and densified. In this case, the interface between matrix and reinforcing cellulose elements might require further investigation as such interactions are crucial to enhance the mechanical performance of the final composites. An interesting approach in that direction would be to compare 3D printed cellulose parts exhibiting different interfacial adhesion properties with the same polymer matrix. For this purpose, cellulose particles with prior chemical modification could be utilized and compared to a pristine reference sample. Additionally, the type of interfacial adhesion (covalent, irreversible or supramolecular) and the resulting properties on the final composite structure could be investigated. A better understanding of the interactions between cellulose and the polymer matrix would enable the fabrication of composites with enhanced load transfer ability and consequently improved mechanical properties. Further research on this topic can potentially enable the production of a wide range of cellulose-reinforced materials where one could envision for example the integration of self-healing molecules at the cellulose-matrix interface. These self-healing properties can result from supramolecular interactions such as reversible hydrogen or ionic bonding. Such materials might exhibit

enhanced mechanical performance because of the reconfigurable nature of cellulose-matrix interface. This reconfigurable interface could lead to prolong the lifetime of the composite, as the properties can be restored to a certain extent if the material is damaged. That prospect is of interest for applications where the composite part is difficult to access once implemented, such as in biomedical implants.

The production of cellulose-laden microbeads or particles also has attracted growing interest for various applications, such as in the stabilization of Pickering emulsions or in model experimental systems for the study of structural reorganization of individual particles in confined environments.^{4, 5} In contrast to the bulk emulsification routes typically used to create such systems, the microfluidic approach used in this thesis is a powerful tool to ensure the reproducible preparation of complex monodisperse droplets and microparticles. This was demonstrated by producing both anisotropic and micro-textured cellulose-laden microparticles. Although limited by the low throughput, major efforts have been invested in making microfluidics more efficient and up-scalable. The possibility demonstrated in chapter 5 to create nanocellulose-containing anisotropic particles which are magnetically responsive and exhibit birefringent optical properties opens novel applications for magneto-optic micro-rheology and magnetically-controlled light modulation. Additionally, preliminary work showed that these magnetically-responsive microparticles can also be used as local reinforcements when dispersed in a polymer matrix. Such a composite would present a hierarchically-organized microstructure with aligned CNCs and microparticles at the nano and micro-scale, respectively. Alternatively, when dispersed in hydrogel matrices, the alignment and positioning of the microparticles can be remotely controlled with magnetic fields prior to the cross-linking step. The resulting hydrogel would exhibit anisotropic swelling response when submerged in a liquid medium due to the tailored orientation of individual microparticles, which should constrain the swelling of the hydrogel along specific directions. Preliminary results obtained in this thesis support this hypothesis. However, the uniform distribution of microparticles within the hydrogel still remains challenging. Such textured hydrogels could also be explored in biomedical applications, by adding chemicals for controlled drug release. Using different concentrations of cellulose to control the release kinetics of various drugs, these textured microparticles could not only serve as reinforcement for the hydrogel implant, but also as cargo system for the delivery of specific drugs or nutrients.^{6, 7} These cargo molecules could, for example, promote the regeneration of the original body tissue, avoid infections or reduce the risk of rejection. In addition to the dispersion of the microparticles in the polymer matrix, the printability of these cellulose-reinforced microparticles using a direct ink writing system was also briefly explored during this thesis. By adjusting the needle diameter to avoid clogging, printed structures with oriented anisotropic microparticles were successfully obtained. Because of the high yield stress required for direct ink writing, the microparticles could not be magnetically-oriented out of plane with respect to the printed line. It would however be of interest to further explore the possibility to magnetically orient them in this printed 3D structure independently of the extrusion orientation. One could potentially use stronger magnetic fields or

alternatively develop a system comprised of a more viscous ink that serves as a mold and of a less viscous medium containing magnetically-response particles. Because the throughput of the microfluidic capillaries used in this work is still relatively low, this research direction would require the use of more efficient emulsification approaches to create larger amounts of textured microparticles. Despite this throughput limitation, the microfluidic approach we utilized to produce anisotropic microparticles is not limited to cellulose-containing polymer systems and can also be applied to various other polymers to generate microparticles with a wide size and compositional range. The size of the microparticles obtained in this work was relatively large, ranging from 400 to 2000 μm in length, depending on the choice of material added to the templating droplets. It is however possible to decrease the droplet size and the resulting anisotropic microparticles size by producing microfluidic glass or PDMS devices with smaller features and respectively a smaller deformation section. However, viscosity and prohibitive pressures will limit the minimum feature that is possible to achieve. Besides broadening the size range of the microparticles, it would also be of interest to create microparticles with core-shell structures using double emulsions made in step emulsification devices. In these devices, different polymer systems could be studied and possibly combined or cured using different light sources. This can find potential use in applications that require multiple controlled cargo release, if the polymer in the outer shell is designed to exhibit self-healing properties. Indeed, microfluidics offers an enormous playground in terms of possible material combinations and microparticle structure. Our magnetically-responsive cellulose-based anisotropic micro-particles are just one example of the many multifunctional systems that can be created using this technology.

To conclude, with every scientific discovery, simple questions are answered and multiple new ones are to be solved. Inspired by the hierarchical materials found in nature, in this thesis we started to understand how we can play with materials at the nano-scale and worked our way to the macro-scale. However, there is still a lot of room for research and scientific discoveries, which will eventually lead to new materials and processes based on sustainable natural resources. I hope that part of the concepts we explored in my thesis will spark new ideas and I am looking forward to follow the future development in the world of cellulose-based materials and beyond. The only limit is your creativity.

References

1. Gantenbein, S., K. Masania, W. Woigk, J.P.W. Sesse, T.A. Tervoort, and A.R. Studart, Three-Dimensional Printing of Hierarchical Liquid-Crystal-Polymer Structures. *Nature*, **2018**. 561: p. 226-230.
2. Caliri, S.R. and J.A. Burdick, A Practical Guide to Hydrogels for Cell Culture. *Nature Methods*, **2016**. 13: p. 405.
3. Tibbitt, M.W. and K.S. Anseth, Hydrogels as Extracellular Matrix Mimics for 3d Cell Culture. *Biotechnology and Bioengineering*, **2009**. 103: p. 655-663.
4. Parker, R.M., B. Frka-Petescic, G. Guidetti, G. Kamita, G. Consani, C. Abell, and S. Vignolini, Hierarchical Self-Assembly of Cellulose Nanocrystals in a Confined Geometry. *ACS Nano*, **2016**. 10: p. 8443-8449.

5. Bai, L., S. Huan, W. Xiang, and O.J. Rojas, Pickering Emulsions by Combining Cellulose Nanofibrils and Nanocrystals: Phase Behavior and Depletion Stabilization. *Green Chemistry*, **2018**. 20: p. 1571-1582.
6. Zhang, F., W. Wu, X. Zhang, X. Meng, G. Tong, and Y. Deng, Temperature-Sensitive Poly-Nipam Modified Cellulose Nanofibril Cryogel Microspheres for Controlled Drug Release. *Cellulose*, **2016**. 23: p. 415-425.
7. Lin, N., A. Gèze, D. Wouessidjewe, J. Huang, and A. Dufresne, Biocompatible Double-Membrane Hydrogels from Cationic Cellulose Nanocrystals and Anionic Alginate as Complexing Drugs Codelivery. *ACS Appl. Mater. Interfaces*, **2016**. 8: p. 6880-6889.



Appendix A

Appendix to “Dynamics of Cellulose Nanocrystals Alignment during 3D Printing”

Appendix A1: Morphology of cellulose nanocrystals and phase transition of CNC suspensions

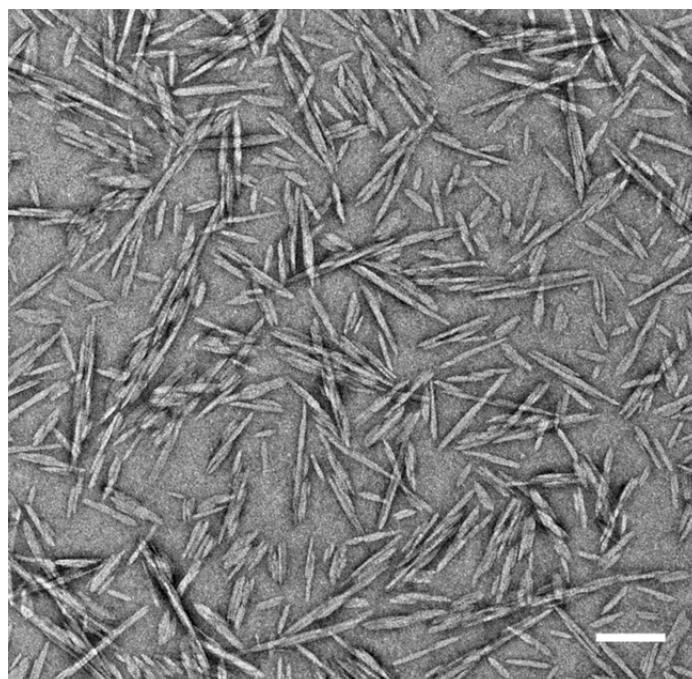


Figure A. 1 TEM image of the investigated CNC particles. Scale bar: 100 nm.

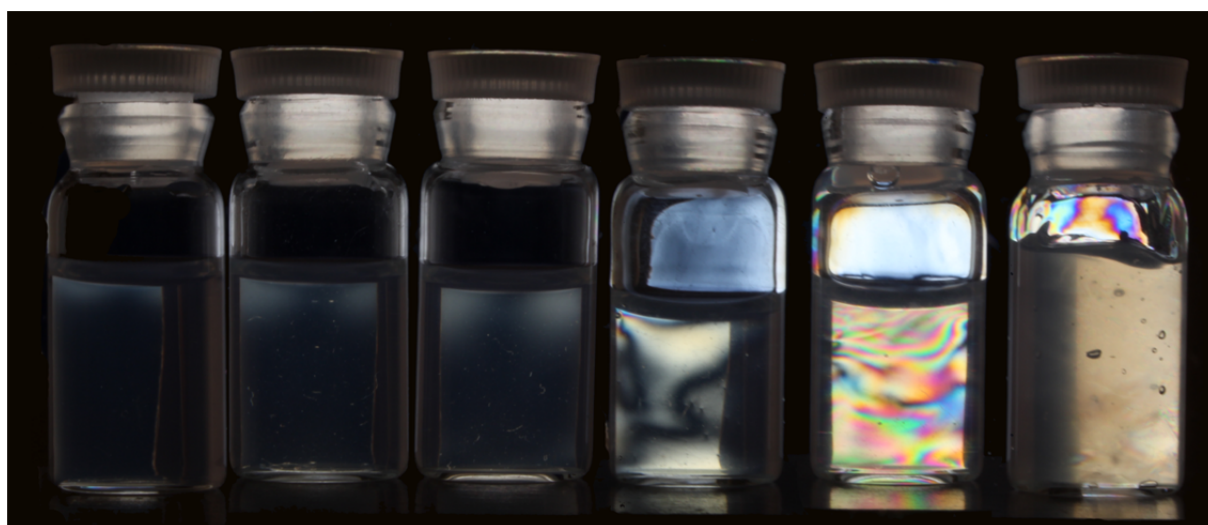


Figure A. 2 Cellulose suspensions with different CNC concentrations under cross-polarizers. Liquid crystal domains are observed at CNC concentrations above 8wt%. CNC concentrations from left to right: 5, 6, 7, 8, 9, 10 wt %.

Appendix A2: Yield stress measurements

Figure A. 3 shows the effect of (a) the parallel plate gap size and (b) the measuring time at each applied stress on the yield stress of a 20 wt % CNC ink. As the measurements did not show a notable effect of these measuring parameters, the parallel plate gap and the measuring time were fixed at 0.2 mm and 25 s, respectively, for all the reported yield stress data.

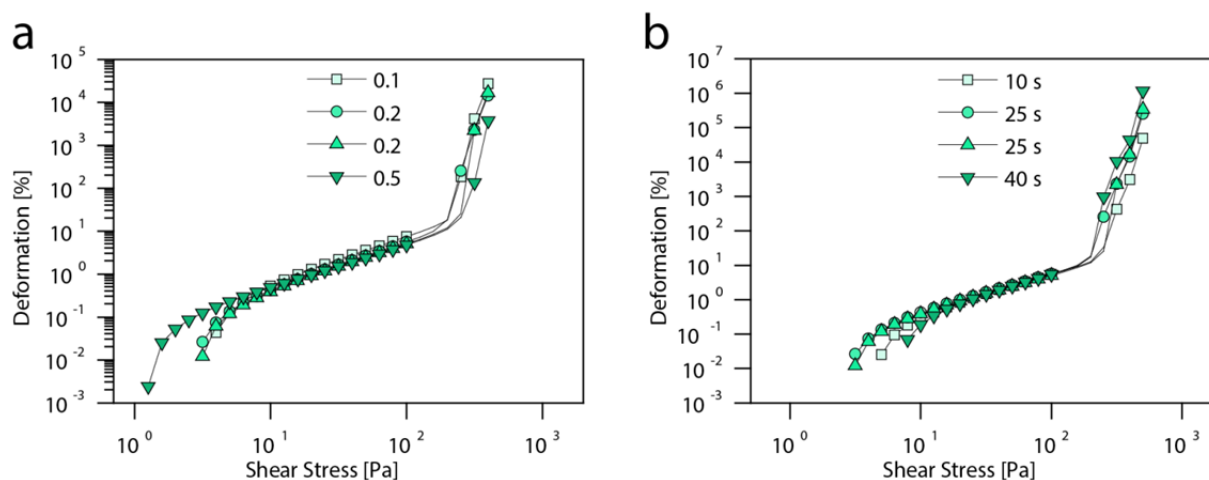


Figure A. 3 Yield stress measurements performed at different (a) parallel plate gaps (in mm) and (b) measuring times at each applied shear.

Appendix A3: Flow curves measured using cone-plate and plate-plate geometries

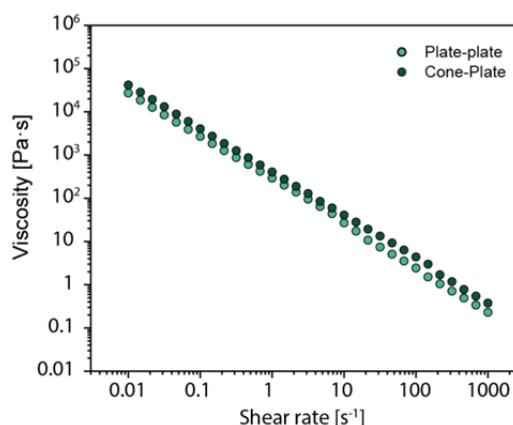


Figure A. 4 Shear rate sweeps from $0.01 s^{-1}$ to $1000 s^{-1}$ carried out using parallel plate and cone-plate geometries. An ink containing 20 wt% CNC was used for these measurements. Both geometries had a diameter of 25 cm. The cone geometry has an angle of 4° .

Appendix A4: Optical imaging under polarized light

Because of the anisotropic nature of cellulose nanocrystals (CNCs), the material possesses an anisotropic ellipsoidal indicatrix. The refractive index along any direction through the crystal can therefore be expressed as a combination of two components: the principal refractive index (also called ordinary refractive index, n_o), directed along the short axis of the ellipsoid, and the principal extraordinary refractive index (n_e), directed along the long axis of the ellipsoid. If a linearly polarized light beam travels for example along the axis corresponding to n_e , the wave front coincides with the circular section of the optical indicatrix and no birefringence is observed, the light beam experiences only n_o . For any other propagation direction, both refractive indices have to be considered and the light is elliptically polarized.¹ Such elliptical polarization allows light to be transmitted through a birefringent material positioned between two cross-polarizers (orthogonally arranged polarizer and analyzer). This provides a powerful tool to optically access the orientation of birefringent particles. Taking our cellulose nanocrystals as an example, the non-preferred orientation of the particles when suspended in a fluid lead to different colors under cross-polarizers. This reflects the distinct orientations of the liquid crystal (LC) domains formed above a critical concentration of particles in the suspension.² As shear is applied through rotation of one of the plates in a parallel plate geometry, these domains are disrupted and the individual nanocrystals tend to orient circularly around the rotational axis of the plate (Scheme 2.1, main text). An alternation of dark and bright regions is observed, forming a pattern similar to a Maltese cross. The dark areas result from the linearly polarized light that travels undisturbed through the sample parallel to one of the main indicatrices and is eventually blocked by the optical analyzer (second polarized filter). When light propagates at any angle laying in between both indices (n_o and n_e), it can cross the analyzer and the image is observed. The intensity of the light crossing the two polarized filters depends on the angle at which the CNCs are oriented in the samples relative to the filters. Maximum intensity is obtained for an angle of 45 °, where the light extinction effect is minimal.

Appendix A5: Percolation threshold and yield stress of CNC suspensions

The yield stress of CNC suspensions is caused by the formation of a volume-filling percolating network of particles. Such network is expected to form when the concentration of particles exceeds a percolation threshold Φ_c . For CNCs, it has been shown that Φ_c can be expressed using the following equation:³⁻⁵

$$\Phi_c = \frac{xd}{L} \quad Eq. 1$$

where x is a coefficient that varies between 0.7 and 1.92 depending on the CNC surface charges, d is the diameter of the particles, and L is the particle length. For the CNC particles

investigated in this work we estimate a percolation threshold around 5 wt % using the equation above.

The dependence of the yield stress (τ_y) on the concentration of CNCs (Φ) above the threshold Φ_c can be phenomenologically described by the Maron-Pierce equation:^{6, 7}

$$\tau_y = \tau_0 \left[\left(1 - \frac{\Phi}{\Phi_m} \right)^{-2} - 1 \right] \quad \text{Eq. 2}$$

where τ_0 is a fitting parameter and Φ_m is the maximal packing fraction. We used this relation to gain further insights into the yield stress behavior of our CNC inks. The maximum packing fraction Φ_m depends on the aspect ratio (p) of the particles and can be estimated using the following empirical relation proposed in the literature for filler fibers⁸: $A = 0.54 - 0.0125p$, where A is taken as an approximation of Φ_m . For the aspect ratio of approximately 15 (given the size distribution) of our CNC particles, we obtain $\Phi_m = 35$ vol%. Taking 35 vol% as the estimated Φ_m we fitted equation (2) to our experimental yield stress data using τ_0 as fitting parameter (Figure A. 5). Using $\tau_0 = 98$ Pa we find that the Maron-Pierce equation describes well the yield stress behavior of our CNC suspensions. This phenomenological description can be used to predict with reasonable accuracy the yield stress of CNC suspensions and complements the physical interpretation of the yield stress based on the power law discussed in the main text (Figure 2.1c).

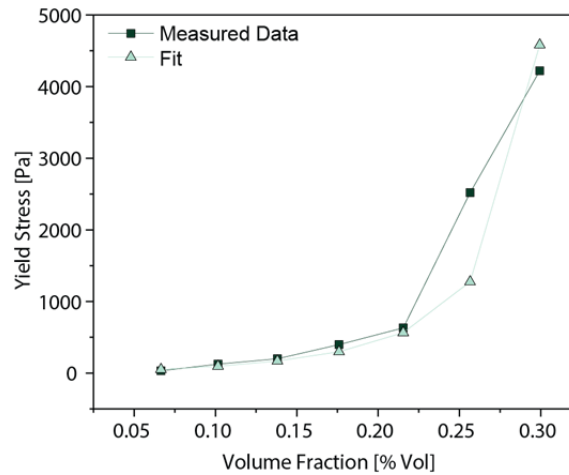


Figure A. 5 Fitting of the yield stress versus CNC volume fraction using the Maron-Pierce phenomenological relation.

Table A. 1 Values displayed in Figure 2.1c of the main paper.

Volume Fraction [Vol %]	Yield Stress [Pa]
6.65	31.7
10.16	126
13.81	200
17.61	398
21.55	632
25.66	2520
29.94	4220

Appendix A6: Alignment dynamics measured by polarized light imaging

The alignment dynamics of CNC inks at different shear rates and particle concentrations was experimentally determined from slices extracted from a stack of cross-polarized images, as explained in the main text. Figure A. 6 displays examples of different slices obtained at fixed applied shear rates and CNC concentrations. In each slice, one can directly visualize the time required for the alignment front to propagate from the rim of the plate towards its center. As the local shear rate increases linearly from the center to the rim, the alignment time at different local shear rates can be extracted from these images.

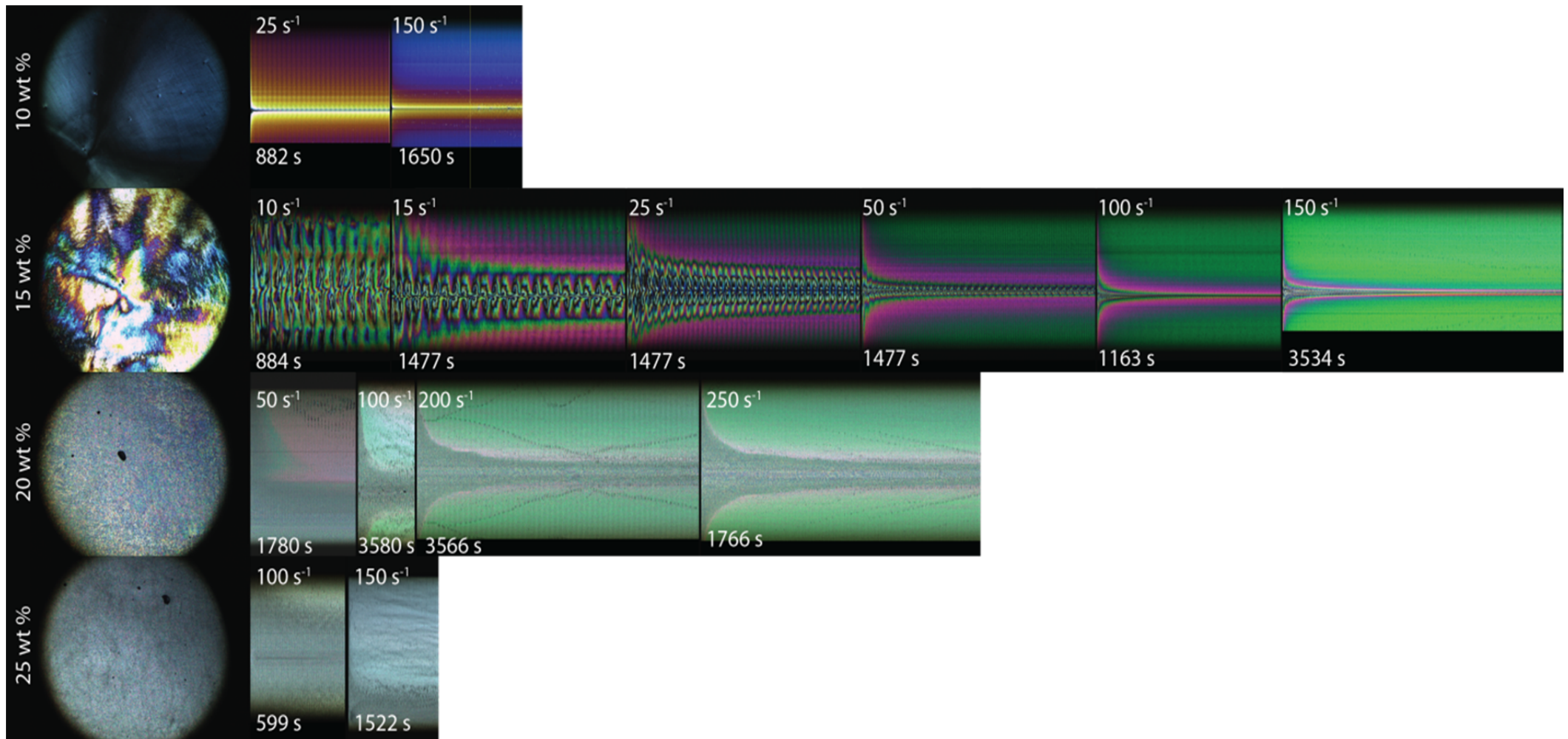


Figure A. 6 Effect of suspension concentration and maximum shear rate on the alignment dynamics of CNC particles. The concentration of CNC particles increases from 10 to 25 wt % from top to bottom. The shear rates applied vary from 25 s^{-1} to 250 s^{-1} . The images show the propagation of the alignment front and the critical radius that defines the non-aligned area. The time indicated refers to the total time recorded at the given shear rate. The image sampling rate varied between 1 and 10 seconds depending on the concentration.

The optical images also indicate the critical radius below which no alignment of CNC particles occur. Since the mechanical properties of the printed filament scales with the area of aligned CNC particles, it is informative to describe the alignment dynamics also in terms of the fraction of aligned particles within the cross-section of the filament. The evolution of the aligned area as a function of time for a 20 wt % ink subjected to different maximum shear rates is shown in Figure A. 7 as an example.

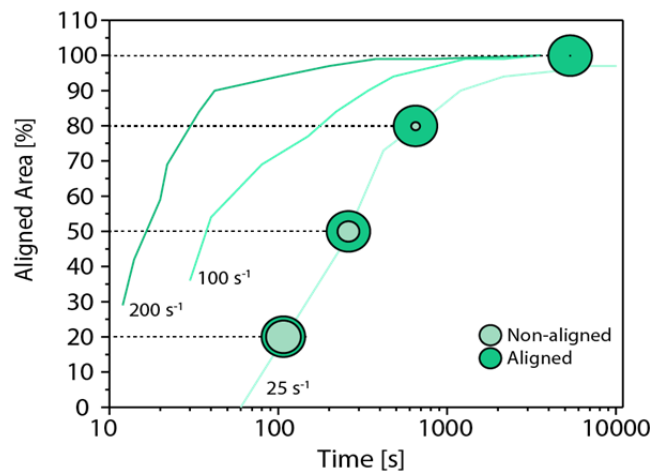


Figure A. 7 Progression of alignment area as a function of time for different applied maximum shear rates. Measurements were carried out for a 20 wt % CNC ink.

Appendix A7: Effect of time and shear rate on the suspension rheology

The CNC suspensions show time-dependent rheological properties, which can be quantified by the hysteresis of the flow curves measured at increasing and decreasing shear rates (shear sweep) and by the time evolution of the suspension viscosity at different shear rates and particle concentrations (Figure A. 8 a-d). The drop in viscosity as a function of time at a given shear rate correlates with the alignment process of the particles. This is illustrated by measurements of the normal force of the suspension under shear (Figure A. 8 a, b) and by the optical polarized images taken during the measurements (Figure A. 8 e, f).

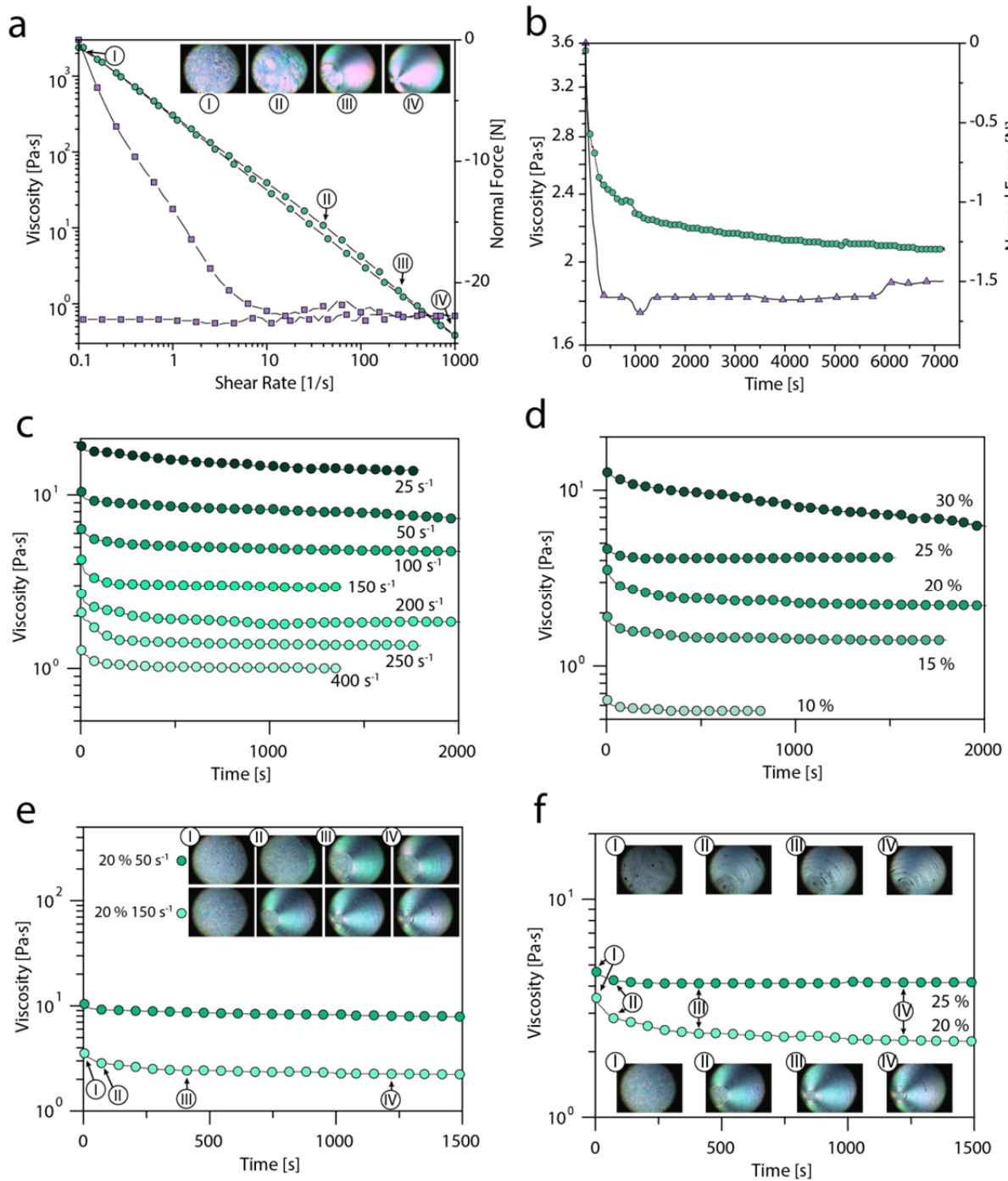


Figure A. (a) Viscosity and corresponding normal force as a function of shear rate for a 20 wt % ink. (b) Viscosity and normal force as a function of time for a 20 wt % ink subjected to a maximum shear rate of 150 s^{-1} . A drop in the normal force indicates shear-induced alignment of the particles. (c) Viscosity as a function of time for a constant concentration of 20 wt % measured at different shear rates from 25 s^{-1} to 400 s^{-1} . (d) Viscosity as a function of time for a fixed shear rate of 150 s^{-1} but varying concentration from 10 wt % to 30 wt %. (e,f) Correlation between the time evolution of the viscosity and the alignment process captured by polarized light snapshots for (e) different maximum shear rates at a CNC concentration of 20 wt % and (f) distinct CNC concentrations at a constant maximum shear rate of 150 s^{-1} .

Table A. 2 Data displayed in Figure 2.2e of the main paper.

	10 wt %		15 wt %		20 wt %		25 wt %	
Shear Rate	Time	Std	Time	Std	Time	Std	Time	Std
[s ⁻¹]	[s]	[-]	[s]	[-]	[s]	[-]	[s]	[-]
0	11.67	7.64	--	--	--	--	--	--
1	1.67	0.58	--	--	--	--	--	--
2	0.67	0.58	--	--	--	--	--	--
3	0	0	--	--	--	--	--	--
4	0	0	373	155.56	--	--	--	--
5	0	0	95.8	79.94	3689.40	218.97	--	--
10	0	0	15.4	2.51	1488.00	396.45	--	--
15	0	0	10	2.71	671.60	198.20	1495	--
20	0	0	7.875	1.65	510.00	118.15	1035.00	349.98
25	0	0	4.75	0.5	373.80	194.65	653.75	37.12
30	0	0	4	0	317.25	97.25	283.13	166.10
35	0	0	3.33	0.289	248.40	96.97	376.25	19.45
40	0	0	3	0	181.50	51.73	315.00	2.50
45	0	0	2.67	0.58	109.50	40.84	242.50	10.61
50	0	0	1.83	0.76	70.75	13.25	167.50	28.28
55	0	0	2	0	65.17	4.48	138.75	5.30
60	0	0	2	0	56.00	5.29	84.63	51.24
65	0	0	2	0	45.33	5.03	116.25	19.45
70	0	0	2	0	37.13	0.85	113.75	19.45
75	0	0	2	0	34.00	1.73	79.00	50.92
80	0	0	1	0	30.83	1.44	100.00	10.61
85	0	0	1	0	27.67	2.52	91.25	1.77
90	0	0	0.25	0.35	22.00	2.16	51.50	34.23
95	0	0	0	0	16.67	5.77	43.75	22.98
100	0	0	0	0	15.63	3.77	23.75	19.45
105	0	0	0	0	14.5	0.71	32.5	--
110	0	0	0	0	13	0	--	--
115	0	0	0	0	12.5	0	--	--
120	0	0	0	0	12.25	0.35	--	--
125	0	0	0	0	12.2	0.28	--	--
130	0	0	0	0	12.03	0.25	31.2	--
135	0	0	0	0	11.9	0.42	--	--
140	0	0	0	0	11.75	0.49	--	--
145	0	0	0	0	11.6	0.57	--	--
150	0	0	0	0	11.25	0.35	--	--
155	0	0	0	0	10.5	--	--	--

160	0	0	0	0	10	--	27.5	--
165	0	0	0	0	9.2	--	--	--
170	0	0	0	0	8	--	--	--
175	0	0	0	0	6.8	--	20	--
180	0	0	0	0	6	--	--	--
185	0	0	0	0	4	--	--	--
190	0	0	0	0	3	--	--	--
195	0	0	0	0	2	--	--	--
200	0	0	0	0	1	--	15	--

Table A. 3 Data shown in Figure 2.2g of the main paper.

Concentration [wt %]	B(Φ) [-]
25	174730.50
20	41982.16
15	263.96

Appendix A8: Plug flow estimation in a 3D printing nozzle

During 3D printing by extrusion, plug flow occurs at the lower shear stresses in the inner part of the extrusion nozzle whereas differential flow occurs at the higher stresses closer to the nozzle walls. The analysis presented in the main text to predict the plug and differential flow regions was carried out for a model glass capillary, which was later used to experimentally test the predictions. Here, we present the same analysis for geometries that are more representative of the nozzles used for 3D printing via direct ink writing.

The type of flow experienced by the fluid depends on the yield stress and the shear stress profile across the nozzle radius. The shear stress (τ) across the nozzle can be calculated as follows:⁹

$$\tau = \frac{\Delta P}{2L}r \quad \text{Eq. 3}$$

where L is the nozzle length, r is the radial position from the nozzle center and ΔP is the pressure difference applied (Figure A. 9a). According to this equation, the maximum shear stress (τ_{max}) occurs at the wall of the nozzle ($r = R$) and decreases linearly towards the center of the nozzle. The radial position at which the applied shear stress is equal to the yield stress of the fluid defines the plug flow radius, r_{pf} (Figure A. 9b).

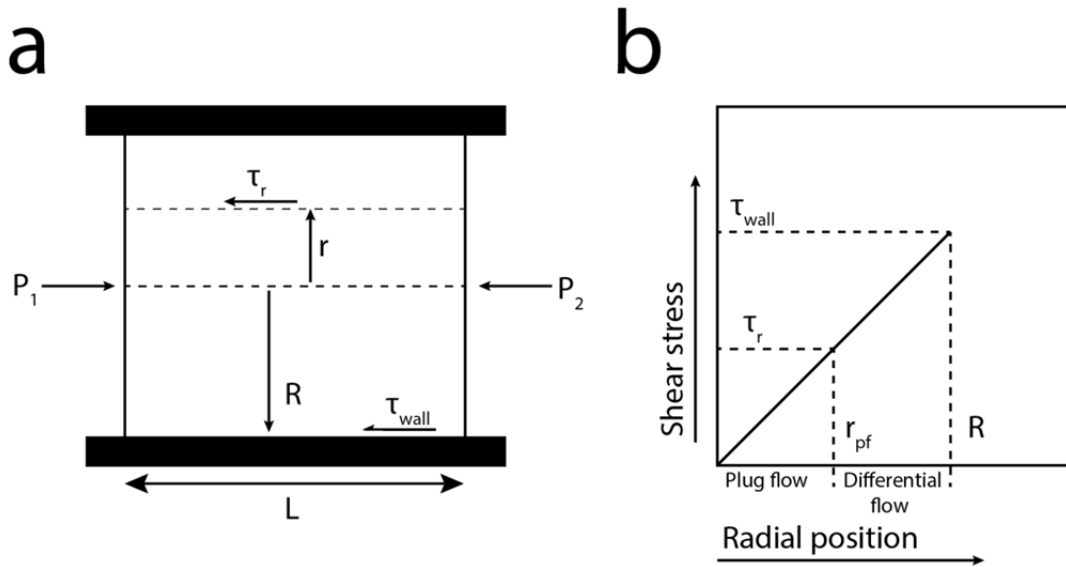


Figure A. 9 Plug and differential flow developed within the material as it is pushed through a cylindrical tube by a pressure difference ($P_1 - P_2$). (a) Cross-section of the tube indicating the relevant geometrical parameters and the shear stresses arising from the friction of the material with the tube wall. (b) Dependence of the shear stress on the radial position in the tube. The material closer to the center of the tube ($r < r_c$) will be subjected to shear stress lower than the yield stress, leading thus to plug flow. By contrast, differential flow develops within the material that is closer to the tube wall ($r_c < r < R$). Figure adapted from Reed et al.⁹

We use equation (3) to estimate the plug flow radius for two typical nozzle dimensions used for 3D printing. These exemplary nozzles have a diameter of $410 \mu\text{m}$, but different lengths. The longer nozzle has a length of 3.1 cm , whereas the shorter one is 1.75 cm long.

Figure A. 10 shows the calculated plug flow radius (r_{pf}) as a function of the yield stress of the ink for different applied pressure differences. The yield stress of the ink depends strongly on the concentration of CNC particles used (Figure 2.1c, main text). As expected, the longer needle results in a higher plug flow radius. The plug flow radius can however be decreased by increasing the applied pressure difference. An increase in the applied pressure results in a higher extrusion rate, which requires higher needle displacement velocities. Although higher needle velocities will reduce the printing time, too fast printing rates might also result in a loss in resolution. Therefore, these parameters have to be optimized according to the boundary conditions set by the resolution, speed and degree of alignment required for the aimed application. The degree of alignment is strongly influenced by the plug-flow radius, as discussed in the following sections.

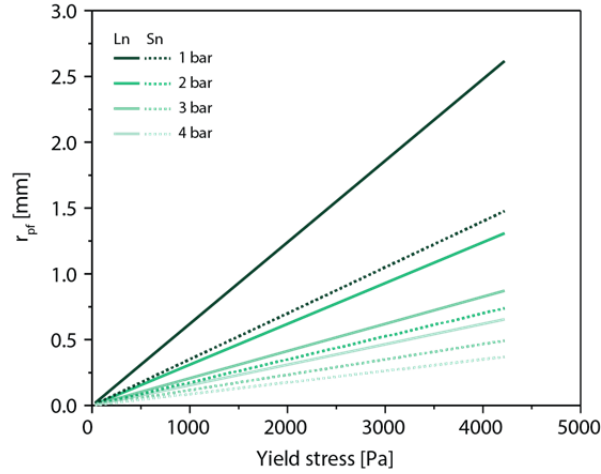


Figure A. 10 Variation of plug flow radius as a function of yield stress of the ink for long nozzles (Ln) and short nozzles (Sn) at different applied pressure differences (from 1 to 4 bar).

Pressure drop along 3D quartz extrusion unit

The above analysis of the shear stress profile in the extrusion nozzle assumes that the pressure at the entrance of the nozzle is equivalent to the external pressure applied by the printer. Here, we show that this is a reasonable assumption for the extrusion unit typically used for 3D printing, which is schematically shown in Figure A. 11.

The pressure at different positions along the extrusion unit can be estimated using Bernoulli's energy conservation law:

$$\rho g h_1 + \frac{\rho V_1^2}{2} + P_1 = \rho g h_2 + \frac{\rho V_2^2}{2} + P_2 \quad Eq. 4$$

where v_x, h_x, P_x , refer to the velocity, the height and the pressure at point $x=1$ or 2 along the printer's extrusion unit (Figure A. 11). ρ, g refer to the density and the gravitational constant, respectively.

The average velocities described in this equation can be estimated using the following relations:

$$Q = \frac{\Delta P * \pi * R^4}{\eta * 8 * l} \quad Eq. 5$$

and

$$Q = \pi R^2 * V_{avg} = \pi * R^2 * \frac{V_m}{2} \quad Eq. 6$$

Where ΔP is the pressure difference, R is the radius of the capillary, l is the length and $V_m = 2 * V_{avg}$, V_m being the maximum velocity and V_{avg} being the average velocity.

Because of flow conservation, the flow rate at the distinct segments of the extrusion unit are equivalent, such that: $Q_1 = Q_2 = Q_3$.

For the typical dimensions shown in Figure A. 11, we use the above equations to finally compare the actual pressures along the extrusion unit. Taking a 20 wt % CNC ink with viscosity of 5 Pas as an example (Table A. 4), we conclude that the pressure at the entrance of the nozzle (segment 3, Figure A. 11) is comparable to the pressure applied by the 3D printer (segment 1, Figure A. 11). This demonstrates the validity of the assumption used for the estimation of the shear stress profile across the nozzle.

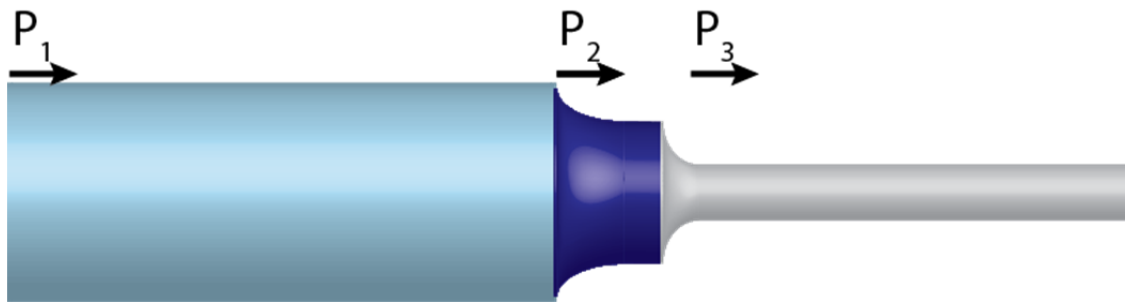


Figure A. 11 Schematic representation of the pressures along the extrusion unit of the 3D printer.

Table A. 4 Geometrical data from a selected extrusion unit.

Parameters	Area 1	Area 2	Area 3
Radius	R1 = 1.26 cm	R2 = 1.54 mm	R3 = 0.15 mm
Length	L1 = 10 cm	L2 = 1 cm	L3 = 8 cm
Pressure	P1 = 3 bar	P2 = ~3 bar	P3 = 2.999 bar
Velocity average	V1 = $2.41 \cdot 10^{-7}$ m/s	V2 = $1.613 \cdot 10^{-5}$ m/s	V3 = 0.0017 m/s

Appendix A9: Particle alignment in the 3D printing nozzle

The fraction of CNC particles aligned during extrusion-based 3D printing can be estimated by determining the shear rate profile within the nozzle (see discussion in the main text). If the rheological properties of the ink are known, the shear rate profile across the printing nozzle can be determined from the shear stress profile. In our analysis, the non-Newtonian properties of the CNC inks are described using two different flow models: a power law or the Herschel-Bulkley model. Here, we calculate the shear rate profile expected for each one of these models and utilize the obtained results to predict the critical nozzle radius for particle alignment (r_c) for an exemplary CNC ink.

Power law

In power law model, the viscosity of the fluid (η) depends on the shear rate ($\dot{\gamma}$) as follows:

$$\eta = k\dot{\gamma}^{n-1} \quad Eq. 7$$

where k is the flow consistency index and n is the flow behavior index.

Our experimental data shows that this relation describes well the non-Newtonian flow behavior of CNC inks containing 15 wt % (Figure 2.3b, main text) and 20 wt % of particles (Figure A. 12c).

For a power-law fluid the velocity profile across the nozzle radius ($v(r)$) can be described as follows¹⁰⁻¹²:

$$v(r) = \frac{3n+1}{n+1} \frac{Q}{\pi R^2} \left(1 - \left(\frac{r}{R} \right)^{1+\frac{1}{n}} \right) \quad Eq. 8$$

The shear rate profile is obtained with the derivative of the above equation:

$$\dot{\gamma} = \frac{dV}{dr} = -\frac{3n+1}{n} \frac{Q}{\pi R^3} \left(\frac{r}{R} \right)^{\frac{1}{n}} \quad Eq. 9$$

Because the time needed for particle alignment (t) depends on the local shear rate, the above equation can be used to estimate the critical radius above which particle alignment is expected (r_c).

From the experimental data shown in the main text (Figure 2.2f), we know that for low shear rates the alignment time can be reasonably described as follows:

$$t = \frac{\beta(\Phi)}{\dot{\gamma}} \quad Eq. 10$$

where $\beta(\Phi)$ is a scaling factor that depends on the concentration of CNC particles in the ink (Figure 2.2g).

The critical alignment radius r_c can be estimated by comparing the alignment time (t) with the residence time (t_{res}) of the ink within the nozzle:

$$t_{res} = \frac{\pi R^2 L}{Q} \quad Eq. 11$$

Introducing Eq. 13 into Eq. 12 and assuming $t = t_{res}$, we obtain:

$$\frac{\beta(\Phi)}{L} = -\frac{3n+1}{nR} \left(\frac{r_c}{R} \right)^{\frac{1}{n}} \quad Eq. 12$$

By re-arranging Eq. 12, one can eventually show that:

$$\frac{r_c}{R} = \left[\frac{R\beta(\Phi)n}{L(3n+1)} \right]^n \quad \text{Eq. 13}$$

which quantifies the effect of the nozzle geometry (L and R) and the rheological properties of the fluid (β and n) on the critical alignment radius.

For a given ink composition with well-defined particle concentration (constant β), we can expect the relative critical radius for alignment (r_c/R) to scale with the relative length of the nozzle (L/R) as follows:

$$\ln\left(\frac{r_c}{R}\right) \sim -n \ln(L/R) \quad \text{Eq. 14}$$

This scaling relationship highlights the fact that the critical radius alignment strongly depends on the length of the nozzle. Such a dependence arises from the increase in residence time with longer nozzles. The estimated thickness of the aligned CNC layer (λ) falls directly from the equations above, since $\lambda = R - r_c - r_{pf}$. Thus, we conclude that nozzles with longer relative length should increase the thickness of the aligned layer.

Herschel-Bulkley model

As an alternative to the power law relation, the rheological properties of non-Newtonian fluids may also be described by the Herschel-Bulkley model, which takes the yield stress as an explicit fluid property.^{13, 14}

In the Herschel-Bulkley model, the shear stress (τ) depends on the shear rate ($\dot{\gamma}$) according to the relation:

$$\tau = \tau_y + k\dot{\gamma}^n \quad \text{Eq. 15}$$

where τ_y is the yield stress of the fluid, k is the viscosity parameter, and n is the shear thinning coefficient.

Fitting the equation above to our experimental data shows that the Herschel-Bulkley can indeed be used to quantify the rheological behavior of the ink containing 20 wt % of CNC particles (Figure A. 12d). A yield stress of 200 Pa was fixed in this fitting.

Following the rationale explained in the previous section, we estimate the critical alignment radius (r_c) from the shear rate profile within the printing nozzle.

Using the fluid parameters described in the Herschel-Bulkley model, the velocity profile can be written as¹⁵:

$$v(r) = \frac{nR}{\tau_w(n+1)} \left(\frac{1}{k}\right)^{\frac{1}{n}} \left[(\tau_w - \tau_y)^{\frac{n+1}{n}} - \left(\frac{\tau_w r}{R} - \tau_y\right)^{\frac{n+1}{n}} \right] \quad Eq. 16$$

where R is the total radius of the pipe, and τ_w is the shear stress at the nozzle wall. τ_w can be calculated from the equation:

$$\tau_w = \frac{R \Delta P}{2L} \quad Eq. 17$$

Eventually, the shear rate can be obtained by deriving the velocity equation with respect to the radius r , which leads to:

$$\dot{\gamma} = \frac{dV}{dr} = \left(\frac{1}{k}\right)^{\frac{1}{n}} \left[\left(\frac{\tau_w r}{R} - \tau_y\right)^{\frac{1}{n}} \right] \quad Eq. 18$$

Using this equation, one can arrive at the following estimation for the critical alignment radius (r_c) based on the Herschel-Bulkley model:

$$r_c = r_{pf} + \frac{2k}{\Delta P} L^{1-n} \left(\frac{\beta Q}{R^2 \pi} \right)^n \quad Eq. 19$$

Analysis of shear rate profile across the nozzle and critical alignment radius for a printing nozzle

The theoretical analysis outlined above is used now to graphically illustrate the shear rate profile and the radial position within the nozzle where particle alignment is expected (r_c) for a 20 wt % CNC ink. In this example, the ink is extruded through a printing nozzle with a length of 31 mm and diameter of 0.41 mm at an external pressure of 1.9 bar. The shear stress radial distribution under such printing conditions is shown in Figure A. 12a. Such shear stress distribution was converted to the shear rate profile using either the power law or the Herschel-Bulkley model, leading to the plots shown in Figure A. 12e, f. Because the Herschel-Bulkley model already incorporates the ink yield stress into the flow equation, the estimated shear rate profile covers the entire radius range. By contrast, the power law applies only to the differential flow region of the nozzle, leading to a shear rate profile that covers the range $R < r < r_{pf}$. Overall, the Herschel-Bulkley model predicts a slower and more gradual increase in shear rate from the center towards the wall of the nozzle (Figure A. 12e, f). Compared to the power law model, the expected shear rates at the nozzle wall are also an order of magnitude lower. Based on the empirical correlation obtained in our study for the shear-induced alignment dynamics of the CNC particles (equation 1, main text), we can estimate the alignment time (t) expected at the different shear rates developed across the radius of the nozzle (Figure A. 12e, f). Comparison of this alignment time with the residence time of the ink within the nozzle (equation 14), we can finally estimate the critical alignment radius (r_c) for the different fluid models employed in our analysis. Interestingly, although the maximum shear rate predicted from the Herschel-Bulkley model is ten-fold lower than that

expected from the power law equation, the thickness of the aligned CNC layer lies within the same order of magnitude independent of the model chosen. Our analysis suggest that a layer thickness in the range 10-30 μm is expected if only shear-induced alignment is considered (untapered nozzles).

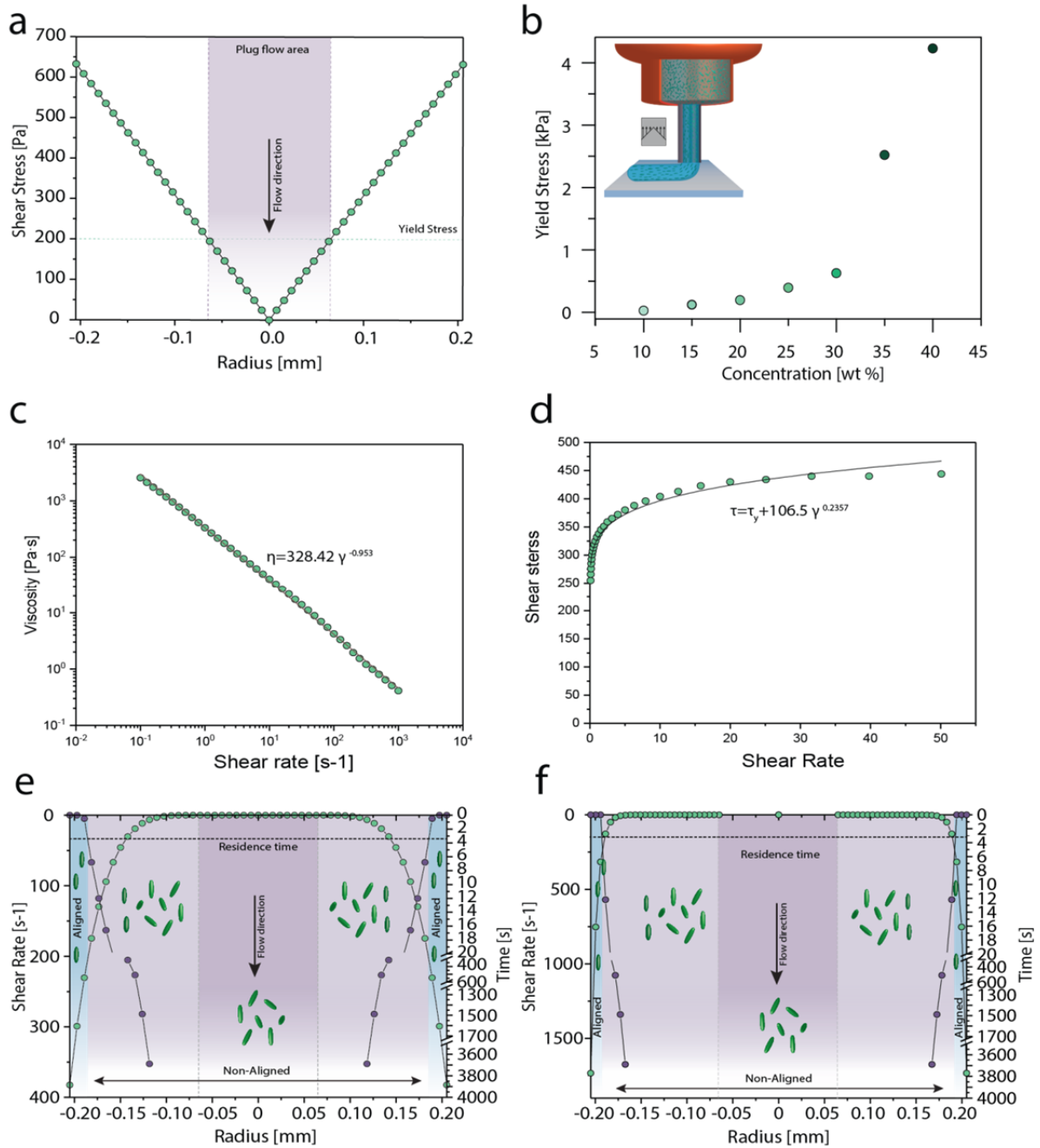


Figure A. 12 Analysis of the flow behavior of a 20 wt % CNC ink through a 31 mm long 3D printing nozzle. (a) Dependence of the experimental yield stress on the CNC concentration of the inks. (b) Calculated shear stress distribution within the nozzle. (c) Experimental viscosity as a function of shear rate fitted using a power law. (d) Experimental data of the shear stress as a function of shear rate and the fitting obtained using the Herschel-Bulkley model. (e,f) Shear rate distribution and corresponding time for alignment of CNCs expected from (e) the Herschel-Bulkley theory and (f) the power law model.

References

1. Volker-Pop, L.M., Optical Methods in Rheology: Polarized Light Imaging. *Chem Listy*, **2014**. 108: p. 707-710.
2. Gray, D.G. and M. Roman, Self-Assembly of Cellulose Nanocrystals: Parabolic Focal Conic Films, in *Cellulose Nanocomposites*. 2006, American Chemical Society. p. 26-32.
3. Hubbe, M.A., P. Tayeb, M. Joyce, P. Tyagi, M. Kehoe, K. Dimic-Misic, and L. Pal, Rheology of Nanocellulose-Rich Aqueous Suspensions: A Review. 2017. Vol. 12. 2017.
4. Favier, V., H. Chanzy, and J.Y. Cavaille, Polymer Nanocomposites Reinforced by Cellulose Whiskers. *Macromolecules*, **1995**. 28: p. 6365-6367.
5. Dufresne, A., Nanocellulose from Nature to High Performance Tailored Materials. 2012, Berlin Walter de Gruyter GmbH.
6. Mueller, S., E.W. Llewellyn, and H.M. Mader, The Rheology of Suspensions of Solid Particles. *Proceedings of the Royal Society a-Mathematical Physical and Engineering Sciences*, **2010**. 466: p. 1201-1228.
7. Maron, S.H. and P.E. Pierce, Application of Ree-Eyring Generalized Flow Theory to Suspensions of Spherical Particles. *J. Colloid Sci.*, **1956**. 11: p. 80-95.
8. Kitano, T., T. Kataoka, and T. Shirota, An Empirical Equation of the Relative Viscosity of Polymer Melts Filled with Various Inorganic Fillers. *Rheol. Acta.*, **1981**. 20: p. 207-209.
9. Reed, J.S., Introduction to the Principles of Ceramic Processing. *Wiley*, **1988**
10. Savvas, T.A., N.C. Markatos, and C.D. Papaspyrides, On the Flow of Non-Newtonian Polymer Solutions. *Applied Mathematical Modelling*, **1994**. 18: p. 14-22.
11. White, F.M., Fluid Mechanics. 2011: McGraw Hill.
12. Munson, B.R., T.H. Okiishi, W.W. Huebsch, and A.P. Rothmayer, Fundamentals of Fluid Mechanics. 2013: Wiley.
13. Feilden, E., C. Ferraro, Q. Zhang, E. Garcia-Tunon, E. D'Elia, F. Giuliani, L. Vandeperre, and E. Saiz, 3d Printing Bioinspired Ceramic Composites. *Sci Rep*, **2017**. 7: p. 13759.
14. Leppiniemi, J., P. Lahtinen, A. Paajanen, R. Mahlberg, S. Metsa-Kortelainen, T. Pinomaa, H. Pajari, I. Vikholm-Lundin, P. Pursula, and V.P. Hytonen, 3d-Printable Bioactivated Nanocellulose-Alginate Hydrogels. *ACS Appl Mater Interfaces*, **2017**. 9: p. 21959-21970.
15. Feilden, E., C. Ferraro, Q. Zhang, E. García-Tuñón, E. D'Elia, F. Giuliani, L. Vandeperre, and E. Saiz, 3d Printing Bioinspired Ceramic Composites. *Scientific Reports*, **2017**. 7: p. 13759.

Appendix B

Appendix to “Complex-shaped cellulose composites made by wet densification of 3D printed scaffolds”

Appendix B1: X-ray diffraction (SAXS) results for a 10 wt % CNC Ink.

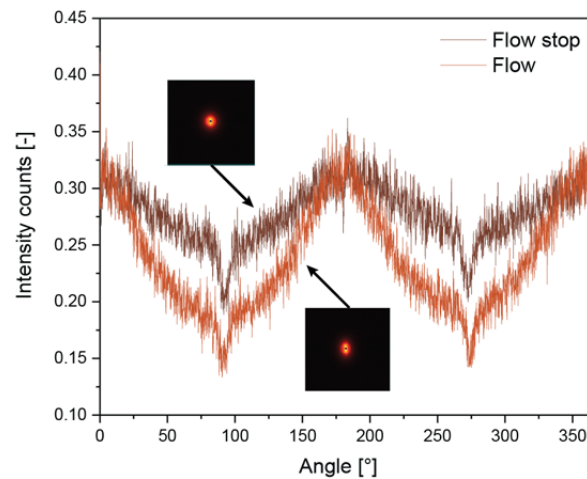


Figure B. 1 SAXS measurements obtained for cellulose nanocrystal inks with 10 wt %CNC under flow and after the flow was stopped. From these diffractograms we measured the full width at half maximum (FWHM) values of 74.5 and 101.6° for inks under flow and after the flow ceased, respectively.

Appendix B2: Angle variation along the capillary length

The quartz capillaries utilized in this project display a slightly tapered geometry. To quantify the level of tapering along the length of the capillary, we measured the angle of the wall relative to the longitudinal axis at 5 different positions along the capillary. The results are shown in Table B. 1. In the first 15 mm of the capillary, the tapering angle continuously decreases from 7.69 ° to 2.35 °, while the 60 mm that follow the entry point shows a tapering lower than 2 °.

Table B. 1 Angle variation along the capillary.

	Position	Angle [°]
1	5-10 mm	7.69
2	10-15 mm	2.35
3	15-30 mm	1.77
4	30-40 mm	0.71
5	40-60 mm	0.60
6	60-80 mm	0

Appendix B3: SAXS measurements along the capillary's length and radius.

Small angle X-ray scattering (SAXS) measurements performed across the capillary over extended time periods are shown in Figure B. 2a. The sample was measured under two different conditions: (i) during flow and (ii) after flow followed by an extended resting period (Figure B. 2b, c). The degree of alignment of the CNC particles was shown to be stable after the flow stopped and over a period of at least 17 h. Measurements across the radius of the capillary were also acquired by moving the beam from one edge to another of the capillary so as to sample different fractions of the material within the capillary. The results indicate that the degree of alignment varies following a parabolic profile and does not change significantly over time. The degree of alignment was found to decrease (increase in FWHM) from the walls towards the center of the capillary. The FWHM data exhibit the symmetric behavior expected for that type of geometry (Figure B. 2b, c). However, the resolution is not as precise as that achieved by cSAXS due to the larger beam size used. With a beam comparable in size to the diameter of the capillary (300 μm) the spatial resolution achieved in these experiments is very limited. Therefore, these experiments were complemented by SAXS measurements performed using a high-coherence beam line at synchrotron facilities.

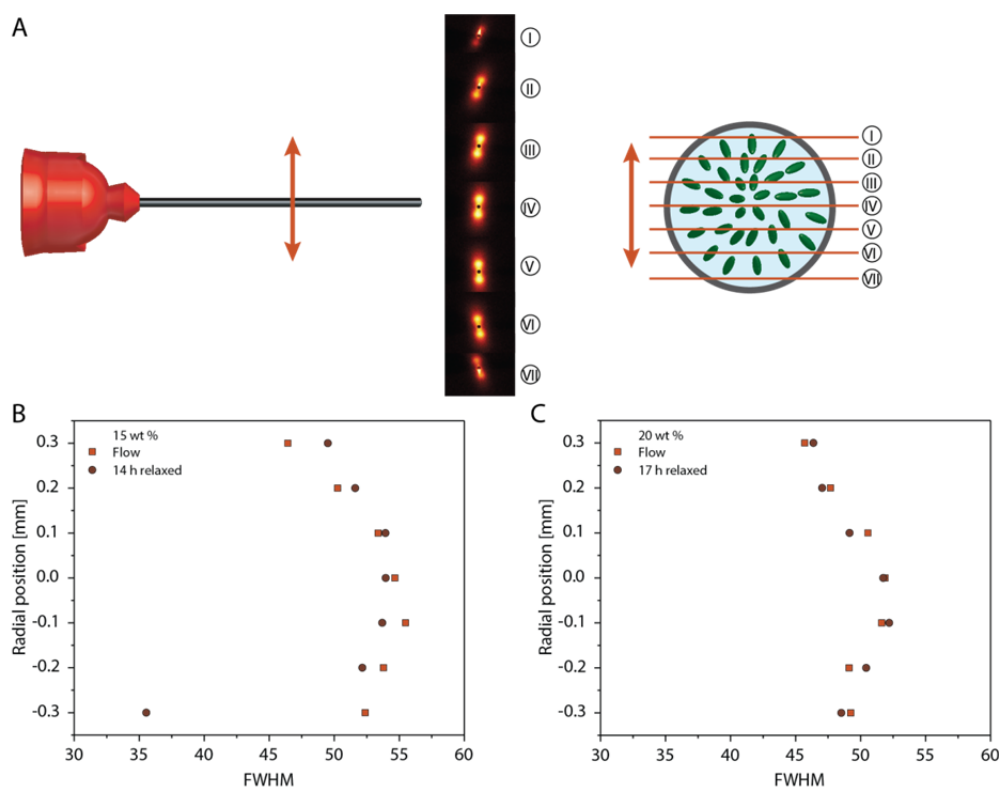


Figure B. 2 Alignment of CNC particles across the radius of the capillary for suspensions containing 15 and 20 wt % CNCs. A) Schematic representation of the experimental setup indicating the scattering patterns measured at different radial positions within the capillary. B,C) Evolution of the FWHM values along the radius of the capillary for (B) 15 wt % and (C) 20wt% CNC suspensions before and after a relaxation time of 14 and 17h, respectively.

In addition to the radial position, the degree of alignment of the CNCs along the length of the capillary was also quantified using SAXS measurements (Figure B. 3). The data obtained support the conclusions derived from the experiments performed using *Coherent Small Angle X-Ray scattering (cSAXS)* at the Paul Scherrer Institute (PSI). By scanning along both the length and the radius of the capillary (Figure B. 3a), we observe tilting of the anisotropic CNC particles close to the capillary walls (Figure B. 3b). Azimuthal integration of the obtained scattering projections allowed us to extract the angular orientation of the nanoparticles and the resulting changes in their orientation from the centre toward the wall of the capillary. Normalization of these data with respect to the centre shows that the tilting effect close to the walls decreases as the suspension moves along the length of the capillary (Figure B. 3d)

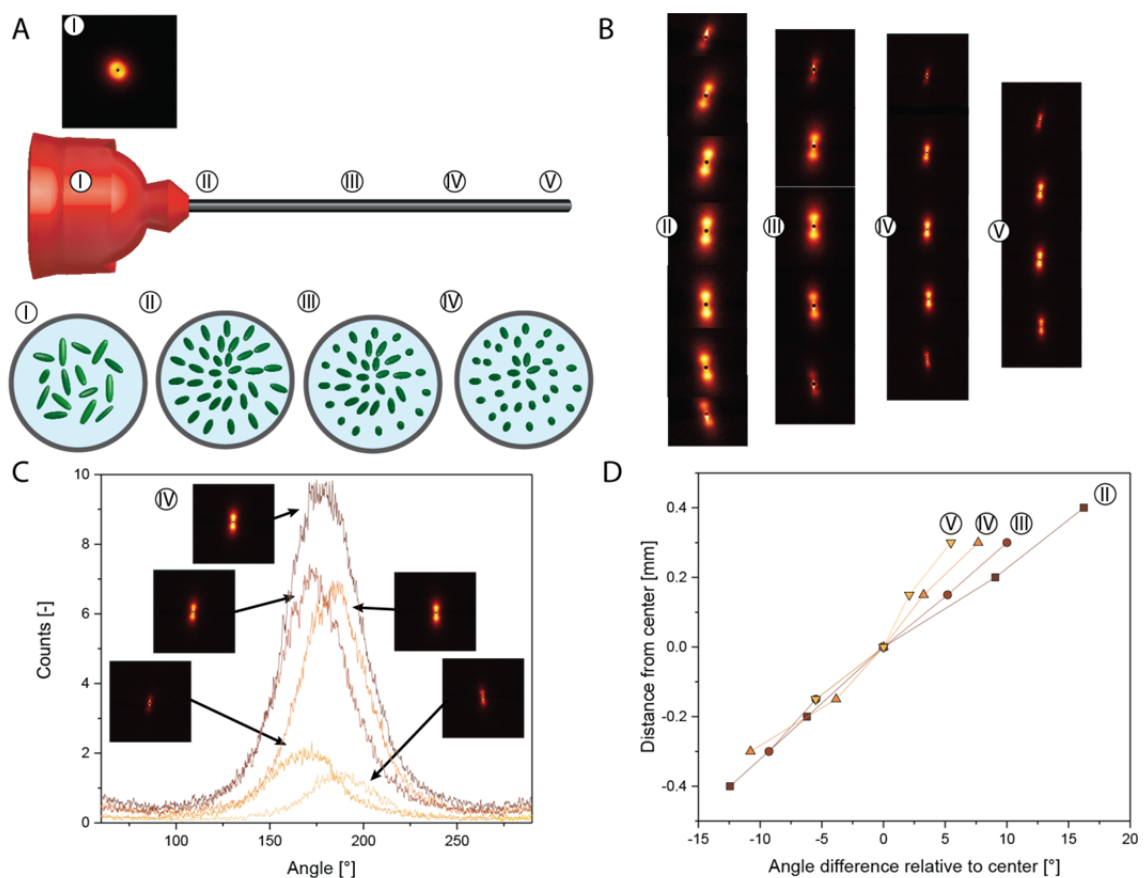


Figure B. 3 Scattering-based measurements of the alignment of cellulose nanoparticles along the length and the radius of the capillary. A) Schematic illustration of the different positions of the capillary where the data were measured. B) Scattering patterns obtained for each position along the radius and the length of the capillary. C) Typical azimuthal integration of the scattering pattern obtained at position IV. D) Difference in alignment angle relative to the centre as a function of the radial position and length of the capillary.

Appendix B4: cSAXS measurements at the Swiss light source (PSI)

cSAXS measurements at the Swiss light source (PSI) confirms the slightly higher alignment of the CNCs at the walls as compared to the centre when the probed suspension is located at the end of the capillary (Figure B. 4 and Figure B. 5).

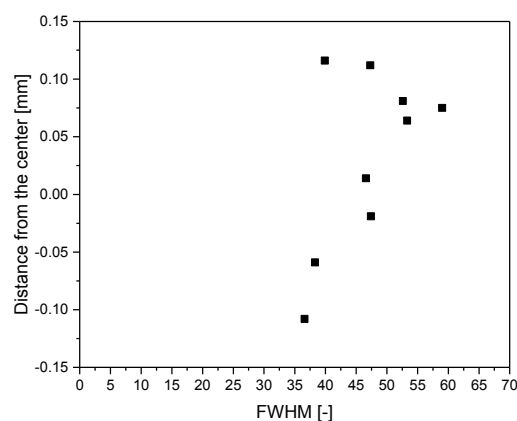


Figure B. 4 Variation of FWHM values as a function of the radial position extracted from 2D scattering projection obtained for a 20wt% ink at the end of the capillary.

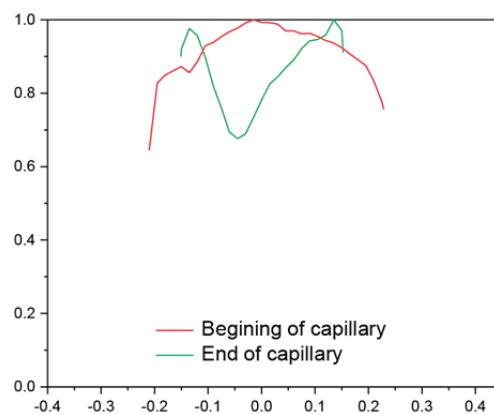


Figure B. 5 Degree of alignment obtained from cSAXS projections of the whole capillary.

The particle alignment data obtained in the cSAXS experiments were analyzed following the procedure described by Liebi *et al.*[1] In this analysis, the actual scattering data is used to generate 3D tomographic images based on a reconstruction protocol. Figure B. 6 and Figure B. 7 are meant to verify if the reconstruction of the tomographic image is correct for samples probed at the beginning and at the end of the capillary, respectively. On the left are the real measured data whereas the simulated counterparts are shown on the right. Each real projection is evaluated and treated using a Matlab code developed and provided by PSI.[1] The code first calculates the preferential orientation and degree of

orientation on a voxel basis and then reconstructs a complete 3D image of the sample. Visual comparison of the real and the simulated images indicates a good qualitative agreement between the obtained particle alignment values, confirming the validity of the reconstruction approach.

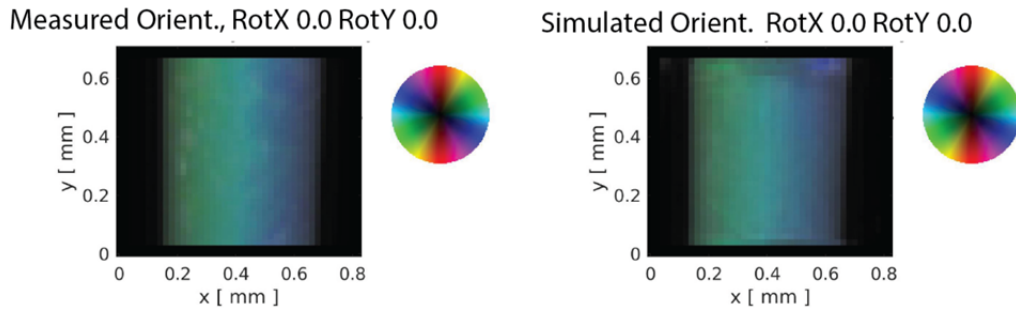


Figure B. 6 Measured and simulated reconstruction of the X-ray scattering 2D projections obtained at the beginning of the capillary for a suspension containing 20 wt % CNC.

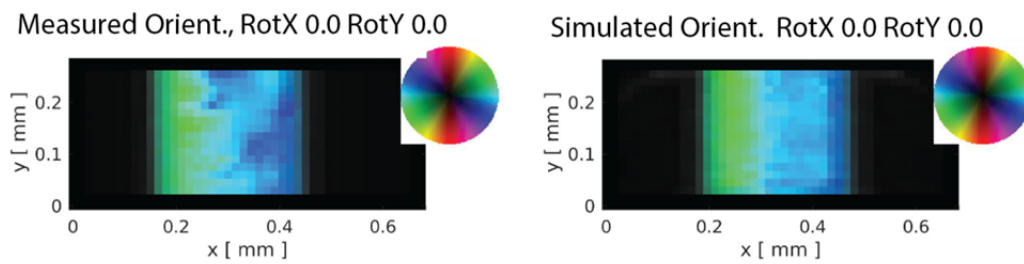


Figure B. 7 Measured and simulated reconstruction of the X-ray scattering 2D projections obtained at the end of the capillary for suspensions containing 20 wt % CNCs.

The quantification of particle alignment using the reconstructed 3D images needs to be carried out by analysing the data obtained in a single slice of the 3D tomographic image, as opposed to the 2D projection of the entire imaged samples. To demonstrate the importance of this slicing procedure, we compare in the local normalized degree of orientation obtained using either slices or 2D projections from the 3D tomographic reconstruction. These values are obtained by normalizing the degree of orientation by the maximum value found in the sample. Figure B. 8a, c represents a slice (cut) through the centre of the capillary at the beginning and the end of the capillary, respectively. Figure B. 8b,d displays the 2D projection of the whole capillary. In the latter case, the relative degree of orientation is extracted from the data by averaging in column the local degree of orientation from each line. Results obtained for both the beginning and the end of the capillary show that the use of 2D projections overestimates the particle alignment degree in the centre of the capillary (Figure B. 8e, f and Figure B. 5). Therefore, the alignment data shown in Figure 3.4c (main text) was obtained from slices of the reconstructed tomographs.

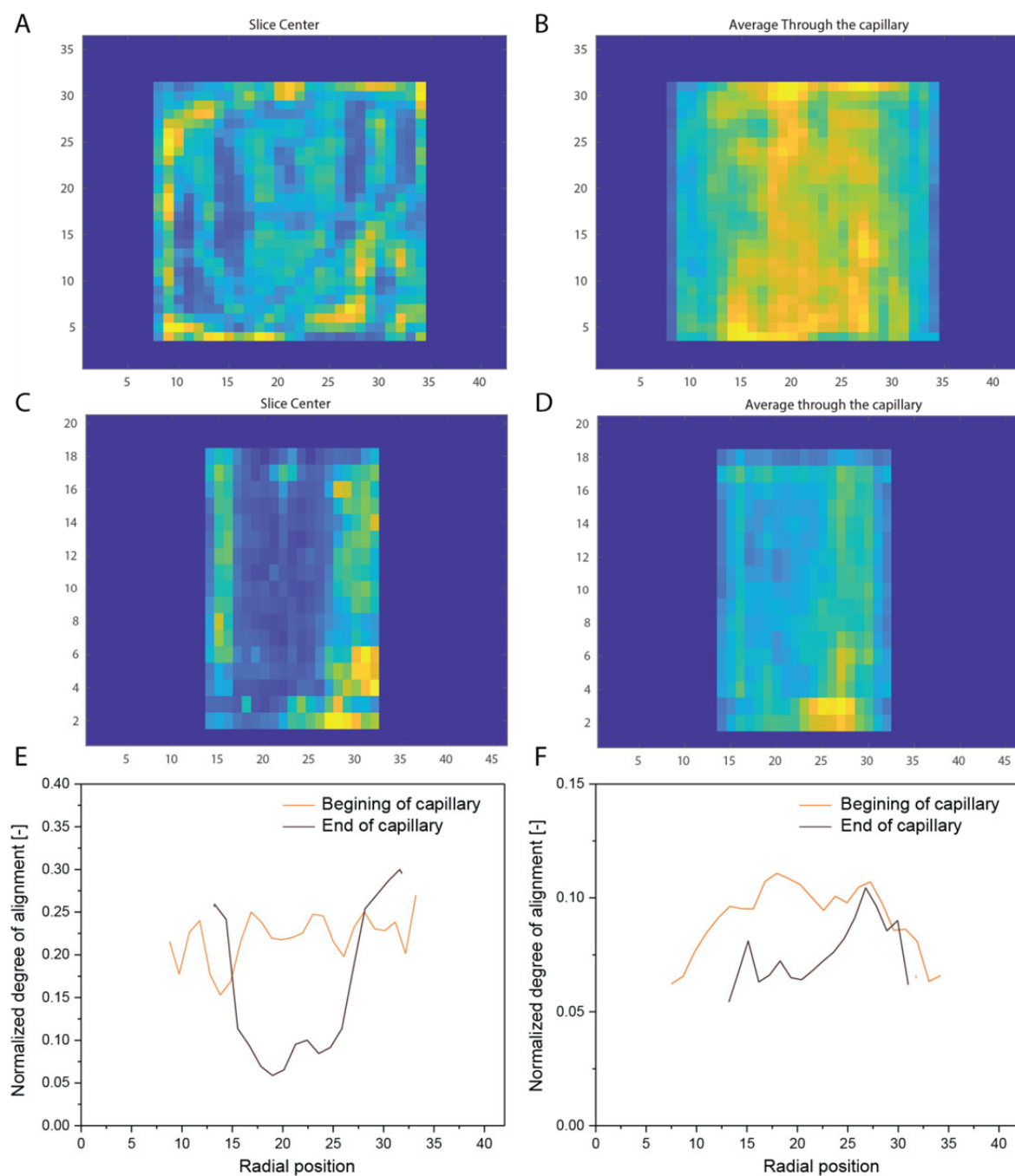


Figure B. 8 Tomography reconstruction and analysis of the degree of particle alignment along the radius of the capillary. A,C) A slice from the centre of the tomography image at (A) the beginning and (C) the end of the capillary. B,D) 2D projection from the whole tomography image at (B) the beginning and (D) the end of the capillary. E,F) Calculated degree of orientation of both (E) slices and (F) 2D projections. The results observed in F) show an identical trend when compared to the real 2D projections (Figure S5). All results show in the figure were obtained for a 20 wt % CNC ink.

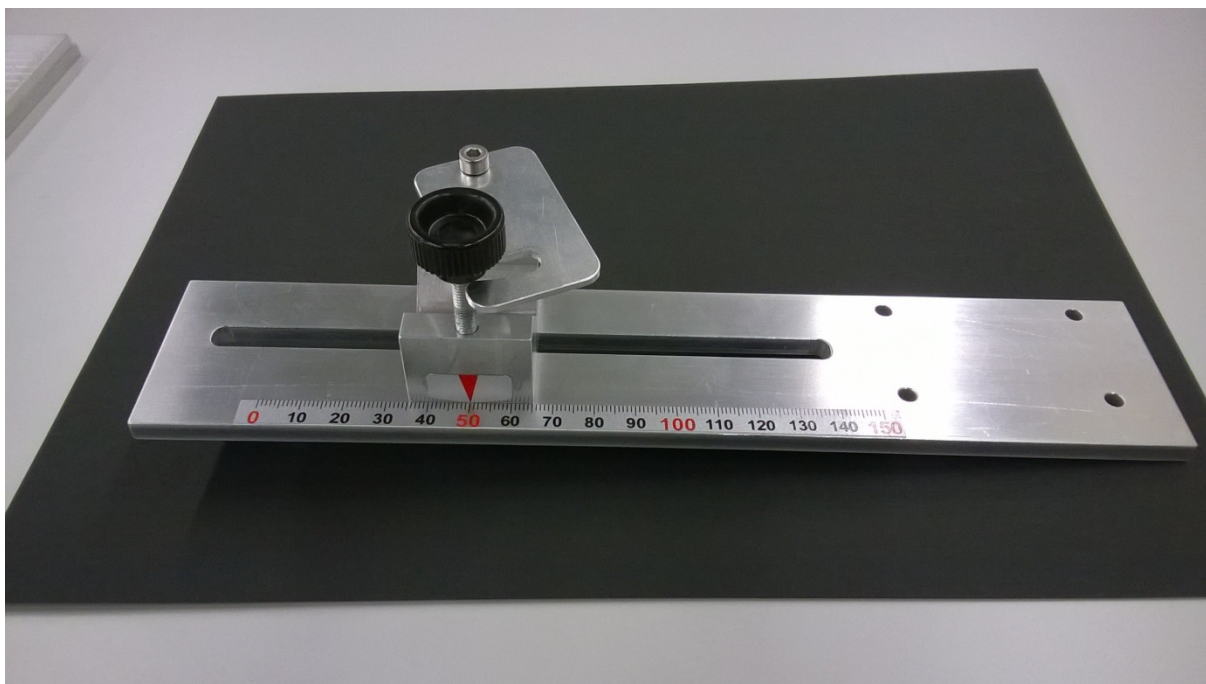
Appendix B5: Cartridge stage utilized for SAXS measurements and for sample preparation

Figure B. 9 Cartridge stage.

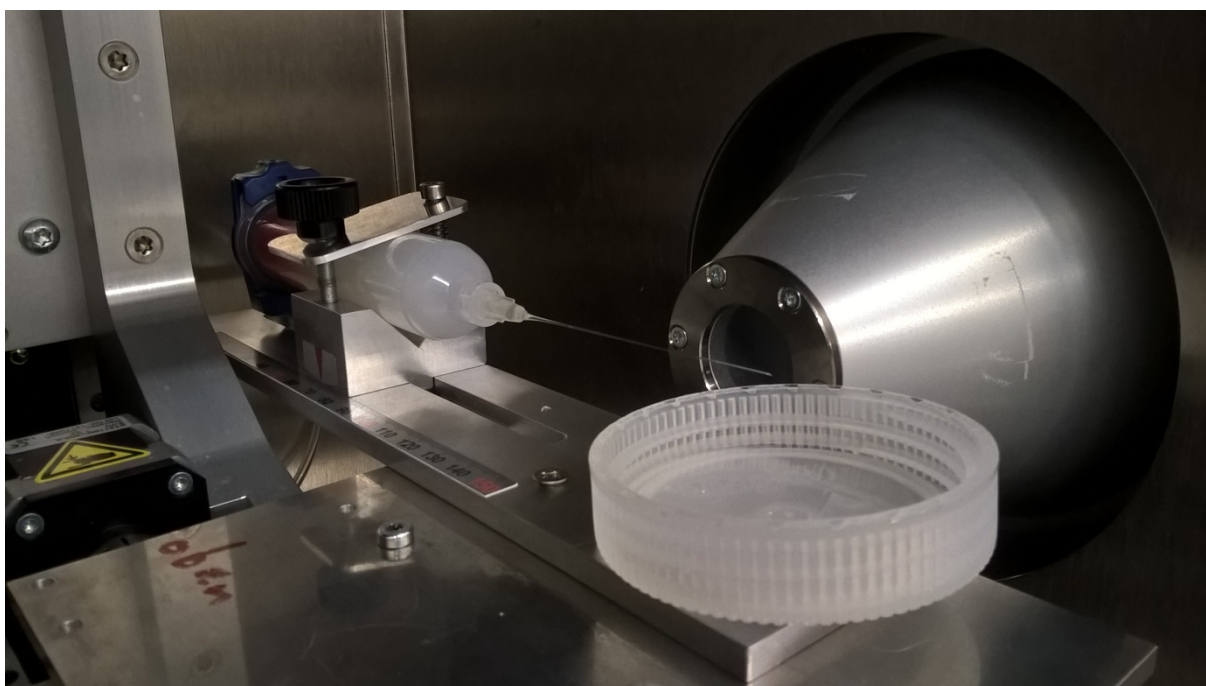


Figure B. 10 Cartridge Stage mounted.

Reference

1. Liebi, M., et al., *Nanostructure surveys of macroscopic specimens by small-angle scattering tensor tomography*. Nature, 2015. **527**: p. 349.

Appendix C

Appendix to “Complex-shaped cellulose composites made by wet densification of 3D printed scaffolds”

Appendix C1: Rheological properties of the ink

The rheological behavior of aqueous suspensions containing CNCs and CNFs was characterized to evaluate their suitability for 3D printing using the direct ink writing technique. To achieve the high yield stress and low-shear storage modulus (G') required for DIW, we first evaluated the effect of CNCs and CNFs on the rheological behavior of the cellulose suspensions (Figure C. 1a, b). The addition of a small fraction of CNF (1.48 wt %) in water is shown to be already enough to establish a percolating network with a well-defined yield stress of 50.2 Pa.¹ Even higher yield stress and modulus values of 200 Pa and 7050 Pa, respectively, can be achieved by simply using a high concentration of CNC particles (20wt %). Experimentally, we found that a combination of 20wt % CNC and 1wt % CNF results in inks with optimum rheological properties for DIW and in printed objects with high dimensional stability during wet densification. The addition of 1wt % CNF to a suspension containing 20wt % CNC increases the yield stress from 200 to 251 Pa and the low-shear storage modulus from 7050 to 8700 Pa Pa (Figure C. 1b).

The rheological response and aging effects of inks with this optimized composition was further evaluated through steady-state and oscillatory measurements (Figure C. 1c, d). The optimum cellulose-based ink exhibits strong shear thinning behavior, as evidenced by the reduction in apparent viscosity by several orders of magnitude upon increasing applied shear rates. Printing experiments showed that the low viscosity values achieved at high strain rates are sufficient to extrude this cellulose-based ink under typical pressures applied at the printer nozzle. This pressure varies between 1 and 2.6 bar depending on the length of the nozzle (nozzle diameter of 0.41 mm). Steady-state and oscillatory rheological measurements indicate that the rheological behavior of the optimum cellulose-based ink remains unaltered if the suspension is stored in the refrigerator over a period of 4 months (Figure C. 1c, d).

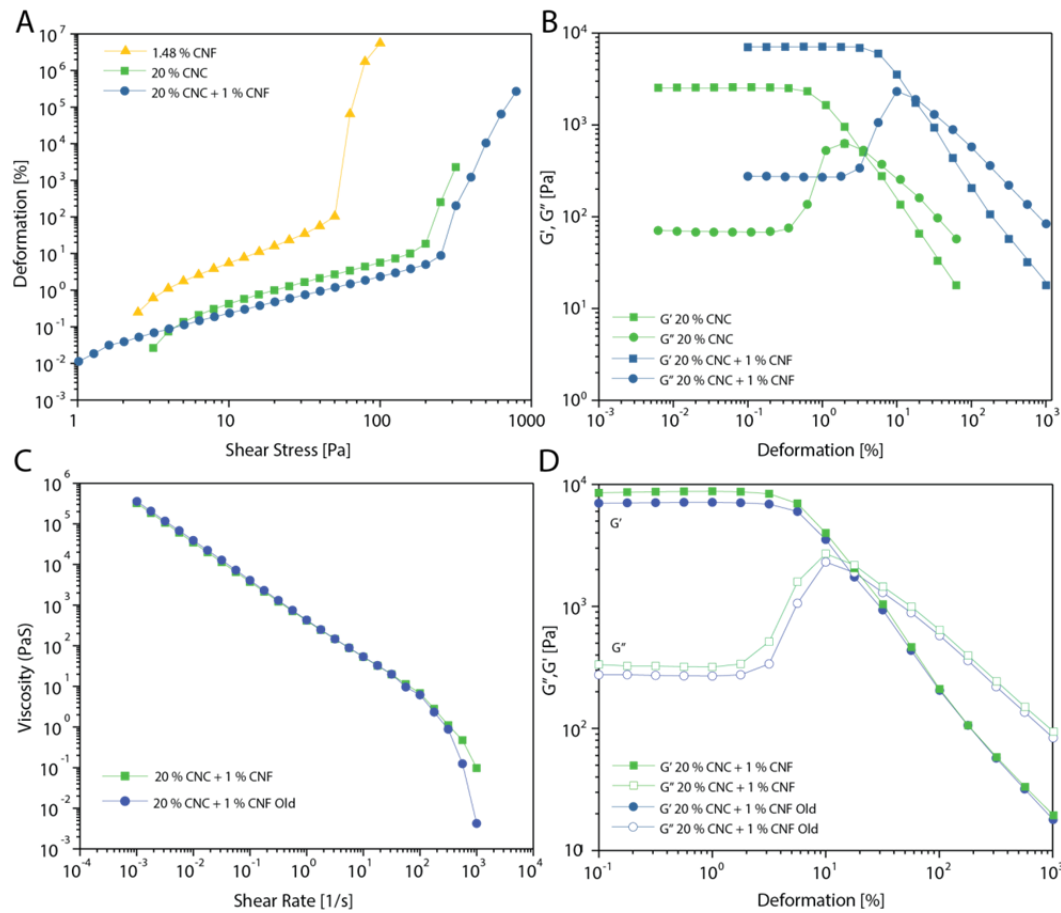


Figure C. 1: Rheological properties of the cellulose-based inks developed in this work. A) Yield stresses of printable inks with different amounts of CNCs and CNFs. B) Storage modulus, G' , and loss modulus, G'' of the cellulose-based ink with and without CNF as a function of the deformation amplitude applied in an oscillatory sweep measurement. C) Shear thinning behavior of the optimum cellulose-based ink evidenced by the decrease in viscosity at high shear rates under steady-state conditions. Such rheological behavior guarantees a consistent flow through the nozzle and enables high accuracy during printing. D) Storage modulus, G' , and loss modulus, G'' of the optimum cellulose-based ink as a function of the deformation amplitude applied in an oscillatory sweep measurement. The aged suspensions were kept in the refrigerator for 4 months.

Appendix C2: Processing routes, morphology of filament after drying and effect on shrinkage with coagulation bath

Wet densification of printed scaffolds and their conversion into cellulose-based composites can be accomplished following different solvent exchange and infusion (infiltration) processes. Figure C. 2 illustrates 3 possible routes to obtain cellulose-reinforced composites.

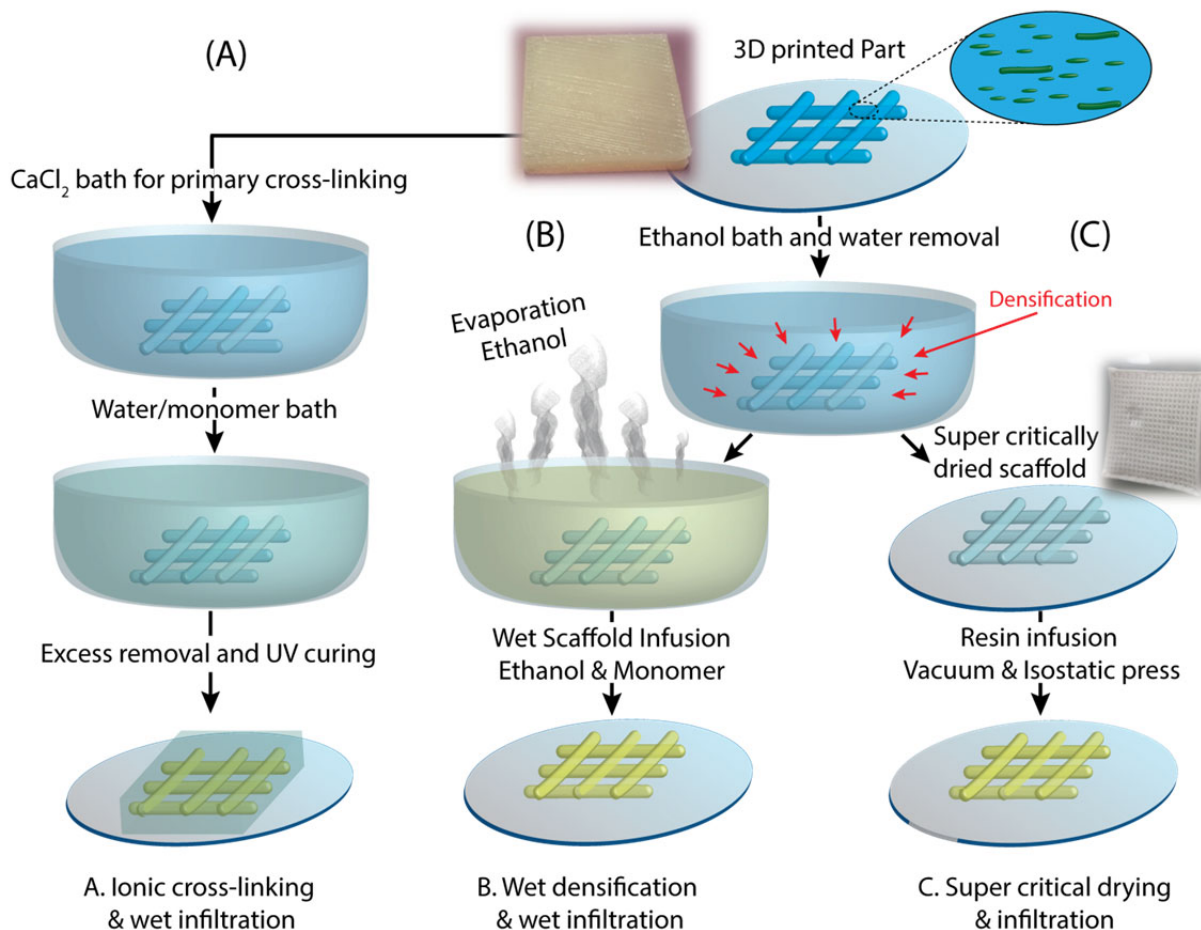


Figure C. 2 Different processing routes explored in this work for the conversion of 3D printed objects into cellulose-based composites. (A) Ionic cross-linking followed by wet infiltration: consolidation (and possibly densification) of 3D printed scaffolds is achieved by dipping them in an aqueous solution of CaCl₂ to induce crosslinking of cellulose particles. The monomer is infiltrated and polymerized while keeping the object in the wet state. (B) Wet densification followed by wet infiltration: densification is achieved via a solvent exchange process in an aqueous bath containing a poor solvent. Monomer infiltration and polymerization occurs in the wet state. (C) Super-critical drying followed by infiltration: water is removed under super-critical conditions and the resulting dried scaffold is infiltrated with a monomer using vacuum and pressure before photopolymerization.

All three methods have their advantages and disadvantages as described in Table C. 1. While the wet densification approach leads to the highest cellulose concentration and offers a broad choice of solvents and polymer systems for densification and infusion, it is also characterized by the most pronounced shrinkage. The addition of CaCl₂ in the cross-

linking approach allows the formation of hydrogels with high water contents that would not be accessible in the absence of Ca^{2+} ions. However, this route is only suitable for the fabrication of hydrogel systems. The super-critical drying approach is a promising method to obtain a dry scaffold with preserved cellulose microstructure, but it requires multiple cumbersome steps and expensive equipment. Examples of complex-shaped structures obtained using the cross-linking and wet densification approaches are depicted in Figure C. 3 and Figure C. 4.

Table C. 1 Comparison between the different approaches used to fabricate composites from 3D printed structures.

Ionic cross-linking & wet infiltration	Advantages	<ul style="list-style-type: none"> - Formation of hydrogels with varying degrees of cross-linking by changing the calcium concentration in the water/solvent mixture. - Possibility to infiltrate the wet scaffold with different monomer compositions - Improved shape fidelity resulting from the ionic cross-linking
	Limitations	<ul style="list-style-type: none"> - High content of residual water leads to shape distortion if dried - High cellulose content is only possible if cross-linking is combined with the wet densification approach
Wet densification & wet infiltration	Advantages	<ul style="list-style-type: none"> - Higher densification resulting from the complete elimination of the good solvent (water) - Wide choice of solvents possible - Wide choice of polymer systems possible depending on the solvent mixture used
	Limitation	<ul style="list-style-type: none"> - Large shrinkage resulting from the densification process - Thickness limitation, maximal dense thickness limited at 5 mm
Super Critical drying & infiltration	Advantages	<ul style="list-style-type: none"> - Dried scaffold with preserved printed microstructure - Post infiltration of different polymer matrices is possible
	Limitations	<ul style="list-style-type: none"> - Typical high viscosity of the polymer system makes infiltration process challenging. Solvents potentially improve infiltration, but require multiple infusion steps. - High pressures are usually required to aid infiltration

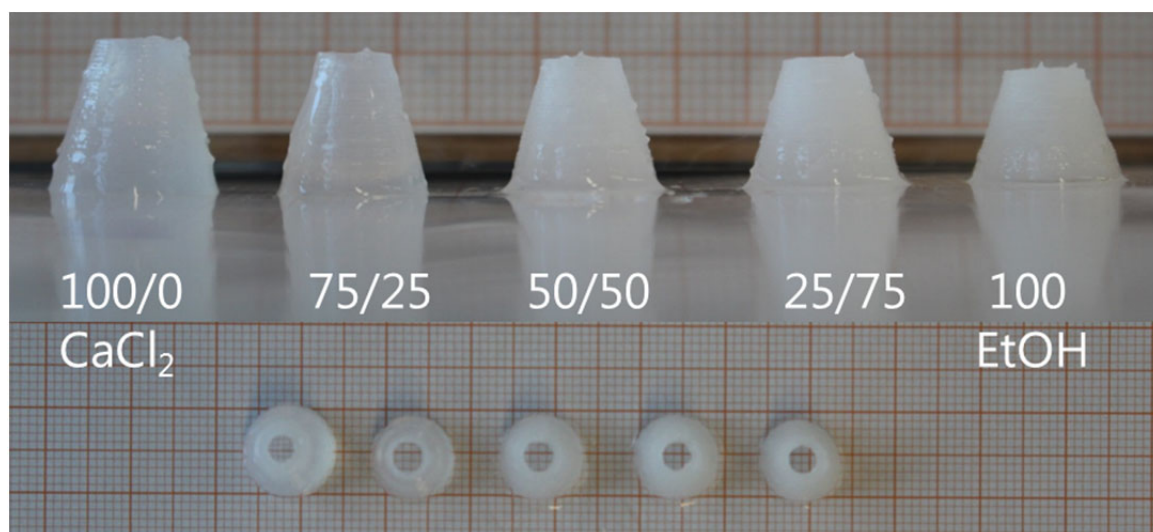


Figure C. 3 Effect of ionic crosslinking with calcium chloride and ethanol on the shrinkage of a printed object immersed in solvent baths containing distinct fractions of CaCl_2 -containing water (4 wt %) relative to ethanol. Increasing the weight fraction of ethanol in the bath from 0 (far left) to 100 % (far right) leads to a higher densification and shrinkage. The minimum unit length in the background scale corresponds to 1 mm. The upper row shows side view, whereas the bottom row displays top view.

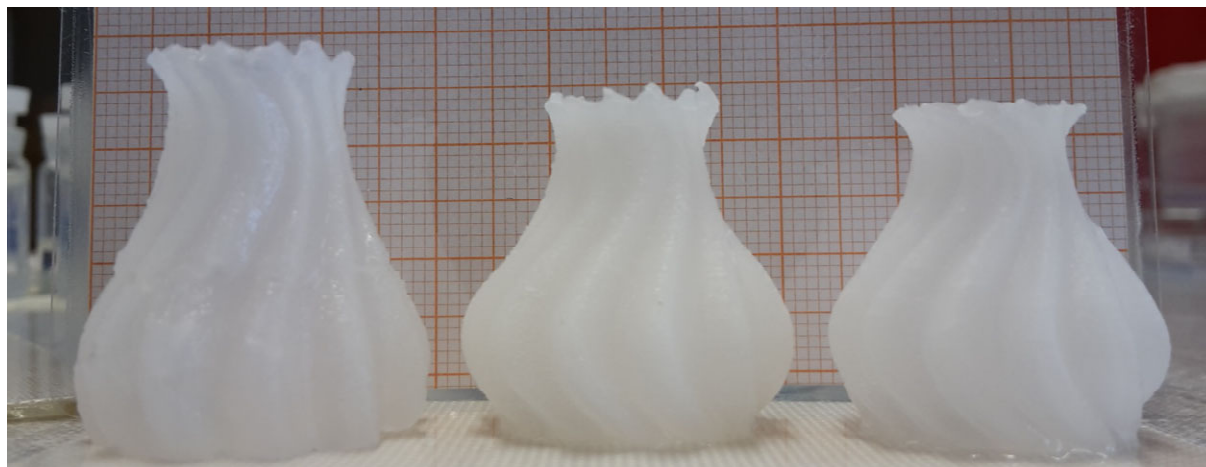


Figure C. 4 Examples of complex-shaped cellulose-based structures obtained right after printing (left) and after cross-linking (center) or wet densification (right). Left: geometry printed with aqueous CNC/CNF hydrogel ink. Center: as-printed geometry after being immersed in CaCl_2 aqueous solution and ethanol (100 wt % ethanol). Right: as-printed geometry immersed directly into ethanol (without ionic crosslinking). The minimum unit length in the background scale corresponds to 1 mm.

Appendix C3: Hansen Solubility parameters

The three different Hansen solubility parameters accounting for dispersive (δ_D), polar (δ_P) and hydrogen bonding (δ_H) molecular interactions were used to assess the quality of the solvent mixtures applied in the wet densification process (Table C. 2).

Table C. 2 Hansen solubility parameters taken from references 2-5.

Solvent	Dispersive δ_D	Polar δ_P	Hydrogen bonding δ_H
Water single molecule	15.5	16.0	42.3
Water >1% soluble in	15.1	20.4	16.5
Water Total miscibility	18.1	17.1	16.9
Ethanol	15.8	8.8	19.4
Acetone	15.5	10.4	7
Acetonitrile	15.3	18	6.1
DMSO	18.4	16.4	10.2
DMF	17.4	13.7	11.3

For mixtures of different solvents, we apply the following simple rule of mixtures to determine the resulting solubility parameter of the mixture:⁶

$$\delta_i = \sum_{k=1}^n \phi_k \delta_{i,k} \quad Eq. 1$$

where δ_i is the solubility parameter of the mixture considered, with $i=P, D, H$ corresponding to polar, dispersive and hydrogen bonding contributions, respectively; $\delta_{i,k}$ and ϕ_k are the solubility parameters and volume fraction, respectively, of solvent k ; and n is the total number of solvents in the mixture. Based on previous work on the interactions of cellulose with water molecules and other solvents, we chose in our analysis the solubility parameters for “water >1% soluble in” to quantify the Hansen solubility values of water (Table C. 2).^{3, 5}

By quantifying the quality of the solvent mixture, the solubility parameters calculated with the above equation allowed us to interpret the macroscopic swelling or shrinkage behavior of the cellulose-based printed objects after immersion in the solvent bath (Figure C. 5). The swelling or shrinking data measured in the selected solvents are in very good agreement with earlier observations made by Bruel et al.³ and were used to calculate the concentration of cellulose (solids content) in the object after solvent exchange (Figure 4.2, main text).

To correlate the experimentally observed swelling/shrinking behavior (Figure C. 5) with the solubility parameters of the solvent mixture, we represent in a ternary phase diagram (Figure C. 6 and Figure 4.1) the composition of the solvent baths according to the

relative contributions of dispersive, polar and hydrogen bonding interactions in that particular mixture. These relative contributions were calculated using the following equation 7:

$$f_i = \frac{\delta_i}{\delta_D + \delta_P + \delta_H} \quad Eq. 2$$

Where i is the type of molecular interaction of interest (D, P or H).

The ternary diagram shows that shrinkage and densification of the object occurs when the solvent mixture exhibits a set of relative Hansen parameters that are positioned away from the values where cellulose particles are expected to be well dispersed (green area in Figure C. 6 and Figure 4.1). A direct correlation between the shrinkage (solids content) and the Hansen solubility parameters is eventually obtained by taking into account the relative change in cohesive energy density resulting from the solvent exchange process, as explained in the main text.

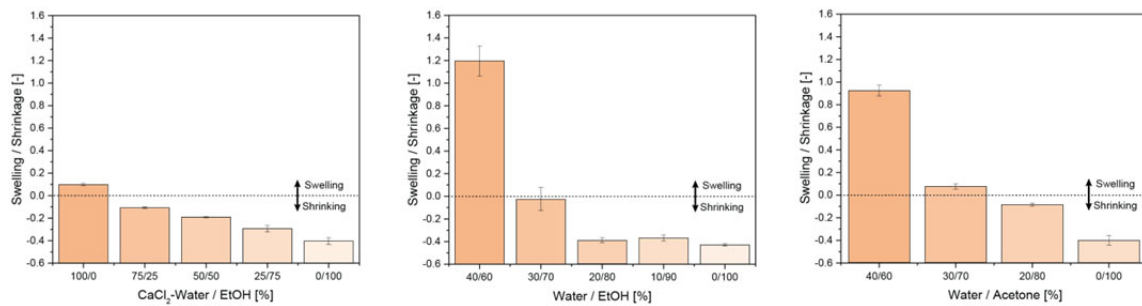


Figure C. 5 Swelling/shrinking behavior of as-printed samples when submerged in different solvent mixtures. Shrinkage/swelling data refer to the ratio between sample length before immersion and initial sample length. For water/EtOH and water/acetone mixtures, samples were found to completely disintegrate if the ethanol concentration is lower than 60%.

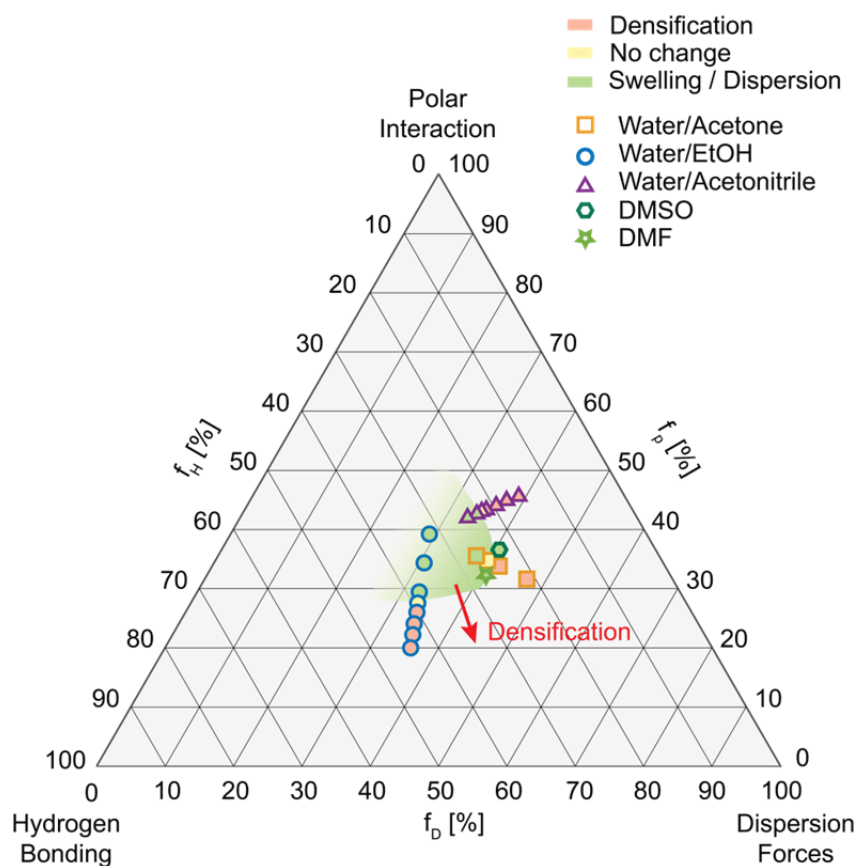


Figure C. 6 Correlation between the densification behavior of cellulose-based scaffolds immersed in different solvent baths and the relative Hansen solubility parameters of the solvent mixtures.

Appendix C4: Drying and infiltration of 3D printed scaffolds

Because polymer-based inks containing high concentrations of CNCs exhibit prohibitively high viscosities to allow extrusion through the printer nozzle, 3D printing of aqueous-based cellulose suspensions followed by infiltration of dried printed scaffolds with a reactive monomer is an effective processing strategy to fabricate complex-shaped composites with high cellulose content. To evaluate the most appropriate procedure to remove the aqueous phase of printed structures that are later infiltrated, we compared the effect of room-temperature drying, freeze-drying and supercritical-drying (SCD) on the morphology and dimensional stability of 3D printed objects. For this purpose, we used aqueous-based inks containing 20 wt % cellulose nanocrystals (CNC) and 1 wt % nanofibrillated cellulose (CNF).

While room-temperature drying resulted in stiff but brittle parts with low dimensional stability, freeze-drying and super-critical drying allowed for the preparation of porous cellulose scaffolds with relatively good shape retention (Figure C. 7). Super-critical drying required the exchange of water with ethanol, which led to significant densification and shrinkage of the printed part due to the net change in cohesive energy density of the solvent (see main text). In spite of the strong shrinkage, the printed parts maintained their shape and presented an interconnected porous structure after super-critical drying.

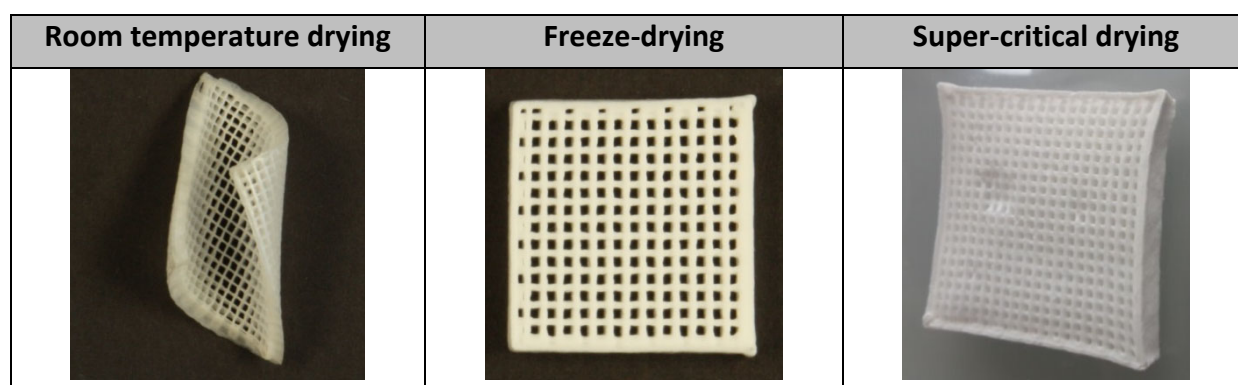


Figure C. 7 Photographs of the 3D printed scaffolds after drying using different procedures.

The high porosity generated upon drying makes the 3D printed scaffolds very fragile, but sufficiently strong to be infiltrated with a liquid monomer. Composites were fabricated by infiltrating the porous scaffolds with a monomer mixture under vacuum followed by cold isostatic pressing (3500 bar for 5 min). The monomer mixture consisted of commercial HEMA/PUA oligomers (BR3741 from Dymax) at a weight ratio of 50/50 and Irgacure 819 as a photoinitiator. The pronounced shrinkage of samples subjected to super-critical drying increased the volume fraction of cellulose from 13.8 vol % up to 29.9-39 vol %. The lower porosity of the resulting structures makes these samples particularly challenging to infiltrate even after being subjected to intensive vacuum and isostatic pressing cycles. Indeed, careful inspection of infiltrated scaffolds using optical microscopy indicates the presence of residual

porosity and polymer-rich regions in samples produced via super-critical drying (Figure C. 8). The high pressure subsequently applied to the infiltrated SCD samples also introduces macroscopic defects in the composite structure, which impair their mechanical properties (Figure C. 9c, d). These flawed specimens contrast with the pore-free microstructures obtained using the wet infiltration route Figure C. 9e, f).

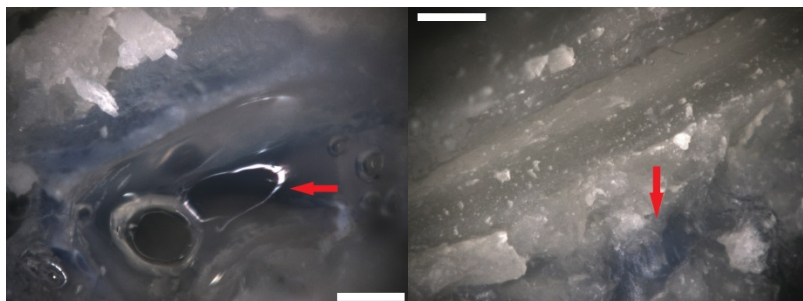


Figure C. 8 Optical microscopy images showing residual porosity and polymer-rich regions (indicated by red arrows) after infiltration of monomers in a super-critically dried scaffold followed by photopolymerization (scale bar 500 μm).

Although the absence of solvent exchange protocols has made freeze-casting a popular route for the fabrication of cellulose-based composites,⁸⁻¹⁰ the formation of ice crystals during the freezing step leads to a partial loss of the alignment of CNCs imposed during printing (Figure C. 9a) and prevents densification of the scaffold. Instead, the approaches involving solvent exchange result in much denser microstructures displaying high degree of orientation of the cellulose particles (Figure C. 9e, f).¹¹

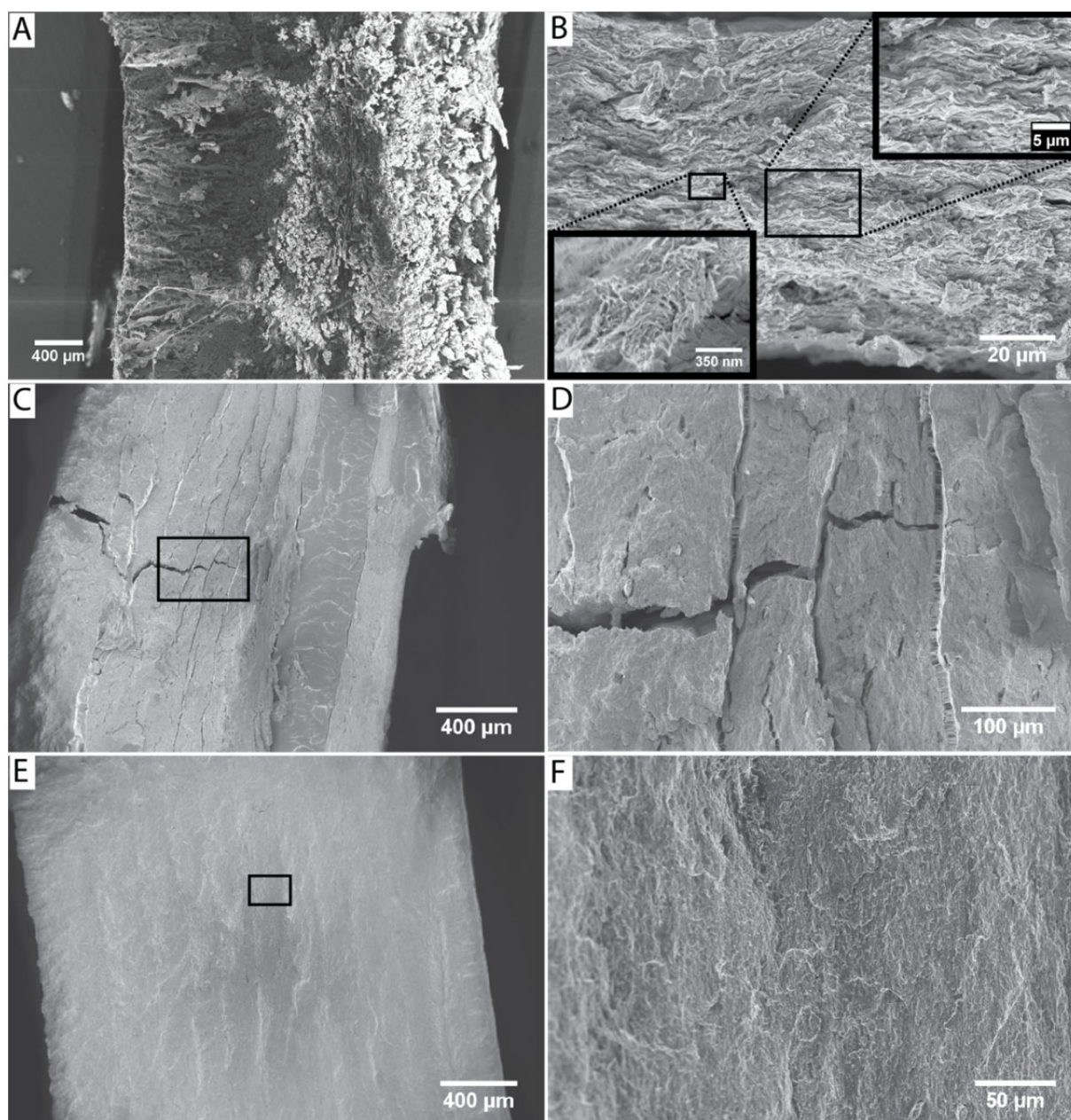


Figure C. 9 SEM images showing cross-sections of 3D-printed scaffolds before and after infiltration. Densified scaffolds obtained by (A) freeze-drying of aqueous-based samples and (B) super-critical drying of specimens immersed in ethanol. (C-D) Composites (infiltrated scaffolds) obtained by infiltration of super-critically dried scaffolds with photocurable monomers using alternate cycles of vacuum and isostatic pressing. (E-F) Composites obtained through the wet-infiltration process.

Appendix C5: Quantification of CNC alignment by 2D WAXD analysis

To explore our technology for the fabrication of bioinspired architectures it is crucial to quantify the level of alignment achieved during the 3D printing process and after infiltration of the densified scaffolds with monomers to generate the CNC-based composites (Figure C. 10). We quantified the level of nanocellulose alignment in single filaments and printed objects before and after infiltration using 2D wide-angle X-ray diffraction (Figure C. 10c-f). Printed objects were manufactured by depositing filaments next to each other so as to form a film, the height of which was twice the filament diameter. The X-ray diffraction data obtained for single filaments and printed objects show the expected strong alignment of the CNC/CNF particles along the printing direction. This is indicated by the two intensity peaks detected in the azimuthal X-ray scans spanning 360 ° in Phi (Figure C. 10c-f). The degree of alignment obtained in this study is comparable to that obtained in previous work using direct ink writing.¹ Infiltration of the nanocellulose filaments and printed films with the monomer result in less intense diffraction peaks, but does not alter the highly aligned nature of the structure (Figure C. 10c-f and Appendix C8 and C9). Because the chosen polymer phase exhibits a similar refractive index to the cellulose nanoparticles, composites with remarkable optical transparency are obtained after infiltration and polymerization of the cellulose-based printed films (Figure C. 10g and Appendix C10). The high transparency achieved also results from the high chemical affinity between the monomer and the nanocellulose, which is essential to promote wetting of the particles and prevent the formation of air pockets in the infiltrated structures.

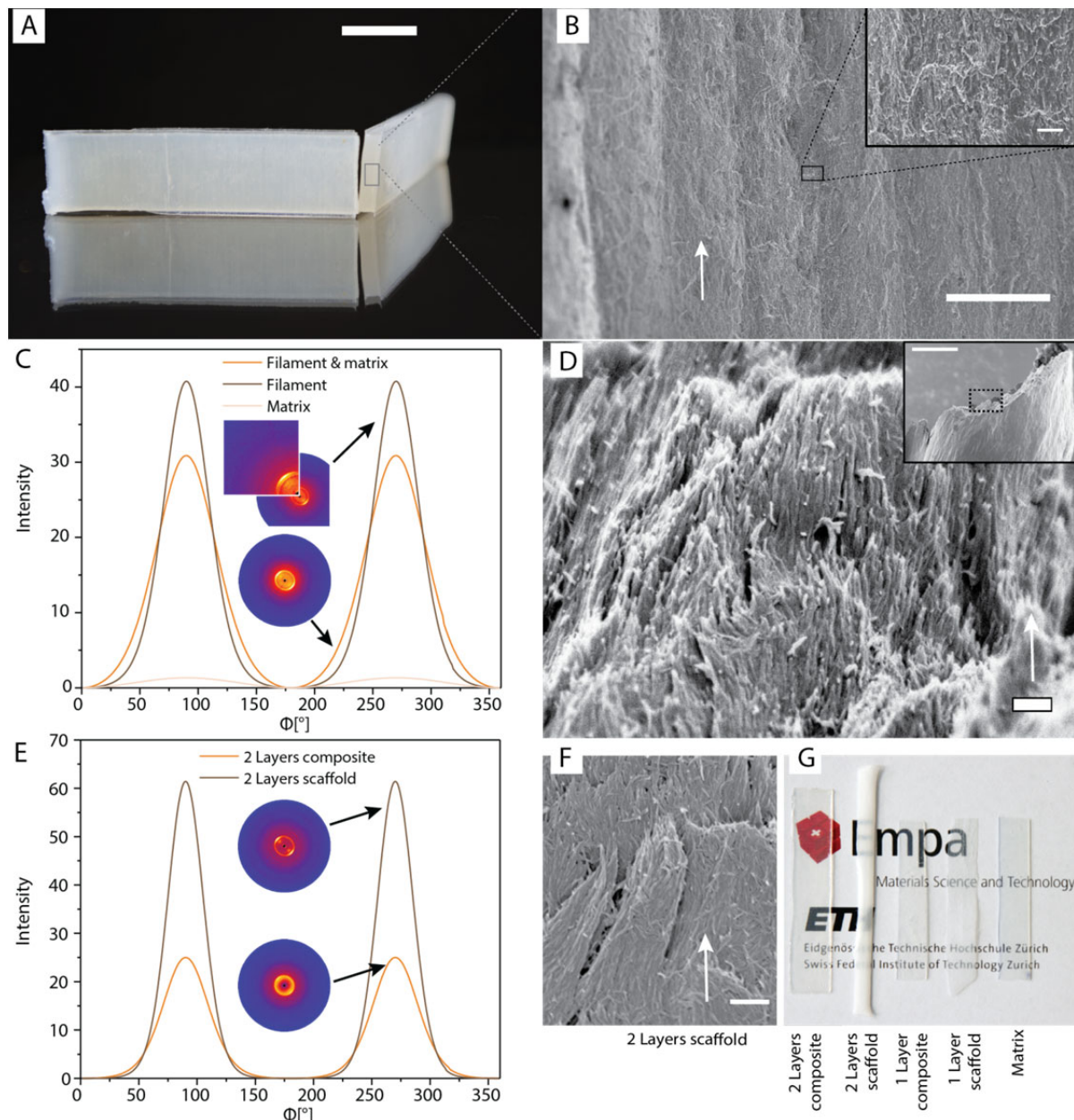


Figure C. 10 Structural characterization of cellulose-based filaments and printed objects before and after infiltration with a polymer matrix. (A) 3D-printed composite fabricated through the wet densification approach (scale bar 1 cm), highlighting in the cross-section shown in (B) the good filament adhesion within the object. Scale bars: 200 μm in (B), and 10 μm in the inset of (B). The white arrow in (B) indicates one printed line. (C) 2D-WAXS profiles of pure matrix, single scaffold filament and infiltrated scaffold filament. (D) SEM image of single filament before infiltration showing high degree of alignment along the printing direction (white arrow). Scale bar: 200 nm. The inset shows the location of the imaged area within the filament (scale bar, 10 μm). (E) 2D-WAXS profiles of 2 printed layers before (scaffold) and after infiltration with the polymer matrix (composite). (F) SEM view of the 2 layer printed scaffold (scale bar, 400 nm). (G) Optical transparency of pure polymer matrix, 3D printed dry scaffolds and composite films with 1 and 2 layers.

2D-WAXS measurements of 3D printed filaments, layers and infiltrated composites were performed to quantify the preferential alignment of CNCs induced by shear and extensional forces developed during the extrusion process. The degree of CNC orientation (π) of distinct structures are summarized in Table C. 3. All the CNC-containing samples show preferential cellulose alignment along the printing direction. The addition of CNFs slightly decreases the degree of orientation from 80 % to 74 %. This is expected as the higher flexibility of CNFs lead to stronger inter-fiber entanglement during flow. An additional loss in degree of orientation from 74 % to 66 % is also observed when the filament is infiltrated with photocurable monomers and polymerized. Because the first layer is typically squeezed onto the glass slide to ensure proper adhesion, composites comprised of only one layer show a slightly lower degree of orientation (61 %) as compared to single filaments (66 %) or printed parts containing 2 layers (74 % and 80 %). The results also reveal that infiltration of scaffolds comprised of two layers leads to a slight loss of degree of orientation from 80 % to 74 %. These values for the degree of orientation are in good agreement with data previously measured for both 3D printed structures and shear-aligned films.^{1, 12}

Table C. 3 Degree of orientation for 3D printed parts, filaments and composites obtained by 2D WAXS analysis.

Sample	FWHM [°]	Degree of orientation π [%]
Pure Matrix	(-)	(-)
Pure CNC Filament	36	80
Pure CNC/CNF Filament	46	74
CNC/CNF Filament composite	61	66
1 layer composite	70	61
2 layers composite	46	74
2 layers scaffold	36	80

(-)Homogeneous intensity

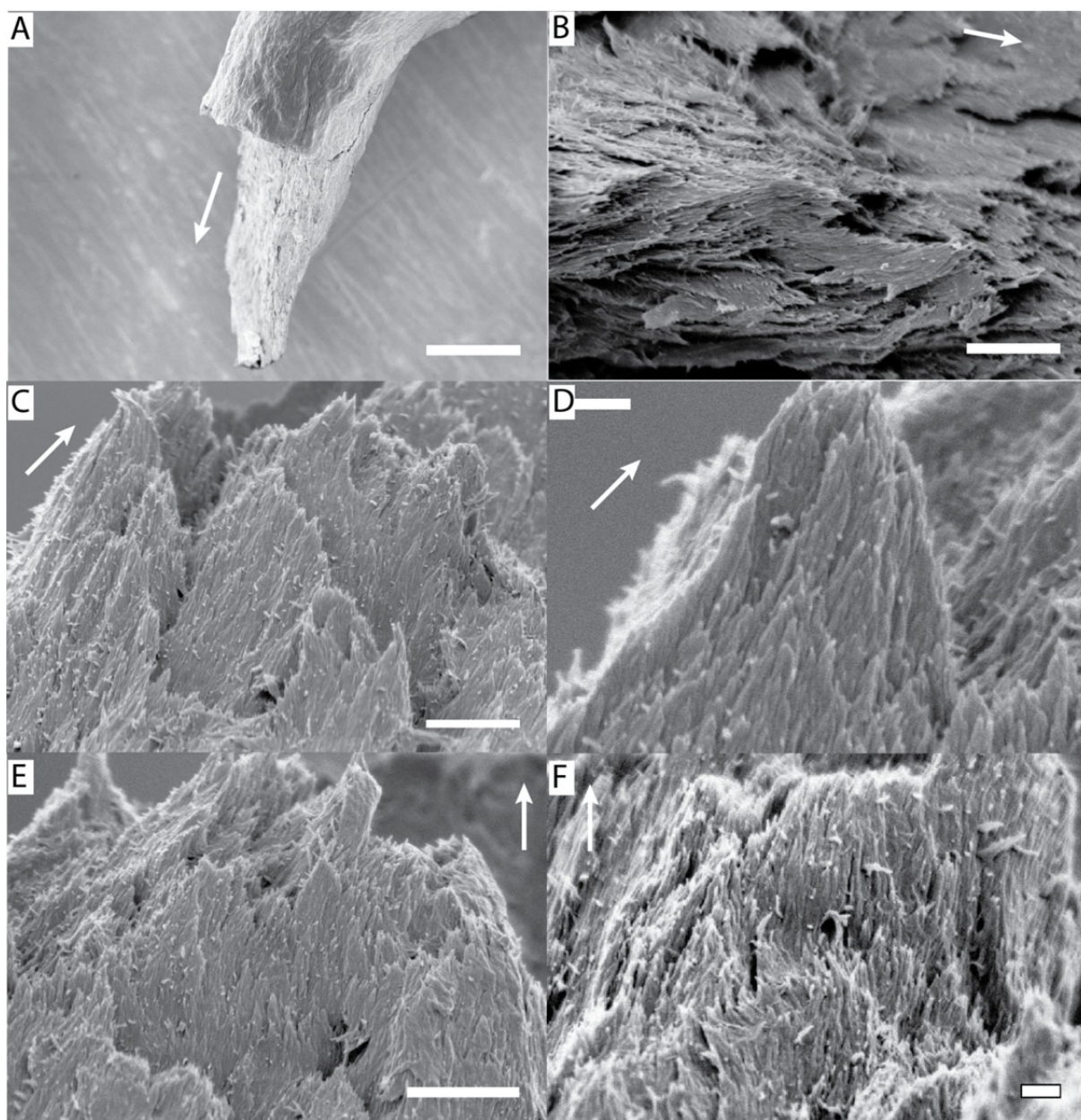
Appendix C6: Morphology of aligned cellulose crystals in printed structures

Figure C. 11 SEM images of fractured surfaces of printed filaments after drying, depicting the preferential alignment of CNCs/CNFs along the printing direction. Scale bars: A:100 μm , B, C and E:1 μm , , D and F: 200 nm. The white arrows indicate the printing direction.

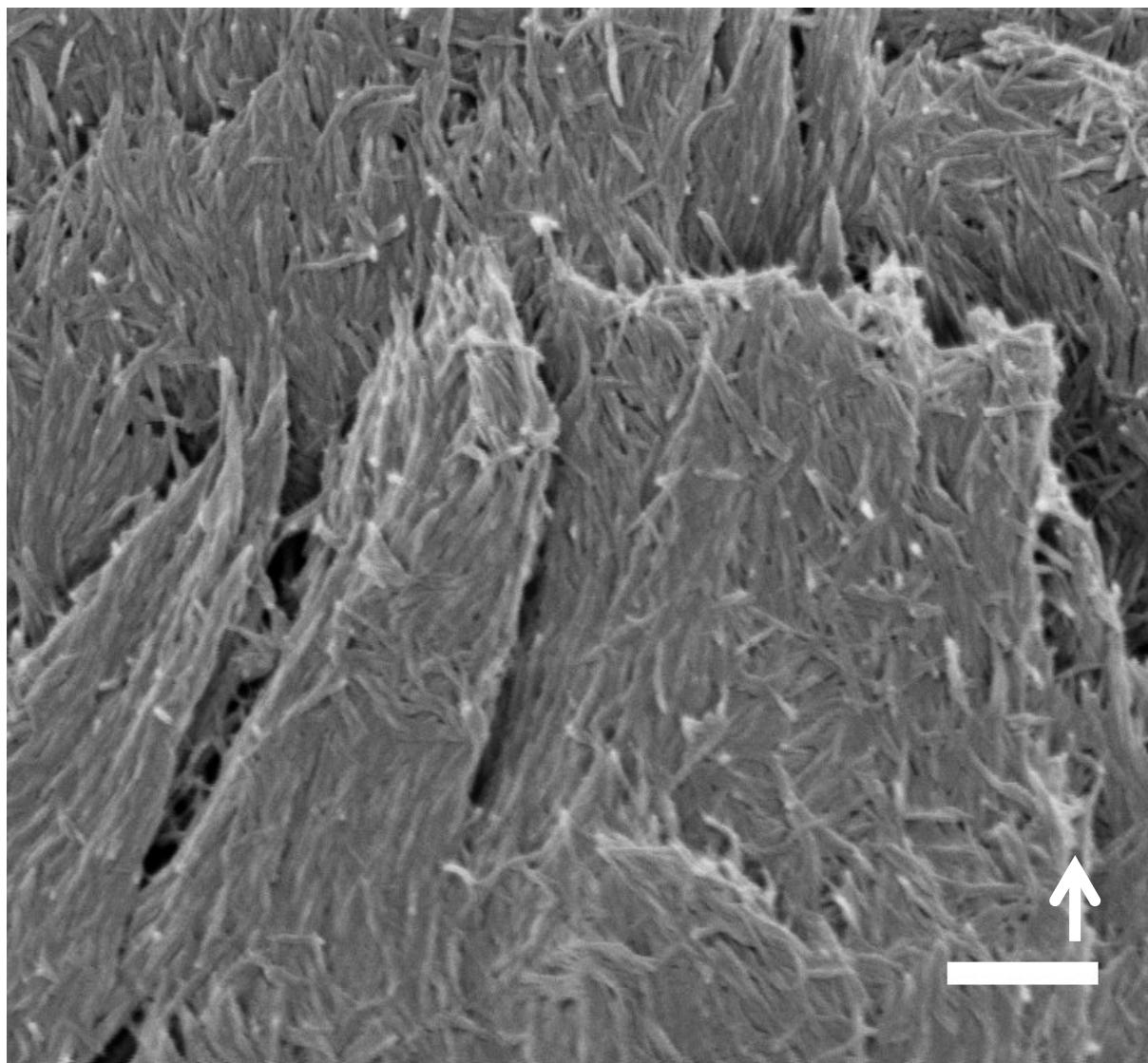


Figure C. 12 SEM image of a delaminated 3D printed scaffold depicting the preferential alignment of CNCs and CNFs along the printing direction. (Scale bar 400 nm). Arrow indicates the printing direction.

Appendix C7: Microstructure of composites obtained via wet densification and infiltration

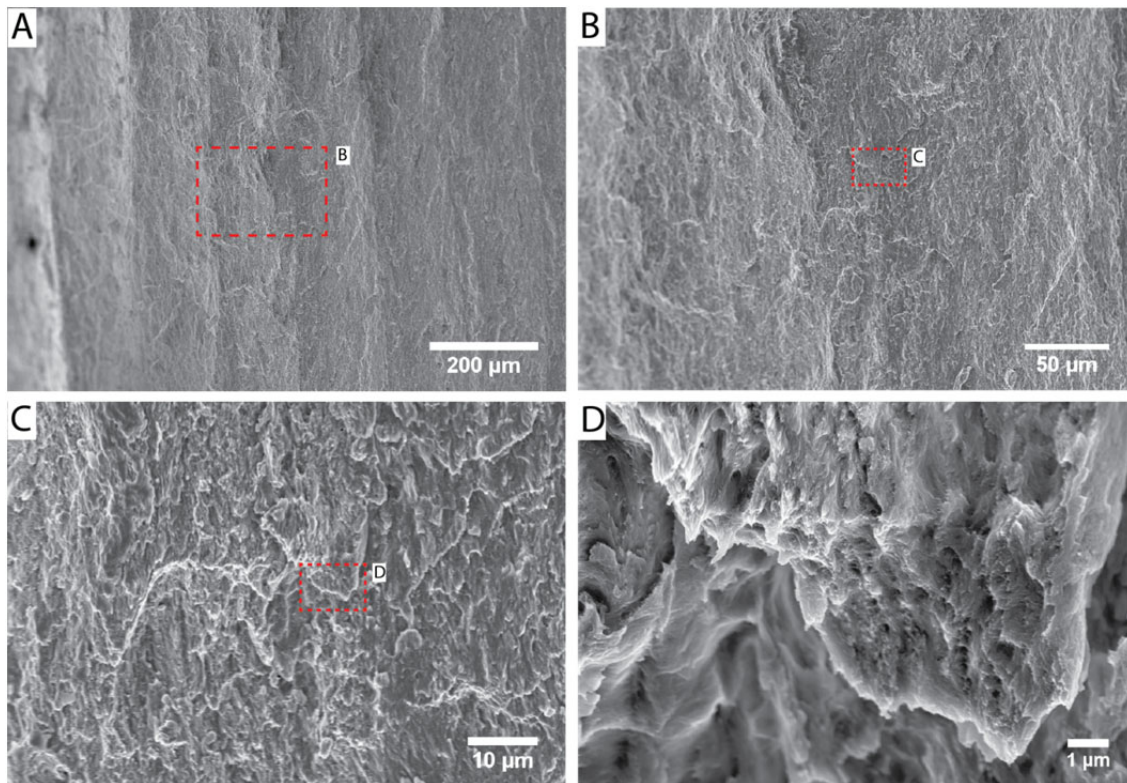


Figure C. 13 SEM images depicting fractured surfaces of a composite obtained through the wet densification and infiltration process. Individual printed lines and filament interfaces free of pores are visible.

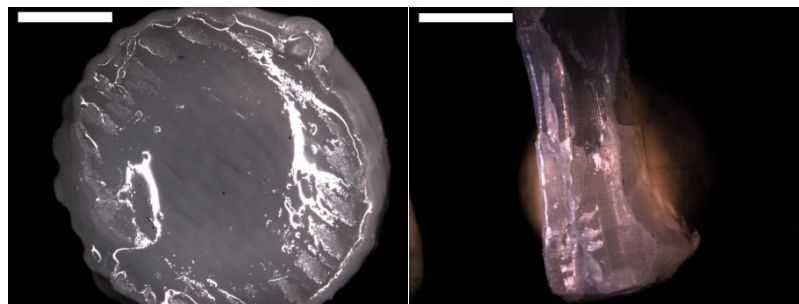


Figure C. 14 Optical microscopy images of composites obtained by the wet densification and infiltration process, showing a dense part free of macroscopic residual porosity. (scale bar 2 mm).



Figure C. 15 Macroscopic shapes of freshly printed gel (top left), after immersion in ethanol bath (top center) and after wet infiltration. Fresh gels and wet-infiltrated scaffolds can withstand loads of 2g and 1 kg, respectively, without undergoing mechanical failure.

Appendix C8: Optical transparency of printed structures measured by UV-Vis spectroscopy

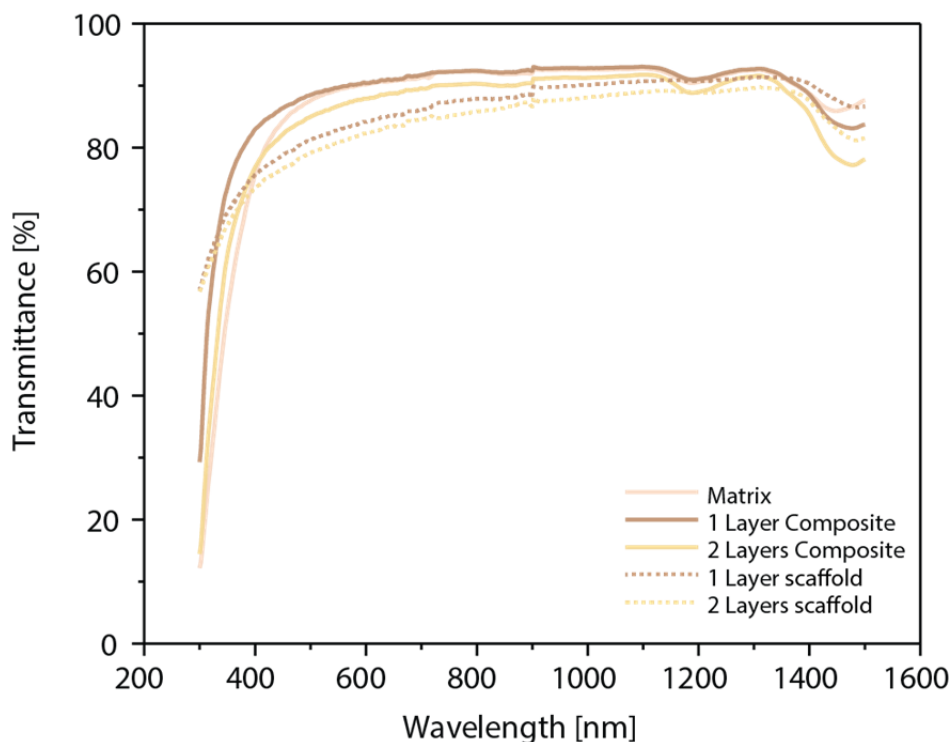


Figure C. 16 Optical transmittance of printed parts as a function of wavelength for different compositions: Matrix, scaffolds and composites comprising 1 and 2 layers. Because of the different thicknesses of the samples (thickness of each layer ≈ 0.3 mm), the transmittance data should be compared between samples of the same thickness (either 1 or 2 layers). Overall, the results show that impregnation of the scaffold with the monomers followed by in-situ polymerization improves the transparency of the final composite.

Appendix C9: Mechanical properties of printed structures under quasi-static and dynamic conditions

The increased mechanical properties of neat cellulose films can be explained partially by the hornification of cellulose fibers during drying. This process results in the formation of additional hydrogen bonds which strongly hold together the fibers and prevent its dispersion if immersed in water.¹³

Flexural tests were conducted to study the effect of nanocellulose alignment and inter-filament adhesion on the mechanical properties of the composites. To this end, samples displaying different filament orientations with respect to the applied bending stresses were tested in a three-point bending setup (Figure C. 17). The results show that composites with nanocellulose particles aligned parallel to the applied stresses (longitudinal configuration) reach a flexural modulus of 7.9 GPa, which is two-fold higher than that obtained when the specimens are tested in the perpendicular direction (transversal configuration). Despite the higher elastic modulus achieved in the longitudinal configuration, the strength of the composite was found to reach a comparable value of 40 MPa irrespective of the CNC alignment direction.

To complement the mechanical properties discussed in the main text (Figure 4.3) and above (Figure C. 17), we present in Figure C. 18 the elongation at break of printed structures tested under (A) tensile and (B) flexural mode. The results indicate that the reinforcing effect of the cellulose particles is accompanied by a significant reduction in the maximum elongation of the polymer matrix.

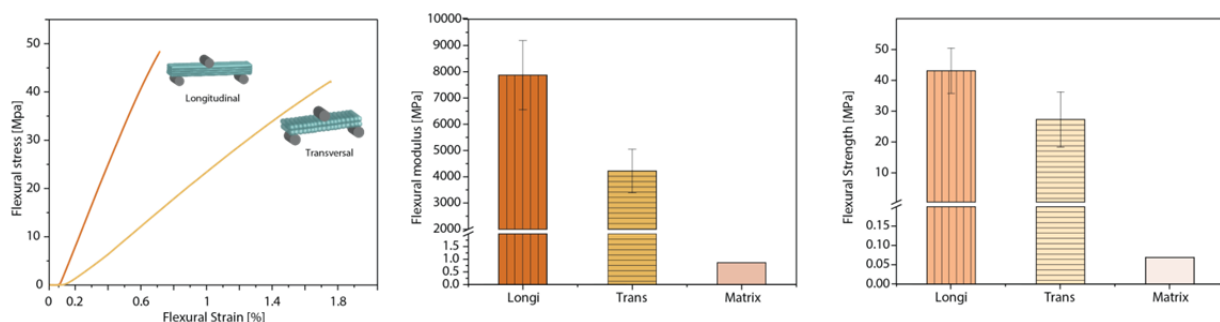


Figure C. 17 Mechanical performance in flexural mode of 3D-printed composites obtained through the wet densification approach. (Left) Representative stress-strain curves of the matrix and 3D-printed composites in flexural mode. (Center) Flexural modulus and (Right) strength of the matrix and of composites tested in the longitudinal and transversal directions.

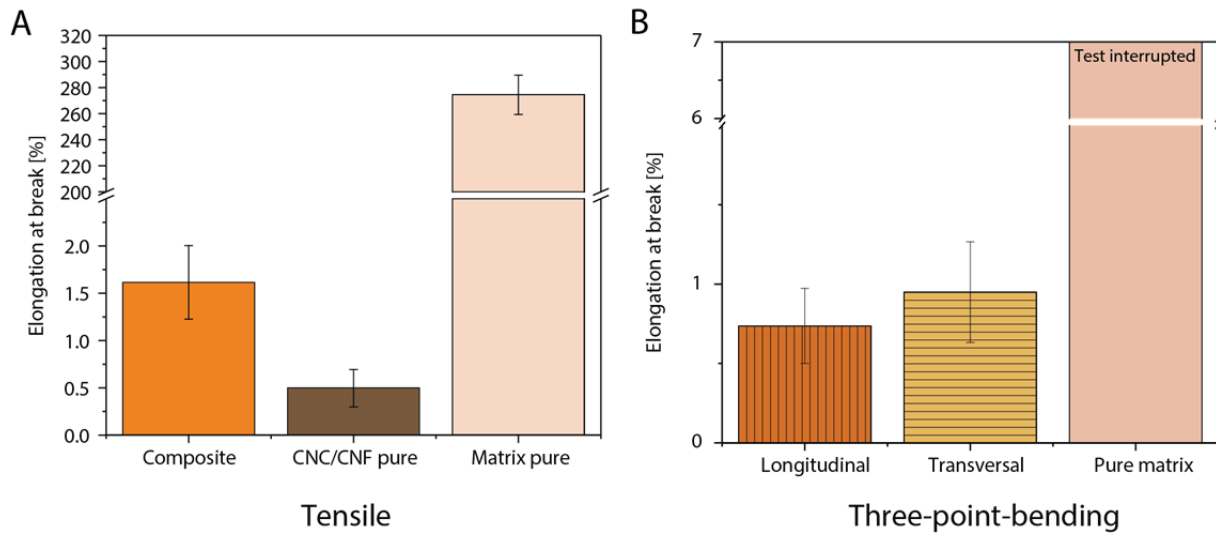


Figure C. 18 Elongation at break for composites tested under A) tensile and B) three-point-bending modes.

The reinforcing effect of CNCs/CNFs particles and the influence of the printing direction on the mechanical properties of the composites were also investigated using Dynamic Mechanical Analysis (DMA, Figure C. 19). In line with the other mechanical tests, the DMA measurements show that the composite materials exhibit a significantly higher storage modulus and lower dissipation factor ($\tan\delta$) as compared to the pure matrix. Composites fabricated with two layers are stiffer than those containing only one layer as the former exhibits higher alignment degree (see Table C. 3). As expected, composites tested perpendicular to the printing direction (T) presents lower storage modulus as compared to those tested in the parallel configuration (L). The effective glass transition temperature of the composites was found to be slightly lower compared to the matrix (Table C. 4), possibly due to the presence of residual water in the cellulose particles that mildly plasticizes the polymer matrix.

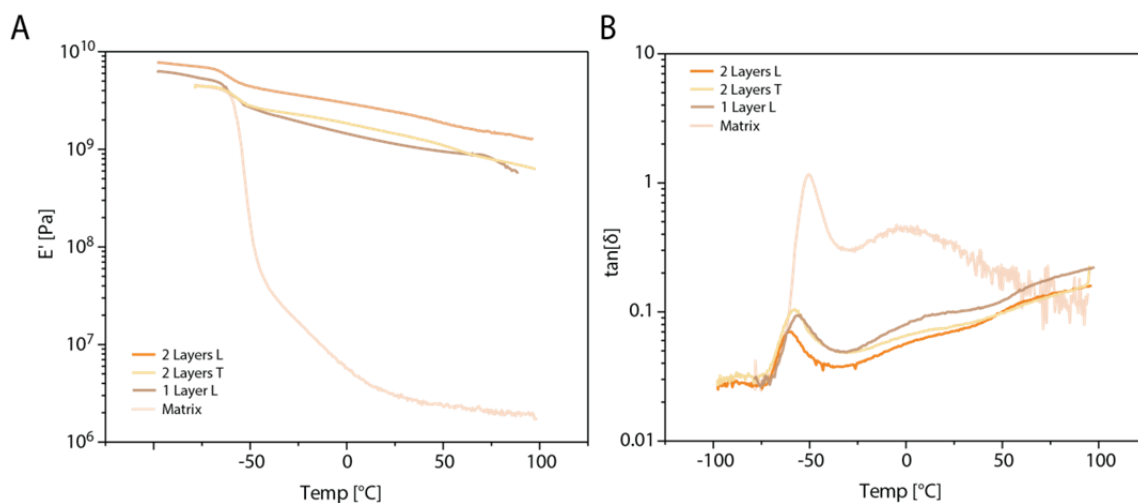


Figure C. 19 Dynamic Mechanical Analysis of pure matrix and cellulose-based composites. (A) Storage modulus and (B) dissipation factor, $\tan\delta$, as a function of temperature.

Table C. 4 Summary of thermo-mechanical data obtained by DMA: glass transition temperature (T_g), dissipation factor ($\tan\delta$) and storage modulus at two different temperatures.

Sample	$\tan(\delta)$ at 25 °C	T_g [°C]	E' [MPa] at 25 °C	E' [MPa] at 50 °C
Matrix	0.2964	-50.63	2.99	2.31
1 Layer L	0.0772	-59.44	1170	973
2 Layers L	0.0710	-57.71	2400	1890
2 Layers T	0.0997	-55.95	1450	1100

Appendix C10: Infiltration of wet densified scaffolds with different polymer matrices

The versatility of the wet densification process allows for the infiltration of wet scaffolds with different photopolymerizable liquid systems, thus enabling tuning of the properties of the final cellulose-based composites. This is demonstrated here by infiltrating a wet-densified scaffold with two polymer matrices with distinct soft and stiff mechanical response (Figure C. 20). Mechanical testing of the resulting composites show that scaffolds infiltrated with a stiffer acrylate / polyurethane (BR571) monomer mixture ¹ display a 2-fold higher elastic modulus compared to samples containing a softer acrylate in the polymer matrix (BR 3741AJ).

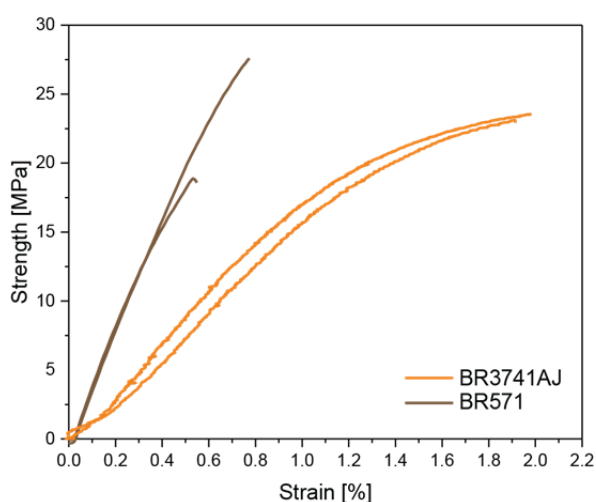


Figure C. 20 Mechanical properties under tensile mode of composites obtained by wet densification followed by wet infiltration with two different oligomer systems based on acrylate/polyurethane mixtures. The grades BR571 and BR3741AJ refer to the stiff and soft polyurethanes, respectively.

Appendix C11: Morphology of cellulose nanocrystals (CNC) and nanofibrillated cellulose (CNF)

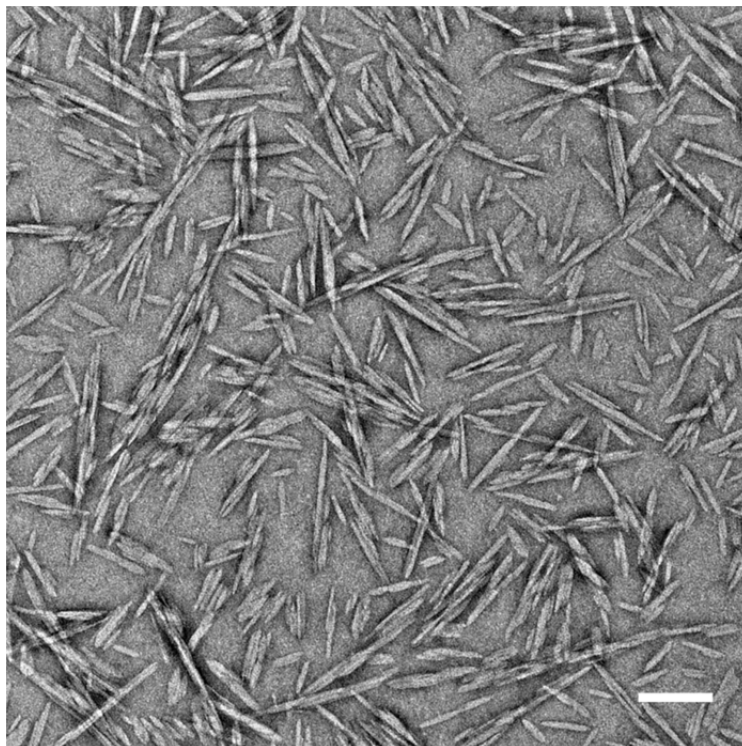


Figure C. 21 Representative TEM image of the CNCs used throughout this study. Scale bar 100 nm.

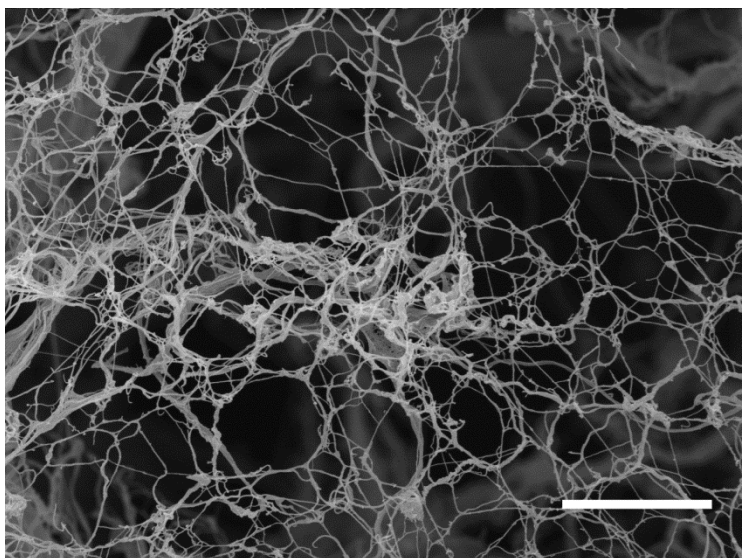


Figure C. 22 Representative SEM image of the nanofibrillated cellulose (CNF) used throughout this study. Scale bar 6 μm .

Appendix C12: Estimation of composite solid content

Two different approaches were used to calculate the volume fraction of cellulose nanocrystals in the final composites: the Archimedes method and a geometrical estimation. As the density of CNCs reported in the literature varies between 1.5 and 1.6 g/cm³,^{14, 15} we measured this value for the CNCs used in this work to maximize the accuracy of the calculated volume fractions. A cellulose density value of 1.56 g/cm³ was obtained by measuring the weight and volume of water-free CNC films. To ensure complete removal of air, the CNC films were soaked in ethyl acetate under vacuum prior to the density measurement. In the Archimedes methods, the density is calculated from the weight of the sample in dried, wet and submerged states.¹⁶ The geometrical approach consists in measuring the weight of individual constituents (resin and CNC/CNF) during the fabrication process and the final volume of the specimen. The cellulose (CNC/CNF) volume fractions were found to be 27.3 ± 1.8 vol % and 28.2 ± 1.67 vol % using the Archimedes and geometrical approaches, respectively.

References

1. Siqueira, G., D. Kokkinis, R. Libanori, M.K. Hausmann, A.S. Gladman, A. Neels, P. Tingaut, T. Zimmermann, J.A. Lewis, and A.R. Studart, Cellulose Nanocrystal Inks for 3d Printing of Textured Cellular Architectures. *Adv. Funct. Mater.*, **2017**. 27: p. 1604619.
2. Reid, M.S., M. Villalobos, and E.D. Cranston, Cellulose Nanocrystal Interactions Probed by Thin Film Swelling to Predict Dispersibility. *Nanoscale*, **2016**. 8: p. 12247-12257.
3. Charles Bruel, Q.B., Jason R. Tavares, Pierre J. Carreau, Marie-Claude Heuzey, The Apparent Structural Hydrophobicity of Cellulose Nanocrystals. *J-FOR*, **2018**. 7.
4. Hansen, C.M., Hansen Solubility Parameters: A User's Handbook. Second edition **2007**, Boca Raton FL: CRC Press, Inc., .
5. Steven Abbott, C.M.H.a.H.Y., Hansen Solubility Parameters in Practice – Complete with Software, Data, and Examples. **2015**: www.hansen-solubility.com.
6. Schneider, L.V., A Three-Dimensional Solubility Parameter Approach to Nonaqueous Enzymology. *Biotechnology and Bioengineering*, **1991**. 37: p. 627-638.
7. Peng, S.X., H. Chang, S. Kumar, R.J. Moon, and J.P. Youngblood, A Comparative Guide to Controlled Hydrophobization of Cellulose Nanocrystals Via Surface Esterification. *Cellulose*, **2016**. 23: p. 1825-1846.
8. Håkansson, K.M.O., I.C. Henriksson, C. de la Peña Vázquez, V. Kuzmenko, K. Markstedt, P. Enoksson, and P. Gatenholm, Solidification of 3d Printed Nanofibril Hydrogels into Functional 3d Cellulose Structures. *Adv. Mater. Technol.*, **2016**: p. 1600096-n/a.
9. Li, V.C.F., A. Mulyadi, C.K. Dunn, Y. Deng, and H.J. Qi, Direct Ink Write 3d Printed Cellulose Nanofiber Aerogel Structures with Highly Deformable, Shape Recoverable, and Functionalizable Properties. *ACS Sustainable Chem. Eng.*, **2018**. 6: p. 2011-2022.
10. Wu, Y., Z.Y. Lin, A.C. Wenger, K.C. Tam, and X. Tang, 3d Bioprinting of Liver-Mimetic Construct with Alginate/Cellulose Nanocrystal Hybrid Bioink. *Bioprinting*, **2018**. 9: p. 1-6.

11. Buchtová, N. and T. Budtova, Cellulose Aero-, Cryo- and Xerogels: Towards Understanding of Morphology Control. *Cellulose*, **2016**. 23: p. 2585-2595.
12. Reising, A.B., R.J. Moon, and J.P. Youngblood, Effect of Particle Alignment on Mechanical Properties of Neat Cellulose Nanocrystal Films. *J-FOR*, **2012**. 2: p. 32-41.
13. Eyholzer, C., N. Bordeanu, F. Lopez-Suevos, D. Rentsch, T. Zimmermann, and K. Oksman, Preparation and Characterization of Water-Redispersible Nanofibrillated Cellulose in Powder Form. *Cellulose*, **2010**. 17: p. 19-30.
14. Dufresne, A., Nanocellulose: A New Ageless Bionanomaterial. *Mater. Today*, **2013**. 16: p. 220-227.
15. Habibi, Y., L. Lucia, A., and O. Rojas, J., Cellulose Nanocrystals: Chemistry, Self-Assembly, and Applications. *Chem. Rev.*, **2010**. 110: p. 3479-3500.
16. Testing, A.S.f. and M.S.C.B.o. Bearings, Standard Test Methods for Density of Compacted or Sintered Powder Metallurgy (Pm) Products Using Archimedes' Principle. **2015**: ASTM International.

Appendix D

Appendix to “Cellulose-based Microparticles for Magnetically-controlled Optical Modulation and Sensing”

Appendix D1: Microfluidic platform

Microfluidic platform used for the preparation of CNC-based microparticles.



Figure D. 1 Microfluidic platform used for the preparation of CNC-based microparticles. Top: Microfluidic setup mounted on an optical microscope. Bottom: Spiraling cylindrical tube used to cure stretched droplets, thus leading to microparticles with birefringent properties and anisotropic shape.

Support Information D2: Rheology of CNC suspensions

Shear sweep measurements under steady conditions reveal that the CNC suspensions show shear thinning behavior and relatively low viscosity for particle concentrations in the range 6 – 10wt% CNC (Figure D. 2). The apparent viscosity at any given shear rate increases with the cellulose content. The addition of SPIONs increases the viscosity of suspensions containing up to 8wt% CNC.

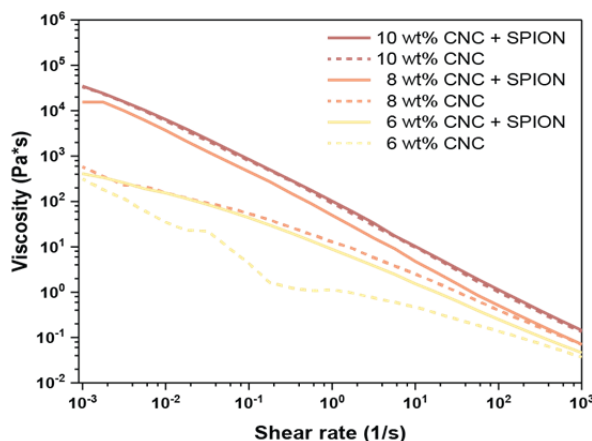


Figure D. 2 Apparent viscosity of CNC suspensions as a function of the shear rate applied in shear sweep measurements performed under steady-state conditions. The investigated suspensions contain cellulose concentrations ranging from 6 to 10 wt % with and without 2 wt% SPIONs.

Appendix D3: Aspect ratio of CNC-laden microparticles

The aspect ratio of the CNC-laden microparticles can be tuned by varying the flow rates of the inner and outer phases used for droplet formation in the microfluidic platform (Figure D. 3 and Figure D. 4). Changes in the ratio of the inner and outer flow rates lead to distinct droplet sizes and flow rates in the collecting tube. From experiments carried out with a wide range of suspension formulations and emulsification conditions (Table D. 1), we observed that the length of the CNC-laden microparticles obtained after droplet polymerization increases linearly with the liquid flow rate in the collecting cylindrical tube.

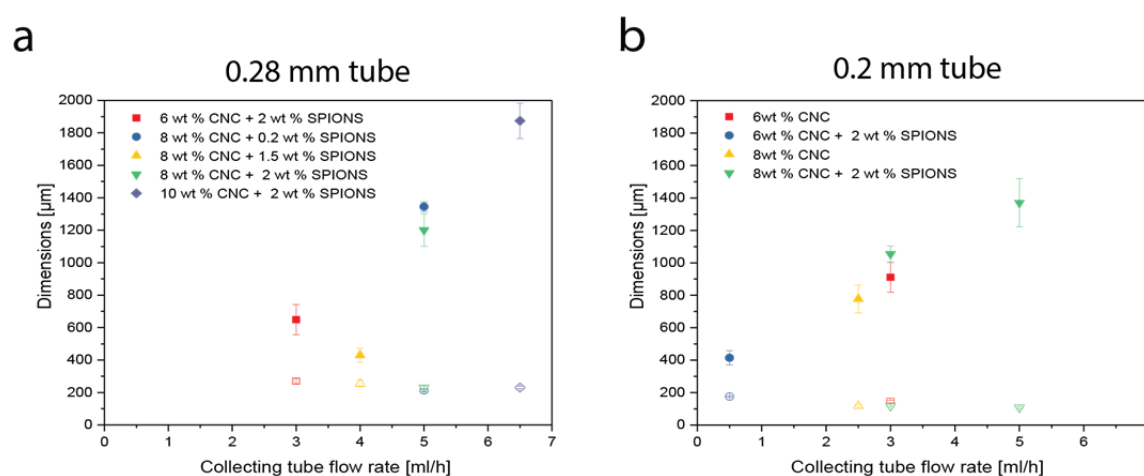


Figure D. 3 Correlation between the length of the microparticles (full symbols) and the experimentally-measured flow rate in the collecting tube. Data are shown for tube diameters of (a) 0.28 mm and (b) 0.20 mm. The diameters of the microparticles are shown as open symbols. The flow rate in the collecting tube was measured by with respect to the extrusion flow set on the syringe pump.

Table D. 1 Suspension formulations and emulsification conditions used to obtain CNC-laden microparticles with tunable aspect ratio.

N°	Composition	Flow rates [$\mu\text{L/h}$]		Tube diameter [mm]	Particle length [μm]		Particle diameter [μm]	
		Inner (Q_i)	Outer (Q_o)		Mean	Standard deviation	Mean	Standard deviation
1	6 wt % CNC	100	1500	0.2	1535.4	230.68	152.1	5.4
2	6 wt % CNC	190	3000	0.2	910.6	92.54	144.7	8.0
3	6 wt % + 25ul SPION	30	500	0.2	414.4	44.93	175.4	4.2
4	6 wt % + 150ul SPION	35	3000	0.2	1570.0	216.82	127.5	7.4
5	8 wt % CNC	75	2500	0.2	777.9	85.6	116.9	7.4
6	8 wt % + 150 SPION	30	3000	0.2	1053.8	49.12	117.4	5.9
7	8 wt % + 150 SPION	30	5000	0.2	1369.8	147.81	106.6	5.1
8	6 wt % + 150ul SPION	40	3000	0.28	648.9	92.59	270.8	10.6
9	8 wt % + 25 SPION	30	5000	0.28	1344.9	29.63	212.9	8.1
10	8 wt % + 150 SPION	70	4000	0.28	430.3	42.44	254.9	19.7
11	8 wt % + 2 wt % SPION	80	2700	0.28	857.2	131.80	263.9	14.50
12	8 wt % + 2 wt % SPION	150	1500	0.28	1445.2	110.50	428.0	32.60
13	8 wt % + 200 SPION	30	5000	0.28	1200.4	99.22	229.6	8.6
14	10 wt % + 200 SPION	30	6500	0.28	1874.1	108.70	230.3	8.0

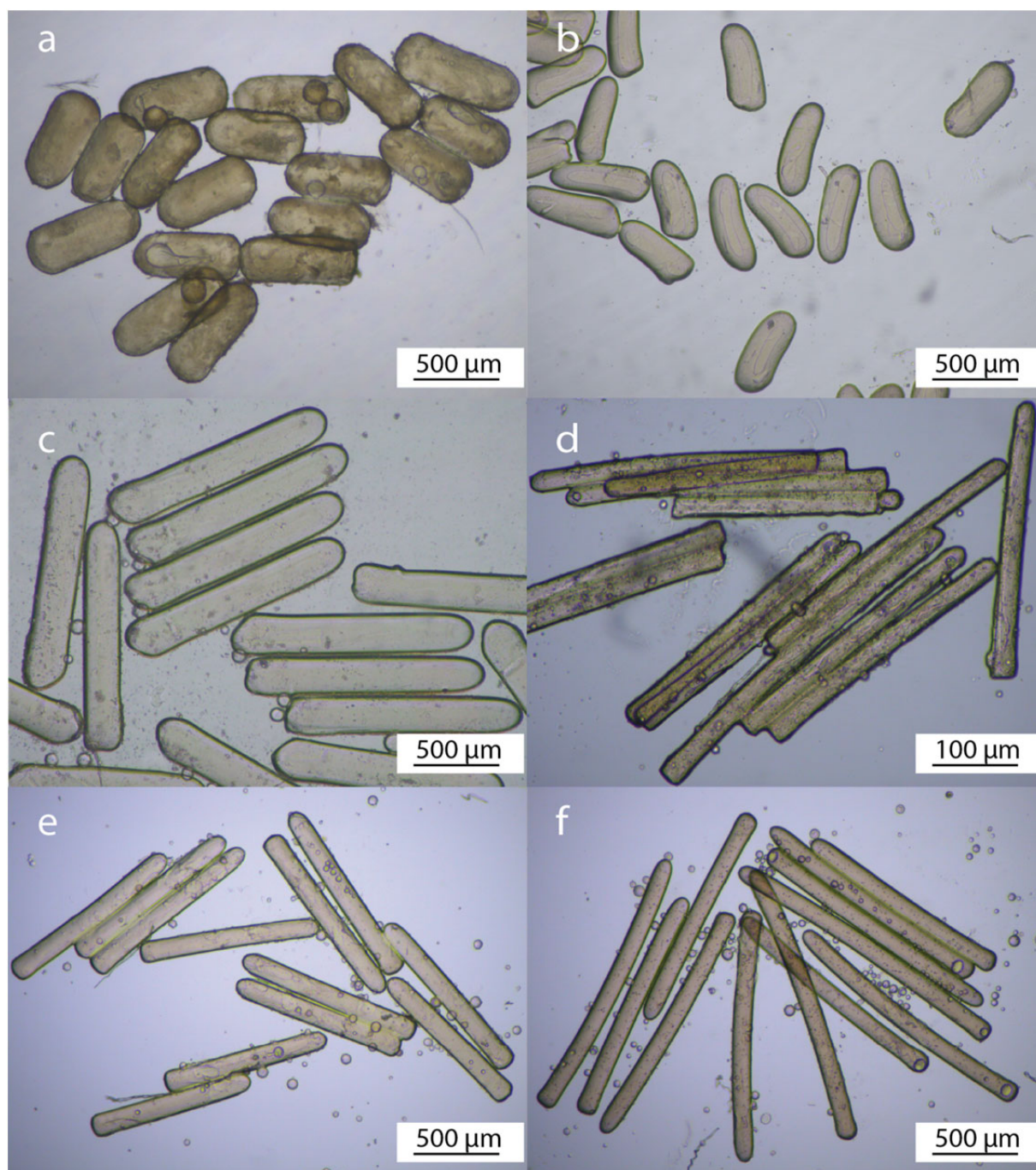


Figure D. 4 Optical microscopy images of CNC-laden microparticles of distinct aspect ratios prepared using some of the compositions and emulsification conditions shown in Table S1: (a) sample N°8, (b) sample N°10, (c) sample N°9, (d) sample N°4, (e) sample N°6, and (f) sample N°7.

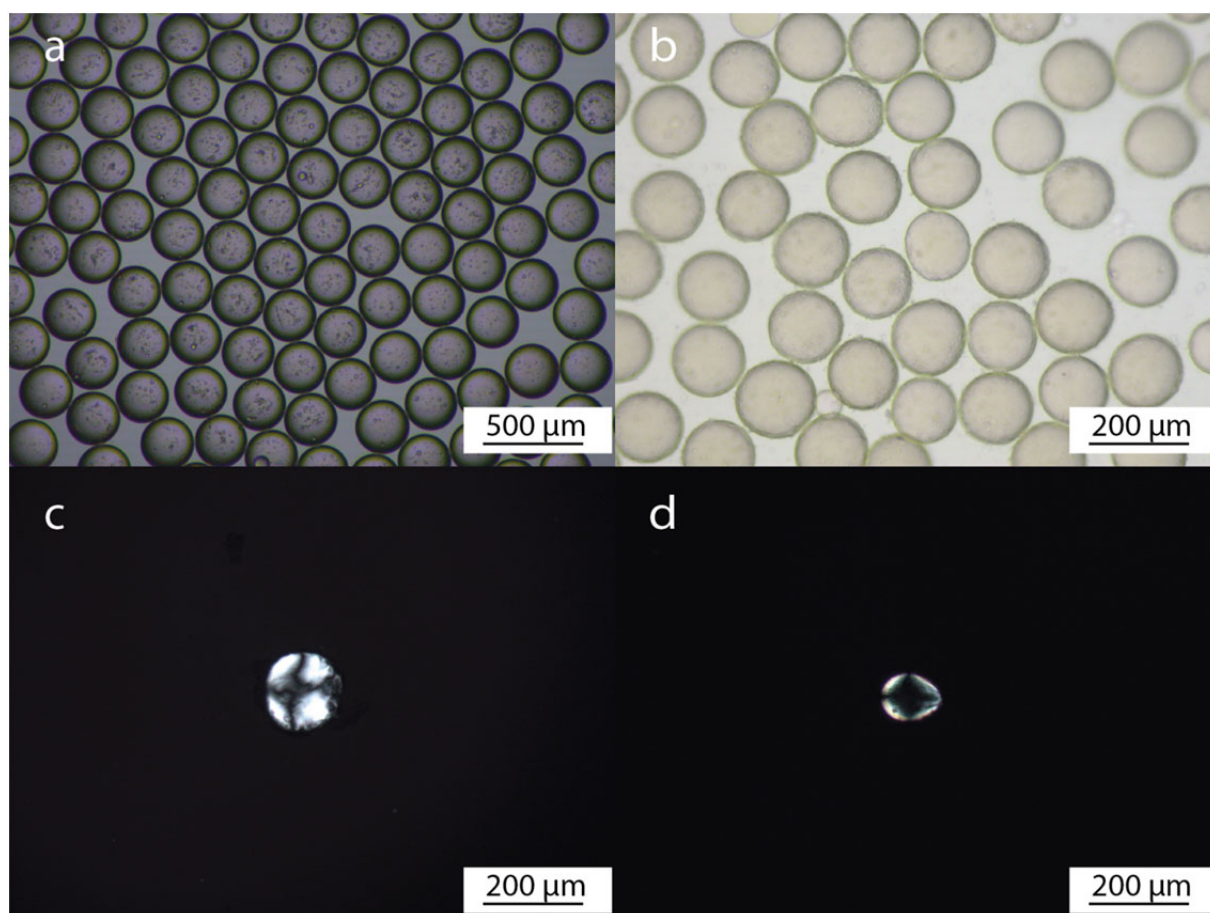


Figure D. 5 Spherical microparticles generated by polymerization of unstretched water droplets of different compositions. The micrographs show optical microscopy images obtained (a,b) without optical filters and (c,d) under cross-polarizers for water droplets containing (a,c) 8 wt% CNC and 2wt% SPIONs or (b,d) 6 wt% CNC and SPIONs.

Appendix D4: Analysis of torque balance as predictive model

A balance between the magnetic and viscous torques acting on a CNC-based microparticle exposed to a rotating magnetic field leads to the following prediction for the critical step-out frequency ($\omega_{mag,c}$, main text):¹

$$\omega_{mag,c} = \frac{\mu_0 (\chi_f \phi_f)^2 H_0^2}{18(f/f_0)\eta(\chi_f \phi_f + 2)} \quad Eq. 1$$

where H_0 is the amplitude of the applied magnetic field, χ_f is the magnetic susceptibility of the SPIONs, ϕ_f is the volume fraction of SPIONs, η is the viscosity of the suspending fluid, μ_0 is the magnetic permeability of free space ($\mu_0 = 4\pi * 10^{-7}$ H/m) and f/f_0 is the Perrin friction factor.

The Perrin friction factor is given by:

$$\frac{f}{f_0} = \frac{4(1 - p^2)}{3(2 - p^2 a S)} \quad Eq. 2$$

where p is the aspect ratio of the microparticle (b/a), a is the microparticle diameter and

$$S = \left(\frac{2}{a}\right) (p^2 - 1)^{-1/2} \tan^{-1}[(p^2 - 1)^{1/2}] \quad Eq. 3$$

This model can predict the step-out frequency of the CNC microparticle only if the magnetically-induced motion of the microparticle is controlled solely by magnetic and viscous forces. Because the only unknown variable in the above equations is the magnetic susceptibility of the SPIONs (χ_f), we use this analysis to test the validity of our assumption. The assumption is tested by comparing the χ_f value predicted from our model with susceptibility data previously reported in the literature. Using the equations above and the data available from our experiments (Table D. 2), we estimate a value of 21.2 for the magnetic susceptibility of the SPIONs. Given the very good agreement of this prediction with the previously reported susceptibility of 21,[1] we conclude that the motion of the CNC-based microparticles are indeed dominated by the viscous and magnetic forces imposed by the suspending fluid and the applied external magnetic field, respectively.

Table D. 2 Experimental parameters relevant for the simple torque balance model.

Parameter	
μ_0	$4\pi * 10^{-7} \text{ H/m}$
H_0	19144.8 A/m
ϕ_f	0.0997 vol%
b	756 μm
a	250 μm
η	0.00089 PaS

Reference

- 1 R.M. Erb, J. Segmehl, M. Charilaou, J.F. Löffler, and A.R. Studart, *Soft Matter*, **2012**. 8: 7604.

Declaration

Dynamics of Cellulose Nanocrystals Alignment during 3D Printing

Jörg Läger provided the rheology setup for *in-situ* polarized light rheology. The contact and relationship between Anton Paar and ETH was possible thanks to Patrick A. Rühs. Patrick A. Rühs and Michael Hausmann designed and executed the experiments and measurements. André R. Studart, Gilberto Siqueira, Michael Hausmann, Patrick A. Rühs, Rafael Libanori and Tanja Zimmermann discussed both results and experimental plan. The paper was co-written by André R. Studart, Michael Hausmann and Patrick A. Rühs. All authors revised the paper and the results.

Alignment dynamics of cellulose nanocrystals under flow in a 3D printing nozzle

The Small Angle X-Ray Scattering measurements (Nanostar) were performed by Felix Reifler and Michael Hausmann, whereas the 2DWAXS experiments were conducted by Antonia Neels. The SAXS and 3D tomography experiments at the Swiss light source were carried out and analysed by Manuel Guizar-Sicairos, Viviane Bueno-Lutz, Rafael Libanori and Michael Hausmann. The experiments and measurements were designed by Michael Hausmann, Rafael Libanori, Gilberto Siqueira, Tanja Zimmermann and André Studart. All the co-authors discussed the measurements and the results. The chapter was written and corrected by André Studart, Rafael Libanori, Gilberto Siqueira and Michael Hausmann.

Complex-shaped cellulose composites made by wet densification of 3D printed scaffolds

Experiments were designed by André R. Studart, Gilberto Siqueira, Rafael Libanori, Tanja Zimmermann and Michael Hausmann, and were conducted by Michael Hausmann. 2DWAXs was performed by Antonia Neels and the polymer system was developed by Dimitri Kokkinis. SEM imaging was conducted by Dimitri Kokkinis and Michael Hausmann. The main paper and the Appendix were co-written by André R. Studart, Gilberto Siqueira, Rafael Libanori and Michael Hausmann. All authors discussed and revised the manuscript.

Cellulose-based Microparticles for Magnetically-controlled Optical Modulation and Sensing

Alina Hauser, André R. Studart, Gilberto Siqueira, Rafael Libanori, Signe Lin Vehusheia, Tanja Zimmermann and Michael Hausmann were involved in the conception and design of the project. The experiments were carried out by Alina Hauser during her Master Thesis, Signe Lin Vehusheia during her Master semester project and by Michael Hausmann. The magnetic alignment experiments were conducted by Michael Hausmann together with Simone Schürle. The main paper and the Appendix were co-written by André R. Studart, Gilberto Siqueira, Rafael Libanori and Michael Hausmann. All authors discussed the results, the conclusions and revised the manuscript at all stages.

